SEARCH FOR TEV-SCALE GRAVITY SIGNATURES IN FINAL STATES WITH LEPTONS AND JETS WITH THE ATLAS DETECTOR AT $\sqrt{S} = 8$ TEV

A Dissertation Presented

by

GERMAN COLÓN

Submitted to the Graduate School of the
University of Massachusetts Amherst in partial fulfillment
of the requirements for the degree of

DOCTOR OF PHILOSOPHY

May 2013

Physics

SEARCH FOR TEV-SCALE GRAVITY SIGNATURES IN FINAL STATES WITH LEPTONS AND JETS WITH THE ATLAS DETECTOR AT $\sqrt{S} = 8$ TEV

A Dissertation Presented

by

GERMAN COLÓN

Approved as to style and content by:

Carlo Dallapiccola, Chair

Stéphane Willocq, Member

Andrea Pocar, Member

Daniela Calzetti, Member

Donald Candela, Department Chair
Physics

ACKNOWLEDGEMENTS

This dissertation marks the culmination of a long, exciting, and sometimes painful journey to obtaining my doctoral degree. Along the way I have received the support, encouragement, nurture and advice of many people, to all of whom I'm indebted. Serve these lines as a recognition of their contributions to this experience.

I would like to thank my advisor, Carlo Dallapiccola, for giving me the opportunity to join his research team. I am grateful for his continuous support, guidance, teachings, and above all, his patience while doing so. Not only was I lectured in physics, but through our engaging conversations, and many cups of coffee, I learned to apply the same rational thinking in everyday life.

A special thanks to the other members of my thesis committee, Stéphane Willocq, Andrea Pocar and Daniela Calzetti, for their questions, their feedback, and all the time dedicated to reading this dissertation in such a short period of time. I would also like to thank my UMass ATLAS colleagues for all their help in this endeavor.

My most sincere thanks to my friends, family and colleagues for their time, their motivation, and for tolerating me all these years. It is not possible to name them all, but I am aware that they have been part of this journey.

ABSTRACT

SEARCH FOR TEV-SCALE GRAVITY SIGNATURES IN FINAL STATES WITH LEPTONS AND JETS WITH THE ATLAS DETECTOR AT $\sqrt{S} = 8$ TEV

MAY 2013

GERMAN COLÓN

B.S., UNIVERSITY OF PUERTO RICO, MAYAGÜEZ

Ph.D., UNIVERSITY OF MASSACHUSETTS, AMHERST

Directed by: Professor Carlo Dallapiccola

Theories postulating extra spatial dimensions into which the gravitational field can propagate provide interesting extensions to the Standard Model addressing the hierarchy problem. These frameworks predict TeV-scale gravity signatures, such as black hole or string ball production, that could be observed at the Large Hadron Collider. Said black holes decay into a high multiplicity of particles with typical energies ranging in the few 100 GeV. The production of events with multiple high transverse momentum particles including charged leptons and jets is measured, using 13.0 fb^{-1} of proton-proton collision data recorded by the ATLAS detector during 2012 at $\sqrt{s} = 8$ TeV. No excess beyond Standard Model expectations is observed, and upper limits on the cross sections for non-Standard Model production of these final states are set.

TABLE OF CONTENTS

APPENDICES

LIST OF TABLES

LIST OF FIGURES

Figure **Page**

INTRODUCTION

The main objective of particle physics is to identify the building blocks of matter and describe the interactions between them. Our current understanding of the laws governing the electromagnetic, weak and strong forces is contained in a quantum field theory called the Standard Model (SM). This theory has been extensively tested for the last 30-40 years, and thus far, no experimental result contradicts the Standard Model predictions. Notwithstanding its great success, it is known that further extensions are required since, among other issues, it does not incorporate gravitational interactions and suffers from the hierarchy problem.

There seems to be two very disparate fundamental scales in nature, the electroweak[1] scale $m_{\rm EW} \sim 10^3$ GeV, and the Planck scale $M_{\rm Pl} = \sqrt{1/G_{\rm N}} \sim 10^{19}$ GeV, where gravitational effects are comparable to the gauge interactions. Explaining this apparent hierarchy has been a driving force in the construction of theories Beyond the Standard Model (BSM). Apart from the striking difference in the magnitude of the scales, there is another distinguishing factor. The electroweak interactions have been probed at lengths of $1/m_{\rm EW}$. However, gravity has not remotely been probed at length scales of $1/M_{\rm Pl} \sim 10^{-33}$ cm, which is 31 orders of magnitude smaller than the current tested scales of $\sim 10^{-3}$ cm.

One approach to solve this problem proposes $m_{\rm EW}$ as the only fundamental scale and spacetime to be 4+n dimensional, with Standard Model fields localized in a 4-d submanifold (brane). The apparent weakness of gravity at large distances is due to the extra spatial dimensions, where gravitons can propagate. This framework thus allows

[1]Electroweak refers to the unified description of the electromagnetic and weak forces.

for the existence of gravitational states such as black holes and, within the context of weakly-coupled string theory, string balls, which could be produced at the Large Hadron Collider (LHC). The black holes or string balls produced in particle colliders have a characteristic decay signature comprising a high multiplicity of particles with typical energies ranging in the few 100 GeV. For this reason, this thesis describes the theoretical motivations and experimental techniques employed in a search for black hole production at the LHC using the ATLAS detector.

The dissertation is structured as follows. Chapter 1 provides an overview of the theoretical motivations for a black hole search. The ATLAS detector and the LHC are described in Chapter 2. The particles reconstruction from detector information is presented in Chapter 3. Chapter 4 describes the event selection and background estimation techniques in the search for black hole events. The results and conclusions are presented in Chapters 5 and 6, respectively. Supporting material is included in the Appendices.

Throughout this document, natural units are used where the speed of light c and Planck's constant $\hbar$ are normalized to unity. In this system, $c = \hbar = 1$, mass and momentum are defined in units of energy (e.g. GeV), while lengths can be defined in units of energy^{-1}.

CHAPTER 1

THEORETICAL BACKGROUND

This chapter provides the theoretical motivation for this dissertation. Section 1.1 introduces the Standard Model of particle physics, while Sec. 1.2 briefly describes the Higgs mechanism. The central question is posited in Sec. 1.3, where the hierarchy problem is explained. The concept of extra dimensions is presented in Sec. 1.4. Section 1.5 is dedicated to the production, decay, and characteristic signatures of TeV-scale gravitational states (black holes and string balls). Previous searches are discussed in Sec. 1.6.

1.1 The Standard Model

There are four known fundamental forces in nature: gravity, electromagnetism, weak and strong. Our knowledge of the strong and electroweak interactions is summarized in the relativistic quantum field theory known as the Standard Model. It comprises spin-$\frac{1}{2}$ fermions as the constituents of matter, and integer spin[1] gauge bosons as force carriers, mediating the interactions. The latter are associated to the gauge symmetry group $SU(3)_C \times SU(2)_L \times U(1)_Y$, where C denotes color charge, L denotes weak isospin, coupling only left-handed fermions, and Y refers to weak hypercharge[2].

[1]Spin is a quantum mechanical phenomenon of an intrinsic form of angular momentum carried by elementary particles and measured in units of $\hbar$.

[2]Weak isospin is a quantum number relating to the weak interaction, where particles with similar properties are regarded as different states of a same particle. It has the same mathematical structure used to describe spin. Weak hypercharge is a conserved quantum number relating the electrical charge and the third component of weak isospin. It acts on both right- and left-handed fermions.

The matter fermions are particles that obey Fermi-Dirac statistics and are classified in two groups: leptons and quarks. The leptons are charged under the $SU(2) \times U(1)$ gauge group, that is, they experience the electroweak force. There are six lepton flavors, not counting their antiparticles. Three have unit electrical charge, in multiples of the elementary charge e, while the others, the neutrinos, are electrically neutral. The leptons can be organized in three "families" or "generations", each generation consisting of a charged and a neutral lepton of the same flavor. Thus, in this arrangement, the electron (e^-) is paired with the electron-neutrino (ν_e), followed by the muon (μ^-) and the tau (τ^-), with the corresponding muon and tau neutrinos (ν_μ and ν_τ).

The quarks are charged under $SU(3) \times SU(2) \times U(1)$, meaning that they couple to all the force carriers. There are six quark flavors, not counting the antiparticles. They are identified as up (u), down (d), charm (c), strange (s), top (t) and bottom (b). Quarks carry fractional electrical charge: $+\frac{2}{3}e$ for u, c and t, and $-\frac{1}{3}e$ for d, s and b. Additionally, quarks posses an internal quantum number called "color" which is the source of the strong force. This strong interaction is described by Quantum Chromodynamics (QCD). In contrast to the leptons, quarks are not found as free particles, but in color-neutral bound states called hadrons[3]. This is a direct consequence of the phenomenon known as "confinement". The quarks can also be arranged in three generations, ordered by increasing mass, including a positively and a negatively charged quark. Table 1.1 outlines the properties of the SM fermions.

The gauge bosons are particles that obey Bose-Einstein statistics and represent the quanta of the gauge fields. In the language of quantum field theory, interactions are described through the exchange of said gauge bosons. In the SM, there are three

[3]Two types of hadrons are found in nature: baryons, comprising three quarks (qqq), and mesons, comprising a quark-antiquark pair ($q\bar{q}$).

Table 1.1. The Standard Model fermions, their mass and electric charge, sorted by generation.

fermion	Generation (Mass [GeV]) i	ii	iii	Q [e]
leptons	ν_e (< 2 x10^{-9})	ν_μ (< 1.9 x10^{-4})	ν_τ (< 1.8 x10^{-2})	0
	e (5.11 x10^{-4})	μ (1.06 x10^{-1})	τ (1.78)	-1
quarks	u ($1.8 - 3.0$ x10^{-3})	c (1.275 ± 0.025)	t (173.5 ± 1.0)	$+\frac{2}{3}$
	d ($4.5 - 5.5$ x10^{-3})	s (9.5 ± 0.5 x10^{-2})	b ($4.15 - 4.68$)	$-\frac{1}{3}$

types of force carriers corresponding to the three fundamental forces in the theory. The properties of these force carriers are summarized in Table 1.2.

The photon (γ) mediates the electromagnetic interactions; the gluons (g) mediate the strong force; and the $W^\pm$ and Z bosons are exchanged in weak interactions. With the exception of the $W^\pm$, all other gauge bosons are electrically neutral, and only the mediators of the weak force are massive[4]. The mechanism by which the weak force carriers acquire mass is of particular interest and is discussed in the next section.

Table 1.2. The Standard Model gauge bosons, their mass, electric charge and the interaction they mediate.

boson	interaction	Mass [GeV]	Q [e]
γ	electromagnetic	0	0
g	strong	0	0
$W^\pm$	weak	80.385 ± 0.015	± 1
Z	weak	91.188 ± 0.002	0

[4]The hypothetical mediator of gravitational interactions in the quantum field theory framework is called the graviton (G). It is expected to be a spin-2 massless particle.

1.2 EWSB and the Higgs Mechanism

At energies below the electroweak scale, the $SU(2)_L \times U(1)_Y$ gauge symmetry group of the Standard Model is broken to the $U(1)_{EM}$ group. The experimentally observed photon, and the $W^{\pm}$ and Z bosons originate from different mixings of the massless $SU(2)_L \times U(1)_Y$ generators (W^i_μ, B_μ). This process of electroweak symmetry breaking (EWSB), in which the gauge field quanta acquire mass, can be accomplished through the Higgs Mechanism [19–22].

The implementation of said mechanism is achieved by introducing to the SM Lagrangian a $SU(2)$ complex doublet of scalar Higgs fields

$$\phi = \frac{1}{\sqrt{2}} \begin{pmatrix} \varphi_1 + i\varphi_2 \\ \varphi_3 + i\varphi_4 \end{pmatrix} = \begin{pmatrix} \varphi^+ \\ \varphi^0 \end{pmatrix}$$

with a (self-interaction) scalar potential of the form

$$V = -\mu^2 \phi^\dagger \phi + \lambda \left(\phi^\dagger \phi\right)^2$$

where λ is the scalar self coupling. Minimizing the potential gives rise to a non-trivial ground state configuration and the scalar field develops a vacuum expectation value[5]

$$\left(\phi^\dagger \phi\right) = \frac{1}{2}\frac{\mu^2}{\lambda} = \frac{1}{2}\upsilon^2.$$

The parameter $\upsilon \approx 246$ GeV is the electroweak scale[6]. Its value can be calculated from the charged current for muon decay[7].

---

[5]For this scalar potential, the extremum $\phi = 0$ does not corresponds to the energy minimum, instead, it is an (unstable) local maximum. The ground state (vacuum) is no longer unique, and Nature has to make a choice for a value of ϕ.

[6]As discussed in Ref. [23], it is possible to construct models of particle physics that resemble the Standard Model, but with a richer spectrum in the range above 100 GeV and below a few TeV. For this reason, the electroweak scale can be extended to $\sim 10^3$ GeV.

[7]The interaction strength for muon decay, $\mu \to e\bar{\nu_e}\nu_\mu$, is measured very accurately to be $G_F = 1.16639 \times 10^{-5}$ GeV^{-2}. Given the relationship, in the low momentum transfer limit,

Evidently, there is a lot of freedom in selecting a minimum that satisfies the condition $\langle 0|\varphi_1^2 + \varphi_2^2 + \varphi_3^2 + \varphi_4^2|0\rangle = \frac{1}{2}\upsilon^2$, but with the appropriate choice [19]:

$$\langle \phi \rangle = \frac{1}{\sqrt{2}} \begin{pmatrix} 0 \\ \upsilon \end{pmatrix}$$

the $SU(2)_L \times U(1)_Y$ symmetry is spontaneously broken. For this choice of minimum, however, the ground state remains invariant under a subset of the symmetry group. Because $\langle \phi \rangle$ is neutral, the $U(1)_{EM}$ symmetry is not broken, resulting in a massless photon. Three of the four degrees of freedom of the scalar doublet are "absorbed" by the gauge fields, thus acquiring mass and generating the physical $W^{\pm}$ and Z bosons[8]. The fermions acquire mass via Yukawa couplings to the Higgs field ϕ. The remaining degree of freedom corresponds to a scalar particle of (bare) mass $m_H = \upsilon\sqrt{2\lambda}$, known as the Higgs boson [25–27]. On July 4, 2012, the ATLAS and CMS Collaborations at CERN announced the discovery of a particle consistent with the Higgs boson [28,29].

Despite the success of the Standard Model, it is recognized not to be a fundamental theory. There are about twenty parameters (i.e. masses, gauge coupling constants, quark-mixing angles, Higgs mass and coupling constant) that are not predicted or calculable, but which values must be determined empirically. Moreover, the SM neglects gravitational interactions. A more fundamental theory would include the GUT[9] scale ($\Lambda_{new} > 10^{16}$ GeV) or the Planck scale ($\Lambda_{new} > 10^{19}$ GeV) as its basic energy scale. The SM could then be regarded as a low energy approximation of this higher energy scale theory. This raises an important issue: the Higgs sector of the

---

$$\frac{G_F}{\sqrt{2}} = \frac{1}{2\upsilon^2}$$

the value of υ is found to be $\upsilon = (\sqrt{2}G_F)^{-1/2} \approx 246$ GeV [24,25].

[8] In principle, gauge mass terms could be inserted explicitly into the Lagrangian, but this makes the theory unrenormalizable, thus losing its predictive power. The interest is in a "spontaneously broken" symmetry, where the symmetry is simply "hidden" by the choice of ground state.

[9] GUT stands for "grand unification theories", which are theoretical attempts to unify the electroweak and strong interactions at some large energy (short distance) scale [25].

SM is sensitive to this new energy scale and the Higgs mass should assume values of order Λ_{new}. However, both theoretical and experimental considerations require the Higgs mass to be of order $m_{\rm EW}$ [23, 24]. These discrepancies in the energy scales are posited as the hierarchy problem.

1.3 The Hierarchy Problem

The Planck scale, $M_{\rm Pl} \sim 10^{19}$ GeV, denotes the energy at which the gravitational force becomes comparable to the gauge interactions. The large discrepancy in the ratio $M_{\rm Pl}/m_{\rm EW} \sim 10^{16}$ is referred to as the hierarchy problem. Some implications of this hierarchy are pertinent to the Higgs sector.

Consider the SM Higgs boson, whose mass is given by

$$m_H^2 = m_{H,0}^2 + \delta m_{H,0}^2$$

where m_H^2 is the physical mass, $m_{H,0}^2$ is the bare mass and $\delta m_{H,0}^2$ represents quantum corrections to the bare mass. The radiative correction from a fermion loop, as displayed in Fig. 1.1(a), is given by [24]

$$-i\Sigma_H(p) = \left(-i\frac{\lambda_F}{\sqrt{2}}\right)^2 \int \frac{d^4k}{(2\pi)^2} \frac{Tr[(k+m_F)((k-p)+m_F)]}{(k^2-m_F^2)[(k-p)^2-m_F]}$$

where λ_F is the fermion coupling and $m_F = \lambda_F \frac{v}{\sqrt{2}}$ is the fermion mass. Integrating with a momentum space cutoff, the contribution to the Higgs mass is found to be

$$\delta m_{H,0}^2 \equiv \Sigma_H(p) = -\frac{\lambda_F^2}{8\pi^2}\left[\Lambda^2 + (m_S^2 - 6m_F^2)\log\left(\frac{\Lambda}{m_F}\right) + ...\right] + \mathcal{O}\left(\frac{1}{\Lambda^2}\right)$$

in which ... indicates terms independent of the cutoff or vanishing when $\Lambda \to \infty$. This one-loop correction is quadratically divergent and shifts $m_{H,0}^2$ by an amount proportional to the (quadratic) cutoff

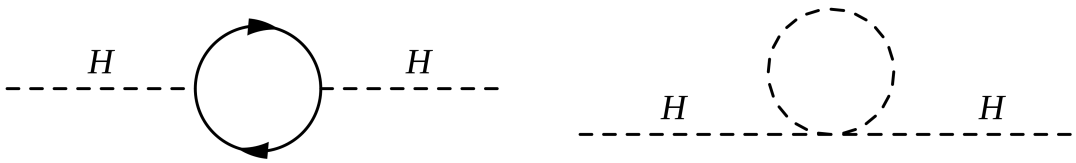

(a) (b)

Figure 1.1. (a) Fermion-antifermion and (b) scalar radiative (one-loop) corrections to the Higgs mass.

$$\delta m_{H,0}^2 \sim \Lambda_{\text{cutoff}}^2 \sim M_{\text{Pl}}^2.$$

To obtain a physical mass squared of order m_{EW}^2, traditional solutions offer three choices [23]:

- Require $m_{H,0}^2$ to be negative and precisely fine-tuned to about 34 orders of magnitude. While technically possible, this seems unnatural.
- Invoke supersymmetry (SUSY), where the quadratic divergence is removed by cancellations between the contribution of fermionic (Fig. 1.1(a)) and bosonic (Fig. 1.1(b)) supersymmetric partners[10].
- Technicolor theories: elementary Higgs scalars do not exist, instead a Higgs-like field is regarded as a composite state of new heavy fermions. EWSB is triggered by non-perturbative strong interactions.

---

[10]The contribution from supersymmetry, which associates two complex scalars with each massive fermion, is given by

$$\begin{aligned}\delta m_{H,0}^2 &= -\lambda_S \int \frac{d^4k}{(2\pi)^2}\left[\frac{i}{k^2 - m_{s_1}^2} + \frac{i}{k^2 - m_{s_2}^2}\right] \\ &= \frac{\lambda_S}{16\pi^2}\left[2\Lambda - 2m_{s_1}^2 \log\left(\frac{\Lambda}{m_{s_1}}\right) - 2m_{s_2}^2 \log\left(\frac{\Lambda}{m_{s_2}}\right)\right] + \mathcal{O}\left(\frac{1}{\Lambda^2}\right).\end{aligned}$$

If $\lambda_S = \lambda_F^2$ the quadratic divergences from the fermion loop are canceled by the supersymmetric partner.

While the aforementioned choices can stabilize the Higgs mass divergence, they still do not fully explain why there are two very different energy scales; why they are so widely spread; or whether there are other scales, or simply a big desert, between m_{EW} and M_{Pl}.

Diverse frameworks of physics beyond the Standard Model have been proposed to address the hierarchy problem. A common feature of their solutions is the preservation of two distinct energy scales: a new effective field theory describes the physics at the weak scale (e.g. SUSY, technicolor), while a true theory of quantum gravity is only revealed at the Planck scale. Therefore, experimental results can provide hints of the structure of theories at high energies, maybe even the Planck scale, but strong gravitational interactions are out of reach. An underlying assumption in these scenarios is that Newtonian gravity stays unmodified over about 30 orders of magnitude from where it is currently measured [30] at $\sim 10^{-3}$ cm down to Planck lengths $\sim 10^{-33}$ cm.

Interesting extensions to the Standard Model are theories that postulate large extra spatial dimensions into which the gravitational field can propagate. The only fundamental scale is then m_{EW}, and the apparent large value of M_{Pl} is a consequence of current experimental limitations in measuring the *true* coupling strength of gravity. A distinctive signature of these scenarios is the production of black hole events at LHC energies.

1.4 Extra Dimensions

The concept of extra dimensions was introduced in the 1920s, first by Theodor Kaluza [31], and later refined by Oskar Klein [32]. The objective of the extra dimension was to facilitate the unification of gravity and electromagnetism. They proposed a five-dimensional spacetime where the fourth spatial dimension is curled and closed into a circle of small radius. This idea of a compactified dimension can be visualized

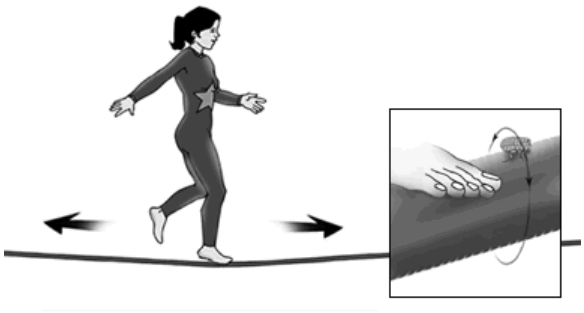

Figure 1.2. A person on a tight rope can travel in only one dimension. A bug on the same rope finds a curled-up second dimension.

in Fig. 1.2 [33]. A person walking on a tight rope can only move forward or backward, thus having only one degree of freedom. A bug on the same rope is not restricted to this dimension but can also move around the rope, effectively having two degrees of freedom. For small (submillimeter) compactification lengths, this opens the door to a rich structure of theoretical possibilities.

The Kaluza-Klein proposal was not successful in unifying gravitational and electromagnetic interactions. However, it illustrates how extra dimensions can assist when combining forces of different strengths, hence providing some guidance to address the hierarchy problem. A simplified "toy model" of the ideas set forth by Kaluza-Klein is as follows.

Consider the interaction of two massive particles at rest in 4+1 dimensions, where the fifth dimension is closed with compactification radius R. Quantum mechanics dictates the allowed energy values in the extra dimension, which translate to a quantization of the de Broglie wavelength λ_{ED}. The boundary conditions are satisfied by $n\lambda = 2\pi R$, where $\lambda = h/p$. The 5-momentum[11] vector of a particle at rest is given by:

$$P^{\mu} = (m,\, 0,\, 0,\, 0,\, p_{ED}), \quad \text{with } p_{ED} = \frac{n\hbar}{R} = \frac{n}{R}.$$

[11]Using Minkowski metric with signature $(+----)$

Noticing that in 3+1 dimensions $P_1 \cdot P_2 = m_1 m_2$, Newton's gravitational law can be extended to higher dimensions by rewriting

$$F = -G_{\rm N}\frac{m_1 m_2}{r^2} \;\rightarrow\; F = -G_{\rm N}\frac{P_1 \cdot P_2}{r^2}.$$

In 4+1 dimensions, however,

$$P_1 \cdot P_2 = m_1 m_2 - p_{ED,1}\, p_{ED,2} = m_1 m_2 - \frac{n_1 n_2}{R^2}.$$

For a compactification radius of length $\frac{1}{e}\sqrt{4\pi\epsilon_0 G_{\rm N}}$, the force is given by

$$F = -G_{\rm N}\frac{m_1 m_2}{r^2} + \frac{1}{4\pi\epsilon_0}\frac{q_1 q_2}{r^2} = F_g + F_e$$

where $q_i = n_i e$, F_g is the gravitational force and F_e is Coulomb's law. While this is an unrealistic example, it shows how two forces could be obtained in a single model, providing some sense, at least qualitatively, of how powerful extra dimensions can be.

Over the last two decades the idea of extra dimensions has been revisited, not for the purpose of unification, but to explain the hierarchy between $M_{\rm Pl}$ and $m_{\rm EW}$. These frameworks postulate that the gravitational field lines spread throughout the full higher-dimensional space, modifying the behavior of gravity.

The case for a single extra compactified dimension is shown in Fig. 1.3. Two massive particles are separated a distance r. A "regular" spatial dimension extends in the $\hat{r}$ direction and the extra compactified dimension is a circle of radius R. This describes a cylinder whose longitudinal axis is the "regular" spatial dimension. The gravitational field can propagate not only in the $\hat{r}$ direction, but can also go around the cylinder. Neglecting the component of the field in the extra dimensions causes the apparent weakness of gravity with respect to the other forces.

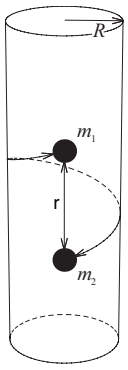

Figure 1.3. Two massive particles interact in a spacetime with two spatial dimensions. One of the dimensions is closed with compactified radius R. The gravitational field propagates in both spatial dimensions [3].

Two particularly interesting novel approaches to extra dimensions could result in similar TeV-scale gravitational signatures. The first one, sometimes referred to as the large extra dimension scenario or ADD model, was postulated by Arkani-Hamed, Dimopoulos and Dvali [34]. The other one, referred to as the warped scenario or RS model, was postulated by Randall and Sundrum [35].

1.4.1 Extra Dimensions in the ADD model

There are a number n of extra spatial dimensions compactified at submillimeter length scales R, leading to a D-dimensional spacetime, where $D = n + 4$. In ADD scenarios, the Standard Model fields are localized in a 4-d submanifold of this higher-dimensional spacetime. The gravitational potential, dictated by Gauss's law, is modified by the geometry of the extra dimensions[12]. The general solution to Poisson's equation yields a potential as a function of the distance r separating two test masses

[12]In D-dimensions Gauss's Law is given by

$$\oint_S \vec{\Phi} \cdot \vec{ds} = const \cdot m_{enc}$$

$$V(r) \sim \frac{-m_1}{M_{\rm D}^{n+2}} \frac{1}{r^{n+1}},\ (r \ll R)$$
$$V(r) \sim \frac{-m_1}{M_{\rm D}^{n+2}\, R^n} \frac{1}{r},\ (r \gg R)$$

where Newton's constant in D-dimensions $G_{\rm D}$ has been expressed in terms of the D-dimensional Planck scale $M_{\rm D}$, where $G_{\rm D} = 1/M_{\rm D}^{n+2}$. The case for $r \ll R$ predicts deviations from the familiar $1/r$ potential. On the other hand, in the limit of large distances, the $1/r$ form is recovered along with a factor $1/R^n$ coming from the volume of the extra dimensions.

Comparing this higher-dimensional potential with Newton's gravitational potential[13], the four-dimensional Planck scale can be redefined as an effective scale related to the "true" Planck scale by $M_{\rm Pl}^2 \sim M_{\rm D}^{n+2} R^n$, and the large value of $M_{\rm Pl}$ is a consequence of the size and the number of extra dimensions.

Setting $M_{\rm D} \sim m_{\rm EW} \sim 1$ TeV and demanding the choice of R to reproduce the observed $M_{\rm Pl}$ yields

$$R \sim 10^{\frac{30}{n}-17}{\rm cm} \cdot \left(\frac{1\ {\rm TeV}}{m_{\rm EW}}\right)^{1+\frac{2}{n}}.$$

---

where S is a closed surface enclosing a D-dimensional volume, $\vec{ds}$ is a vector representing an infinitesimal element of said surface, $\vec{\Phi}$ is the gravitational field, and m_{enc} is the enclosed mass. Since gravity is a conservative force, it is often convenient to write the gravitational field as the gradient of a scalar potential

$$\Phi = -\nabla V(r)$$

and solve the Poisson's equation

$$\nabla^2 V(r) = 4\pi G_{\rm D}\, \rho(r)$$

A complete derivation of the gravitational force in D-dimensions using Gauss's Law or using Newton's Law with a vector decomposition into ordinary and compactified dimensions can be found in [3, 36].

[13] In 4-d the potential is given by

$$V(r) \sim \frac{-m_1}{M_{\rm Pl}^2} \frac{1}{r}$$

The compactification lengths R for a number n of extra dimensions are summarized in Table 1.3. The case for $n = 1$ is empirically excluded, as it implies deviations from Newtonian gravity over solar system distances. The values for $n \geq 2$, are within acceptable range. Planned experiments for direct gravity measurements [30] in the 10^{-2} cm range will be able to test the case for two extra dimensions.

Table 1.3. Compactification size of extra dimensions for different values of n.

number n of extra dimensions	1	2	3	4	5	6
size R of extra dimensions [cm]	10^{13}	10^{-2}	10^{-7}	10^{-10}	10^{-11}	10^{-12}

1.4.2 Extra Dimension in the RS model

There is one single extra dimension with a warped geometry. This setup is illustrated in Fig. 1.4. The universe is a five-dimensional spacetime bounded by two 3-branes[14]: the Planck (Gravity) brane and the TeV (Weak) brane. The higher-dimensional metric is given by

$$ds^2 = e^{-2kR\phi}\eta_{\mu\nu}dx^\mu dx^\nu + Rd\phi^2$$

where k is a scalar of order Planck scale, x^μ are the coordinates for the familiar 4-dimensions, while $0 \leq \phi \leq \pi$ is the coordinate for the extra dimension, whose size is set by the compactification radius R. The two 3-branes are located at $\phi = 0$ and $\phi = \pi$, respectively. The SM fields are confined in the TeV brane. The graviton wave function, localized in the Planck brane, is exponentially suppressed away from this 3-brane along the extra dimension.

[14]The 3-branes can support 3+1 dimensional field theories.

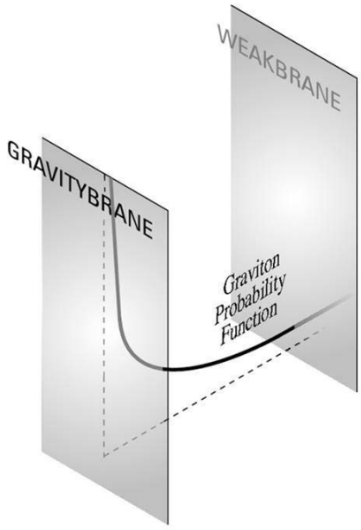

Figure 1.4. In the RS model, spacetime has one extra spatial dimension, bounded by the Planck 3-brane and the Electroweak 3-brane. The gravitational field propagates into the extra dimension [4].

In this scenario there is one fundamental scale, either the Planck scale or the TeV scale, one being derived from the other as a consequence of the exponential factor $e^{-2kR\phi}$ appearing in the metric[15]. The large Planck scale (that is, the weakness of gravity) arises from the small overlap of the graviton wave function in the 5^{th} dimension (which is the warp factor) with the visible brane.

1.5 TeV-Scale Gravity Signatures

In the framework of large extra dimensions, there are a number of dramatic experimental signatures. For instance, deviations in the gravitational force law at sub-millimeter distances are expected and could be measured by new experiments [30]. Additionally, the gravitational field propagating in the bulk can be expressed as a series of states known as a Kaluza-Klein tower of massive, neutral, spin-2 graviton

[15]This change in viewpoint is established by the appropriate change of coordinates $x^\mu \to e^{kR\pi}x^\mu$.

excitations (KK gravitons). At lepton or hadron collliders, these graviton modes can be produced in association with a jet or a photon[16]. The gravitons will pass through the detector undetected, resulting in a signature of a single jet or photon accompanied by large missing transverse energy. Current limits for these final states are presented in Sec. 1.6.

Another exciting prediction, and the central topic of this thesis, is the production and decay of black holes, which is discussed in the following section.

1.5.1 Black Hole Production

A striking signature of this higher-dimensional spacetime is the possibility of black hole production as a consequence of the modifications to the gravitational force. The energy density necessary in the standard 3+1 dimensional spacetime is beyond our technical capabilities. However, by incorporating extra dimensions, the gravitational field becomes stronger at small distances and therefore the event horizon is located at a larger radius. By lowering the Planck scale $M_{\rm Pl}$ closer to the electroweak scale $m_{\rm EW}$ (i.e. $M_{\rm Pl} \to M_{\rm D}$), these mini black holes could be produced during high energy scattering processes with center-of-mass (c.o.m.) energies $\sqrt{s} > M_{\rm D}$.

A black hole is a body with such a great mass density that prevents even light from escaping it due to the gravitational field surrounding said black hole. The radius within which the gravitational force is this strong is called the horizon (or Schwarzschild) radius R_H. In 4+n dimensional spacetime the horizon radius is given by

$$R_H = \left(\frac{2}{n+1} \cdot \frac{M_{BH}}{M_{\rm D}} \right)^{\frac{1}{n+1}} \frac{1}{M_{\rm D}}$$

[16]The production processes include interactions such as: $qg \to qG$, $gg \to gG$, $qq \to gG$, $q\bar{q} \to \gamma G$, $q\bar{q} \to gG$, $e^+e^- \to \gamma G$, where G stands for graviton, q for quark, and g for gluon.

where M_{BH} is the black hole mass[17].

By setting $M_{\rm D} \sim m_{\rm EW} \sim 1$ TeV, it is possible to calculate values for the horizon radius as a function of the n extra dimensions and the black hole mass. This is represented in Fig. 1.5. For black hole masses between $1 - 5$ TeV, the horizon radius ranges from $10^{-3} - 10^{-4}$ GeV^{-1}. Assuming $M_{BH} \sim 5$ TeV, the radii values are of order 10^{-4} fm as shown in Table 1.4[18].

Table 1.4. Black hole horizon radii for different values of n [1].

number n of extra dimensions	1	2	3	4	5	6	7
R_H [10^{-4} fm]	4.06	2.63	2.22	2.07	2.00	1.99	1.99

[17]To derive the Schwarzschild radius of a 4+n dimensional black hole [3], we need to equate the 4+n dimensional potential energy needed to bring a particle of mass m from infinity to the surface of the black hole, to the kinetic energy of a particle with speed c. The 4+n dimensional potential energy is given by

$$U = \frac{1}{n+1} \cdot \frac{G_{\rm D} M_{BH} m}{R_H^{n+1}} = \frac{1}{n+1} \cdot \frac{M_{BH} m}{R_H^{n+1} M_{\rm D}^{n+2}}$$

where M_{BH} is the mass of the black hole.

A more rigorous solution using the Schwarzschild metric has been derived in [7]. The metric takes the form

$$ds^2 = g_{\mu\nu} dx^\mu dx^\nu = -\gamma(r) dt^2 + \gamma(r)^{-1} dr^2 + r^2 d\Omega_{3+n}^2$$

where $d\Omega_{3+n}$ is the surface element of the 3+n dimensional unit sphere and

$$\gamma(r) = 1 - \left(\frac{R_H}{r}\right)^{n+1}.$$

The constant R_H can be found by requiring reproduction of the Newtonian limit for $r \gg R$, that is, $\frac{1}{2}\partial_r \gamma$ has to yield the Newtonian potential:

$$\frac{n+1}{2} \left(\frac{R_H}{r}\right)^{1+n} \frac{1}{r} = \frac{1}{M_{\rm D}^{n+2}} \frac{M_{BH}}{r^{n+2}}.$$

Thus, we get

$$\gamma(r) = 1 - \frac{2}{n+1} \frac{M_{BH}}{M_{\rm D}^{n+2}} \frac{1}{r^{n+1}}.$$

[18]Using the conversion 1 m $= 5.07 \times 10^{15}$ GeV^{-1}.

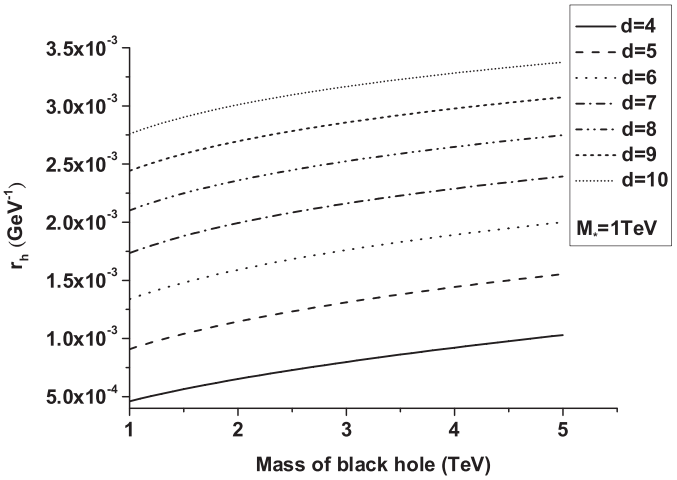

Figure 1.5. Black hole horizon radius in units of 1/GeV for different number n of extra dimensions, where $n = d - 3$ [5].

At the energy regime of the LHC, the Compton wavelengths associated to the colliding particles will be small ($\lambda_C \propto 1/E$), the wave packet will be tightly packed, and therefore, it would be possible to bring these particles closer together than their horizon. Such an event is depicted in Fig. 1.6. Two incoming partons approach each other in a high c.o.m. energy proton-proton collision (Fig. 1.6(a)). If the impact parameter b is sufficiently small, a region of spacetime with a very high energy density is produced. If this region is smaller than the Schwarzschild radius associated to the energy of the partons, i.e. $b < 2R_H$ (Fig. 1.6(b)), the system will form a (higher-dimensional) black hole.

Because a black hole is not a Standard Model particle, its correct quantum theoretical treatment is unknown. However, for trans-Planckian energies (collisions with $\sqrt{s} \gg M_{\rm D}$), a semi-classical treatment is available. In the semi-classical formalism, the product of the collision would have a mass larger than the scale of quantum gravity and for these objects, quantum gravitational effects can be ignored. The black hole production cross section, in this high energy limit, can be approximated by the classical geometric cross section:

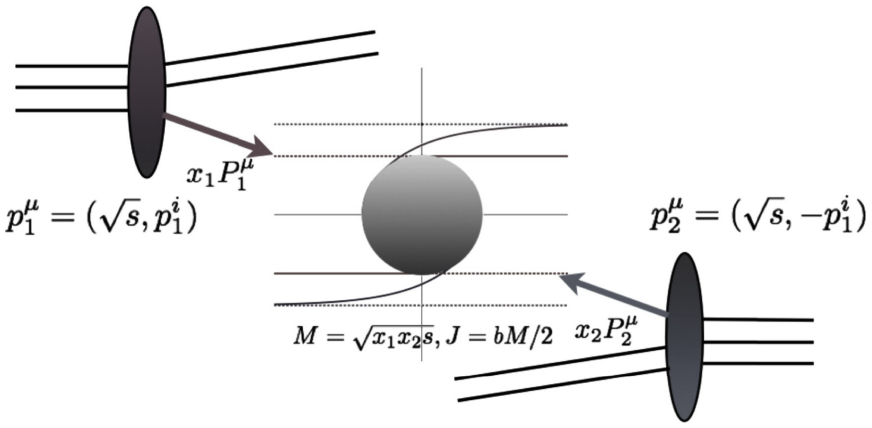

(a)

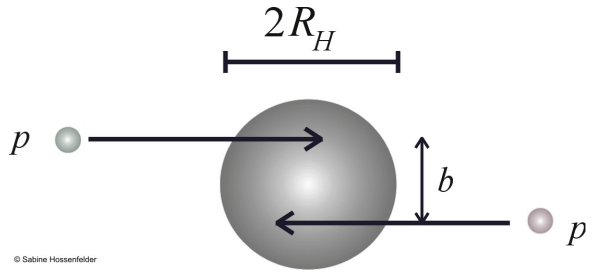

(b)

Figure 1.6. In a high energy proton-proton collision, two partons are brought closer together (a). If the impact parameter b is smaller than $2R_H$ a black hole is produced (b) [6, 7].

$$\sigma(M_{BH}) = F_n \pi R_H^2$$

where F_n are formation factors[19] that take into account the size of the impact parameter, the angular momentum, the charge, and the fraction of the initial energy that is captured behind the horizon. These formation factors depend on the number of extra dimensions and are assumed to be of order unity.

Further corrections take into account that the colliding partons only carry a fraction of the proton energy. For this reason, a summation must be made over all parton

[19]For a discussion on formation factors and the resulting limits to black hole masses, maximum impact parameters and the semi-classical approximation of the cross section, see [1, 7].

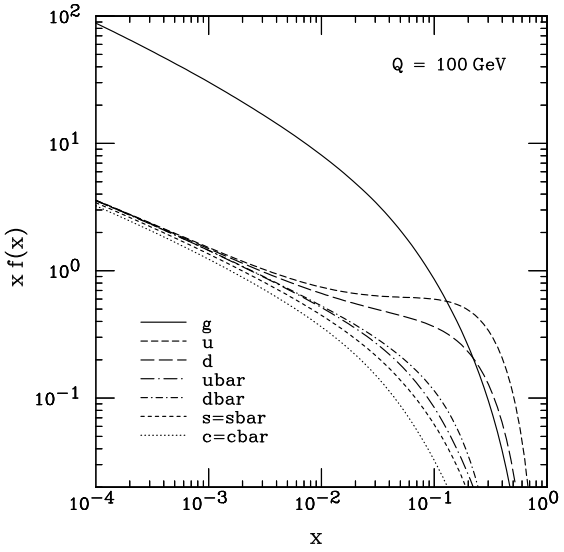

Figure 1.7. Parton distribution functions defined by probability densities for finding a parton with a certain momentum fraction x, as a function of x [8].

pairs with enough energy to produce a black hole, using parton distribution functions (PDFs) $f_i(x)$ which give the probability of finding parton i with a fraction x of the momentum (c.f. Fig. 1.7). The total cross section for the production of a black hole from the collision of particles A and B is given by

$$\sigma_{AB\to BH}(\tau_m, s) = \sum_{i,j} \int_{\tau_m}^{1} d\tau \int_{\tau}^{1} \frac{dx}{x} f_i(x) f_j(\frac{\tau}{x})\, \sigma_{ij}(\tau s, n),$$

where $\tau = x_i x_j$ is the parton-parton c.o.m. energy squared fraction, $\sqrt{\tau_m s}$ is the minimum c.o.m. energy necessary for the creation of a mini black hole, and $\sigma_{ij} \simeq F_n \pi R_H^2$. Expected values for the black hole production cross sections range from $10^{-1} - 10^3$ pb. Figure 1.8 illustrates the cross section as a function of M_{BH} and $n+3$.

The produced black holes are characterized by a non-vanishing temperature T_H, whose value is inversely proportional to the horizon radius R_H. Hawking [37] showed that, when quantum effects are considered, a black hole at a temperature T_H radiates particles with a characteristic thermal radiation spectrum and an almost blackbody

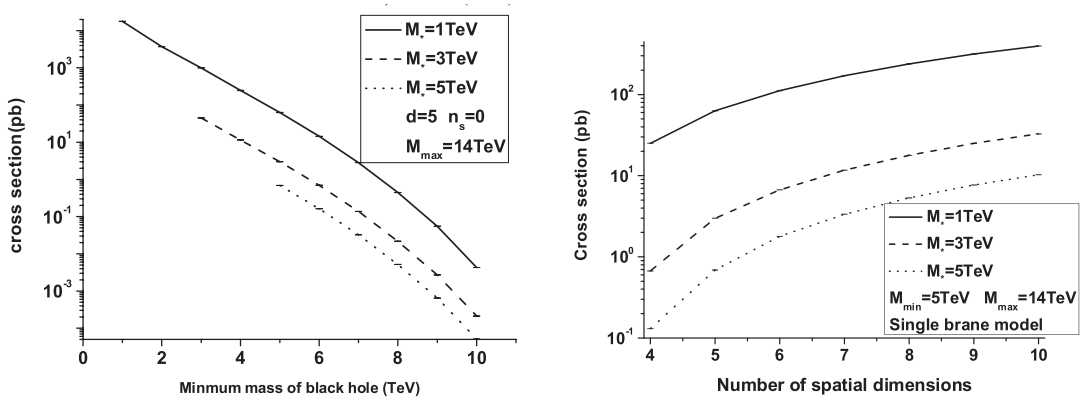

(a) (b)

Figure 1.8. Black hole production cross section versus (a) black hole mass and (b) number of spatial dimensions $(n+3)$ [5].

profile. The temperature of a 4+n dimensional black hole has been calculated [1, 7] and is given by

$$T_H = \frac{n+1}{4\pi}\frac{1}{R_H}.$$

Figure 1.9 illustrates temperature profiles as a function of black hole mass and the number of spacetime dimensions, in units of TeV. Assuming a black hole of mass $M_{BH} \sim 5$ TeV and $M_{\rm D} \sim 1$ TeV, values of the temperature for different n extra dimensions may be calculated[20]. These values are shown in Table 1.5.

Table 1.5. Black hole temperature for different values of n, with $M_{BH} \sim 5$ TeV and $M_{\rm D} \sim 1$ TeV [1].

number n of extra dimensions	1	2	3	4	5	6	7
T_H [GeV]	77	179	282	379	470	553	629

[20]Ref. [1] stresses that the semi-classical calculation of Hawking emission is only reliable when the energy ω of the emitted particle is small compared to the black hole mass (i.e. $\omega \ll M_{BH}$). This in turn requires $T_H \ll M_{BH}$, which is equivalent to demanding $M_{BH} \gg M_{\rm D}$.

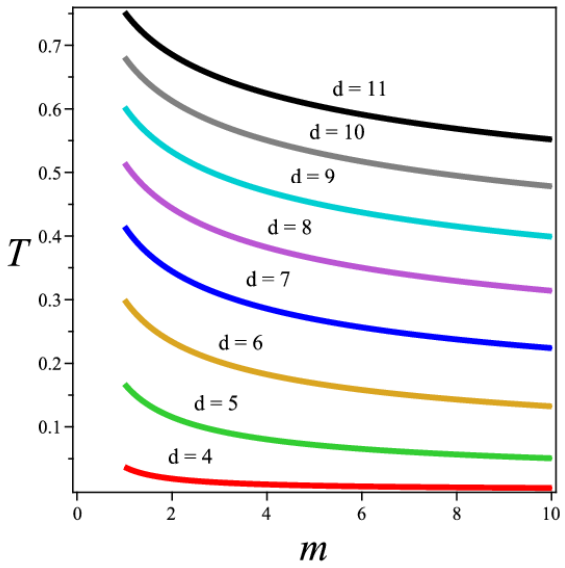

Figure 1.9. Temperature of a black hole versus its mass for different spacetime dimensions, with $d = n + 4$, and $M_{\mathrm{D}} = 1$ TeV. Mass and temperature are in TeV [9].

1.5.1.1 Corrections to Black Hole Production Rate: Mass Threshold and String Balls

The first set of calculations estimated a large black hole production rate for $M_{\mathrm{D}} \sim 1$ TeV. However, later developments showed that there could be a significant suppression rate: a threshold for black hole production below which the semi-classical approach is no longer valid. From General Relativistic arguments, two point-like particles in a head on collision with zero impact parameter will always form a black hole, no matter how large or small their energy. At low energies, this is expected to be impossible due to the smearing of the wave function by the uncertainty relation. As a result, there is a necessary minimal energy to allow for the required close approach. This threshold is of order M_{D}, though the exact value is unknown since quantum gravity effects should play an important role for the wave functions of the colliding particles [7]. A necessary but not sufficient condition is $\sqrt{s} > M_{\mathrm{D}}$.

Several criteria have been studied for the formation of a truly thermal black hole [10,12,38]. Meade and Randall [10] have concisely summarized the conditions imposed on the masses to be classified as General Relativity (GR) black holes, in terms of the parameter x_{min}, defined as

$$x_{min} = \frac{M_{BH}^{min}}{M_{\rm D}},$$

where M_{BH}^{min} is the minimal black hole mass. They considered arguments on high entropy[21], change in Hawking temperature per particle emission ("MBH LT"), emitted particle energy being much smaller than the black hole mass ("MBH/(n+3)T" and "3/(n+3) N"), and lifetime exceeding the black hole radius ("LT/R"), among others. Some of the strongest criteria are plotted in Fig. 1.10, as a function of x_{min}. Figures 1.10(a) and 1.10(b) correspond to an ADD scenario with $n = 6$ and a RS scenario ($n = 1$), respectively. In these plots, the vertical axis is an arbitrary scale where every curve is greater than one if the criteria is satisfied. From these distributions, black holes may be considered thermal if $x_{min} \gtrsim 3$ or 4.

One commonly used condition is that the entropy of the black hole must be greater than 25 [6, 11, 39], which leads to the requirement $x_{min} \gtrsim 5$. For $M_{\rm D} \sim 1$ TeV, this translates to the requirement of $M_{BH} \geq 5$ TeV. Because the cross section drops with increasing black hole mass, the most probable black holes produced are those closest to the fundamental Planck scale, and consequently, the least theoretically understood.

One exciting possibility is to treat the energy scale below the GR threshold (i.e. quantum gravity) in the context of weakly coupled string theory. Embedding the large extra dimensions into string theory could enable calculations near $M_{\rm D}$, providing an understanding of the strong gravity regime and a picture of the evolution

[21]For Schwarzschild black holes, the entropy requirement also ensures that the Compton wavelength of the black hole is less than its horizon radius [11].

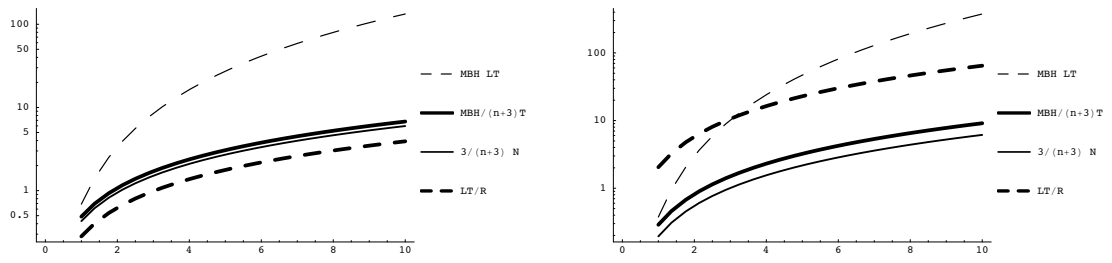

(a) (b)

Figure 1.10. Possible criteria for GR black holes as a function of x_{min}, for (a) ADD scenario with $n = 6$ and (b) RS scenario. The vertical axis is in an arbitrary scale where the criteria is satisfied for values greater than one [10].

of a black hole at the last stages of evaporation [11, 40]. In these string models, a typical energy hierarchy has the form

$$M_{\rm s} < M_{\rm D} < \frac{M_{\rm s}}{g_s} < \frac{M_{\rm s}}{g_s^2}$$

where $M_{\rm s} \sim 1$ TeV is the string scale and g_s is the string coupling constant[22]. According to the theory, a black hole can be treated General Relativistically above a minimum mass $M_{min} \sim M_{\rm s}/g_s^2$. Therefore, there is a mass range between $M_{\rm s}$ and M_{min} inside which the GR approximation fails and the spectrum is intrinsically stringy.

If the parton-parton scattering energy is comparable to $M_{\rm s}$, the point-particle description will have to be replaced by a string-string interaction. Above this scale, the string states will become highly excited, jagged and entangled. Such string states are commonly referred as string balls. At even higher energies ($\sim M_{\rm s}/g_s^2$), a transition point is reached where the string ball turns into a black hole. It is not known how much higher above the string scale $M_{\rm s}$ the energy must be to be in the stringy regime.

[22]The coupling g_s must be smaller than one for a valid perturbative treatment of the theory.

Following arguments similar to the black hole threshold, the validity of the long, jagged picture of string balls is expected for

$$\frac{M_{SB}}{M_{\rm s}} > 3$$

where M_{SB} is the string ball mass.

The Correspondence Principle establishes that the properties of a black hole with mass M_{min} match those of a string ball with the same mass [11, 40]. Said correspondence picture also suggests that the production cross section for string balls will match the black hole cross section at c.o.m. energies around $M_{\rm s}/g_s^2$ [23]. Dimopoulos and Emparan [40] calculated the string ball production cross section imposing the validity of the perturbative approximation and unitarity conditions. For $M_{\rm s} < M_{SB} < M_{\rm s}/g_s$, the production cross section grows with s. Above the scale $M_{\rm s}/g_s$, called the unitarity point, the calculations violate perturbative unitarity, requiring the introduction of some *ad hoc* unitarization scheme. After imposing this scheme, the production cross section no longer grows with s but remains constant at a value proportional to the string length squared l_s^2.

The parton-parton cross section for string ball and black hole production, in their valid regimes, are summarized as follows

$$\sigma \sim \begin{cases} \dfrac{g_s^2 M_{SB}^2}{M_{\rm s}^4} & M_{\rm s} \ll M_{SB} \leq \frac{M_{\rm s}}{g_s}, \\ \dfrac{1}{M_{\rm s}^2} & \frac{M_{\rm s}}{g_s} < M_{SB} \leq \frac{M_{\rm s}}{g_s^2}, \\ \dfrac{1}{M_{\rm D}^2}\left(\dfrac{M_{BH}}{M_{\rm D}}\right)^{\frac{2}{n+1}} & \frac{M_{\rm s}}{g_s^2} < M_{BH}. \end{cases}$$

---

[23] That is,

$$\sigma(SB)\mid_{M_{SB}=\frac{M_{\rm s}}{g_s^2}} \sim \sigma(BH)\mid_{M_{BH}=\frac{M_{\rm s}}{g_s^2}}$$

where $M_{\rm s}/g_s^2$ is called the correspondence point.

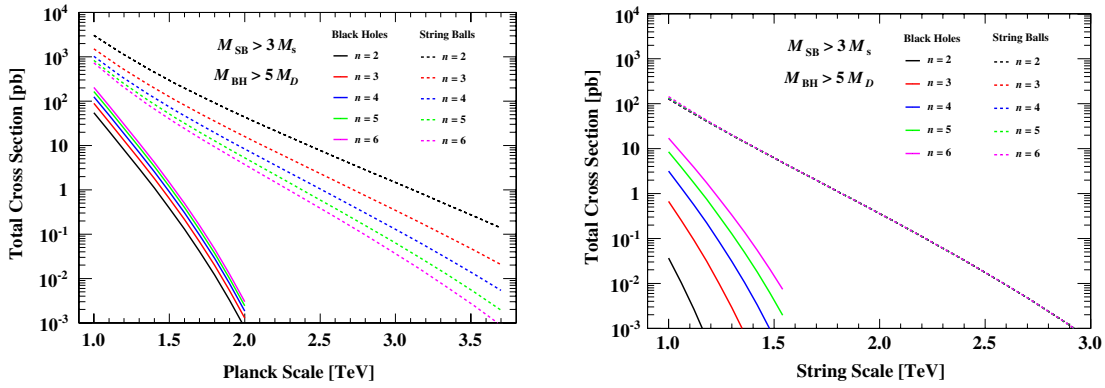

(a) (b)

Figure 1.11. Total proton-proton cross section versus (a) the fundamental Planck scale M_{D} and (b) the string scale M_{s}, for the production of black holes (solid curves) and black holes plus string balls (dashed curves) for various numbers of extra dimensions n [11].

Gingrich and Martell [11] compared the production cross sections of black holes and black holes plus string balls. The distributions are shown in Fig. 1.11, as a function of (a) the fundamental Planck scale M_{D} and (b) the string scale M_{s}, for various numbers of extra dimensions. In both cases, the cross section for black holes plus string balls are at least one order of magnitude higher and probe an enhanced range of M_{D} or M_{s}.

When looking for high-mass states above or near the Planck scale, the technique comprises a search for an excess of events beyond a certain invariant mass threshold. Thus, an important quantity is the integrated cross section above said invariant mass. As an example, Fig. 1.12 shows the integrated cross section versus minimum mass threshold for $n = 3$ extra dimensions. Clearly visible is the correspondence point around 7.5 TeV.

The absence of a complete theory of gravity, which results in theoretical uncertainties near the fundamental Planck scale ($\sim$ 1 TeV), clouds our knowledge of the black hole production cross section. The GR approximation is assumed valid mainly

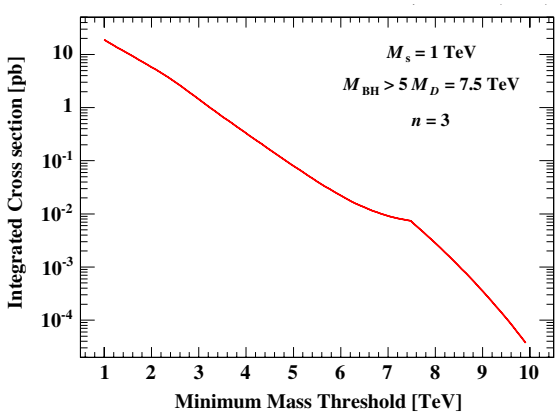

Figure 1.12. Integrated proton-proton cross section versus minimum mass threshold for the production of black holes plus string balls for three extra dimensions [11].

for $M_{BH}/M_{\rm D} \gtrsim 5$. In the context of string theory, string balls (high-entropy string excitations) with properties similar to black holes are produced in the regime where the General Relativistic treatment fails. The combined search for black holes and string balls extends the mass range in the search for TeV-scale gravity signatures. Because the production and decay of these gravitational states are similar, unless stated otherwise, the term "black hole" will refer to both black holes and string balls.

1.5.2 Black Hole Evaporation

Black holes produced in high energy collisions will undergo an evaporation process via the emission of elementary particles. The radiation spectrum, which is a thermal one, has an almost blackbody profile with the peak of the curve at energies very close to the black hole temperature. This spectrum carries information about the higher-dimensional Planck scale and the number of extra dimensions. To understand the signatures associated to black hole production, the decay properties must be examined.

The evaporation process proceeds through several stages [6, 7, 12], as illustrated in Fig. 1.13:

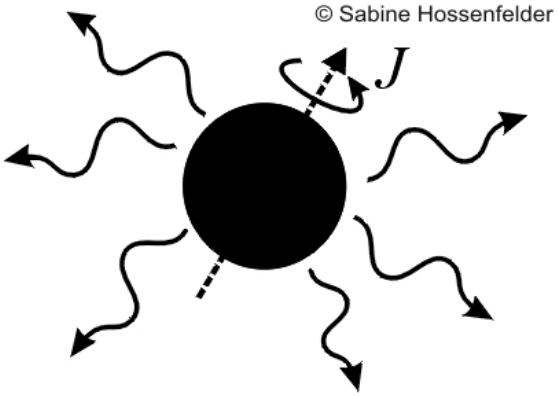

(a) Balding Phase

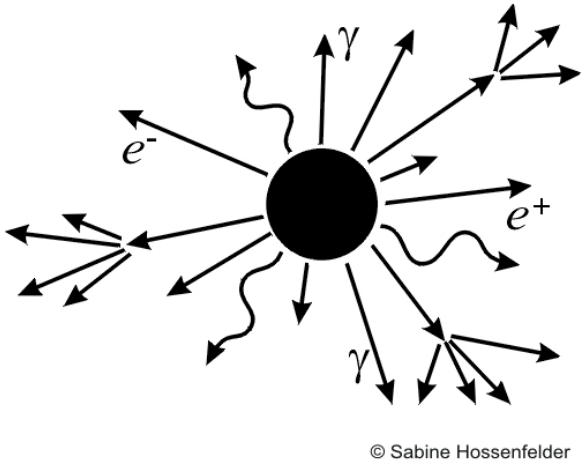

(b) Evaporation Phase

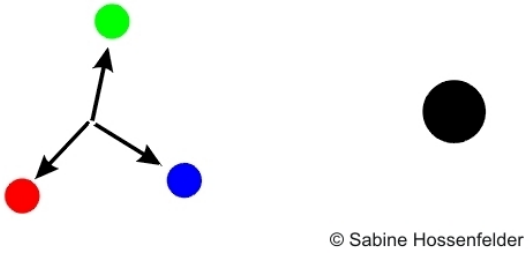

(c) Planck Phase

Figure 1.13. Stages of black hole evaporation [7].

- The *balding phase*: the black hole loses its 'hair' according to the 'no-hair' theorem [41].

- The *evaporation phase*: the black hole evaporates through semi-classical Hawking radiation in a two-stage process: a *spin-down phase*, where the angular momentum is shed, and a *Schwarzschild phase*, where the emissions carry signatures of the black hole temperature and entropy.

- The *Planck phase*: the black hole mass decreases to the fundamental Planck scale (or string scale) and a quantum gravitational description is required.

Considering the violent environment of the collision and merging of particles, the black hole horizon is likely to be very asymmetric at the early stages of production. The black hole state will carry 'hair', inherited from the initial parton pair, corresponding to multipole moments for the distribution of gauge charges and energy-momentum within the asymmetric horizon. In the initial balding phase, the black hole will lose the 'hair' and settle down in a 'hairless' state. In the large mass limit, this occurs by emitting energy, angular momentum and charge in the form of gravitational radiation and gauge field emission (Fig. 1.13(a)). It is unclear what fraction of the energy is lost as gravitational radiation during this stage, but four-dimensional calculations estimate about 15%. This result should be indicative of the total energy lost in the higher-dimensional case since gravitational radiation is expected to dominate [1, 12].

After the balding phase, the black hole will decay more slowly via the semi-classical Hawking evaporation process. This evaporation stage begins with a spin-down phase in which the Hawking radiation carries away the angular momentum and the black hole becomes more spherically symmetric. About 25% of the initial energy is expected to be lost during the spin-down [1]. The evaporation proceeds to the Schwarzschild phase with the emission of thermally distributed quanta, until the black hole mass

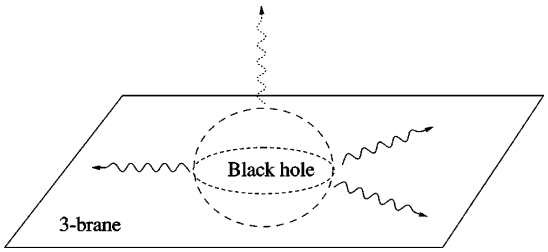

Figure 1.14. A D-dimensional black hole bound to a 3-brane. The black hole emits Hawking radiation predominantly into brane modes (solid lines) and also into bulk modes (dotted lines) [12].

decreases to the fundamental Planck scale M_{D} or the string scale M_{s}. During the Schwarzschild phase, where most of the initial energy is expected to be emitted, the Hawking radiation will be distributed in a rather symmetric and democratic way (equal for each species).

The black hole will emit modes both along the brane and into the extra dimensions, as shown in Fig. 1.14. However, radiation along the brane is the dominant mechanism for mass loss, as argued by Ref. [42]. This means that the spectrum of the evaporation will predominantly consist of Standard Model particles (Fig. 1.13(b)). The distinctive signature of a black hole is characterized by events with large multiplicity (following SM degrees of freedom and spin statistics) and large total (transverse) energy. For the expected black holes from proton-proton collisions with temperatures in the order of a few 100 GeV, the emission rate per unit energy and time is given by [12]

$$\frac{dN_{i,E,l,m,\lambda}}{dEdt} = \frac{1}{2\pi}\frac{\gamma_{i,E,l,m,\lambda}}{e^{(E-m\Omega)/T_H} \mp 1}$$

where i denotes species; l, m, angular momentum numbers; λ, polarization; $\Omega = \frac{1}{R_H}\Omega_*$ is the surface angular frequency of the black hole, and Ω_*, the dimensionless frequency. The γ are graybody factors[24] which modify the spectrum of the emitted particles from

that of a perfect thermal blackbody. Detailed calculations of graybody factors are given in Ref. [1]. Their effect is to suppress or enhance - depending on the spin of the particle, the dimensionality of spacetime and the energy regime - the emission rates. This suppression or enhancement is then reflected at the location of the peak of the emission curve[25].

The energy spectrum of the emitted particles is calculated by integrating the above equation. The dominant radiation is at energies $1/R_H \sim T_H$, determined by the initial black hole mass. The total number of particles emitted is characteristic of the entropy of the initial black hole $N \sim S_{BH}$.

Once the black hole mass has reached a value close to the Planck or string scale, it enters the Planck phase. This is the regime of quantum gravity and predictions become increasingly difficult. It is generally assumed that the black hole will either completely decay into some last few Standard Model particles or a stable remnant will be left, which carries away the remaining energy (Fig. 1.13(c)). A summary motivating the idea of black hole relics can be found in Ref. [7].

1.5.3 TeV-Scale Gravity Observables

The majority of the decay products of a black hole are Standard Model quanta emitted on the brane. Such an event is characterized by a very distinctive signature of large multiplicity and large transverse energy, compared to traditional SM processes. The average multiplicity of particles produced during black hole evaporation is given by [43]:

---

[24]The presence of graybody factors can be attributed to the fact that any particle emitted by a black hole has to traverse a strong gravitational background before reaching an observer at infinity, unlike what happens with a blackbody in flat spacetime.

[25]For example, the graybody factor for gauge bosons is suppressed at the low energy regime, shifting the peak of the spin-1 particles emission curve towards higher energies.

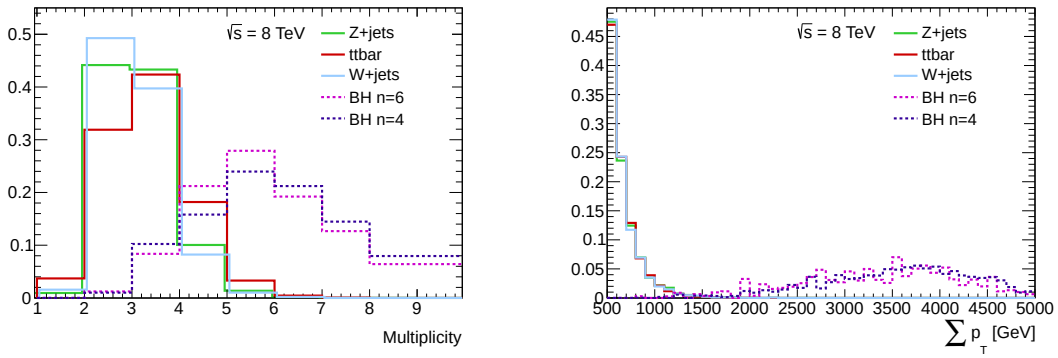

(a) (b)

Figure 1.15. (a) Average multiplicity and (b) sum of transverse momenta for traditional Standard Model processes and black hole events produced in collisions at a c. o. m. energy of 8 TeV. All distributions are normalized to unit area.

$$\begin{aligned}\langle N\rangle &= \langle\frac{M_{BH}}{E}\rangle \\ &\approx \frac{M_{BH}}{2T_H} \\ &\approx \frac{2\pi}{n+1}\left(\frac{2}{n+1}\right)^{\frac{1}{n+1}}\left(\frac{M_{BH}}{M_{\mathrm{D}}}\right)^{\frac{n+2}{n+1}}\end{aligned}$$

where E is the energy spectrum of the emitted quanta. From this relation it follows that $\langle N\rangle$ increases for larger black hole masses, but decreases for greater number of extra dimensions. The black hole daughter particles have typical energies given by the Hawking temperature T_H, ranging in the few 100 GeV.

Figure 1.15(a) illustrates the average multiplicity for common SM processes and black hole events, where the decay products have transverse momenta of at least 100 GeV. The sum of the transverse momenta of all the particles in the event is shown in Fig. 1.15(b). As evidenced by these distributions, a black hole search is enhanced (or SM backgrounds are suppressed) by requiring events with a large number of particles and large sum of transverse momenta.

In addition, because of the rapidly falling parton distribution functions with increasing parton c. o. m. energy, a black hole of any given mass is produced without

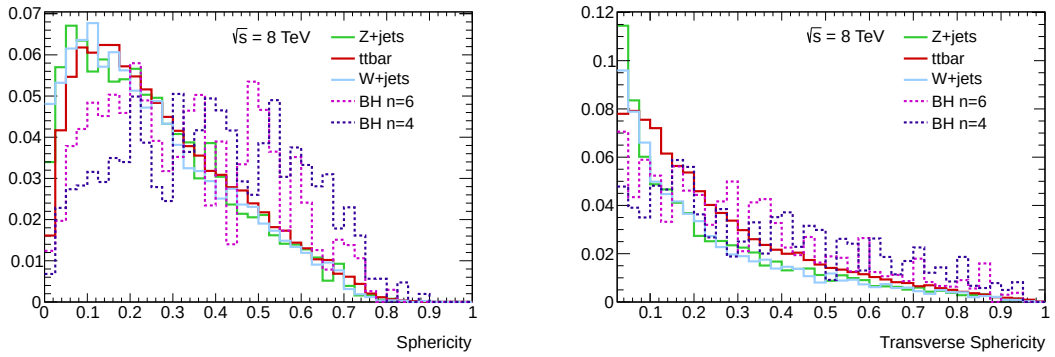

(a) (b)

Figure 1.16. (a) Sphericity and (b) transverse sphericity for traditional Standard Model processes and black hole events produced in collisions at a c. o. m. energy of 8 TeV. All distributions are normalized to unit area.

a large boost in the laboratory frame. This implies that the black hole is essentially at rest, and the emitted particles are not highly boosted either [12]. Given the thermal properties of the evaporation phase, most of the Hawking radiation is isotropic, resulting in events with a high degree of sphericity. Figure 1.16 shows the sphericity and transverse sphericity of typical SM and black hole events. Standard Model backgrounds are significantly less spherical than the expected black hole signature. Due to this moderate boost and high sphericity, the total visible transverse energy of a black hole event is between $\frac{1}{3}$ and $\frac{1}{2}$ of the total visible energy.

Black holes produced in proton-proton collisions are mostly formed from partons with high momentum fractions. These are generally valence quarks, so the black hole is expected to be charged with an average value of $\sim +\frac{2}{3}(e)$[26]. The average black hole charge $\langle Q_{BH} \rangle$ can be measured by determining the average charge of the charged leptons $\langle Q_{Lept} \rangle$. The latter should be equal to the average black hole charge times the probability of emitting a charged lepton [44]. Values for $\langle Q_{Lept} \rangle$ in events requiring at least one charged lepton are displayed in Fig. 1.17.

[26]The rest of the proton charge is expected to disappear down the beam pipes [44].

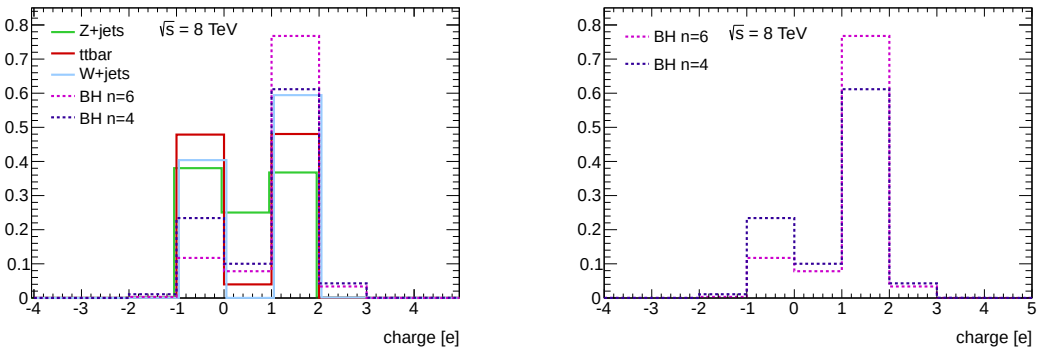

(a) (b)

Figure 1.17. Average charge of the charge leptons $\langle Q_{Lept} \rangle$ in (a) Standard Model and black hole events requiring at least one charged lepton. (b) The same distribution only for black hole events.

Another feature of the thermal decay is flavor blindness: it does not discriminate between particles species. Black holes decay with roughly equal probabilities to all of the ≈ 60 Standard Model particles. This implies that $\sim 10\%$ of the decay products are hard, primary charged leptons, each carrying hundreds of GeV of energy [12, 43]. Triggering on events with such leptonic activity provides a clean signal with reduced background, as SM production of leptons in high multiplicity events occurs at a much smaller rate.

1.6 Previous Searches

Within the context of extra-dimensional scenarios, experimental lower limits on the value of $M_{\rm D}$ have been obtained from experiments at LEP [13] and the Tevatron [14, 45], by searching for the production of Kaluza-Klein gravitons associated with the extra dimensions. Figure 1.18(a) shows the 95% CL exclusion contours in the $M_{\rm D}$ versus n plane for LEP and D0, while Fig. 1.18(b) shows them for LEP and CDF.

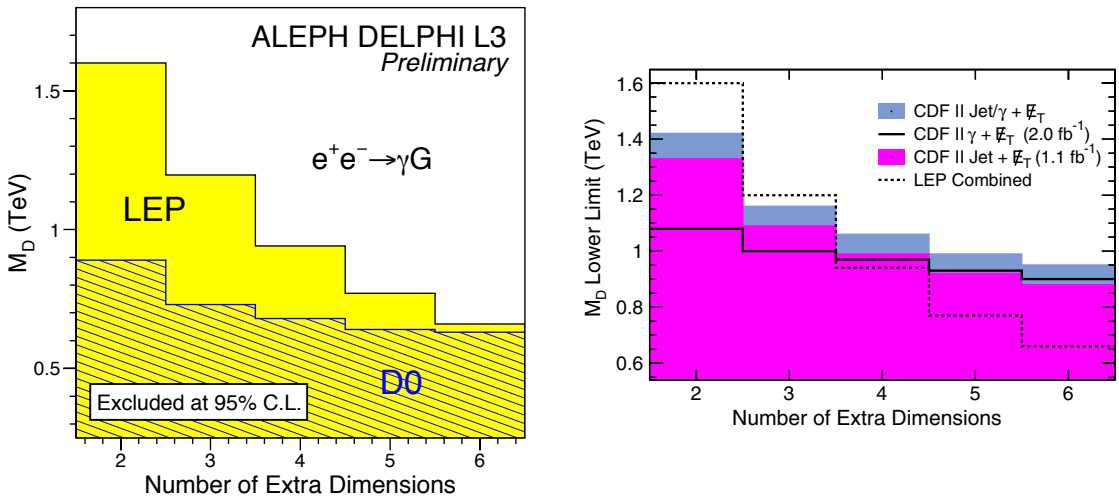

(a) (b)

Figure 1.18. The 95% CL exclusion contours in the M_{D} vs. n plane for (a) the graviton-photon emission at LEP, including limits from D0 [13]; and (b) graviton-jet/γ emission at CDF, including the limits from LEP [14].

Complementary searches have been performed at ATLAS [15] and CMS [16], looking for the invariant mass, the scalar sum of transverse momenta, or the scalar sum of transverse energy of all the objects in multi-object events. Exclusion contours of minimum black hole mass as a function of M_{D} are illustrated in Fig. 1.19.

The must stringent limits [17] come from LHC analyses that search for non-interacting gravitons recoiling against a single jet (monojet and large missing transverse energy. These limits on M_{D} versus n extra dimensions are shown in Fig. 1.20.

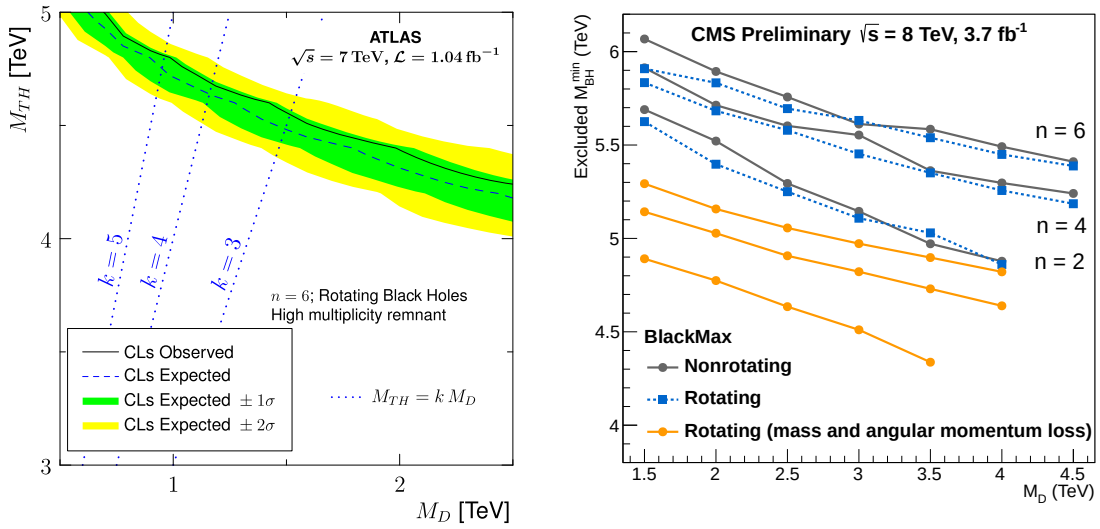

(a) (b)

Figure 1.19. (a) Exclusion limits in the M_{TH}-M_{D} plane for rotating black holes with six extra dimensions at ATLAS [15]. (b) Exclusion limits in the M_{BH}^{min}-M_{D} plane for rotating and non-rotating black holes with 2, 4, or 6 extra dimensions at CMS [16].

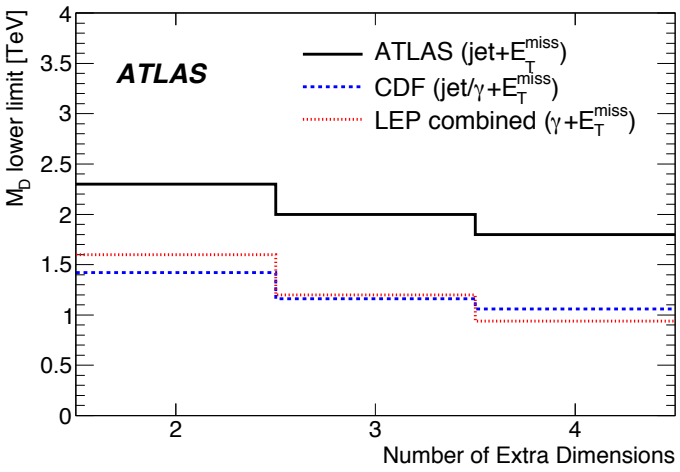

Figure 1.20. The 95% observed lower limits on M_{D} for different numbers of extra dimensions for ATLAS, CDF and LEP [17].

CHAPTER 2

THE ATLAS EXPERIMENT AT THE LHC

This chapter provides a brief description of the experimental setting. Section 2.1 summarizes the LHC complex while Sec. 2.2 is dedicated to the ATLAS detector and its components.

2.1 The Large Hadron Collider

The Large Hadron Collider [18] is a two-ring particle accelerator and collider located beneath the border between Switzerland and France, and operated by the European Organization for Nuclear Research (CERN). It mainly consists of a 27 km ring of superconducting magnets with a number of accelerating structures, installed about 100 m underground. The LHC is designed to collide proton beams with a c.o.m. energy of 14 TeV and an unprecedented luminosity of 10^{34} $\mathrm{cm}^{-2}\mathrm{s}^{-1}$ [1]. Additionally, it can collide heavy (Pb) ions with an energy of 2.8 TeV per nucleon at a peak luminosity of 10^{27} $\mathrm{cm}^{-2}\mathrm{s}^{-1}$.

CERN's accelerator complex is a succession of particle accelerators that can reach increasingly higher energies, as depicted in Fig. 2.1. Each accelerator boosts the speed of a beam of particles before injecting it into the next one in the sequence. Protons are obtained by removing electrons from hydrogen atoms. They are injected from the linear accelerator (LINAC2) into the Proton Synchrotron (PS) Booster, followed by the Proton Synchrotron. The PS has a circumference of 628 m and operates at up

[1] In 2012, the LHC was running at a c.o.m. energy of 8 TeV with a peak luminosity of 7.7×10^{33} $\mathrm{cm}^{-2}\mathrm{s}^{-1}$.

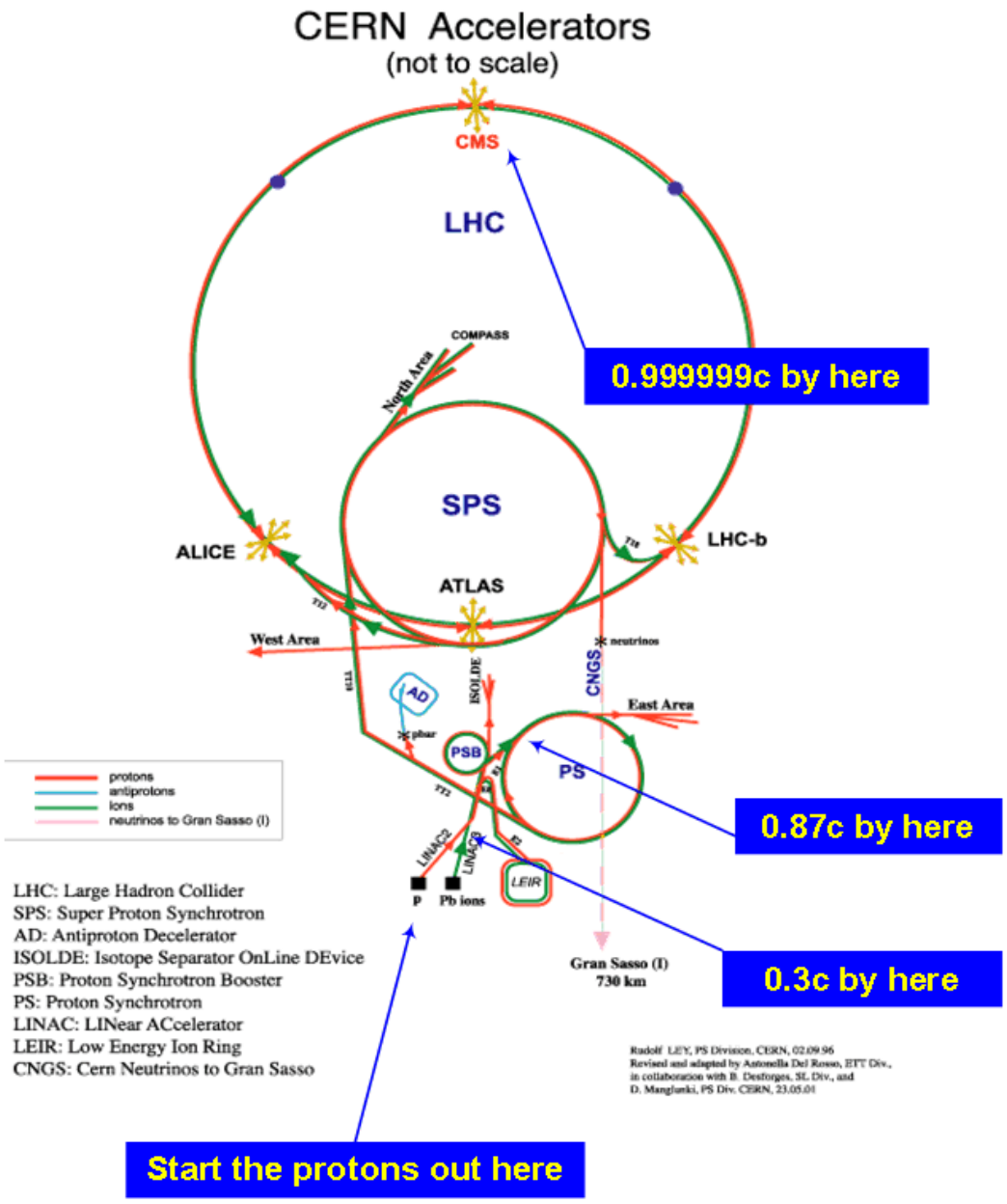

Figure 2.1. The CERN accelerator complex comprising the LINAC2, Booster, PS, SPS and the LHC, as described in Ref. [18].

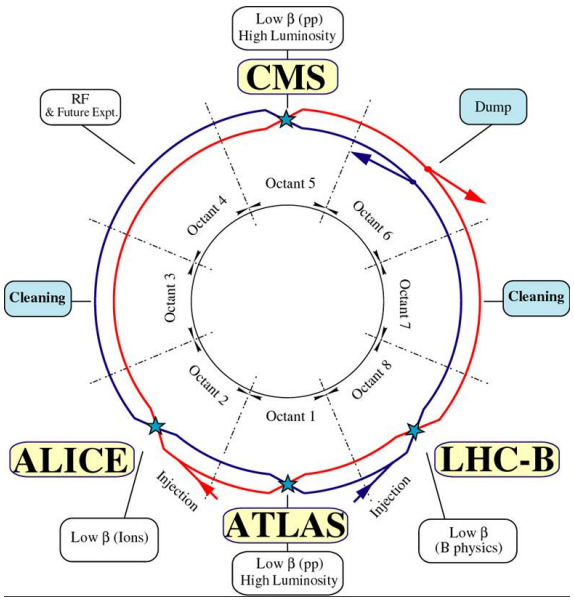

Figure 2.2. Schematic layout of the LHC, including experimental locations [18].

to 25 GeV. After the PS, the beams are transferred to the Super Proton Synchrotron (SPS), which measures about 7 km in circumference and operates at up to 450 GeV. From the SPS, they are finally injected to the LHC. Said injected protons are then accelerated by radio frequency cavities from 450 GeV up to 7000 GeV, at which point the particles in the beam are "squeezed" closer together to increase the chances of collisions at certain interaction locations.

Figure 2.2 shows the basic layout of the LHC. It comprises eight arcs and eight straight sections, each straight sections being approximately 528 m long and can serve as an experimental or utility insertion. Two large, general purpose detectors, ATLAS and CMS, are located at diametrically opposite sections referred to as Point 1 and Point 5. In addition, two medium-size experiments, ALICE and LHCb, having specialized detectors are located at Point 2 and Point 8, respectively.

The aim of the LHC is to reveal the physics beyond the Standard Model with c.o.m. collision energies of up to 14 TeV. The number of events per second generated in the LHC collisions is given by

$$N_{\text{event}} = L\sigma_{\text{event}}$$

where σ_{event} is the cross section for the event under study and L the instantaneous luminosity. The instantaneous luminosity depends only on the beam parameters and can be written for a Gaussian beam distribution as

$$L = \frac{N_b^2 n_b f_{\text{rev}} \gamma_r}{4\pi\varepsilon_n \beta^*} F$$

where N_b is the number of particles per bunch, n_b the number of bunches per beam, f_{rev} the revolution frequency, γ_r the relativistic gamma factor, ε_n the normalized transverse beam emittance, β^* the beta function at the collision point, and F the geometric luminosity reduction factor due to the crossing angle at the interaction point (IP)

$$F = \left(1 + \left(\frac{\theta_c \sigma_z}{2\sigma*}\right)^2\right)^{-1/2}$$

in which θ_c is the full crossing angle at the IP, σ_z the RMS bunch length, and $\sigma*$ the transverse RMS beam size at the IP. The above expression assumes round beams with $\sigma_z \ll \beta$, and with equal beam parameters for both beams. The exploration of rare events in the LHC collisions therefore requires both high beam energies and high beam intensities.

2.2 The ATLAS Detector

ATLAS (A Toroidal LHC ApparatuS) [2] is one of two general-purpose detectors at the LHC, designed to investigate a wide range of signals at high energy and luminosity. It has a nominally forward-backward symmetric cylindrical geometry. The detector measures 25 m in height and 44 m in length, and weights approximately 7000 tonnes.

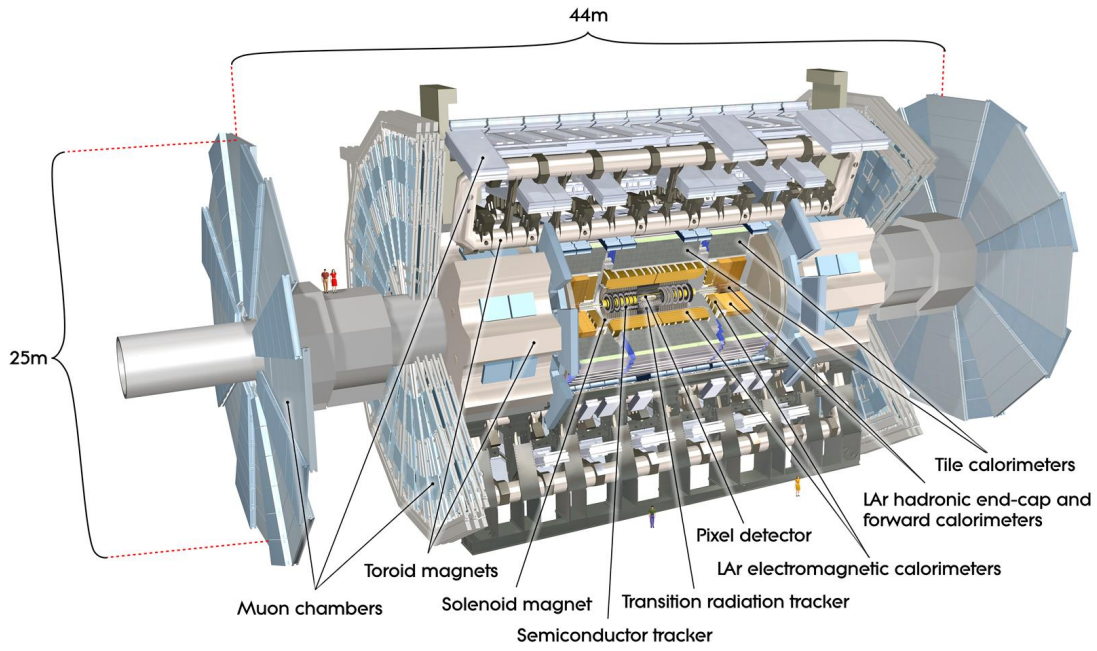

Figure 2.3. Illustration of the ATLAS detector [2]. It measures 25 m in height and 44 m in length, and weights about 7000 tonnes. The different subdetectors are identified.

ATLAS uses a coordinate system where the nominal interaction point is defined as the origin, the beam direction defines the z-axis and the x-y plane is transverse to the beam direction. The positive x-axis is defined as pointing from the interaction point to the center of the LHC ring (c.f. Fig. 2.2) and the positive y-axis is defined as pointing upwards. The azimuthal angle ϕ is measured around the beam axis, and the polar angle θ is the angle from the beam axis. The pseudorapidity is defined as $\eta = -\ln \tan(\theta/2)$, while the rapidity is given by $y = 1/2 \ln[(E + p_z)/(E - p_z)]$.

The ATLAS detector layout is shown in Fig. 2.3. It comprises a magnet system including a thin superconducting solenoid surrounding the inner detector cavity, and three large superconducting toroids (one barrel and two endcaps) arranged with an eight-fold azimuthal symmetry around calorimeters. High granularity liquid-argon (LAr) electromagnetic (EM) sampling calorimeters cover the pseudorapidity range

$|\eta| < 3.2$. Hadronic calorimetry in the range $|\eta| < 1.7$ is provided by a scintillator tile calorimeter. In the endcaps ($|\eta| > 1.5$), LAr technology is also used for the hadronic calorimeters, matching the outer η limits of endcap electromagnetic calorimeters. LAr forward calorimeters provide both electromagnetic and hadronic energy measurements, and extend the pseudorapidity coverage to $|\eta| = 4.9$. The calorimeter is surrounded by the muon spectrometer (MS). The MS defines the overall dimensions of the ATLAS detector.

2.2.1 The Inner Detector

The high luminosity conditions create a very large track density in the inner detector. To achieve the momentum and vertex resolution requirements imposed by the benchmark physics process, high precision measurements must be made with fine detector granularity. Pixel and silicon microstrips (SCT) trackers, used in conjunction with the straw tubes of the Transition Radiation Tracker (TRT), offer these features.

The layout of the inner detector (ID) is illustrated in Fig. 2.4. Its basic parameters are summarized in table 2.1. The ID is immersed in a 2 T magnetic field generated by the central solenoid, which extends over a length of 5.3 m with a diameter of 2.5 m. The precision tracking detectors (pixels and SCT) cover the region $|\eta| < 2.5$. In the barrel region, they are arranged on concentric cylinders around the beam axis while in the endcap regions they are located on disks perpendicular to the beam axis. The highest granularity is achieved around the vertex region using silicon pixel detectors. The pixel layers are segmented in $R - \phi$ and z with typically three pixel layers crossed by each track. All pixel sensors are identical and have a minimum pixel size in $R - \phi \times z$ of 50×400 μm^2. The intrinsic accuracies in the barrel are 10 μm ($R - \phi$) and 115 μm (z).

For the SCT, eight strip layers are crossed by each track. In the barrel region, this detector uses small-angle (40 mrad) stereo strips to measure both coordinates, with

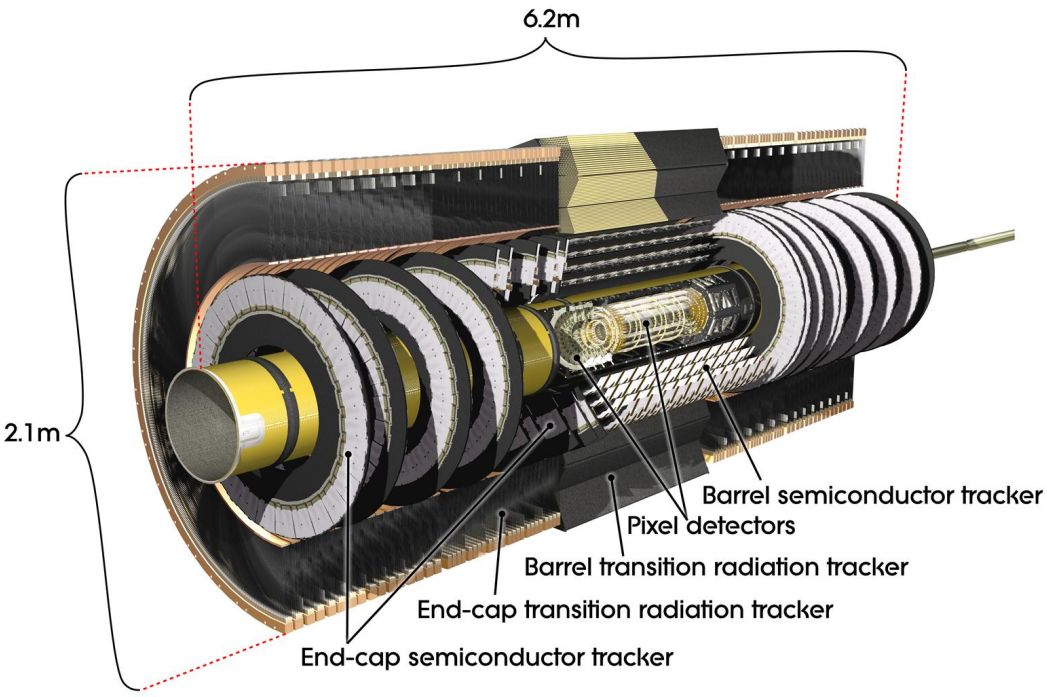

Figure 2.4. Illustration of the inner detector including the pixel, SCT and TRT technologies [2].

one set of strips in each layer parallel to the beam direction, measuring $R-\phi$. They consist of two 6.4 cm long daisy-chained sensors with a strip pitch of 80 μm. In the endcap region, the detectors have a set of strips running radially and a set of stereo strips at an angle of 40 mrad. The mean pitch of the strips is also approximately 80 μm. The intrinsic accuracies per module in the barrel are 17 μm ($R-\phi$) and 580 μm (z) and in the disks are 17 μm ($R-\phi$) and 580 μm (R).

A large number of hits (typically 36 per track) is provided by the 4 mm diameter straw tubes of the TRT, which enables track-following up to $|\eta| = 2.0$. The TRT only provides $R-\phi$ information, for which it has an intrinsic accuracy of 130 μm per straw. In the barrel region, the straws are parallel to the beam axis and are 144 cm long, with their wires divided into two halves, approximately at $\eta = 0$. In the endcap region, the 37 cm long straws are arranged radially in wheels.

Table 2.1. Main parameters of the inner detector, as disclosed in Ref. [2].

Item		Radial extension [mm]	Length [mm]
Overall ID envelope		$0 < R < 1150$	$0 < \|z\| < 3512$
Beam pipe		$29 < R < 36$	
Pixel	Overall envelope	$45.5 < R < 242$	$0 < \|z\| < 3092$
3 cylindrical layers	Sensitive barrel	$50.5 < R < 122.5$	$0 < \|z\| < 400.5$
2×3 disks	Sensitive endcap	$88.8 < R < 149.6$	$495 < \|z\| < 650$
SCT	Overall envelope	$255 < R < 549$ (barrel)	$0 < \|z\| < 805$
		$251 < R < 610$ (endcap)	$810 < \|z\| < 2797$
4 cylindrical layers	Sensitive barrel	$299 < R < 514$	$0 < \|z\| < 749$
2×9 disks	Sensitive endcap	$275 < R < 560$	$839 < \|z\| < 2735$
TRT	Overall envelope	$554 < R < 1082$ (barrel)	$0 < \|z\| < 780$
		$617 < R < 1106$ (endcap)	$827 < \|z\| < 2744$
73 straw planes	Sensitive barrel	$563 < R < 1066$	$0 < \|z\| < 712$
160 straw planes	Sensitive endcap	$644 < R < 1004$	$844 < \|z\| < 2710$

The inner detector system provides tracking measurements in a range matched by the precision measurements of the electromagnetic calorimeter. The electron identification capabilities are enhanced by the detection of transition-radiation photons in the xenon-based gas mixture of the straw tubes. The semiconductor trackers also allow impact parameter measurements and vertexing for heavy-flavor and τ-lepton tagging. The secondary vertex measurement performance is enhanced by the innermost layer of pixels, at a radius of about 5 cm.

2.2.2 The Calorimeters

A view of the calorimeters is presented in Fig. 2.5. The calorimeters cover the range $|\eta| < 4.9$, using different techniques suited to the widely varying requirements of the physics processes of interest and of the radiation environment over this large η-range. Over the η region matched to the inner detector, the fine granularity of the EM calorimeter is ideally suited for precision measurements of electrons and photons.

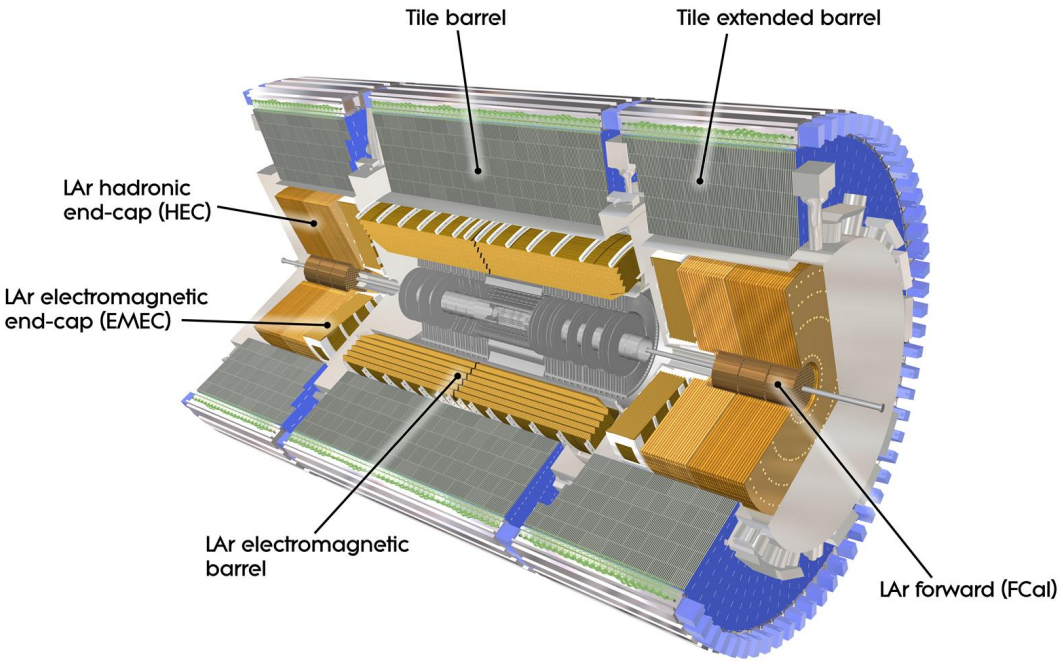

Figure 2.5. Illustration of ATLAS calorimeter system [2].

The coarser granularity of the rest of the calorimeter is sufficient to satisfy the physics requirements for jet reconstruction and missing transverse energy measurements.

Calorimeters must provide good containment for electromagnetic and hadronic showers, and must also limit punch-through into the muon system. Hence, the total thickness of the EM calorimeter is > 22 radiation lengths (X_0) in the barrel and > 24 X_0 in the endcaps. The approximate 9.7 interaction lengths (λ) of active calorimeter in the barrel (10 λ in the endcaps) are adequate to provide good resolution for high energy jets.

2.2.2.1 LAr Electromagnetic Calorimeter

The EM calorimeter is divided into a barrel part ($|\eta| < 1.475$) and two endcap components ($1.375 < |\eta| < 3.2$), each housed in their own cryostat. The position of the central solenoid in front of the EM calorimeter demands optimization of the

material in order to achieve the desired calorimeter performance. As a consequence, the central solenoid and the LAr calorimeter share a common vacuum vessel, thereby eliminating two vacuum walls. The barrel calorimeter consists of two identical half-barrels, separated by a small gap (4 mm) at $z = 0$. Each endcap calorimeter is mechanically divided into two coaxial wheels: an outer wheel covering the region $1.375 < |\eta| < 2.5$, and an inner wheel covering the region $2.5 < |\eta| < 3.2$. The EM calorimeter is a lead-LAr detector with accordion-shaped kapton electrodes and lead absorber plates over its full coverage. The accordion geometry provides complete ϕ symmetry without azimuthal cracks.

2.2.2.2 Hadronic Calorimeters

Tile Calorimeter: The tile calorimeter is placed directly outside the EM calorimeter envelope. Its barrel covers the region $|\eta| < 1.0$, and its two extended barrels the range $0.8 < |\eta| < 1.7$. It is a sampling calorimeter using steel as the absorber and scintillating tiles as the active material. The barrel and extended barrels are divided azimuthally into 64 modules. Radially, the tile calorimeter extends from an inner radius of 2.28 m to an outer radius of 4.25 m. It is segmented in depth in three layers, approximately 1.5, 4.1 and 1.8 interaction lengths thick for the barrel and 1.5, 2.6, and 3.3 λ for the extended barrel. The total detector thickness at the outer edge of the tile-instrumented region is 9.7 λ at $\eta = 0$.

LAr Hadronic Endcap Calorimeter: The hadronic endcap calorimeter (HEC) consists of two independent wheels per endcap, located directly behind the endcap electromagnetic calorimeter and sharing the same LAr cryostats. To reduce the drop in material density at the transition between the endcap and the forward calorimeter (around $|\eta| = 3.1$), the HEC extends out to $|\eta| = 3.2$, thereby overlapping with the forward calorimeter. Similarly, the HEC η range also slightly overlaps that of the tile calorimeter ($|\eta| < 1.7$) by extending to $|\eta| = 1.5$. Each wheel is built from 32 identical

wedge-shaped modules, assembled with fixtures at the periphery and at the central bore. Each wheel is divided into two segments in depth, for a total of four layers per endcap. The wheels closest to the interaction point are built from 25 mm parallel copper plates, while those further away use 50 mm copper plates (for all wheels the first plate is half-thickness). The outer radius of the copper plates is 2.03 m, while the inner radius is 0.475 m (except in the overlap region with the forward calorimeter where this radius becomes 0.372 m). The copper plates are interleaved with 8.5 mm LAr gaps, providing the active medium for this sampling calorimeter.

LAr Forward Calorimeter: The forward calorimeter (FCal) is integrated into the endcap cryostats, as this provide clear benefits in terms of uniformity of the calorimetric coverage as well as reduced radiation background levels in the muon spectrometer. The FCal is approximately 10 interaction lengths deep, and consists of three modules in each endcap: the first, made of copper, is optimized for electromagnetic measurements, while the other two, made of tungsten, measure predominantly the energy of hadronic interactions. Each module consists of a metal matrix, with regularly spaced longitudinal channels filled with the electrode structure consisting of concentric rods and tubes parallel to the beam axis. The LAr in the gap between the rod and the tube is the sensitive medium.

2.2.3 The Muon Spectrometer

The conceptual layout of the muon spectrometer is shown in Fig. 2.6 and the main parameters of the muon chambers are listed in table 2.2. It is based on the magnetic deflection of muon tracks in the large superconducting air-core toroidal magnets, and it is instrumented with separate trigger and high-precision tracking chambers. Over the range $|\eta| < 1.4$, magnetic bending is provided by the large barrel toroid. For $1.6 < |\eta| < 2.7$, muon tracks are bent by two smaller endcap magnets located at both ends of the barrel toroid. Over $1.4 < |\eta| < 1.6$, usually referred to as the transition

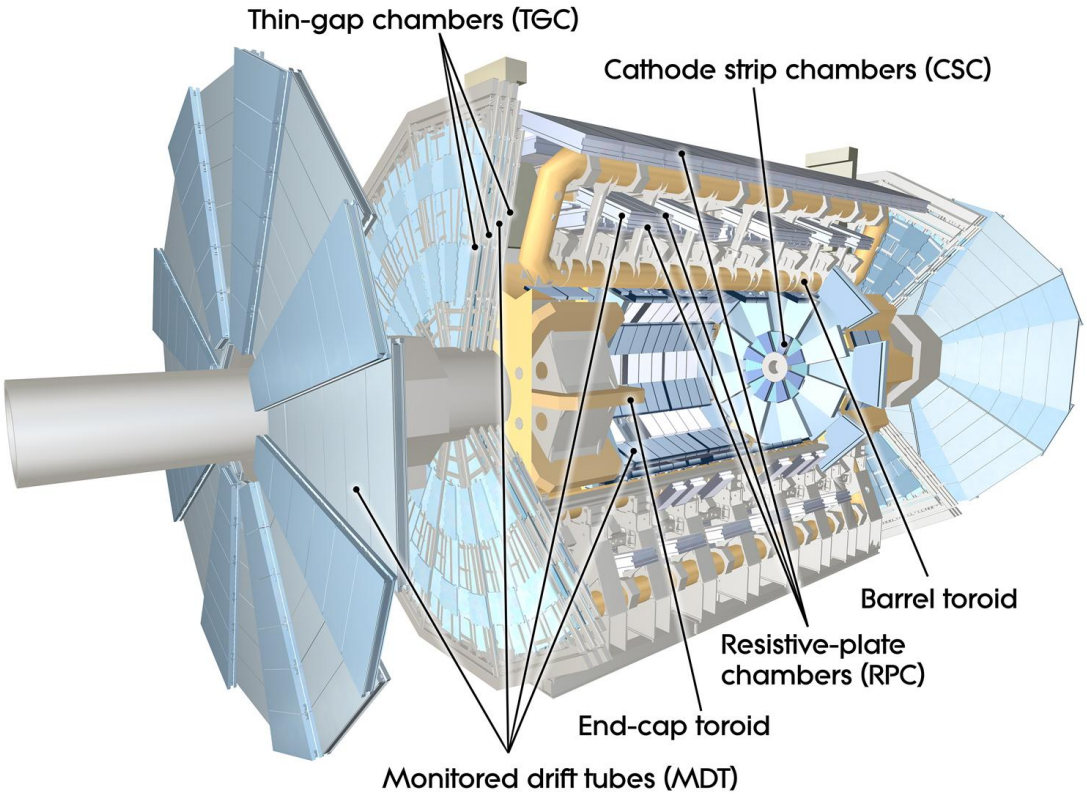

Figure 2.6. Illustration of ATLAS muon spectrometer, including MDTs, CSCs, RPCs and TGCs [2].

region, magnetic deflection is provided by a combination of barrel and endcap fields. The two endcap toroids are inserted in the barrel toroid at each end and line up with the central solenoid. Each of the three toroids consists of eight coils assembled radially and symmetrically around the beam axis. The endcap toroid coil system is rotated by 22.5° with respect to the barrel toroid coil system in order to provide radial overlap and to optimize the bending power at the interface between the two coil systems. The barrel toroid coils are housed in eight individual cryostats. Each endcap toroid consists of eight racetrack-like coils in an aluminium alloy housing. This magnet configuration provides a field which is mostly orthogonal to the muon trajectories, while minimizing the degradation of resolution due to multiple scattering.

Table 2.2. Main parameters of the muon spectrometer, as disclosed in Ref. [2].

Monitored drift tubes	**MDT**
- Coverage	$\|\eta\| < 2.7$ (innermost layer: $\|\eta\| < 2.0$)
- Number of chambers	1150
- Number of channels	354 000
- Function	Precision tracking
Cathode strip chambers	**CSC**
- Coverage	$2.0 < \|\eta\| < 2.7$
- Number of chambers	32
- Number of channels	31 000
- Function	Precision tracking
Resistive plate chambers	**RPC**
- Coverage	$\|\eta\| < 1.05$
- Number of chambers	606
- Number of channels	373 000
- Function	Triggering, second coordinate
Thin gap chambers	**TGC**
- Coverage	$1.05 < \|\eta\| < 2.7$ (2.4 for triggering)
- Number of chambers	3588
- Number of channels	318 000
- Function	Triggering, second coordinate

The anticipated high level of particle flux has had a major impact on the choice and design of the spectrometer instrumentation, affecting performance parameters such as rate capability, granularity, ageing properties, and radiation hardness. In the barrel region, tracks are measured in chambers arranged in three cylindrical layers around the beam axis; in the transition and endcap regions, the chambers are installed in planes perpendicular to the beam, also in three layers.

Over most of the η-range, a precision measurement of the track coordinates in the principal bending direction of the magnetic field is provided by Monitored Drift Tubes (MDTs). At large pseudorapidities, Cathode Strip Chambers (CSCs, which are multiwire proportional chambers with cathodes segmented into strips) with higher granularity are used in the innermost plane over $2 < |\eta| < 2.7$. The stringent requirements on the relative alignment of the muon chamber layers are met by the combination of

precision mechanical-assembly techniques and optical alignment systems both within and between muon chambers.

The trigger system covers the pseudorapidity range $|\eta| < 2.4$. Resistive Plate Chambers (RPCs) are used in the barrel and Thin Gap Chambers (TGCs) in the endcap regions. The trigger chambers for the muon spectrometer serve a threefold purpose: provide bunch-crossing identification, provide well-defined p_{T} thresholds, and measure the muon coordinate in the direction orthogonal to that determined by the precision-tracking chambers.

2.2.4 Trigger and Data Acquisition

The Trigger and Data Acquisition (collectively TDAQ) systems are partitioned into sub-systems, typically associated with subdetectors, which have the same logical components and building blocks. The trigger system has three distinct levels: L1, L2, and the event filter. Each trigger level refines the decisions made at the previous level and, where necessary, applies additional selection criteria. The data acquisition system receives and buffers the event data from the detector-specific readout electronics, at the L1 trigger accept rate. The first level uses a limited amount of the total detector information to make a decision in less than 2.5 μs, reducing the rate to about 75 kHz. The two higher levels access more detector information for a final rate of up to 200 Hz with an event size of approximately 1.3 MB.

The L1 trigger searches for high transverse momentum muons, electrons, photons, jets, and τ-leptons decaying into hadrons, as well as large missing and total transverse energy. Its selection is based on information from a subset of detectors. High transverse momentum muons are identified using trigger chambers in the barrel and endcap regions of the spectrometer. Calorimeter selections are based on reduced-granularity information from all the calorimeters. Results from the L1 muon and calorimeter triggers are processed by the central trigger processor, which implements

a trigger 'menu' made up of combinations of trigger selections. Pre-scaling of trigger menu items is also available, allowing optimal use of the bandwidth as luminosity and background conditions change. Events passing the L1 trigger selection are transferred to the next stages of the detector-specific electronics and subsequently to the data acquisition.

In each event, the L1 trigger also defines one or more Regions-of-Interest (RoIs), i.e. the geographical coordinates in η and ϕ, of those regions within the detector where its selection process has identified interesting features. The RoI data include information on the type of feature identified and the criteria passed, e.g. a threshold. This information is subsequently used by the high-level trigger.

The L2 selection is seeded by the RoI information provided by the L1 trigger over a dedicated data path. L2 selections use, at full granularity and precision, all the available detector data within the RoIs (approximately 2% of the total event data). The L2 menus are designed to reduce the trigger rate to approximately 3.5 kHz, with an event processing time of about 40 ms, averaged over all events. The final stage of the event selection is carried out by the event filter, which reduces the event rate to roughly 200 Hz. Its selections are implemented using offline analysis procedures within an average event processing time of the order of four seconds.

CHAPTER 3

OBJECT RECONSTRUCTION

This Chapter briefly describes how the information recorded by the different sub-detectors is processed to build the objects used in the analysis and determine their kinematics. Sections 3.1 and 3.2 address the track and vertex reconstructions, respectively. The electron reconstruction and identification is described in Sec. 3.3. The measurement and calibration of jets is presented in Sec. 3.4. The last section, Sec. 3.5, covers the muon identification.

3.1 Track Reconstruction

The trajectories of charged particles traversing the inner detector are represented by tracks. The track reconstruction is divided in three stages [46, 47]:

- A pre-processing stage, in which the hits from the pixel and SCT detectors are converted into clusters, and the TRT information is translated to calibrated drift circles.

- A track-finding stage, where different tracking strategies are implemented. The default technique uses pixel clusters to form track seeds that are extended, first to the SCT, and then to the TRT.

- A post-processing stage, in which a vertex finder is used to reconstruct the primary vertex.

In the track-finding stage, the primary ID pattern recognition algorithm follows an "inside-out" strategy. The first step in the inside-out tracking reconstruction is

the creation of SpacePoint objects; these are three-dimensional representations of the clusters in the silicon detectors. Collections of SpacePoints form track candidate seeds. Once the track seeds are created, a road building process starts. The road building comprises a search for hits associated to the track candidate in other detector elements, an extension toward those elements, and a track fitting step. A Kalman fitter[1] is used to simultaneously follow the trajectory and include successive hits in the track candidate fit.

This procedure produces a very high number of track candidate segments, some of which are incomplete or share hits. Therefore, an ambiguity solving step is employed before extending the track candidates to the TRT. Here, the track segments are ranked, via a track-scoring strategy, in their likelihood to describe the real trajectories of particles in the event. In an iterative procedure, the track segments with the highest score are bundled and the segments that fall beyond a certain quality cut are neglected for further processing. The bundled tracks are used as input to find compatible sets of TRT measurements. These TRT-extended tracks are refitted with the full information of all the three detectors (i.e. pixel, SCT and TRT).

A complementary "outside-in" algorithm searches for unused track segments in the TRT. Such segments are extended to the SCT and pixel detectors to improve tracking efficiency for secondary tracks. Both of these algorithms require a track transverse momentum (p_{T}) greater than 500 MeV. In order to reconstruct tracks all the way down to 100 MeV, the inside-out algorithm is re-run with the remaining hits.

3.2 Vertex Reconstruction

The reconstruction of primary vertices comprises two stages: (i) a primary vertex finding algorithm, dedicated to associate reconstructed tracks to vertex candidates,

[1] A Kalman fitter combines forward filtering, backward smoothing and an outlier rejection. It uses the extrapolation engine with its underlying reconstruction geometry for filter step predictions [47].

and (ii) a vertex fitting algorithm, dedicated to reconstruct the vertex position and error matrix. The latter also refits the associated tracks constraining them to originate from the reconstructed interaction point. For the vertex finding stage, the tracks are require to satisfy the following conditions [48, 49]:

- $p_{\mathrm{T}} > 150$ MeV,
- $|d_o| < 4$ mm,
- $\sigma(d_0) < 5$ mm,
- $\sigma(z_0) < 10$ mm,
- at least 4 hits in the SCT detector, and
- at least 6 hits in the pixel and SCT detectors,

where d_0 and z_0 represent the transverse and longitudinal impact parameter with respect to the beam-spot, and $\sigma(d_0)$ and $\sigma(z_0)$ represent the corresponding uncertainties.

The reconstruction follows an iterative strategy, first pre-selecting the tracks compatible with an interaction region origin. A vertex seed is formed by looking for the global maximum in the distribution of z-coordinates of the tracks. The vertex position is determined using a vertex fitter, which takes as input the seed position and the tracks around it. The vertex fitter is a robust χ^2 based fitting algorithm that handles outlying track measurements by down-weighting their contribution to the overall vertex χ^2. Tracks displaced from the vertex by more than 7σ are used to seed a new vertex. The procedure is repeated until no unassociated tracks are left in the event or no additional vertex can be found.

3.3 Electron Reconstruction

The standard electron reconstruction procedure [50, 51] is based on clusters in the electromagnetic calorimeter associated to tracks of charged particles in the inner detector. A track-to-cluster matching forms the central part of the strategy. Information from both detectors is used to allow electron identification while reducing the amount of background.

The electron reconstruction begins with the creation of a preliminary set of seed clusters. The seed clusters are 3×5 in η/ϕ middle layer cell units and have energies above 2.5 GeV. In the pseudorapidity range covered by the tracker (i.e. $|\eta| < 2.5$), a track-to-cluster matching is performed by extrapolating the tracks from their last measurement point to the second layer of the calorimeter. Electromagnetic showers characterized by tracks associated to the seed clusters are considered electron candidates. The electromagnetic cluster is then recomputed and corrected using a 3×7 (5×5) sliding window in η/ϕ middle layer cell units in the barrel (endcaps). The electron four-momentum is computed adding the information from the best track matched to the original seed cluster. The energy is computed as a weighted average between the cluster energy and the track momentum.

For the electron identification and background ("fakes") rejection, selection requirements are imposed to variables that rely on calorimeter, tracker and combined calorimeter-tracker information. Cuts on these variables define three sets of reference points with increasing background rejection power: loose, medium and tight[2]. Shower shape variables of the second calorimeter layer and hadronic leakage variables are used in the loose selection. First calorimeter layer cuts, track quality requirements and track-cluster matching are added at the level of medium selection. The

[2]In this analysis, variations of the electron identification referred as 'plus-plus' (e.g. medium++, tight++) are used. They are described in Refs. [50, 51].

tight selection adds E/p, b-layer hits and the particle identification potential of the TRT.

3.4 Jet Reconstruction

Hadronic jets are reconstructed using the anti-k_{T} jet clustering algorithm[3] [52] starting from the energy depositions of electromagnetic and hadronic showers in the calorimeter. Jet finding [53, 54] is done in $y-\phi$ coordinates while jet corrections and performance are usually done in $\eta-\phi$ coordinates. The jet p_{T} reconstruction threshold is $p_{\mathrm{T}}^{jet} > 7$ GeV. The inputs to the jet algorithm are energy deposits in topological calorimeter clusters (topo-clusters) or calorimeter towers, where only topo-clusters or towers with positive energy are considered; or reconstructed tracks in the inner detector constrained to the hardest[4] primary vertex (track-jets).

The topo-clusters formation starts from a seed cell whose signal-to-noise (S/N) ratio is above a threshold of S/N = 4. Cells neighboring the seed (or the cluster being formed) that have a signal-to-noise of at least S/N = 2 are included. All cells in a topo-cluster are searched for local maxima in terms of energy content; the local maxima are then used as seeds for a new iteration. A topo-cluster is defined to have an energy equal to the energy sum of all the included calorimeter cells, zero mass and a reconstructed direction calculated from the weighted averages in pseudorapidities and azimuthal angles of the constituent cells, pointing back to the primary vertex.

Calorimeter towers are static $\Delta\eta \times \Delta\phi = 0.1 \times 0.1$ grid elements build directly from calorimeter cells.

---

[3]The anti-k_{T} jet algorithm belongs to a class of infrared and collinear safe sequential recombination algorithms. It has sensible phenomenological behavior, notably, the resilience of its jet boundaries with respect to soft radiation, that is, soft particles do not modify the shape of the jet while hard particles do.

[4]This is the vertex with maximum $\sum(p_{\mathrm{T}}^{track})^2$.

For reconstructed track-jets, tracks with $p_{\mathrm{T}}^{track} > 0.5$ GeV and $|\eta| < 2.5$ are selected. Additional requirements are imposed on the track impact parameters, namely $|d_0| < 1.5$ mm and $|z_0 sin\theta| < 1.5$ mm. Track-jets must have at least two constituent tracks and a total transverse momentum $p_{\mathrm{T}}^{track\,jet} > 3$ GeV.

The uncertainty in jet energy measurements is the dominant experimental uncertainty for numerous physics results, including the analysis presented in this thesis. To this end, ATLAS has developed several jet energy scale calibration schemes to ensure the correct measurements. The jet calibration corrects for detector effects such as: calorimeter non-compensation[5], dead material, leakage, out of calorimeter jet cone, noise threshold and particle reconstruction efficiency. The impact of these effects and the different calibration schemes are not described here, but detailed information can be found elsewhere [53–56].

3.5 Muon Reconstruction

Muon identification and reconstruction algorithms use complementary approaches resulting in four types of muon candidates: standalone muons, combined muons, segment-tagged muons and calorimeter-tagged muons [57, 58].

The standalone muon reconstruction is entirely based on the tracks reconstructed in the muon spectrometer. The track parameters (p_{T}, η, ϕ, vertex position) are obtained from the muon spectrometer track fit and they are extrapolated to the interaction point taking into account both multiple scattering and energy loss in the calorimeters.

The combined muon reconstruction associates a standalone muon spectrometer track to an inner detector one, selecting the tracks to be paired on the basis of a match χ^2, defined from the difference between the two sets of track parameters

[5]The calorimeter gives a lower response to hadrons than to electrons or photons.

weighted by their combined covariance matrix. The combined track parameters are derived either from a statistical combination of the two tracks or from a refit of the full track.

A segment-tagged muon is identified if an inner detector track extrapolated to the muon spectrometer was associated with straight track segments in the precision muon chambers. The track parameters are those of the inner detector track.

For calorimeter-tagged muons, a track in the inner detector is identified as a muon if the associated energy depositions in the calorimeters is compatible with the hypothesis of a minimum ionizing particle.

For each of these kinds of muons, two sequences of algorithms are available, referred to as chain 1 (STACO) and chain 2 (MUID).

For chain 1, the muon reconstruction is initiated locally in a muon chamber by the search for straight line track segments in the bending plane. Hits in the precision chambers are used and the segment candidates are required to point to the center of the detector. A minimum of two track segments in different muon stations are combined to form a muon track candidate using three-dimensional tracking in the magnetic field. The resulting standalone track, extrapolated to the interaction point, is statistically combined to an inner detector track using tight matching cuts to provide combined muons. Unused segments are used to tag extrapolated inner detector tracks

For chain 2, a global pattern recognition, based on Hough transforms, is run on the full muon spectrometer, independently in the bending and non bending projections, to search for track patterns. Patterns in the two projections are then combined to seed the segment finding. Straight line segments are reconstructed in each chamber and hits from the trigger detectors from the same pattern are associated with them. The track candidates are built from segments associated to the same pattern and compatible with a curved track. Segments in the outermost chambers are used to

seed a track fit with all the segments in the next chamber closer to the interaction point. All the successful combinations are considered in extending the track fit to the segments in the innermost station. Ambiguities are solved keeping the higher quality track, on the basis of the number of associated hits and fit quality. The track is then refit with full treatment of material effects.

Combined muons are obtained by fitting the standalone track with an inner detector track. All segments can be used to tag extrapolated inner detector tracks.

CHAPTER 4

TEV-SCALE GRAVITY SIGNATURE SEARCH

TeV-scale gravity models predict the production and decay of black holes at the energy reach of the LHC. The decay is thermal and characterized by a large multiplicity of particles with large transverse momenta. Typical energies for these particles are in the range of a few 100 GeV, corresponding to the Hawking temperature of the black hole. A feature of the thermal decay is the "democratic" coupling of gravity: the emitted particles are produced primarily according to Standard Model degrees of freedom. All the ≈ 60 SM particles have roughly equal probability to be produced.

This implies that the final states are dominated by jet emissions. However, signatures with at least one charged lepton are expected in 15-50% of black hole events. Additionally, the requirement of at least one charged lepton, which from now on refers to either an electron or a muon, can greatly reduced SM backgrounds, especially the contribution from QCD multijet processes.

Given the high number of particles with large transverse momenta, a black hole signal will manifest itself at high p_{T}. An effective variable providing great discriminating power between signal and Standard Model backgrounds is

$$\sum p_{\mathrm{T}} = \sum_{i=objects} p_{\mathrm{T},i}$$

which is the scalar sum of the transverse momenta of selected final state reconstructed objects (c.f. Fig. 1.15).

This Chapter describes a search for evidence of black hole or string ball production in events including high-energy leptons. Specifically, it describes a search for final

states containing at least three objects ("high multiplicity") with $p_{\mathrm{T}} > 100$ GeV ("large transverse momenta"), where at least one of the objects is a charged lepton. The events are separated into mutually exclusive channels according to the flavor of the leading lepton. Background estimations in the signal region rely on studies performed using Monte Carlo (MC) simulated events or data-driven methods, in control regions enhanced for a particular SM process.

Section 4.1 outlines the MC simulated samples used in this analysis. The experimental dataset is described in Sec. 4.2. The object and event selections are presented in Sec. 4.3 and Sec. 4.4, respectively. Section 4.5 addresses the Standard Model background estimation, while Sec. 4.6 describes the systematic uncertainties.

4.1 Monte Carlo Simulated Samples

Monte Carlo simulated event samples are used to estimate some of the backgrounds and determine signal acceptances. All the MC samples are made with the official ATLAS Monte Carlo production system and use either the full `Geant` [59–61] version or the fast detector simulation (AtlFast-II) [62] of the processing chain. All samples are initially reweighted to correspond to 13.0 fb^{-1} of integrated luminosity[1]. Additional weights are applied (c.f. Sec. 4.3), where applicable, to bring the simulated data into better agreement with the experimental data collected in 2012.

Further details of the simulated signal and background samples, including their process cross sections are provided in Appendix A.

[1]It is worth pointing out that, while these samples are reweighted to 13 fb^{-1}, the statistics available for most of the dominant backgrounds correspond to a lower integrated luminosity. For both W+jets and Z+jets, the number of events generated correspond to an integrated luminosity in the range between 2-10 fb^{-1}. For $t\bar{t}$, however, the events available amount to a greater integrated luminosity. As it will become evident in Chapter 5, limited statistics are the dominant source of uncertainties.

4.1.1 Background Samples

4.1.1.1 W/Z+Jets Samples

The W+jets and Z+jets samples are generated using `Sherpa` 1.4.0 [63] with the `CT10` [64] PDF set. The events in the exclusive samples are reweighted to represent the best estimate of expected rates for 13.0 fb^{-1} of integrated luminosity. The reweighting makes use of the exclusive sample cross sections predicted by `DYNNLO` [65], constraining the sum of their cross sections to match the best estimates of the inclusive cross sections: $\sigma\left(W\left(\rightarrow \ell\nu\right) + \text{jets}\right) = 12.19$ nb and $\sigma\left(Z\left(\rightarrow \ell\ell\right) + \text{jets}\right) = 1.15$ nb (NNLO) per charged lepton flavor.

For systematics studies, samples generated with `Alpgen` [66] – including both light- and heavy-flavor jets (e.g. $W+bb$, $W+cc$, $Z+bb$, $Z+cc$) added to the nominal W/Z+jets datasets – interfaced with `Pythia` [67] and with PDF set `CTEQ6L1` [8] are used. The nominal W/Z+jets dataset comprises exclusive samples with zero to five additional partons.

4.1.1.2 $t\bar{t}$ Samples

The $t\bar{t}$ sample was simulated using `Powheg` [68] with the `CT10` PDF set. The top mass is set to 172.5 GeV. The events are reweighted to represent the best estimate of expected rates for 13.0 fb^{-1} of integrated luminosity using the cross section of 238.06 pb calculated by `HATHOR` 1.2 [69].

4.1.1.3 Single Top Samples

Single top samples corresponding to three production modes, s-channel, t-channel and Wt-channel, have been generated separately. For the s-channel and Wt-channel, the events were generated with `MC@NLO` 4.06 [70], interfaced to `Herwig` for parton showering and fragmentation, and `Jimmy` for the underlying event. In reweighting events to represent the best estimate of expected rates for 13.0 fb^{-1}, the total cross sections of 5.61 pb and 22.4 pb are used for the s-channel and Wt-channel, respec-

tively. The t-channel events are generated with `AcerMC` [71] using the `CT10` PDF set. Events are reweighted using the cross section of 87.8 pb.

4.1.1.4 Diboson Samples

The diboson (WW, WZ, ZZ) samples are generated with `Sherpa` 1.4.0 [63] with the `CT10` PDF set.

4.1.2 Signal Samples

4.1.2.1 `Charybdis` Samples

`Charybdis` 2 1.0.3 [72] is used to generate the string ball and black hole Monte Carlo signal events. The shower evolution and hadronization are simulated with `Pythia`. The `MSTW2008lo [73]` PDF set is used.

`Charybdis` can model final remnant decays in a range of different ways. When the black hole mass falls below the Planck scale, either a two-body phase space decay (low multiplicity remnant) occurs, or the number of final-state particles is chosen from a Poisson distributed with mean of four (high multiplicity remnant).

Most of the `Charybdis` parameters are set to their default values. The following model parameters have been changed from the defaults:

- YRCSEC = FALSE: In all cases, do not use Yoshino-Rychkov factors in the cross section.
- BHSPIN = TRUE/FALSE: Rotating or non-rotating black holes and string balls.
- MJLOST = TRUE/FALSE. Turn on or off initial-state graviton radiation.
- NBODY = 2 or 4: Two- or four-body decay of remnant.
- NBODYVAR = TRUE/FALSE: Variable (Poisson distributed) N-body decay, or fixed N-body decay of remnant.

A set of parameter-scan samples are produced, where for each model the following are varied:

- TOTDIM: Total number of dimensions.
- MINMSS: Minimum production mass, M_{TH}.
- MPLNCK: Planck scale, M_{D}.
- DGMS: String scale, M_{s}, if string balls (DGSB = TRUE).

The string-ball samples all have the number of extra dimensions set to six and the string coupling set to 0.4.

4.1.2.2 `BlackMax` Samples

`Blackmax` 2.01 [74,75] is also used to generate alternative black hole signal events. The shower evolution and hadronization are simulated with `Pythia` 6.421. The `MSTW2008lo [73]` PDF set is used. Most of the `Blackmax` parameters are set to their default values. The following model parameters have been changed from the defaults:

- number_of_conservations = 0 or 3: Lepton number is conserved, or not.
- turn_on_graviton = 0: No gravitons in simulation.
- size_of_brane(1/Mpl) = 0.0: No brane thickness.
- extradimension_size(1/Mpl) = 0.0: Infinite size of extra dimensions.
- Choose_a_case = tensionless_nonrotating/rotating_nonsplit: Rotating or non-rotating black holes.

When performing the parameter scans, the following parameters were varied or changed:

- number_of_extra_dimensions: Number of extra dimensions.
- Minimum_mass(GeV): Minimum production mass, M_{TH}.
- M_pl(GeV): Planck scale, M_{D}.

4.1.2.3 Representative Signal Samples

Two baseline signal samples are used to guide the analysis, both generated using `Charybdis`, and corresponding to a rotating black hole and a rotating string ball.

- Black hole sample, ID 158532: number of extra dimensions set to six; M_{D} set to 2 TeV; and M_{TH} set to 5 TeV. This sample has a cross section of 0.046 pb calculated by `HATHOR`.
- String ball sample, ID 159256: number of extra dimensions set to six; M_{s} set to 1.0 TeV; g_s set to 0.4; and M_{TH} set to 5 TeV. This sample has a cross section of 0.0078 pb calculated by `HATHOR`.

4.2 Data Sample

This search uses proton-proton collisions recorded between April and September of 2012 with the ATLAS detector at $\sqrt{s} = 8$ TeV. The collision data is divided into streams, each stream comprising events that pass a predetermined trigger menu. In this study, the "Egamma" and "Muon" streams are used for the electron and muon channels, respectively. After the application of beam, detector and data quality requirements, the dataset corresponds to an integrated luminosity of 13.0 fb^{-1}. Figure 4.1 shows the total integrated luminosity recorded by ATLAS in 2012. The partial dataset considered in this analysis includes up to the third plateau region.

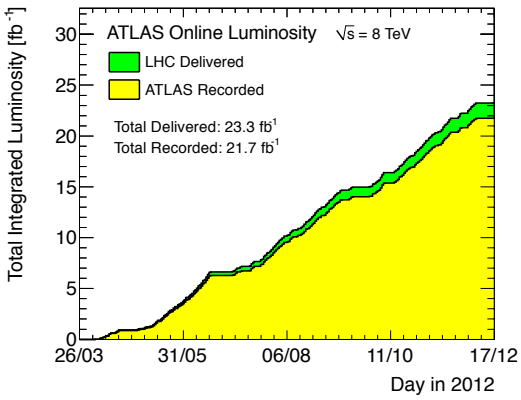

Figure 4.1. Total integrated luminosity recorded by ATLAS in 2012. This analysis uses the data collected up to 17 September 2012, corresponding to the third plateau region in the figure.

4.3 Object Selection

As stated in the Chapter's introduction, the starting point of the analysis is identifying events with three or more high p_{T} objects (i.e. leptons, jets), at least one of which is required to be an electron or a muon. Photons and hadronically-decaying tau leptons are not explicitly identified in this analysis, and are reconstructed as jets. The baseline selection criteria used to define reconstructed objects are described in the following sections.

For the data-driven estimation method, the object selection criteria vary slightly from that of the MC based methods and the signal region. For example, the selection criteria for leptons is loosened for the purpose of estimating the QCD background. Such differences in selection criteria are noted in the appropriate sections.

4.3.1 Electrons

The electron four-momentum combines information from the calorimeter clusters and the matching inner detector track. The direction of the electron is calculated in one of two ways. If the ID track has at least four silicon hits (pixel + SCT), the ID track η, ϕ parameters are used; otherwise (basically, TRT standalone tracks), the

cluster η, ϕ parameters provide the electron direction. The calorimeter cluster energy is corrected or rescaled by applying energy scales obtained from resonances such as $Z \to e^+e^-$, $J/\psi \to e^+e^-$, or E/p studies using isolated electrons from $W \to e\nu$. The electron or cluster energy rescaling is applied in bins of (η, ϕ) and have been derived from 2012 data.

Preselected electrons must pass at least the medium++ identification criteria (c.f. Sec. 3.3). They are required to have $p_{\mathrm{T}} > 60$ GeV, which allows for the trigger (at a lower threshold) to be fully efficient and with little p_{T} dependence. These electron candidates are restricted to the pseudorapidity range $|\eta_{cluster}| < 1.37$ or $1.52 < |\eta_{cluster}| < 2.47$, to be within the geometrical acceptance of the inner detector and to avoid the overlap region between the barrel and endcap calorimeters, where there is limited calorimeter instrumentation.

Electron candidates must also be isolated. The isolation cut applied requires that the sum of the transverse momentum of ID tracks in a cone of $\Delta R = 0.2$ around the electron candidate (excluding the electron candidate itself) to be less than 10% of the electron p_{T}. That is, $\sum p_{\mathrm{T}}^{tracks}(\mathrm{cone}\,\Delta R = 0.2)/p_{\mathrm{T}}^{electron} < 0.1$, where $\Delta R = \sqrt{(\Delta\eta)^2 + (\Delta\phi)^2}$. To avoid double counting of objects and reduce the number of non-prompt electrons, electron candidates with a distance to the closest jet of $0.2 < \Delta R < 0.4$ are discarded. The specifics of this overlap removal procedure are described in Sec. 4.3.5.

Measurements of electron reconstruction, identification and trigger efficiencies in data show minor differences in p_{T}, η distributions compared to Monte Carlo simulated data. Efficiency corrections or scale factors in (p_{T}, η) bins are applied as a weight to each MC simulated event to account for these discrepancies.

The above requirements describe the baseline selection applied to all electrons in the event. For the purpose of channel assignment, as described in Sec. 4.4, addi-

tional selection criteria is imposed. Those electrons are required to pass the tight++ identification and match the object that triggered the event[2].

4.3.2 Muons

Preselected muons are required to have $p_{\mathrm{T}} > 60$ GeV and $|\eta| < 2.4$. These conditions allow the muon candidate to be within the geometrical acceptance of the trigger system (RPC and TGC) and at a p_{T} threshold permitting the trigger to be fully efficient.

Muon candidates are required to have tracks in both the inner detector and the muon spectrometer, forming a combined muon (c.f. Sec. 3.5). The reconstructed tracks comprise specific detector hit requirements to ensure a properly measured muon track. The muon candidate must have sufficient hits in all the ID technologies (pixel, SCT, TRT). Additionally, to guarantee the best possible resolution at hight p_{T} in the MS, muon candidates must have precision hits in all three measurement stations and no hits in detector regions with limited alignment precision. This requirement effectively restricts the muon acceptance to the barrel region ($|\eta| < 1.0$) and a portion of the endcap region ($1.3 < |\eta| < 2.0$). The hit requirements are summarized in Table 4.1.

For Monte Carlo simulated data, a resolution correction is applied through a (q/p_{T}) smearing procedure. These corrections have been derived by comparing the dimuon mass resolution measured in experimental and simulated data. The p_{T} corrections are propagated to the combined muon four-momentum, as well as to the corresponding ID and MS momentum measurements.

To ascertain a proper match between the inner detector and the muon spectrometer tracks, a momentum consistency test is implemented. The momentum consistency

[2]A reconstructed electron is considered trigger-matched if it is located within $\Delta R < 0.15$ of the electron trigger object.

Table 4.1. Muon track hit requirements and rejection. In the inner detector, for $|\eta| \leq 0.1$ or $|\eta| \geq 1.9$, the TRT rejection only applies if the number of Hits plus Outliers is greater than 5. In the muon spectrometer, tracks in the barrel are rejected if they include hits in the endcap, and vice versa.

Detector Technology	Hit Requirement	Track Rejection
	Inner Detector	
Pixel B-Layer	if expected, > 0	
Pixel	Hits + Dead Sensors > 1	Pixel Holes + SCT Holes > 2
SCT	Hits + Dead Sensors > 4	Pixel Holes + SCT Holes > 2
TRT $0.1 < \|\eta\| < 1.9$	Hits + Outliers > 5	Outlier fraction > 0.9
TRT $\|\eta\| \leq 0.1$ or $\|\eta\| \geq 1.9$	if Hits + Outliers > 5	then, if Outlier fraction > 0.9
	Muon Spectrometer	
MDT Barrel	Hits ≥ 3, Stations $= 3$	Endcap, BIS78 Hits
RPC	Hits ≥ 1, Layers ≥ 2	
MDT Endcap	Hits ≥ 3, Stations $= 3$	Barrel, BEE, EE, CSC Hits
TGC	Hits ≥ 1, Layers ≥ 2	

is defined as $|(q/p)_{ID} - (q/p)_{MS}|/\sigma_c < 5$, where σ_c is the combined (q/p) uncertainty for the ID and MS measurements.

Similar to electrons, the muon candidates must also be isolated. The isolation cut applied requires that the p_{T} sum of ID tracks within a cone of $\Delta R = 0.3$ around the muon candidate (excluding the muon candidate itself) to be less than 5% of the muon p_{T}. That is, $\sum p_{\mathrm{T}}^{tracks}(\mathrm{cone}\,\Delta R = 0.3)/p_{\mathrm{T}}^{muon} < 0.05$. To reduce the number of non-prompt muons, muon candidates with a distance to the closest jet of $\Delta R < 0.4$ are discarded. The specifics of this overlap removal procedure are described in Sec. 4.3.5. In order to reject muons resulting from cosmic rays, tight cuts are applied on the proximity of the muon trajectory to the primary vertex. The requirements are given by $|z_0| < 1$ mm and $|d_0| < 0.2$ mm, where z_0 and d_0 are the impact parameters in the longitudinal and transverse plane, respectively.

Measurements of muon reconstruction, identification and trigger efficiencies in data show minor differences in p_{T}, η, ϕ distributions compared to Monte Carlo simulated data. Efficiency corrections or scale factors in (p_{T},η,ϕ) bins are applied as a weight to each MC simulated event to account for these discrepancies.

The above requirements describe the baseline selection applied to all muons in the event. For the purpose of channel assignment, as describe in Sec. 4.4, additional selection criteria is imposed. Those muons are required to match the object that triggered the event[3].

4.3.3 Jets

Preselected jets are reconstructed using the anti-k_{T} jet algorithm with distance parameter $R = 0.4$, from energy deposits in topological clusters (c.f. Sec. 3.4). The measured jet candidate energy is corrected for inhomogeneities and the non-compensating nature of the calorimeter by using the local cluster calibration scheme (LCW) [53].

Jet candidates are required to have $|\eta| < 2.8$, to avoid the endcap-forward transition region where the calorimeter instrumentation is limited[4]. Events with preselected jets having $p_{\mathrm{T}} > 20$ GeV, and not passing jet quality criteria against noise and non-collision backgrounds are rejected[5].

Jet candidates within a distance of $\Delta R < 0.2$ of a preselected electron are discarded, since these jets are likely to be electrons also reconstructed as jets. The details of this overlap removal procedure are presented in Sec. 4.3.5. Additionally, preselected jets are required to have $p_{\mathrm{T}} > 60$ GeV. This cut provides a p_{T} uniformity among all the reconstructed objects in the analysis while also removes jets not associated with the hard scattering of interest (PV).

The above requirements describe the baseline selection applied to all jets in the event. For background estimation of some SM processes, additional criteria may be imposed. For example, in a $t\bar{t}$ enhanced control region, at least two jets are

---

[3]A reconstructed muon is considered trigger-matched if it is located within $\Delta R < 0.10$ of the muon trigger object.

[4]See Table 1 and Fig. 2 of Ref. [55].

[5]See Table 1 of Ref. [53].

required to pass the "b-tagging" selection. A b-tagging algorithm exploiting both impact parameter and secondary vertex information is used to identify jets containing a B-hadron decay. This algorithm has a 70% efficiency for tagging b-jets in a MC simulated sample of $t\bar{t}$ events, with a mis-tag rate for light quarks and gluons of $\sim 1\%$.

4.3.4 Missing Transverse Energy

The missing transverse energy $E_{\mathrm{T}}^{\mathrm{miss}}$ (or MET) is reconstructed from the vector sum of all calorimeter cells contained in topological clusters. Calorimeter cells are uniquely associated to a single physics object in a given order: electrons, jets and muons. Cells belonging to electrons are calibrated at the electron energy scale, such that all electron energy corrections (c.f. Sec. 4.3.1) are propagated to the $E_{\mathrm{T}}^{\mathrm{miss}}$. Likewise, cells belonging to jets are taken at the corrected energy scale using the LCW scheme (c.f. Sec. 4.3.3). The contributions from any calorimeter cells associated with muons are subtracted, and the muon terms are replaced with a looser collection of preselected muons[6]. The remaining cells not associated with electrons or jets are included at the electromagnetic scale.

$E_{\mathrm{T}}^{\mathrm{miss}}$ is not considered as an object in this analysis and is used solely in the definitions of some control regions for background estimation.

4.3.5 Overlap Removal

Overlap removal between objects is applied to avoid double counting of said objects. This procedure is especially important for electrons and jets because they are both identified in the calorimeter. The overlap removal comprises the following steps:

[6]This loose collection of preselected muons satisfies the following cuts: $p_{\mathrm{T}} > 10$ GeV, $|\eta| < 2.4$, the inner detector hit requirement (Table 4.1), and the combined or segment-tagged identification (c.f. Sec. 3.5).

- Apply the object preselection described above to electrons, jets and muons[7].
- Reject the jet hypothesis and assume the electron hypothesis if ΔR(electron, jet) < 0.2, since these are likely to correspond to the same physics object. The collection of jets passing this overlap removal step is referred to simply as 'jets'.
- Impose further ΔR isolation: preselected leptons within a distance of $\Delta R = 0.4$ from any jet are removed. This effectively means $0.2 < \Delta R$(jet, electron) < 0.4 and ΔR(jet, muon) < 0.4.

4.4 Event Selection

The following sections describe the event selection criteria in a search for TeV-scale gravity signatures. These requirements are applied to both real and simulated events, and are chosen such that they define a signal region with reduced Standard Model backgrounds. The collection of all these selection requirements is referred to as the "cut flow".

Criteria that are only applicable to either experimental data or MC simulations are properly identified in their respective sections.

4.4.1 Pileup

One of the challenges for the ATLAS detector is the object reconstruction in an environment characterized by a large number of proton-proton collisions per bunch crossing, μ. During 2012, the proton bunches were typically separated by 50 ns. Depending on the length of the read-out window of the subdetector, signals from neighboring bunch crossings can be present when the detector is read-out[8].

---

[7]For electrons, this essentially refers to the p_{T}, η, medium++ and isolation cuts; for jets, it refers to p_{T} and η cuts. Because the muons are not used to overlap-remove other objects, the specific cuts applied at this stage are not important.

[8]In the liquid argon calorimeter cells, the reconstructed energy is sensitive to proton-proton interactions in approximately 24 preceding and one immediately following bunch crossing, in addition

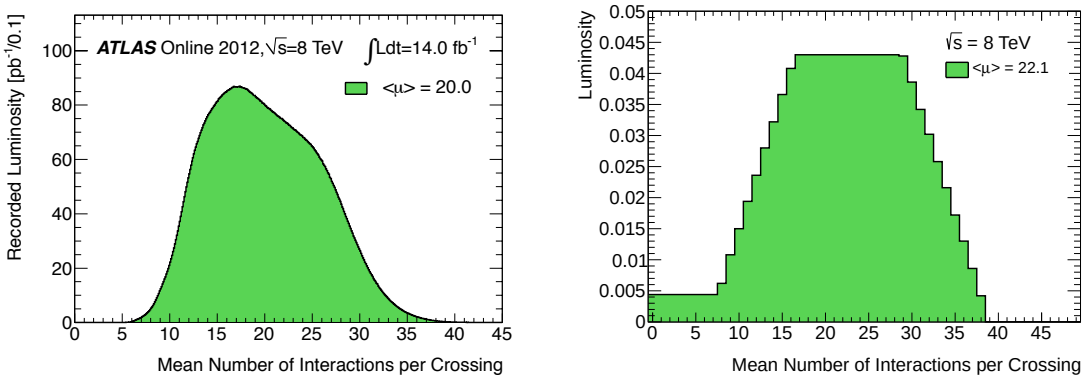

(a) (b)

Figure 4.2. Mean number of interactions per crossing in (a) data and (b) Monte Carlo simulation. The distribution to the left corresponds to the data-taking period studied in this analysis ($\sim$ 14 fb^{-1} before the application of beam, detector and data quality requirements), while the MC is given in arbitrary units and normalized to unit area.

The impact of the interactions from neighboring bunch crossings is referred to as out-of-time pileup, while additional interactions in the same bunch crossing are regarded as in-time pileup. Because the number of interactions per bunch crossing decreases with decreasing beam intensity, and varies between bunches, it is often convenient to refer to the mean number of interactions per bunch crossing $\langle\mu\rangle$[9].

Usually, Monte Carlo simulated samples are produced before or during a given data taking period. By that design, only a best-guess of the data pileup conditions can be incorporated into the Monte Carlo simulation. Thus, there is the need at the analysis level to reweight the Monte Carlo pileup conditions. Figures 4.2(a) and 4.2(b)

to interactions in the current bunch crossing. This is due to the relatively large charge collection time in these calorimeters ($\sim$ 400 ns).

[9]This corresponds to the mean of the Poisson distribution on the number of interactions per crossing for each bunch. It is calculated by:

$$\mu = \frac{L \times \sigma_{inel}}{n_{bunch} f_r}$$

where L is the luminosity, σ_{inel} is the total inelastic cross section, n_{bunch} is the number of colliding bunches, and f_r is the LHC revolution frequency [76].

show the $\langle\mu\rangle$ distributions for data and MC simulation, respectively. Dedicated tools are available in ATLAS to reweight (and thus, reshape) the MC pileup distribution to have better agreement with what is found in the data.

4.4.2 Data Quality Criteria (Good Runs List)

Data quality (DQ) flags form the mechanism to assign 'good runs lists' (GRL)[10] for physics analysis. Said flags ensure that the DQ assessment is applied consistently throughout the data.

The DQ status flags establish the requirements that declare the data good, flawed, or bad, for a given physics object or quantity (e.g. electrons, muon, jets, $E_{\mathrm{T}}^{\mathrm{miss}}$, trigger, luminosity determination). Physics groups determine which final states are relevant for their analysis and derive the corresponding DQ status. The physics DQ status, couple with other requirements (e.g. beam energy, stable beams) determines the appropriate GRL for physics analysis.

This analysis uses most reconstructed objects, so it is necessary that all detectors in ATLAS are in good condition and recording quality data. After the application of the GRL and triggers (c.f. Sec. 4.4.3), the integrated luminosity in both the egamma stream and the muon stream is 13.0 fb^{-1}. The uncertainty on the luminosity calculation is 3.6%, following the method disclosed in Ref. [76].

4.4.3 Trigger

Events are required to pass a single lepton (either electron or muon) trigger to be considered in this analysis. The single lepton trigger menu employed here comprises the lowest unprescaled trigger applicable to all data-taking periods, and a secondary higher threshold unprescaled trigger.

---

[10]The DQ flags actually select lists of good luminosity blocks, but GRL is a common nomenclature.

In order to collect data for the electron channel, events from the egamma stream must pass either the lowest unprescaled single electron trigger with a p_{T} threshold at 24 GeV and a trigger object isolation requirement, or the highest unprescaled single electron trigger with a p_{T} threshold at 60 GeV. This trigger combination (using a logical "OR") compensates for a drop in efficiency at high p_{T} in the lowest threshold trigger.

Similarly for the muon channel, events from the muon stream must pass either the lowest unprescaled single muon trigger with a p_{T} threshold at 24 GeV and a trigger object isolation requirement, or a single muon trigger with a p_{T} threshold at 36 GeV [11].

The trigger efficiency for electrons with $p_{\mathrm{T}} > 25$ GeV is about 97%, while the trigger efficiency for muons with $p_{\mathrm{T}} > 25$ GeV is about 75% (90%) in the barrel (endcaps). These trigger thresholds ensure that the current selection of leptons with $p_{\mathrm{T}} > 60$ GeV lie comfortably in the efficiency plateau.

4.4.4 Vertex

To remove non-collision or cosmic ray events, the first reconstructed primary vertex (c.f. Sec. 3.2), defined to be the one with the highest summed track p_{T}^2, is required to have at least five tracks associated with it. Events not satisfying this requirement are rejected.

4.4.5 Event Cleaning

Noise bursts in the electromagnetic calorimeter may result in bad quality clusters or fake energy deposits, thus affecting the reconstruction and identification of electrons. Data quality flags (e.g. "LAr error") have been implemented to identify such

[11] There is a subtlety that requires further clarification. Because the egamma and muon streams are not mutually exclusive, passing the single electron (muon) triggers is a necessary but not sufficient condition to be identified as an electron (muon) channel event. The conditions that must be met to be classified as either an electron or muon channel event are discussed in Sec. 4.4.6.

occurrences which compromise the data integrity. Events in data characterized by noise bursts in the liquid argon calorimeter are vetoed.

The jet reconstruction can also be affected by non-collision backgrounds. The main sources leading to fake jets are calorimeter electronics noise, cosmic ray muons and beam-halo events. A jet cleaning procedure has been developed in ATLAS to identify events with "bad" jets. The procedure applies a set of discriminating variables (e.g. electromagnetic energy fraction, jet charge fraction, jet time) to remove most of the bad or fake jets with a very small jet inefficiency ($\lesssim 0.2\%$).

In this analysis, events with a bad jet having $p_{\mathrm{T}} > 20$ GeV are rejected. The cleaning procedure is applied to both experimental and simulated data.

4.4.6 Channel Assignment

At this stage of the cut flow, a collection of events triggered by leptons and passing baseline data quality criteria have been selected. The following set of requirements relies solely on the number and the kinematics of the physics objects (especially the leptons), and chooses those events that resemble the expected signature of a black hole decay.

Electrons, muons and jets having $p_{\mathrm{T}} > 60$ GeV and following the selection prescription described in Sec. 4.3 are identified. Events without a lepton of any flavor are removed from consideration.

The next step consists of an assignment strategy where events from the different lepton streams are separated into two statistically independent channels by requiring the presence of a trigger-matched leading lepton. For electrons, this corresponds to the highest p_{T} trigger-matched electron passing the tight++ identification, while for muons, it refers to the highest p_{T} trigger-matched muon in the event. Events without a trigger-matched leading lepton are rejected.

Given the analysis selection criteria, the majority of events comprises leptons of a single type and the channel assignment is trivial: Events in the egamma (muon) stream with a trigger-matched leading electron (muon) are classified in the electron (muon) channel. However, a small fraction of events contain both an electron and a muon (at least one of which is trigger-matched) and therefore appear in both the egamma and muon streams. In order to resolve this event overlap (or double counting), the highest p_{T} trigger-matched leading lepton is used to classify the event.

The purpose of the trigger-matching requirement is to facilitate the channel assignment and, in the case of Monte Carlo simulated data, to identify the leading lepton whose parameters determine the trigger efficiency scale factor to be applied (c.f. Secs. 4.3.1 and 4.3.2). After the event classification, there is no particular advantage in identifying the trigger-matched object. Accordingly, the trigger-matching is henceforth decoupled from the leading lepton selection. A direct consequence of this decoupling is the presence of a fraction of events ($< 1\%$) with a counter-intuitive channel assignment (e.g. an electron channel event with a non-trigger-matched muon as the leading lepton).

4.4.7 Event Variables

The last step in the cut flow is the construction of event variables with discriminating power between signal and Standard Model processes: high multiplicity of high p_{T} objects and the scalar sum of the transverse momenta of all selected objects, $\sum p_{\mathrm{T}}$ (c.f. Fig. 1.15). Another useful quantity with discriminating power similar to the $\sum p_{\mathrm{T}}$ is the effective event invariant mass

$$M_{inv} = \sqrt{\left(\sum_{i=objects} p_i + p^{\mathrm{miss}}\right)^2}$$

where p_i is the four-momentum of all selected objects and the missing transverse energy "four-momentum" is defined as $p^{\mathrm{miss}} = (E_{\mathrm{T}}^{\mathrm{miss}}, E_{\mathrm{x}}^{\mathrm{miss}}, E_{\mathrm{y}}^{\mathrm{miss}}, 0)$. However, M_{inv}

Table 4.2. Event selection cut flow in data for the egamma and muon streams. From the row labeled "Channel Selection" onwards, the number of events in each column is mutually exclusive and correspond to the electron and muon channels. The total integrated luminosity is 13.0 fb^{-1}.

Requirement	Data Stream	
	Egamma	Muon
All Events	396 636 992	366 769 184
GRL	371 719 680	339 327 808
Trigger	195 117 008	147 622 976
Vertex	193 069 152	145 284 256
LAr Error	192 109 824	144 573 536
Jet Cleaning	191 985 120	144 459 808
Number of Leptons > 0	7 280 337	2 410 523
Lead Lepton/Channel Selection	4 983 741	2 318 273
Number of Objects (p_{T}>100 GeV) ≥ 3	54 936	24 265
$\sum p_{\mathrm{T}} > 700$ GeV	11 450	5 072

introduces a greater model dependence via the inclusion of $E_{\mathrm{T}}^{\mathrm{miss}}$. For this reason, $\sum p_{\mathrm{T}}$ is preferred.

Events are required to have at least three objects passing the 100 GeV p_{T} threshold, where one of said objects is an electron or a muon. All final state reconstructed objects (electrons, muons and jets) having $p_{\mathrm{T}} > 60$ GeV and passing the selection requirements are considered for the $\sum p_{\mathrm{T}}$ calculation[12]. Events with $\sum p_{\mathrm{T}} \leq 700$ GeV are rejected. The cut flow numbers for the described selection criteria in data are shown in Table 4.2.

This constitutes the baseline event selection for all studies described hereinafter.

4.4.8 Signal and Sideband Regions

Signal processes are characterized, not by a resonance structure at high M_{inv}, but by a (model-dependent) threshold "turn-on" M_{TH} of order 1 TeV, followed by an

[12]The same objects are also used for the M_{inv} calculation, with the inclusion of $E_{\mathrm{T}}^{\mathrm{miss}}$. No minimum threshold is imposed on the latter.

approximately exponential or power-law decay. This feature translates to an excess of events from the Standard Model predictions at energies $\gtrsim M_{\mathrm{TH}}$. Containing a high number of decay products with large transverse momenta, the black hole signal manifests itself at high-$\sum p_{\mathrm{T}}$. In view of previous results for TeV-scale gravity searches (c.f. Sec. 1.6) a signal region (SR) is defined by $\sum p_{\mathrm{T}} > 1500$ GeV. Thus, events are considered signal candidates if they satisfy the baseline event selection (as described in Sec. 4.4) and have $\sum p_{\mathrm{T}} > 1500$ GeV.

The stringent high-$\sum p_{\mathrm{T}}$ requirement strongly suppresses Standard Model contributions to the SR. Consequently, the number of Monte Carlo simulated background statistics in this $\sum p_{\mathrm{T}}$ range is quite limited. Furthermore, the predictions of the MC simulations in this region of phase space may differ from what is observed in the data. To study SM backgrounds and possible data-simulation discrepancies, without suffering from highly-limited statistics, a sideband region is defined. The sideband is kinematically similar to the signal region (i.e. it uses the same baseline event selection) but at a lower $\sum p_{\mathrm{T}}$ range with negligible signal contamination, namely, 700 GeV $<$ sideband $<$ 1200 GeV.

The $\sum p_{\mathrm{T}}$ range between 1200 GeV and 1500 GeV is referred to as the validation region (VR), and is used as a test ground for the corrections obtained in the sideband region, in a $\sum p_{\mathrm{T}}$ range with minimal signal contamination. The different regions defined for signal and background studies are summarized in Table 4.3.

Table 4.3. The $\sum p_{\mathrm{T}}$ ranges for background and signal studies. All the regions comprise the same event selection, and only differ by their $\sum p_{\mathrm{T}}$ bounds.

Region	$\sum p_{\mathrm{T}}$ Range [GeV]
Sideband	$700 < \sum p_{\mathrm{T}} < 1200$
Validation	$1200 \leq \sum p_{\mathrm{T}} \leq 1500$
Signal	$\sum p_{\mathrm{T}} > 1500$

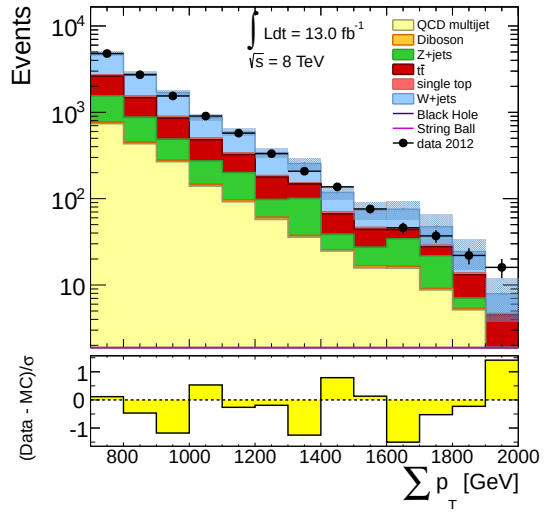

(a) Electron Channel

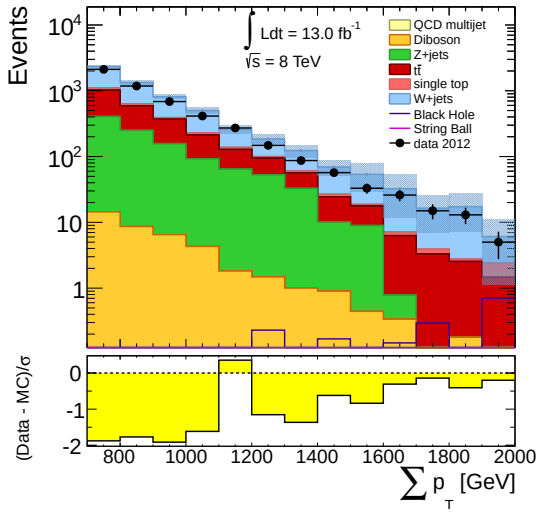

(b) Muon Channel

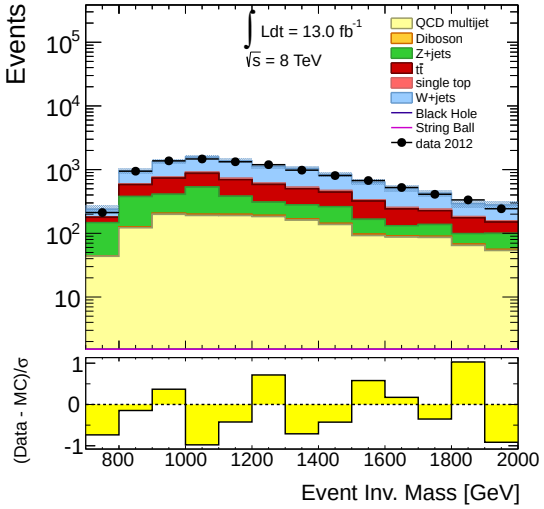

(c) Electron Channel

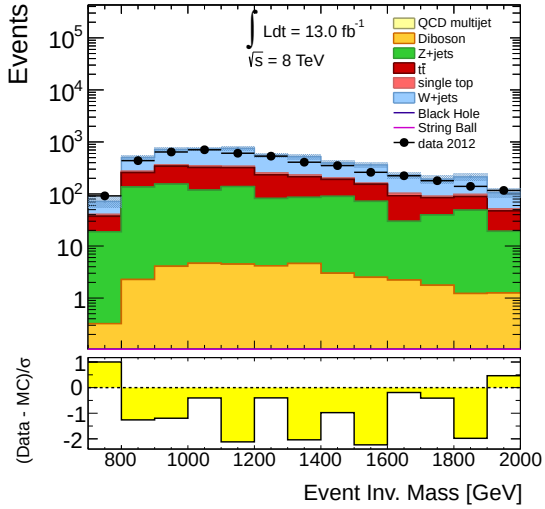

(d) Muon Channel

Figure 4.3. $\sum p_{\mathrm{T}}$ and M_{inv} distributions in the sideband, validation region and a portion of the signal region, for the electron and muon channels. The Monte Carlo simulation is normalized to an integrated luminosity of 13.0 fb^{-1}, but no other corrections (scale factors) have been applied. Only the statistical error is shown.

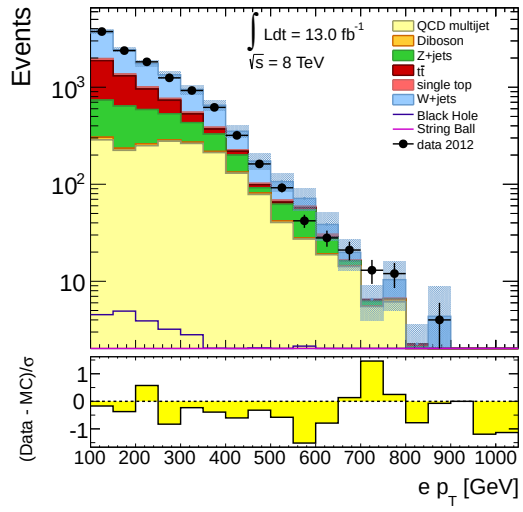

(a) Electron Channel

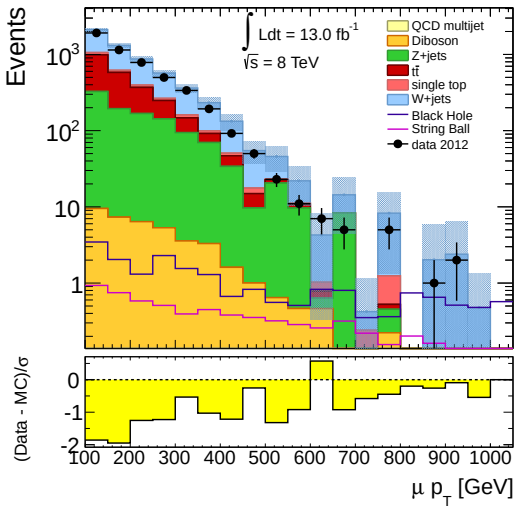

(b) Muon Channel

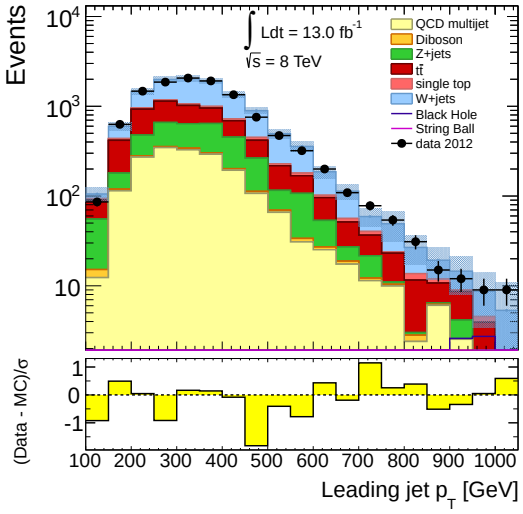

(c) Electron Channel

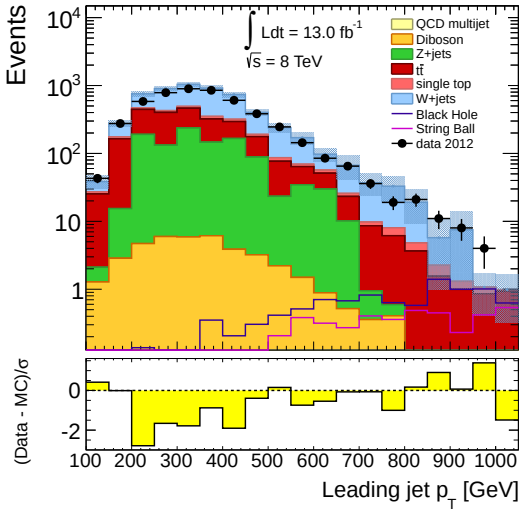

(d) Muon Channel

Figure 4.4. Lepton and jet p_{T} distributions in the sideband, validation region and a portion of the signal region, for the electron and muon channels. The Monte Carlo simulation is normalized to an integrated luminosity of 13.0 fb^{-1}, but no other corrections (scale factors) have been applied. Only the statistical error is shown.

Figures 4.3 and 4.4 show the $\sum p_{\mathrm{T}}$, event invariant mass and lepton p_{T} for both data and MC simulation, in a $\sum p_{\mathrm{T}}$ range including the sideband, the validation region and a portion of the signal region. The bottom pane of each subfigure displays the difference between data and simulation over their statistical error. The number of events predicted by the simulation in an area with negligible signal contamination, i.e. the sideband, is greater than what is observed in the data. The next section discusses the studies performed to improve the data-simulation agreement in the sideband region, such that reliable predictions can be made of the background component in the signal region.

4.5 Background Estimation

The dominant Standard Model sources of background in the signal region are: W+jets, Z/γ^*+jets and $t\bar{t}$ events, and for the electron channel, QCD multijet production. In W+jets, Z/γ^*+jets and $t\bar{t}$ processes, events are produced with real prompt leptons and associated additional jets. In multijet events, reconstructed high p_{T} leptons are present either due to the production of a real lepton within a jet, via semileptonic quark decays (dominantly heavy flavor decays), or due to a jet being misreconstructed from calorimeter clusters as a high p_{T} electron. Isolation requirements, as well as the 100 GeV threshold in lepton p_{T}, reduce this background to very small levels in the muon channel. Additional background processes such as single top and diboson are considered, but their contribution is small.

The backgrounds are estimated using a combination of data-driven and Monte Carlo based techniques. Said background estimates make use of control regions (CR) which comprise specific selection criteria to enhance a particular background. The starting point for the MC-based CRs, used for W+jets, Z/γ^*+jets and $t\bar{t}$, is the sideband region[13]. For the QCD multijet contribution, estimated via a data-driven

technique, the starting point is similar to the sideband, but with a looser lepton selection.

Although the lepton definition may vary, all control regions comprise the following cuts:

- Number of objects (lepton + jets) with $p_{\mathrm{T}} > 100$ GeV ≥ 3.
- At least one lepton with $p_{\mathrm{T}} > 100$ GeV.
- 700 GeV $< \sum p_{\mathrm{T}} < 1200$ GeV.

4.5.1 MC-based Control Regions - Prompt Leptons

For prompt lepton backgrounds, Monte Carlo simulated samples are used to describe the shapes of relevant distributions (i.e. $\sum p_{\mathrm{T}}$), with possible deviations considered separately as sources of systematic uncertainty (c.f. Sec. 4.6). The background normalization is accomplished by comparing in data and MC simulation the observed number of events in the control regions and defining scale factors (SF). These scale factors are then used to rescale the prediction from the MC simulation (e.g. in the signal region). The single top and diboson represent a very small background to this analysis and their normalizations are taken directly from the MC simulation.

The scale factor for a background X is given by

$$\mathrm{SF}_X = \frac{N_{\mathrm{data}} - N_{\mathrm{MC}}^{non-X}}{N_{\mathrm{MC}}^{X}}$$

where N_{data} (N_{MC}^{X}) is the number of data (X MC simulated) events in the X background CR, and N_{MC}^{non-X} corresponds to the estimated number of MC simulated events for backgrounds other than X.

[13] In other words, each control region consists of a subset of the events in the sideband.

4.5.1.1 Z+jets Background

The Z+jets scale factor SF_Z is calculated by simply counting events in both data and Monte Carlo simulation in a control region enriched in Z+jets events. The CR comprises, in addition to the sideband selection, the following requirements:

- exactly two oppositely-charged electrons (in the electron channel) or muons (in the muon channel); and
- 80 GeV $\leq M_{\ell\ell} \leq$ 100 GeV

where $M_{\ell\ell}$ is the dilepton invariant mass.

4.5.1.2 $t\bar{t}$ Background

The $t\bar{t}$ scale factor $\mathrm{SF}_{t\bar{t}}$ is calculated by counting events in both data and Monte Carlo simulation in a control region enriched in $t\bar{t}$ events. To reduce W+jets contamination in this CR, b-tagging identification is imposed (c.f. Sec. 4.3.3). The $t\bar{t}$ control region comprises, in addition to the sideband selection, the following requirements:

- exactly one electron or muon in the event;
- number of b-tagged jets > 1;
- 30 GeV $< E_{\mathrm{T}}^{\mathrm{miss}} <$ 300 GeV; and
- 40 GeV $< M_{\mathrm{T}} <$ 100 GeV

where M_{T} is the "transverse (W) mass" defined as $M_{\mathrm{T}} = \sqrt{2p_{\mathrm{T}}E_{\mathrm{T}}^{\mathrm{miss}}(1 - cos\,\varphi_{l\nu})}$, where $\varphi_{l\nu}$ is the angle between the transverse momentum of the lepton and the $E_{\mathrm{T}}^{\mathrm{miss}}$.

4.5.1.3 W+jets Background

The W+jets control region, from which the W+jets scale factor SF_W is calculated, is kinematically similar to the $t\bar{t}$ CR, except for the b-tagging requirement. While this provides a control region with significant $t\bar{t}$ contamination, the latter can be

properly estimated given the sufficiently high purity of the $t\bar{t}$ CR. To reiterate, the W+jets control region comprises, in addition to the sideband selection, the following requirements:

- exactly one electron or muon in the event;
- 30 GeV $< E_{\mathrm{T}}^{\mathrm{miss}} <$ 300 GeV; and
- 40 GeV $< M_{\mathrm{T}} <$ 100 GeV.

4.5.2 Data-Driven Control Regions - QCD Multijets

A data-driven method is required to estimate the background from QCD multijet processes, where one jet "fakes" an isolated lepton (jet misidentified as an electron or lepton from heavy flavor decay). This analysis uses the matrix method, as described in Ref. [77], to estimate the size of this background.

The central assumption is that events in the signal region can be cleanly separated into two categories: those with real, prompt leptons (non-QCD multijet backgrounds as well as possible signal), and those with fake leptons (QCD multijet events). By comparing the observed number of events in the SR for both the nominal, tight lepton selection criteria and for a looser criteria, wherein the fake lepton contribution is expected to be much larger, the size of the QCD multijet background can be determined. The events passing the tighter lepton requirement are then a subset of the events passing the looser cuts. Thus, relative efficiencies can be defined for leptons to pass the nominal selection criteria given that they have passed the looser one. These conditions can be summarized as follows

$$N_{\mathrm{loose}} = N_{\mathrm{loose}}^{\mathrm{real}} + N_{\mathrm{loose}}^{\mathrm{fake}}$$

$$N_{\mathrm{tight}} = N_{\mathrm{tight}}^{\mathrm{real}} + N_{\mathrm{tight}}^{\mathrm{fake}} = \epsilon_{\mathrm{real}} N_{\mathrm{loose}}^{\mathrm{real}} + \epsilon_{\mathrm{fake}} N_{\mathrm{loose}}^{\mathrm{fake}}$$

where N_{tight} (N_{loose}) is the number of SR events observed after applying the tighter (looser) selection criteria, and ϵ_{real} and ϵ_{fake} are the relative efficiencies for real and fake leptons, respectively.

To determine the number of QCD multijet events passing the nominal selection (i.e. $N_{\text{tight}}^{\text{fake}}$), it is necessary to first estimate the relative efficiencies ϵ_{real} and ϵ_{fake}. They are taken to be the ratios of number of events that pass the nominal (tight) lepton selection to the number that pass the looser selection:

$$\epsilon_{\text{real}} = \frac{N_{\text{tight}}^{\text{real}}}{N_{\text{loose}}^{\text{real}}} \quad \text{and} \quad \epsilon_{\text{fake}} = \frac{N_{\text{tight}}^{\text{fake}}}{N_{\text{loose}}^{\text{fake}}}.$$

In the electron channel, the looser selection is obtained by relaxing the electron identification criteria from tight++ to medium++. For the muon channel, this looser selection removes both the lepton isolation and the jet-muon overlap requirements.

The ϵ_{fake} and ϵ_{real} efficiencies are determined from events in control regions enhanced by sources of fake and real leptons: a QCD multijet CR and a Z+jets CR, respectively (c.f. Secs. 4.5.2.1 and 4.5.2.2). Because these efficiencies rely on a comparison between loose and tight lepton requirements, the starting point for the control regions cannot be the sideband selection explicitly, but a looser version of it. This is accomplished by following the baseline event selection or cut flow, as described in Sec. 4.4, but with the relaxed lepton definitions.

After measuring the real and fake lepton efficiencies, the QCD multijet contribution can be estimated by simultaneously solving the equations for N_{loose} and N_{tight}, which results in

$$N_{\text{tight}}^{\text{fake}} = \frac{\epsilon_{\text{fake}}}{\epsilon_{\text{real}} - \epsilon_{\text{fake}}} \left(\epsilon_{\text{real}} N_{\text{loose}} - N_{\text{tight}}\right).$$

4.5.2.1 Fake Lepton Control Region

The fake-dominated control region for the ϵ_{fake} estimation comprises, in addition to the looser sideband selection, the following requirements:

- exactly one electron or muon in the event (using the relaxed lepton criteria);
- $M_{\text{T}} < 40$ GeV; and
- $M_{\text{T}} + E_{\text{T}}^{\text{miss}} < 60$ GeV.

Fake leptons from QCD multijet events tend to have low $E_{\text{T}}^{\text{miss}}$ and low transverse W mass. The triangular cut using M_{T} and $E_{\text{T}}^{\text{miss}}$, as described in Ref. [78], effectively separates these QCD events from other Standard Model processes. The observed number of loose (tight) data events in this CR consists of loose (tight) QCD events and loose (tight) real prompt lepton events. The contribution from the prompt lepton component is subtracted, taking the MC simulation prediction, normalized according to Sec. 4.5.1.

4.5.2.2 Real (Prompt) Lepton Control Region

The real lepton dominated control region for the ϵ_{real} estimation is similar to the Z+jets control region and comprises, in addition to the looser sideband selection, the following requirements:

- exactly two oppositely-charged electrons (in the electron channel) or muons (in the muon channel); and
- 80 GeV $\leq M_{\ell\ell} \leq$ 100 GeV.

The contribution of fake leptons to this CR is negligible. The contribution from non-Z backgrounds is estimated from MC simulation and subtracted.

4.5.3 Iteration Method

In the Z+jets control regions, both the MC based and the data-driven, the contribution from other backgrounds is negligible and does not alter the scale factor or efficiency calculations. The other control regions, however, do not feature this high level of purity. An accurate computation of one scale factor requires simultaneous knowledge of the other backgrounds. For example, to measure the $\mathrm{SF}_{t\bar{t}}$, the W+jets and QCD multijet contamination in the $t\bar{t}$ control region must be understood; at the same time, there is $t\bar{t}$ and QCD contamination in the W+jets CR, while the ϵ_{fake} measurement requires the subtraction of normalized $t\bar{t}$ and W+jets events.

To account for this interdependence, an iterative process is employed where the results from a previous iteration are then used to calculate the next one, until each scale factor and efficiency converges[14].

The iteration method comprises the following steps:

- step 1: The Z+jets SF and the ϵ_{real} are calculated.
- step 2: The ϵ_{fake} is measured using the normalized Z+jets contribution (based on the SF from step 1), and assuming the $t\bar{t}$ and W+jets prediction from MC simulation as correct.
- step 3: The $t\bar{t}$ SF is computed, using the normalized Z+jets contribution, estimating the QCD background using the ϵ_{real} and $\epsilon_{\mathrm{fakel}}$ from steps 1 and 2, and assuming the W+jets prediction from MC simulation as correct.
- step 4: The W+jets SF is calculated, relying on the scale factors and efficiencies from steps 1-3. At this point, updated values are obtained for the $t\bar{t}$ and W+jets SFs, and the ϵ_{fake}.

[14]In this context, "convergence" is reached when the magnitude of the difference between the previous value and the current value is smaller than 10^{-4}.

- step 5: Steps 2-4 are repeated with the updated scale factors and efficiencies until their values converge.

The average number of iterations needed for convergence is between 4 and 5.

4.6 Systematic Uncertainties

This section outlines the sources of systematic uncertainty considered in the analysis. These systematic uncertainties are evaluated using standard ATLAS procedures and tools, when applicable. The most significant uncertainties are associated with jet energy scale and resolution, b-tagging, and the extrapolation from control regions to the signal region.

The systematics are applied in the analysis and propagated to the final distributions, including fake estimation and scale factor dependence. They are then compared, background by background, with the nominal case (i.e. no systematics applied) and the difference is taken as a 1σ deviation. The individual systematics are then added in quadrature, along with the statistical uncertainties.

The use of control regions with similar kinematic properties to those in the signal region strongly suppresses the majority of these uncertainties.

- Luminosity: The preliminary uncertainty on the luminosity estimate is 3.6%, using the techniques described in Ref. [76].

- Statistical uncertainty: This is the uncertainty due to the limited Monte Carlo statistics.

- Scale factor uncertainty: The uncertainty in the derived scale factors for the individual Monte Carlo simulated backgrounds. It is computed from the statistical uncertainties on data and simulation.

- QCD estimation: The uncertainty on the fake and true efficiencies from the matrix method.

- Theoretical uncertainties: These include uncertainties which arise from choice of generator. They are estimated from the difference between the Sherpa and Alpgen predictions for W/Z+jets events.

- PDF: The uncertainty on the PDF set used, evaluated according to its PDF error (`CT10` or `CTEQ6L1` in the case of all major backgrounds to this search). There are several uncertainties associated with the different parameters of the PDF, and they are added in quadrature.

- JES: The jet energy scale uncertainty is derived from MC-based studies and in-situ measurements, and provided by ATLAS central tools. The uncertainty, given as a function of p_{T} and η, is evaluated by varying the energy scale (at LCW calibration) of each jet up or down by 1σ. This change is propagated to the $E_{\mathrm{T}}^{\mathrm{miss}}$ calculation. The tools also provide the additional uncertainty to the JES due to pileup events and jet flavor.

- JER: The jet energy resolution, evaluated by smearing the jet energy in MC simulations, affects the predicted background event counts, as its variation can cause migrations from bin-to-bin, and into or out of control and signal regions.

- b-tagging: Tagging of b-quark jets is used to differentiate the $t\bar{t}$ and W control regions. An efficiency correction is applied to heavy flavor jets, in addition to a mis-tagging correction for jets of light flavor. These corrections are subject to systematic uncertainties arising from the methods used to measure the efficiency and mis-tag rates in data and simulation, and are provided by dedicated ATLAS tools.

- Muon smearing: The uncertainties arising from varying the muon MS and ID tracks $\mathrm{q}/p_{\mathrm{T}}$ separately.

- Electron energy scale and resolution: The effect of the electron energy scale uncertainty is evaluated by varying the energy scale of each electron up or down by 1σ. These uncertainties take into account the Z peak used for calibration, material corrections and energy smearing corrections.

- Lepton identification, reconstruction and trigger: These are the uncertainties on the scale factors applies to all leptons. They are small, sub-dominant, and affect control and signal regions concordantly, leaving negligible uncertainties on the final expectations.

CHAPTER 5

RESULTS AND INTERPRETATION

5.1 Background Normalization in the Sideband Region

5.1.1 Z+jets Scale Factor

The Z+jets scale factor, as defined in Sec. 4.5.1, is given by the quotient of Z+jets data events over simulated data events. The number of Z+jets events in data is taken as the total number of data events in this control region, minus the MC simulation prediction for non-Z backgrounds. It is assumed that these non-Z backgrounds are small and no scaling or correction to the MC simulation prediction is necessary. Supporting this position is the fact that the purity[1] of the Z+jets CR is 98.7% in both the electron and the muon channels.

Figures 5.1-5.4 illustrate a plurality of distributions, such as dilepton invariant mass, $\sum p_{\mathrm{T}}$, and objects kinematics, in the Z+jets control region. The error bars for each subfigure include statistical as well as systematic uncertainties. The obtained values for the Z+jets scale factors, whether in the nominal condition or systematic variations thereof, are summarized in tables 5.1 and 5.2. The resulting scale factors for the different channels are

$$\mathrm{SF(electron)} = 0.902 \pm 0.099^{+0.061}_{-0.067}$$

$$\mathrm{SF(muon)} = 0.980 \pm 0.164^{+0.021}_{-0.055}.$$

[1]The purity is calculated from Monte Carlo simulation as $N^{Z}_{\mathrm{MC}}/N^{\mathrm{all}}_{\mathrm{MC}}$, and from data as $N^{Z}_{\mathrm{data}}/N^{\mathrm{all}}_{\mathrm{data}} = (N^{\mathrm{all}}_{\mathrm{data}} - N^{\mathrm{non-Z}}_{\mathrm{MC}})/N^{\mathrm{all}}_{\mathrm{data}}$.

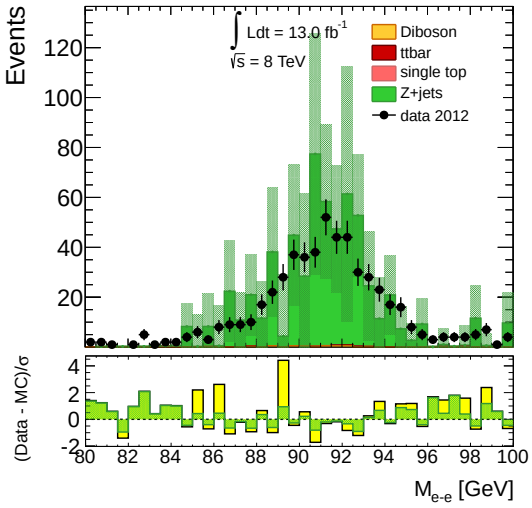

(a) Electron Channel

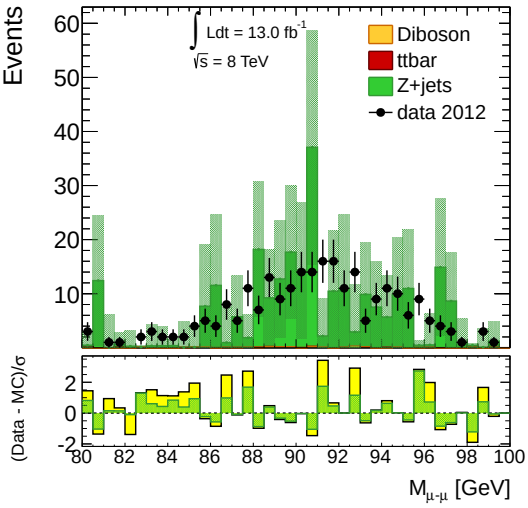

(b) Muon Channel

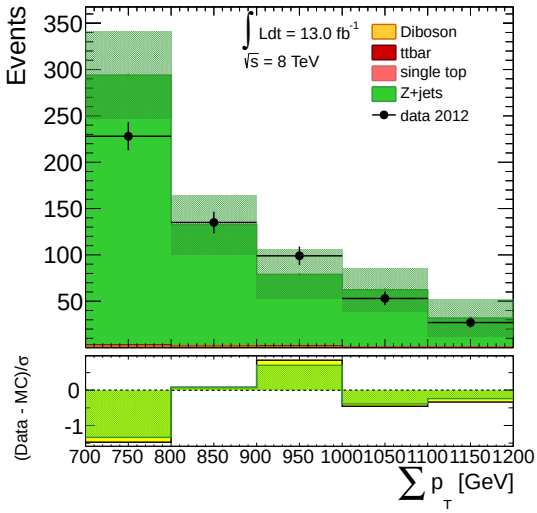

(c) Electron Channel

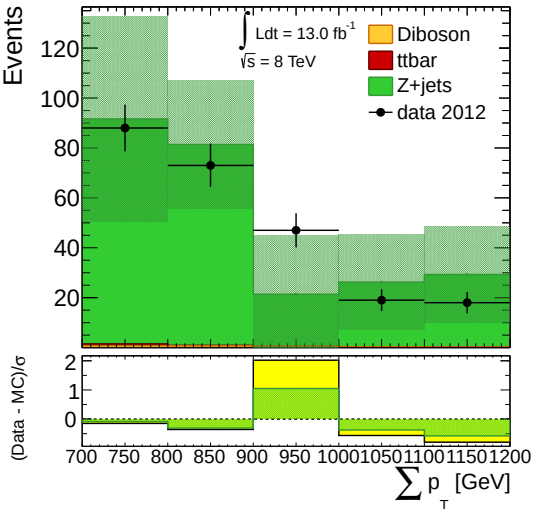

(d) Muon Channel

Figure 5.1. Dilepton invariant mass and $\sum p_{\mathrm{T}}$ distributions in the Z+jets CR, before the application of the scale factor. The Monte Carlo simulation is normalized to an integrated luminosity of 13.0 fb^{-1}. The error bars include both statistical and systematic uncertainties. The bottom pane of each subfigure displays the difference between data and simulation over their statistical uncertainty (yellow band) or statistical+systematic uncertainties (green band). Appendix B.1 shows the corresponding distributions after the application of the obtained scale factor while App. B.2 shows them for the alternate `Alpgen` generator.

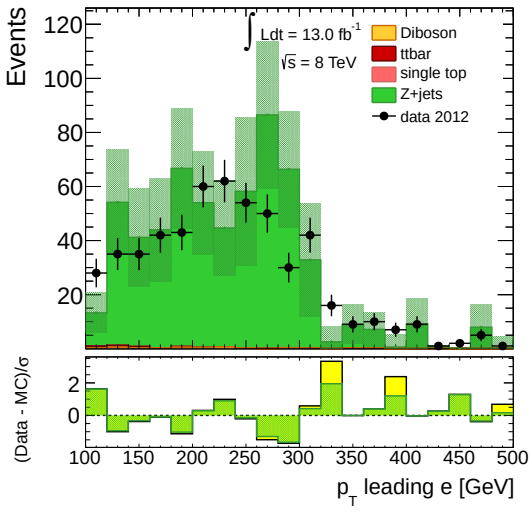

(a) Electron Channel

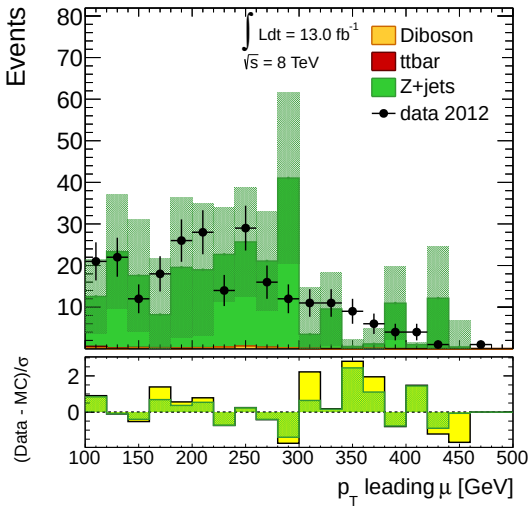

(b) Muon Channel

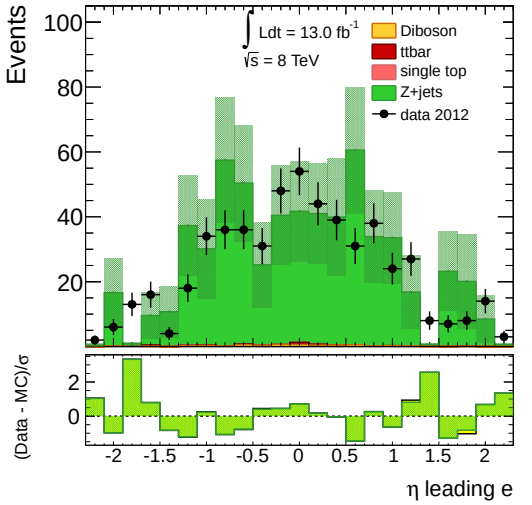

(c) Electron Channel

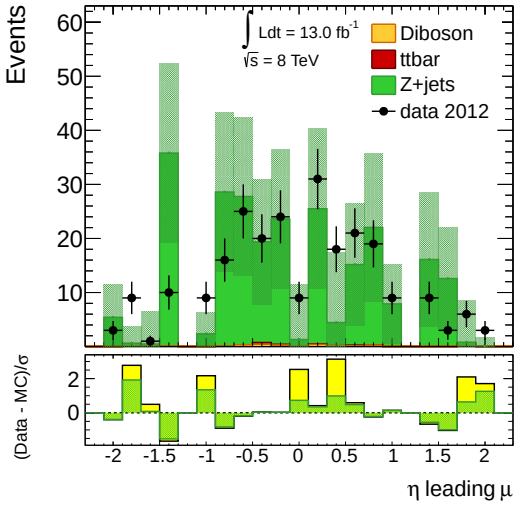

(d) Muon Channel

Figure 5.2. Leading lepton p_{T} and η distributions in the Z+jets CR, before the application of the scale factor. The Monte Carlo simulation is normalized to an integrated luminosity of 13.0 fb^{-1}. The error bars include both statistical and systematic uncertainties. The bottom pane of each subfigure displays the difference between data and simulation over their statistical uncertainty (yellow band) or statistical+systematic uncertainties (green band).

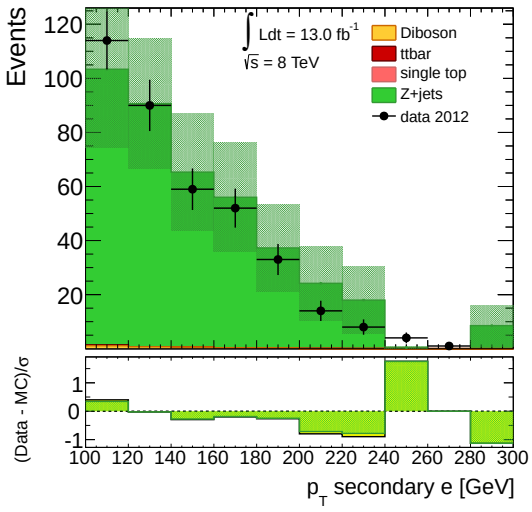

(a) Electron Channel

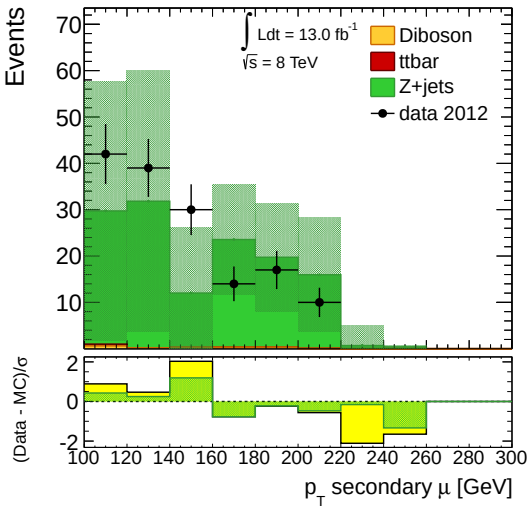

(b) Muon Channel

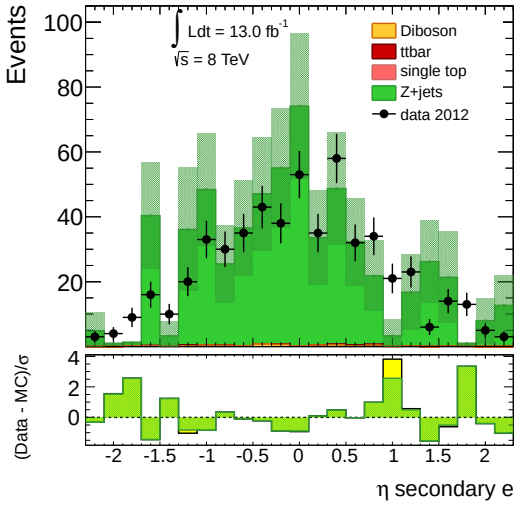

(c) Electron Channel

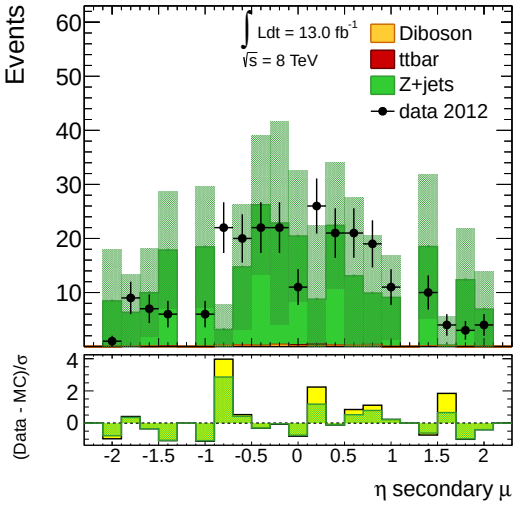

(d) Muon Channel

Figure 5.3. Secondary lepton p_{T} and η distributions in the Z+jets CR, before the application of the scale factor. The Monte Carlo simulation is normalized to an integrated luminosity of 13.0 fb^{-1}. The error bars include both statistical and systematic uncertainties. The bottom pane of each subfigure displays the difference between data and simulation over their statistical uncertainty (yellow band) or statistical+systematic uncertainties (green band).

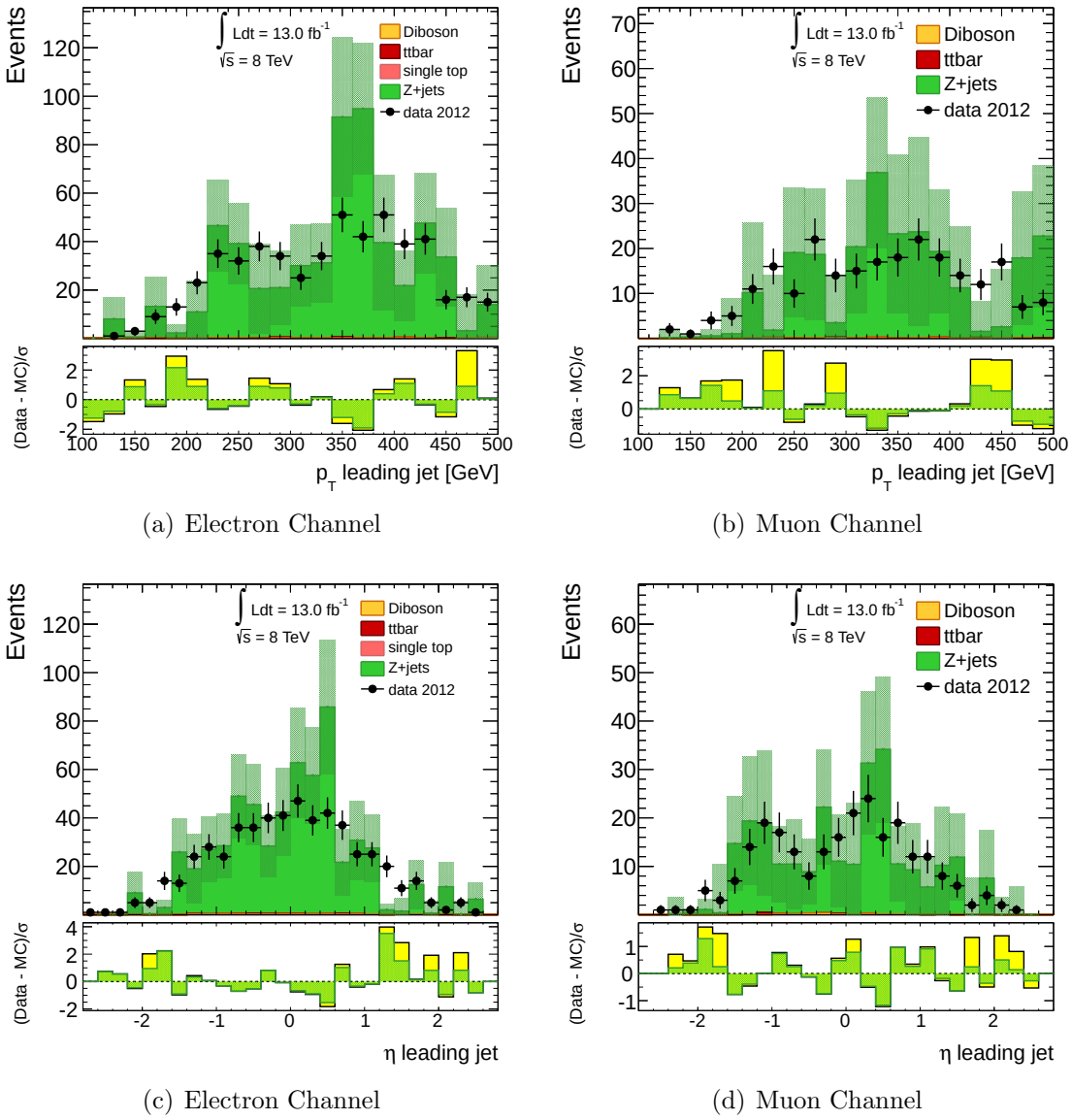

(a) Electron Channel

(b) Muon Channel

(c) Electron Channel

(d) Muon Channel

Figure 5.4. Leading jet p_{T} and η distributions in the Z+jets CR, before the application of the scale factor. The Monte Carlo simulation is normalized to an integrated luminosity of 13.0 fb^{-1}. The error bars include both statistical and systematic uncertainties. The bottom pane of each subfigure displays the difference between data and simulation over their statistical uncertainty (yellow band) or statistical+systematic uncertainties (green band).

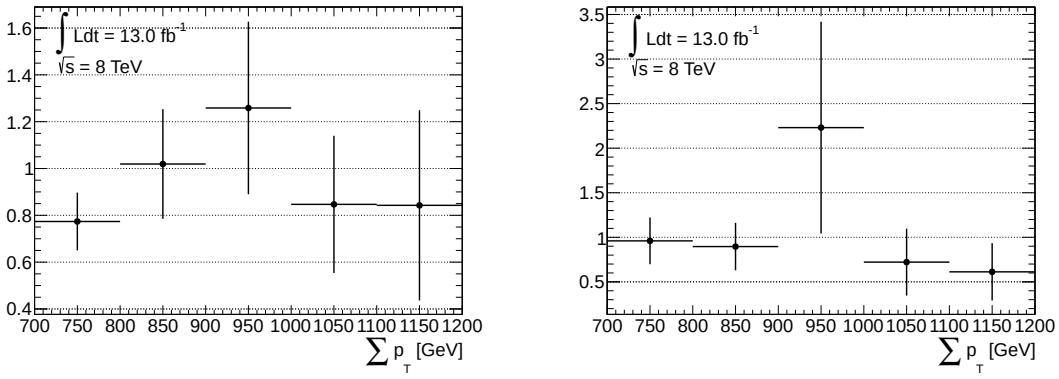

(a) Electron Channel

(b) Muon Channel

Figure 5.5. Z+jets scale factor versus $\sum p_{\mathrm{T}}$. These plots correspond to the ratio of data over MC simulated events in Fig. 5.1.

Figure 5.5 displays the scale factor as a function of $\sum p_{\mathrm{T}}$. When the uncertainties are considered, the SF for the electron channel is substantially constant over the $\sum p_{\mathrm{T}}$ range. For the muon channel, however, there seems to be some dependence on the $\sum p_{\mathrm{T}}$. This behavior seems to be a feature of the MC simulated sample (`Sherpa` generator) and is not observed with the alternate `Alpgen` sample (c.f. App. B.2). The difference in the generator predictions are eventually added as a systematic uncertainty.

Table 5.1. Z+jets scale factors and uncertainties in the electron channel. Systematics variations are propagated through the whole analysis and a new scale factor is derived. The difference from the nominal is taken as the systematic uncertainty. The JES is one of the dominant sources of systematic uncertainties.

Systematics	Scale Factor	Deviation from Nominal (%)
Nominal	0.902 ± 0.099	-
JES Up	0.835 ± 0.089	-7.451
JES Down	0.956 ± 0.108	$+5.905$
JER	0.915 ± 0.101	$+1.405$
b-tag Up	0.902 ± 0.099	0
b-tag Down	0.902 ± 0.099	0
EES Up	0.913 ± 0.101	$+1.211$
EES Down	0.921 ± 0.102	$+2.037$
EER Up	0.912 ± 0.101	$+1.108$
EER Down	0.914 ± 0.101	$+1.253$
Final	$0.902 \pm 0.099^{+0.061}_{-0.067}$	

Table 5.2. Z+jets scale factors and uncertainties in the muon channel. Systematics variations are propagated through the whole analysis and a new scale factor is derived. The difference from the nominal is taken as the systematic uncertainty. The JES is one of the dominant sources of systematic uncertainties.

Systematics	Scale Factor	Deviation from Nominal (%)
Nominal	0.980 ± 0.164	-
JES Up	0.932 ± 0.152	-4.915
JES Down	0.999 ± 0.169	$+1.930$
JER	0.989 ± 0.165	$+0.894$
b-tag Up	0.980 ± 0.164	0
b-tag Down	0.980 ± 0.164	0
MS Up	0.980 ± 0.163	0
MS Down	0.980 ± 0.163	0
ID Up	0.979 ± 0.163	-0.083
ID Down	0.954 ± 0.158	-2.704
Final	$0.980 \pm 0.164^{+0.021}_{-0.055}$	

5.1.2 $t\bar{t}$ Scale Factor

The $t\bar{t}$ scale factor, as defined in Sec. 4.5.1, is given by the quotient of $t\bar{t}$ data events over simulated data events. The number of $t\bar{t}$ events in data is taken as the total number of data events in this control region, minus the MC simulation prediction for non-$t\bar{t}$ backgrounds. The contributions from W+jets and QCD multijet backgrounds are estimated following the iteration method described in Sec. 4.5.3. The requirement of b-tagged jets provides a control region dominated by top events. The purity of this CR, considering only $t\bar{t}$ events, is $\sim 84\%$ for both channel; while the purity for top events (i.e. $t\bar{t}$ + single top) is $\sim 92\%$. The remaining $\sim 8\%$ corresponds mainly to W+jets events, followed by Z+jets, QCD multijets and diboson.

Figure 5.6 shows the M_{T} and $E_{\mathrm{T}}^{\mathrm{miss}}$ distributions after requiring only one lepton and more than one b-tagged jet. To reduce the contribution from other Standard Model processes, such as QCD multijets, the additional requirements on $E_{\mathrm{T}}^{\mathrm{miss}}$ (i.e. 30 GeV $< E_{\mathrm{T}}^{\mathrm{miss}} <$ 300 GeV) and M_{T}, discussed in Sec. 4.5.1, are imposed, thus defining the $t\bar{t}$ CR.

Figures 5.7-5.10 illustrate a plurality of distributions, such as $\sum p_{\mathrm{T}}$, number of b-tagged jets, and objects kinematics, in the $t\bar{t}$ control region. The error bars for each subfigure include statistical as well as systematic uncertainties. The obtained values for the $t\bar{t}$ scale factors, whether in the nominal condition or systematic variations thereof, are summarized in tables 5.3 and 5.4. The resulting scale factors for the different channels are

$$\mathrm{SF(electron)} = 1.020 \pm 0.086^{+0.292}_{-0.264}$$

$$\mathrm{SF(muon)} = 1.118 \pm 0.120^{+0.345}_{-0.304}.$$

Figure 5.11 displays the scale factor as a function of $\sum p_{\mathrm{T}}$. When the uncertainties are considered, the SFs for both channels are substantially constant over the

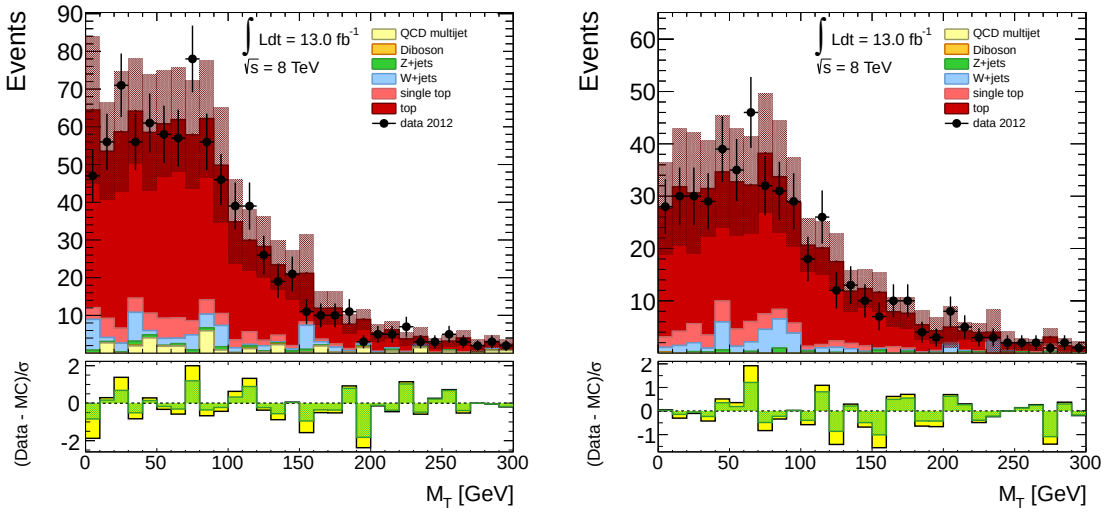

(a) Electron Channel

(b) Muon Channel

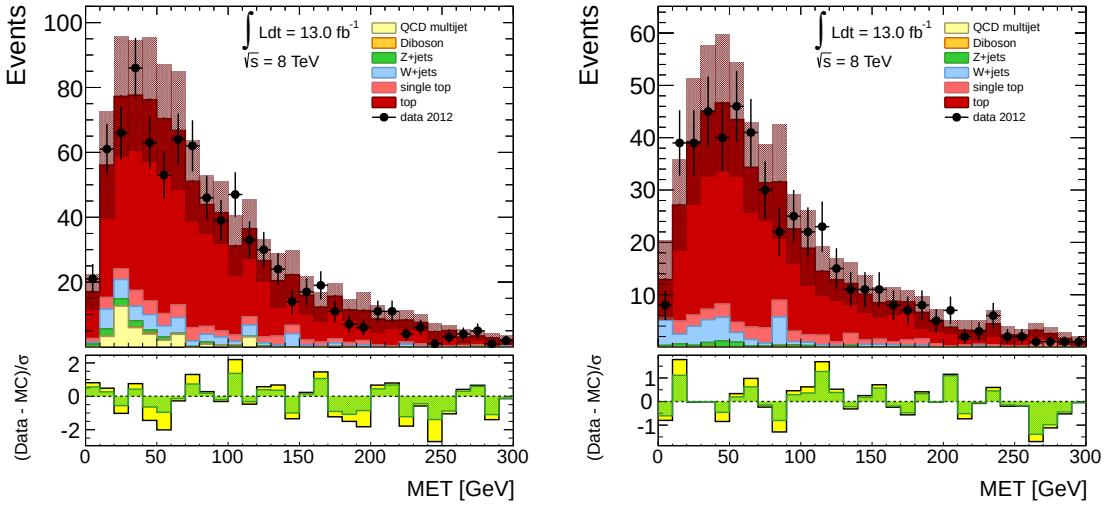

(c) Electron Channel

(d) Muon Channel

Figure 5.6. M_{T} and $E_{\mathrm{T}}^{\mathrm{miss}}$ distributions used to define a $t\bar{t}$ control region. The Monte Carlo simulation is normalized to an integrated luminosity of 13.0 fb^{-1}. The error bars include both statistical and systematic uncertainties. The bottom pane of each subfigure displays the difference between data and simulation over their statistical uncertainty (yellow band) or statistical+systematic uncertainties (green band).

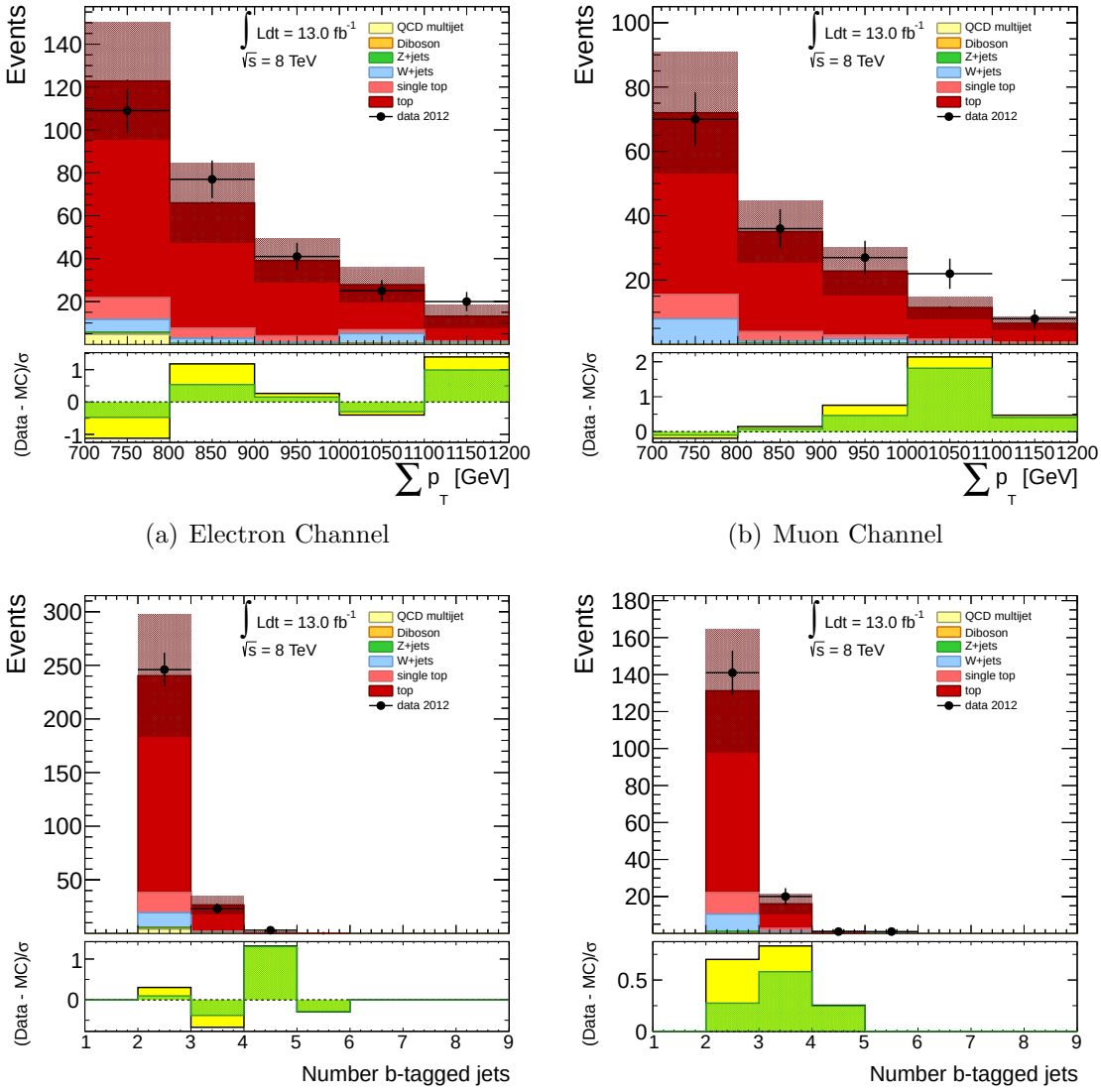

(a) Electron Channel

(b) Muon Channel

(c) Electron Channel

(d) Muon Channel

Figure 5.7. $\sum p_{\mathrm{T}}$ and number of b-tagged jets distributions in the $t\bar{t}$ CR, after scaling all non-$t\bar{t}$ backgrounds. The Monte Carlo simulation is normalized to an integrated luminosity of 13.0 fb^{-1}. The error bars include both statistical and systematic uncertainties. The bottom pane of each subfigure displays the difference between data and simulation over their statistical uncertainty (yellow band) or statistical+systematic uncertainties (green band). Appendix C.1 shows the corresponding distributions before and after the application of the obtained scale factor while App. C.2 shows them when using the alternate `Alpgen` generator for W/Z+jets.

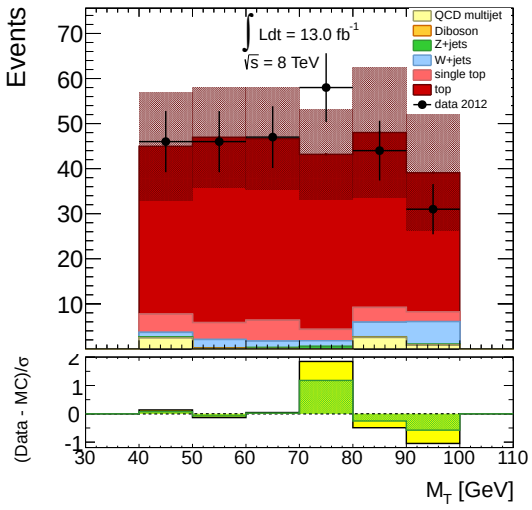

(a) Electron Channel

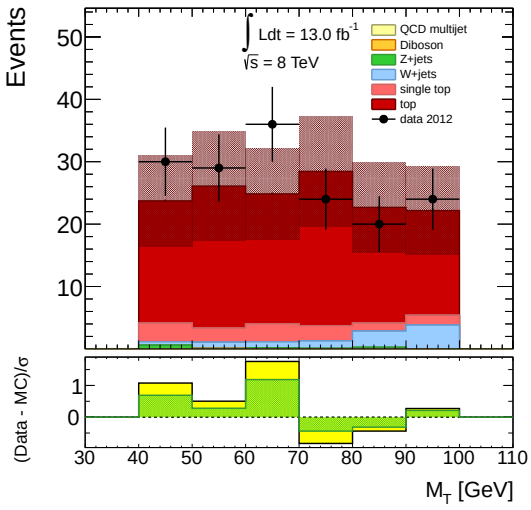

(b) Muon Channel

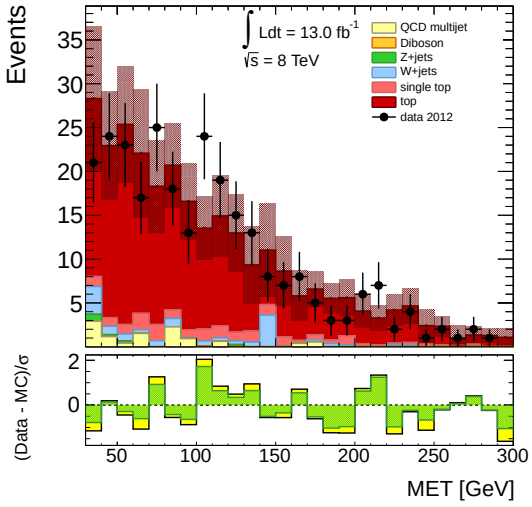

(c) Electron Channel

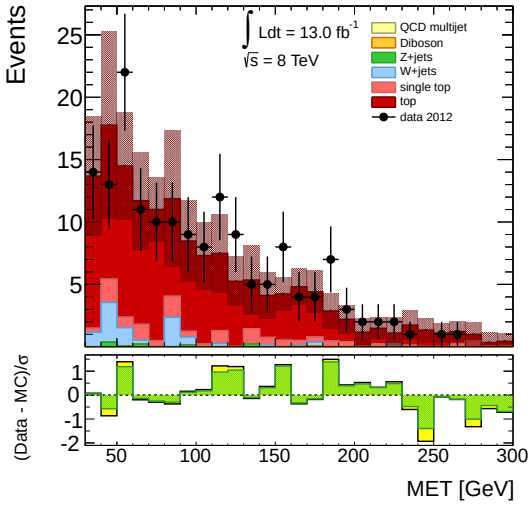

(d) Muon Channel

Figure 5.8. M_{T} and $E_{\mathrm{T}}^{\mathrm{miss}}$ distributions in the $t\bar{t}$ CR, after scaling all non-$t\bar{t}$ backgrounds. The Monte Carlo simulation is normalized to an integrated luminosity of 13.0 fb^{-1}. The error bars include both statistical and systematic uncertainties. The bottom pane of each subfigure displays the difference between data and simulation over their statistical uncertainty (yellow band) or statistical+systematic uncertainties (green band).

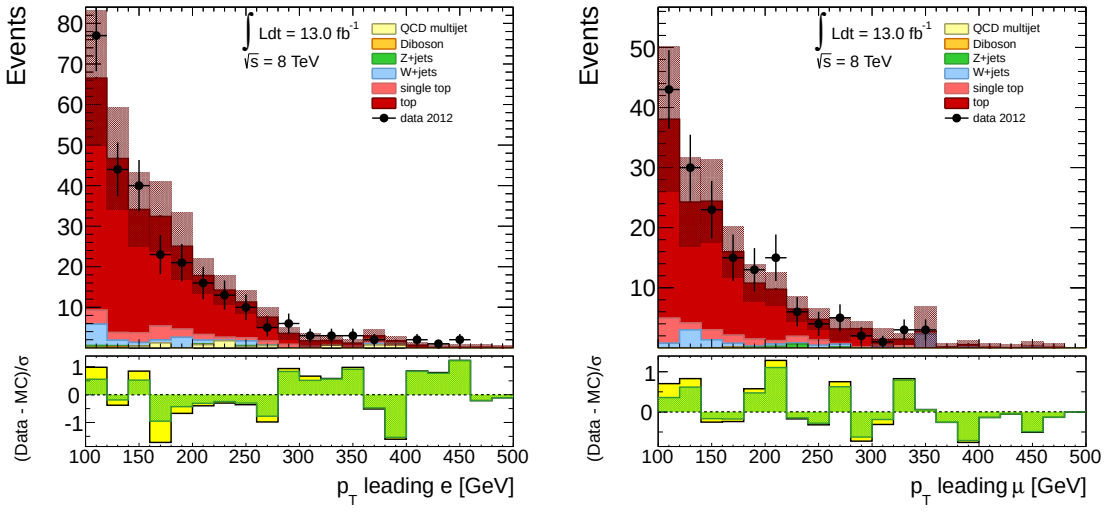

(a) Electron Channel

(b) Muon Channel

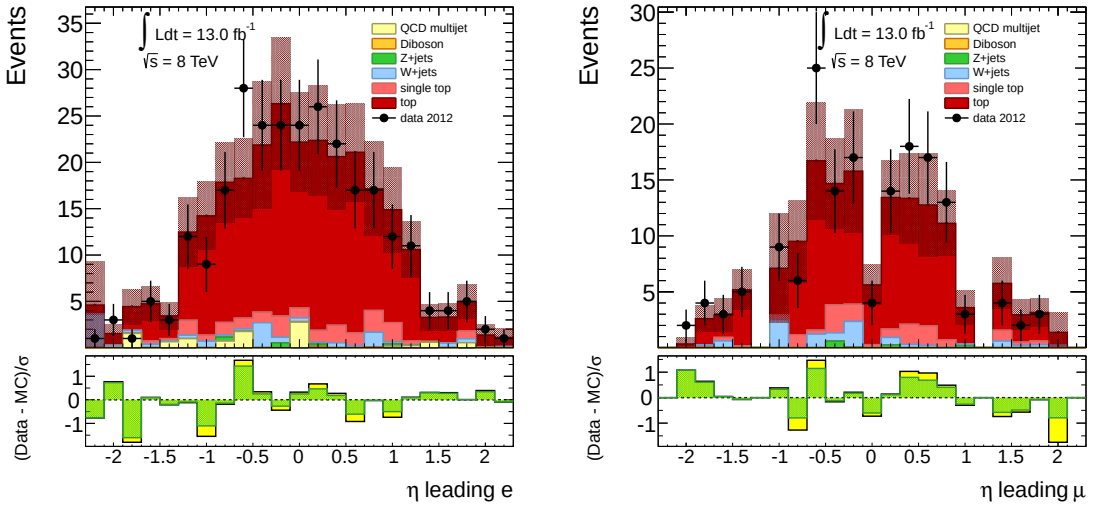

(c) Electron Channel

(d) Muon Channel

Figure 5.9. Leading lepton p_{T} and η distributions in the $t\bar{t}$ CR, after scaling all non-$t\bar{t}$ backgrounds. The Monte Carlo simulation is normalized to an integrated luminosity of 13.0 fb^{-1}. The error bars include both statistical and systematic uncertainties. The bottom pane of each subfigure displays the difference between data and simulation over their statistical uncertainty (yellow band) or statistical+systematic uncertainties (green band).

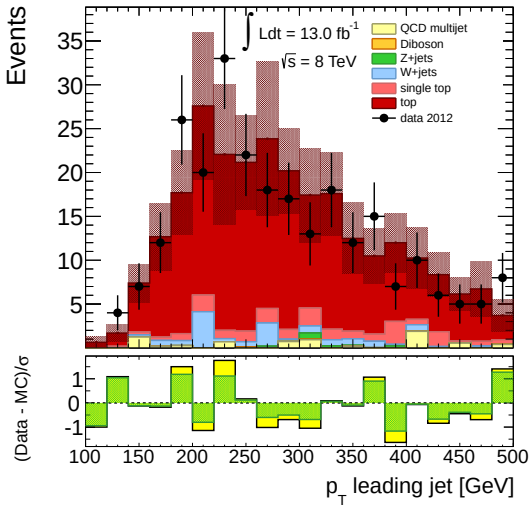

(a) Electron Channel

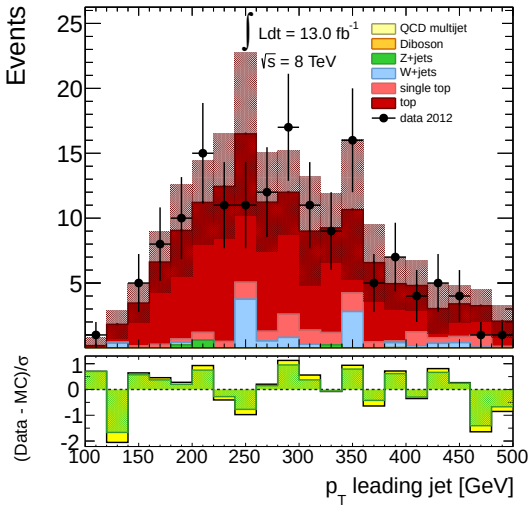

(b) Muon Channel

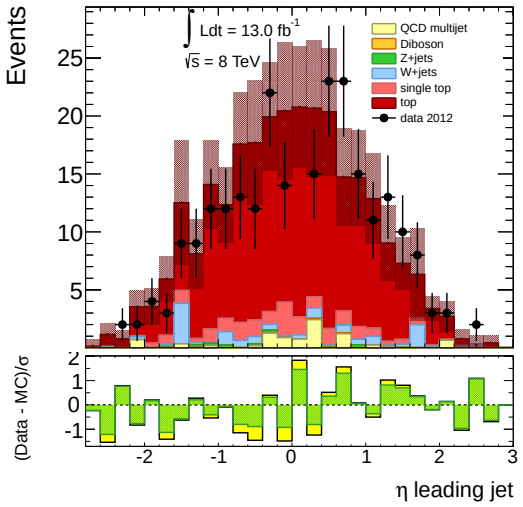

(c) Electron Channel

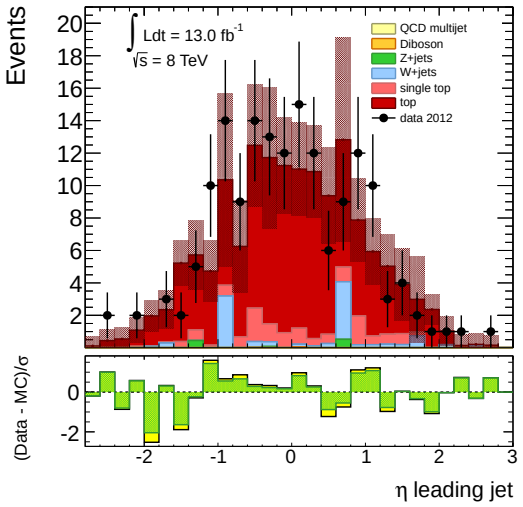

(d) Muon Channel

Figure 5.10. Leading jet p_{T} and η distributions in the $t\bar{t}$ CR, after scaling all non-$t\bar{t}$ backgrounds. The Monte Carlo simulation is normalized to an integrated luminosity of 13.0 fb^{-1}. The error bars include both statistical and systematic uncertainties. The bottom pane of each subfigure displays the difference between data and simulation over their statistical uncertainty (yellow band) or statistical+systematic uncertainties (green band).

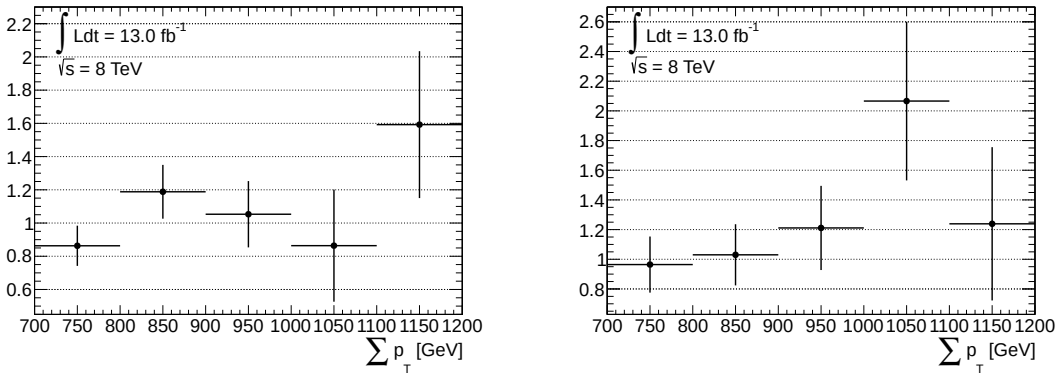

(a) (b)

Figure 5.11. The $t\bar{t}$ scale factor versus $\sum p_{\mathrm{T}}$. These plots correspond to the ratio of data over MC simulated events in Fig. 5.7.

$\sum p_{\mathrm{T}}$ range. Appendix C.2 shows the scale factors obtained when the W/Z+jets backgrounds are generated with `Alpgen`.

Table 5.3. The $t\bar{t}$ scale factors and uncertainties in the electron channel. Systematics variations are propagated through the whole analysis and a new scale factor is derived. The difference from the nominal is taken as the systematic uncertainty. The JES is one of the dominant sources of systematic uncertainties. The scale factor is particularly sensitive to the b-tagging uncertainties.

Systematics	Scale Factor	Deviation from Nominal (%)
Nominal	1.020 ± 0.086	-
JES Up	0.839 ± 0.071	-17.718
JES Down	1.157 ± 0.105	$+13.397$
JER	1.054 ± 0.094	$+\ 3.299$
b-tag Up	0.828 ± 0.073	-18.809
b-tag Down	1.276 ± 0.105	$+25.105$
EES Up	1.016 ± 0.086	$-\ 0.402$
EES Down	1.016 ± 0.086	$-\ 0.424$
EER Up	1.022 ± 0.086	$+\ 0.221$
EER Down	1.016 ± 0.086	$-\ 0.344$
Final	$1.020 \pm 0.086^{+0.292}_{-0.264}$	

Table 5.4. The $t\bar{t}$ scale factors and uncertainties in the muon channel. Systematics variations are propagated through the whole analysis and a new scale factor is derived. The difference from the nominal is taken as the systematic uncertainty. The JES is one of the dominant sources of systematic uncertainties. The scale factor is particularly sensitive to the b-tagging uncertainties.

Systematics	Scale Factor	Deviation from Nominal (%)
Nominal	1.118 ± 0.120	-
JES Up	0.901 ± 0.103	-19.437
JES Down	1.313 ± 0.141	$+17.452$
JER	1.104 ± 0.122	$-\ 1.293$
b-tag Up	0.907 ± 0.103	-18.899
b-tag Down	1.403 ± 0.143	$+25.479$
MS Up	1.114 ± 0.120	$-\ 0.393$
MS Down	1.117 ± 0.120	$-\ 0.082$
ID Up	1.121 ± 0.120	$+\ 0.234$
ID Down	1.113 ± 0.120	$-\ 0.499$
Final	$1.118 \pm 0.120^{+0.345}_{-0.304}$	

5.1.3 W+jets Scale Factor

The W+jets scale factor, as defined in Sec. 4.5.1, is given by the quotient of W+jets data events over simulated data events. The number of W+jets events in data is taken as the total number of data events in this control region, minus the MC simulation prediction for non-W+jets backgrounds. The contributions from $t\bar{t}$ and QCD multijet backgrounds are estimated following the iteration method described in Sec. 4.5.3. There is a significant contribution of top events in this control region, followed by QCD multijets in the electron channel. The purity of this CR is $\sim 55\%$ in the electron channel and $\sim 58\%$ in the muon channel.

Figure 5.12 shows the M_{T} and $E_{\mathrm{T}}^{\mathrm{miss}}$ distributions after requiring that there is only one electron or muon in the event. To reduce the contribution from other Standard Model processes, such as QCD multijets, the additional requirements on $E_{\mathrm{T}}^{\mathrm{miss}}$ (i.e. 30 GeV $< E_{\mathrm{T}}^{\mathrm{miss}} <$ 300 GeV) and M_{T}, discussed in Sec. 4.5.1, are imposed, thus defining the W+jets CR.

Figures 5.13-5.16 illustrate a plurality of distributions, such as $\sum p_{\mathrm{T}}$, number of b-tagged jets, and objects kinematics, in the W+jets control region. The error bars for each subfigure include statistical as well as systematic uncertainties. The obtained values for the W+jets scale factors, whether in the nominal condition or systematic variations thereof, are summarized in tables 5.5 and 5.6. The resulting scale factors for the different channels are

$$\mathrm{SF(electron)} = 0.801 \pm 0.099^{+0.106}_{-0.221}$$

$$\mathrm{SF(muon)} = 0.818 \pm 0.112^{+0.219}_{-0.204}.$$

Figure 5.17 displays the scale factor as a function of $\sum p_{\mathrm{T}}$. When the uncertainties are considered, the SFs for both channels are substantially constant over the $\sum p_{\mathrm{T}}$ range. Appendix D.2 shows the scale factors obtained when the W/Z+jets backgrounds are generated with `Alpgen`.

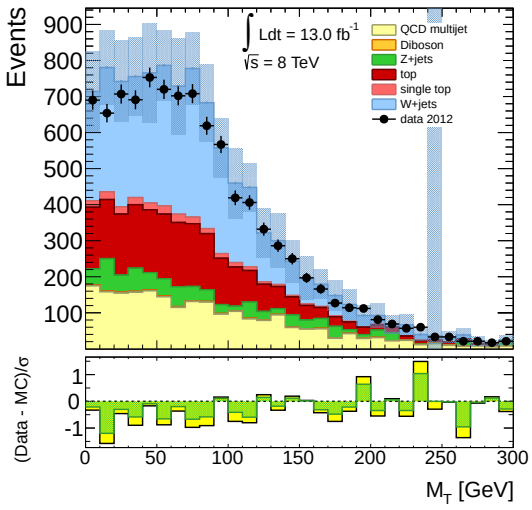

(a) Electron Channel

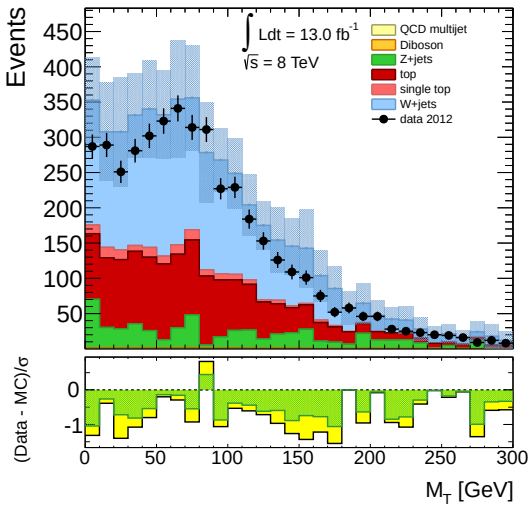

(b) Muon Channel

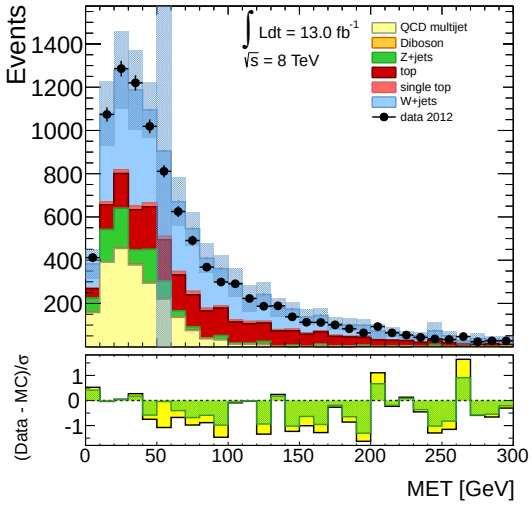

(c) Electron Channel

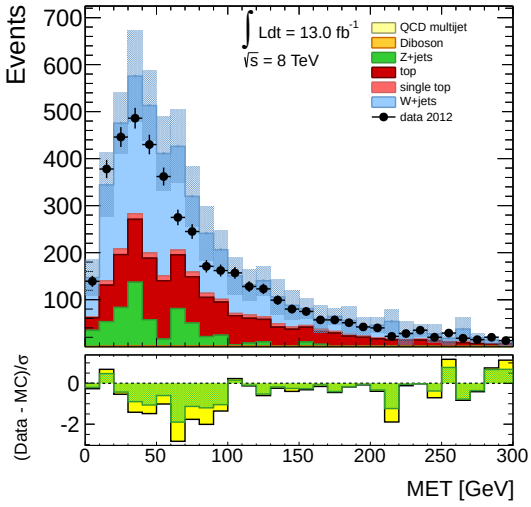

(d) Muon Channel

Figure 5.12. M_{T} and $E_{\mathrm{T}}^{\mathrm{miss}}$ distributions used to define a W+jets control region. The Monte Carlo simulation is normalized to an integrated luminosity of 13.0 fb^{-1}. The error bars include both statistical and systematic uncertainties. The bottom pane of each subfigure displays the difference between data and simulation over their statistical uncertainty (yellow band) or statistical+systematic uncertainties (green band)

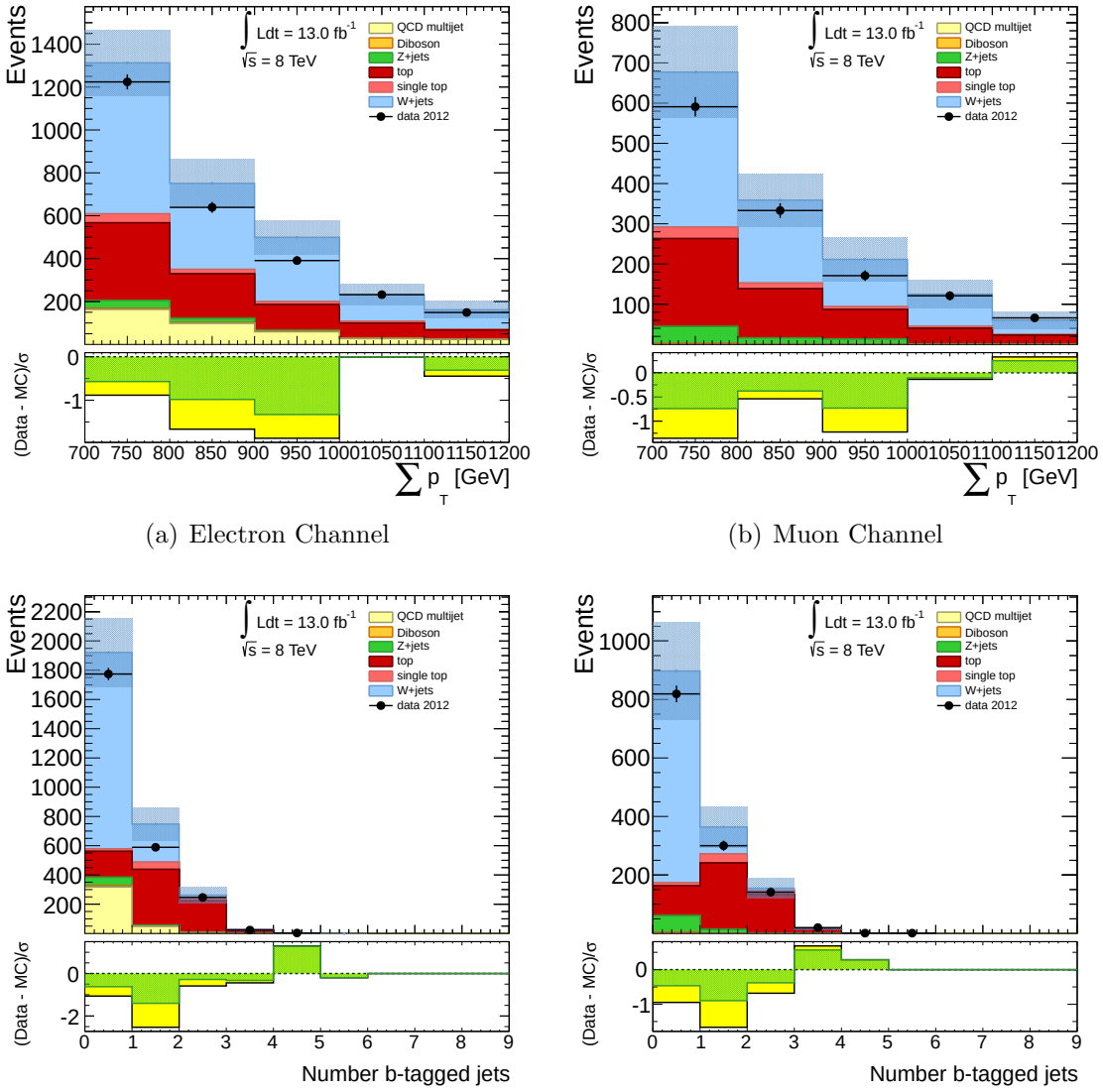

(a) Electron Channel

(b) Muon Channel

(c) Electron Channel

(d) Muon Channel

Figure 5.13. $\sum p_{\mathrm{T}}$ and number of b-tagged jets distributions in the W+jets CR, after scaling all non-W+jets backgrounds. The Monte Carlo simulation is normalized to an integrated luminosity of 13.0 fb^{-1}. The error bars include both statistical and systematic uncertainties. The bottom pane of each subfigure displays the difference between data and simulation over their statistical uncertainty (yellow band) or statistical+systematic uncertainties (green band). Appendix D.1 shows the corresponding distributions before and after the application of the obtained scale factor while App. D.2 shows them when using the alternate `Alpgen` generator for W/Z+jets.

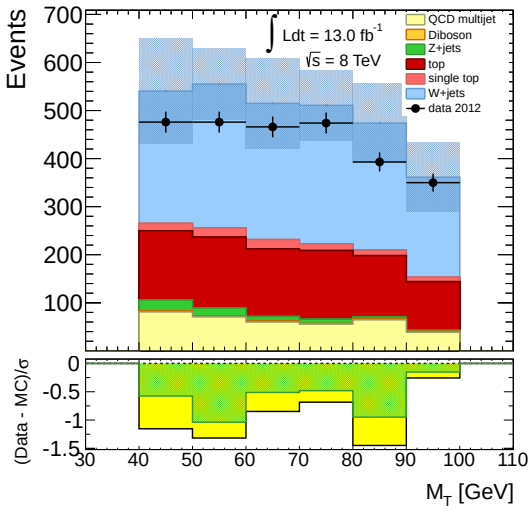

(a) Electron Channel

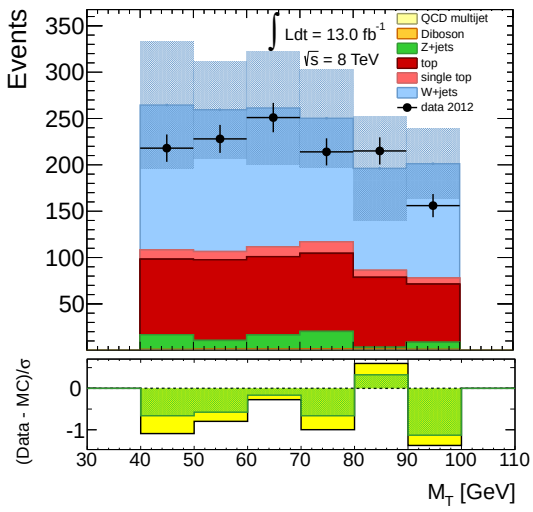

(b) Muon Channel

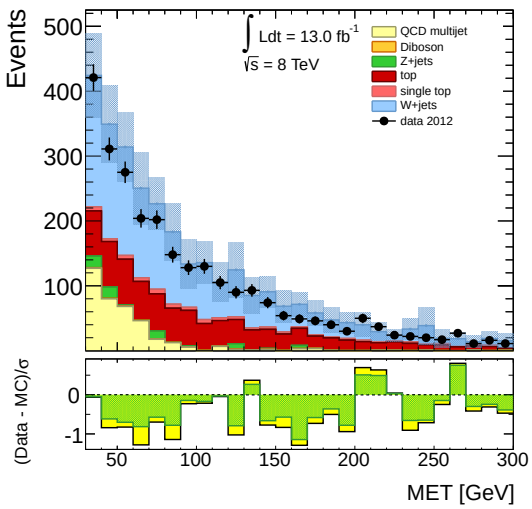

(c) Electron Channel

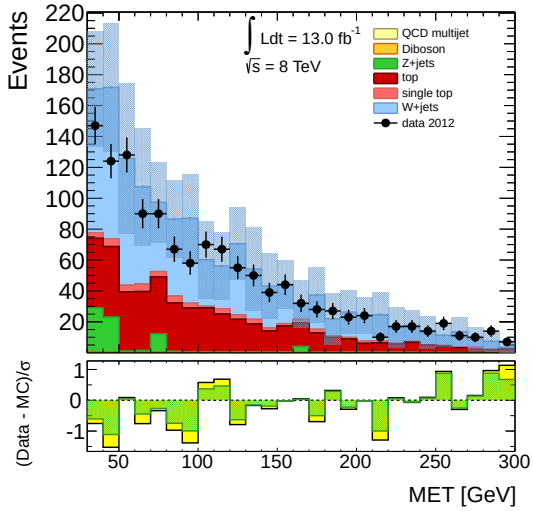

(d) Muon Channel

Figure 5.14. M_{T} and $E_{\mathrm{T}}^{\mathrm{miss}}$ distributions in the W+jets CR, after scaling all non-W+jets backgrounds. The Monte Carlo simulation is normalized to an integrated luminosity of 13.0 fb^{-1}. The error bars include both statistical and systematic uncertainties. The bottom pane of each subfigure displays the difference between data and simulation over their statistical uncertainty (yellow band) or statistical+systematic uncertainties (green band).

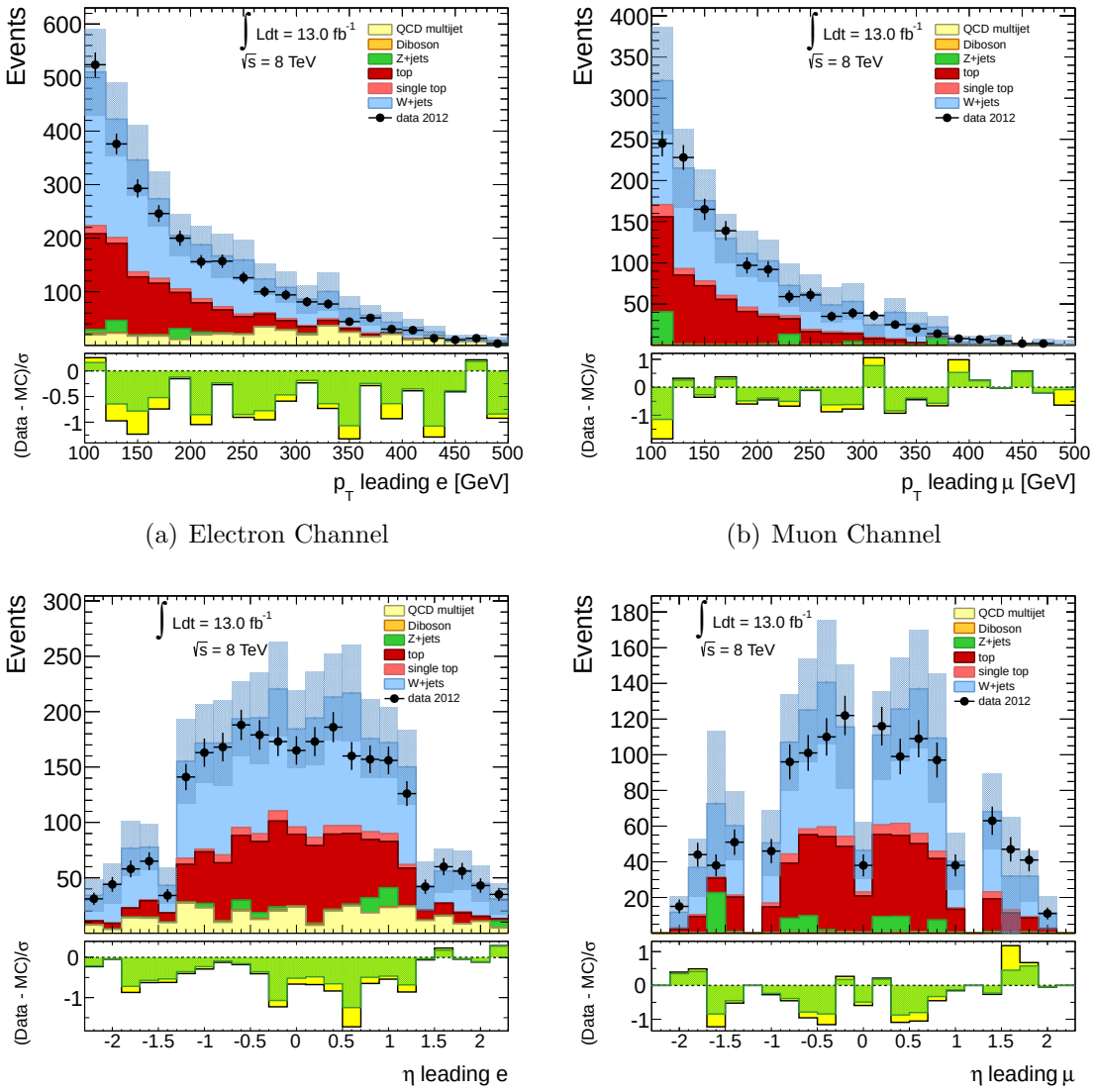

(a) Electron Channel

(b) Muon Channel

(c) Electron Channel

(d) Muon Channel

Figure 5.15. Leading lepton p_{T} and η distributions in the W+jets CR, after scaling all non-W+jets backgrounds. The Monte Carlo simulation is normalized to an integrated luminosity of 13.0 fb^{-1}. The error bars include both statistical and systematic uncertainties. The bottom pane of each subfigure displays the difference between data and simulation over their statistical uncertainty (yellow band) or statistical+systematic uncertainties (green band).

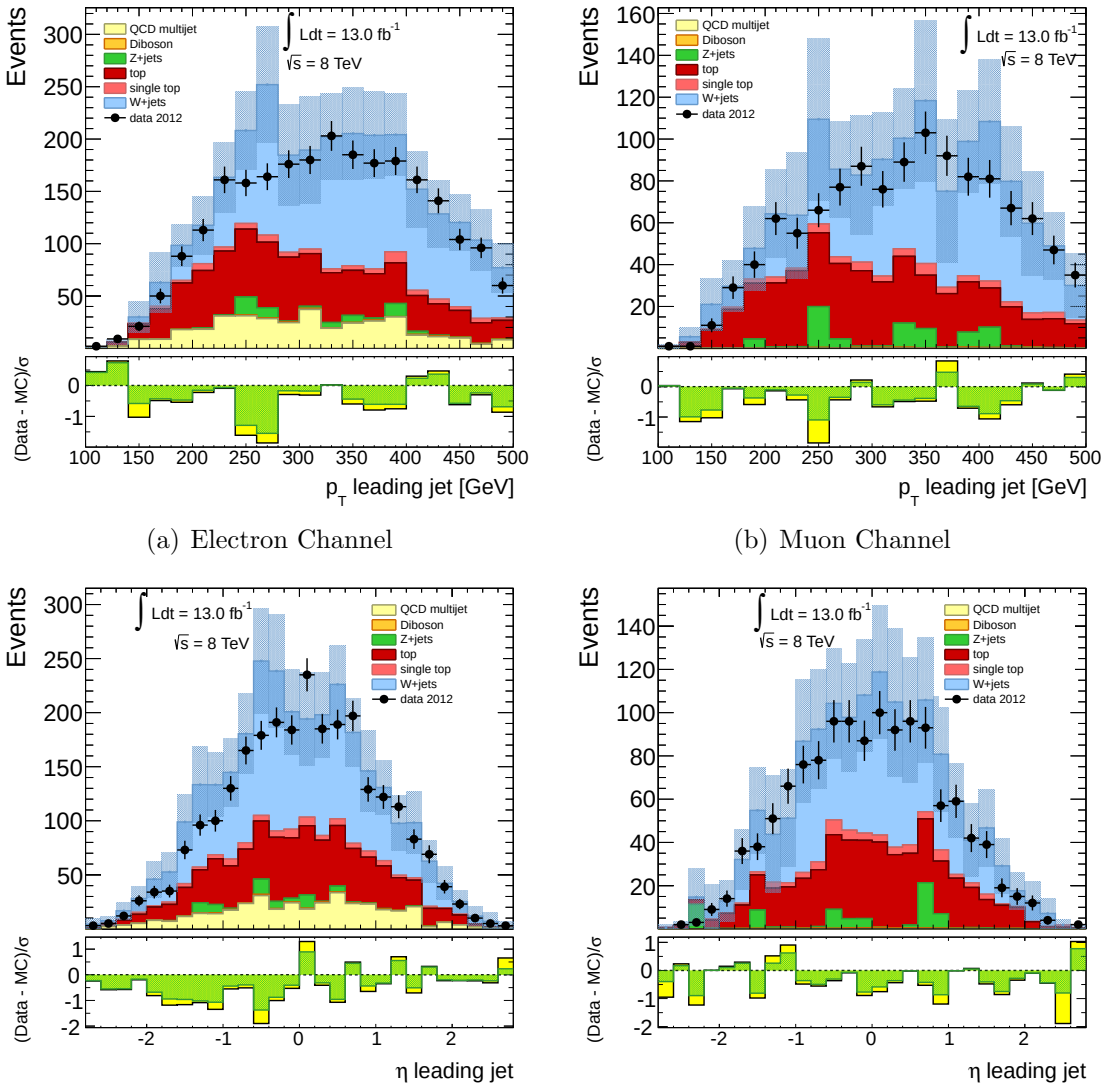

(a) Electron Channel

(b) Muon Channel

(c) Electron Channel

(d) Muon Channel

Figure 5.16. Leading jet p_{T} and η distributions in the W+jets CR, after scaling all non-W+jets backgrounds. The Monte Carlo simulation is normalized to an integrated luminosity of 13.0 fb^{-1}. The error bars include both statistical and systematic uncertainties. The bottom pane of each subfigure displays the difference between data and simulation over their statistical uncertainty (yellow band) or statistical+systematic uncertainties (green band).

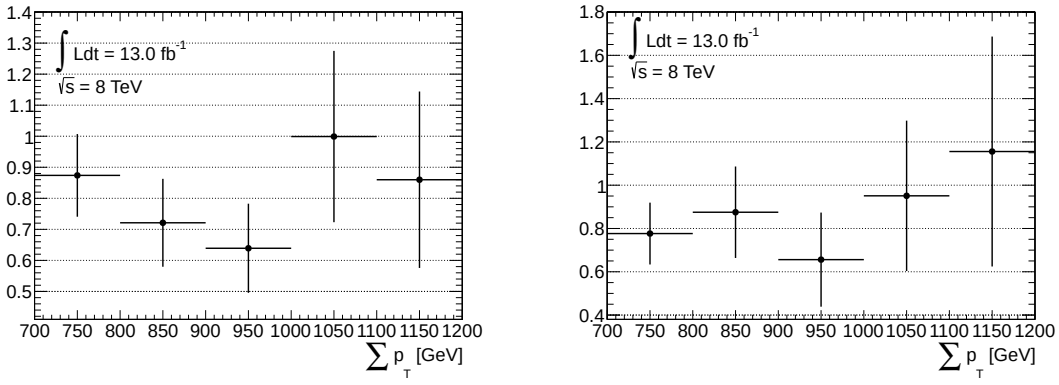

(a) Electron Channel (b) Muon Channel

Figure 5.17. The W+jets scale factor versus $\sum p_{\mathrm{T}}$. These plots correspond to the ratio of data over MC simulated events in Fig. 5.13.

Table 5.5. W+jets scale factors and uncertainties in the electron channel. Systematics variations are propagated through the whole analysis and a new scale factor is derived. The difference from the nominal is taken as the systematic uncertainty. The JES is one of the dominant sources of systematic uncertainties. The scale factor is particularly sensitive to the b-tagging uncertainties due to the large contribution of top events in the W+jets control region.

Systematics	Scale Factor	Deviation from Nominal (%)
Nominal	0.801 ± 0.099	-
JES Up	0.659 ± 0.080	-17.731
JES Down	0.820 ± 0.131	$+\ 2.376$
JER	0.703 ± 0.110	-12.331
b-tag Up	0.904 ± 0.101	$+12.773$
b-tag Down	0.665 ± 0.098	-17.054
EES Up	0.815 ± 0.100	$+\ 1.669$
EES Down	0.800 ± 0.097	$-\ 0.105$
EER Up	0.801 ± 0.099	$-\ 0.042$
EER Down	0.814 ± 0.099	$+\ 1.633$
Final	$0.801 \pm 0.099^{+0.106}_{-0.221}$	

Table 5.6. W+jets scale factors and uncertainties in the muon channel. Systematics variations are propagated through the whole analysis and a new scale factor is derived. The difference from the nominal is taken as the systematic uncertainty. The JES is one of the dominant sources of systematic uncertainties. The scale factor is particularly sensitive to the b-tagging uncertainties due to the large contribution of top events in the W+jets control region.

Systematics	Scale Factor	Deviation from Nominal (%)
Nominal	0.818 ± 0.112	-
JES Up	0.691 ± 0.091	-15.530
JES Down	1.008 ± 0.140	$+23.200$
JER	0.757 ± 0.111	$-\ 7.437$
b-tag Up	0.927 ± 0.114	$+13.233$
b-tag Down	0.671 ± 0.111	-17.942
MS Up	0.818 ± 0.111	$+\ 0.099$
MS Down	0.821 ± 0.112	$+\ 0.282$
ID Up	0.814 ± 0.111	$-\ 0.567$
ID Down	0.821 ± 0.112	$-\ 0.387$
Final	$0.818 \pm 0.112^{+0.219}_{-0.204}$	

5.1.4 QCD Multijet Fake Lepton Efficiency (ϵ_{fake})

The fake lepton efficiency ϵ_{fake}, as defined in Sec. 4.5.2, is given by the quotient of tight QCD data events over loose QCD data events. The number of loose (tight) QCD events in data is taken as the total number of loose (tight) data events in this control region, minus the MC simulation prediction for backgrounds with prompt leptons passing the loose (tight) selection criteria. The contribution from backgrounds with prompt leptons are estimated following the iteration method described in Sec. 4.5.3. The purity of this CR, defined as the number of loose QCD events over the total number of events passing the loose selection criteria, is $\sim 55\%$ in the electron channel and $\sim 65\%$ in the muon channel.

Figures 5.18 and 5.19 show the distributions that define the QCD multijet CR (i.e. M_{T}, $E_{\text{T}}^{\text{miss}}$, $M_{\text{T}} + E_{\text{T}}^{\text{miss}}$). The excess of data events over the backgrounds with prompt leptons is attributed to QCD. The light yellow histogram in the upper pane of each subfigure is used for illustration purposes only (i.e. not to calculate ϵ_{fake}), and describes the QCD multijet prediction according to the Monte Carlo simulation. The poor description of QCD multijet processes by the simulation motivated the data-driven technique employed here. Figures 5.20-5.22 illustrate the $\sum p_{\text{T}}$ and lepton kinematics in the QCD CR. The error bars for each subfigure displays only the statistical uncertainty and include the contribution of QCD events predicted by the MC simulation.

The obtained values for ϵ_{fake}, whether in the nominal condition or systematic variations thereof, are summarized in tables 5.7 and 5.8. As described in Sec. 4.5.2, the fake lepton efficiency is given by

$$\epsilon_{\text{fake}} = \frac{N_{\text{tight}}^{\text{fake}}}{N_{\text{loose}}^{\text{fake}}} = \frac{N_{\text{tight}}^{\text{data}} - N_{\text{tight}}^{\text{MC,prompt}}}{N_{\text{loose}}^{\text{data}} - N_{\text{loose}}^{\text{MC,prompt}}}$$

and the statistical error is calculated as

$$\delta\epsilon_{\text{fake}} \approx \frac{1}{N_{\text{loose}}^{\text{fake}}}\sqrt{(1-\epsilon_{\text{fake}})^2\left[\left(\sqrt{N_{\text{tight}}^{\text{data}}}\right)^2+\left(\delta N_{\text{tight}}^{\text{MC,prompt}}\right)^2\right]+\epsilon_{\text{fake}}^2\left(\sqrt{N_{\text{not-tight}}^{\text{data}}}\right)^2}$$

where $N_{\text{not-tight}}^{\text{data}} = N_{\text{loose}}^{\text{data}} - N_{\text{tight}}^{\text{data}}$, and $\delta N_{\text{not-tight}}^{\text{MC}}$ is considered negligible[2]. The resulting fake lepton efficiencies for the different channels are

$$\epsilon_{\text{fake}}(\text{electron}) = 0.432 \pm 0.052^{+0.110}_{-0.020}$$
$$\epsilon_{\text{fake}}(\text{muon}) < 0.062\,(95\%\,\text{CL}).$$

The ϵ_{fake} as a function of $\sum p_{\text{T}}$ and lepton η is displayed in Fig. 5.23. For the electron channel, when the uncertainties are taken into account, the value of ϵ_{fake} stays constant over the $\sum p_{\text{T}}$ range. For the muon channel, the QCD contribution is negligible and consistent with zero when the uncertainties are considered. Appendix E shows the ϵ_{fake} values and distributions obtained when the W/Z+jets backgrounds are generated with `Alpgen`.

[2]The prompt leptons produced in processes such as W/Z+jets and $t\bar{t}$ are fairly isolated and loosening the selection criteria does not significantly increase their contribution to this control region.

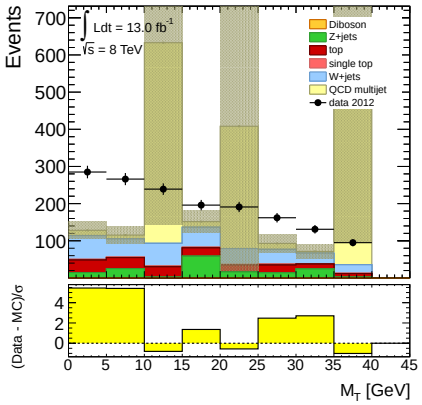

(a) Electron Channel, Loose

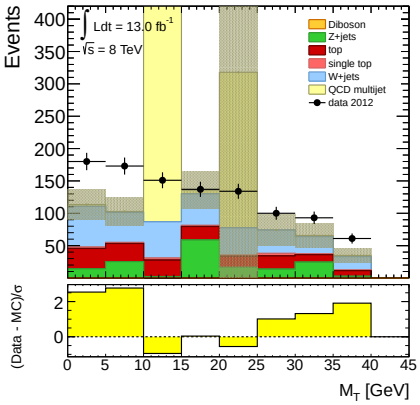

(b) Electron Channel, Tight

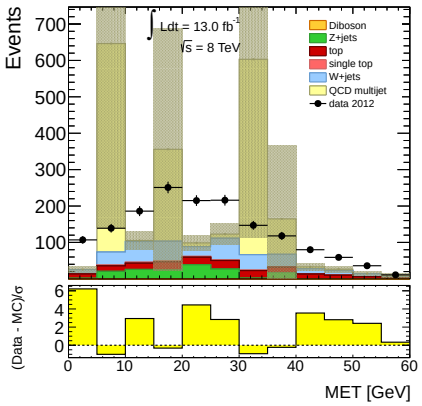

(c) Electron Channel, Loose

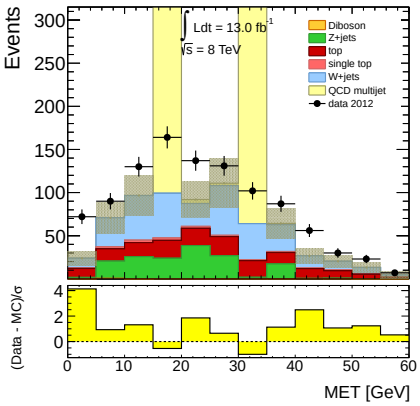

(d) Electron Channel, Tight

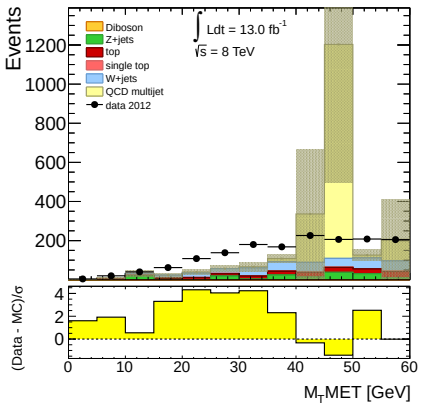

(e) Electron Channel, Loose

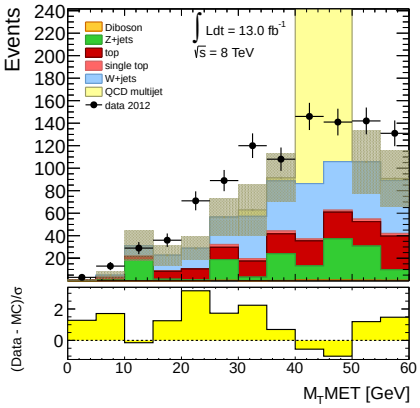

(f) Electron Channel, Tight

Figure 5.18. Loose and tight M_{T}, $E_{\mathrm{T}}^{\mathrm{miss}}$ and $M_{\mathrm{T}} + E_{\mathrm{T}}^{\mathrm{miss}}$ distributions in the electron channel used to define a QCD multijet control region. The Monte Carlo simulation is normalized to an integrated luminosity of 13.0 fb^{-1}. The error bars include the statistical error only. The bottom pane of each subfigure displays the difference between data and simulation over their statistical uncertainty.

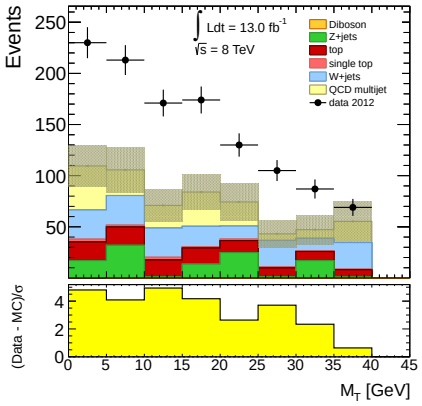

(a) Muon Channel, Loose

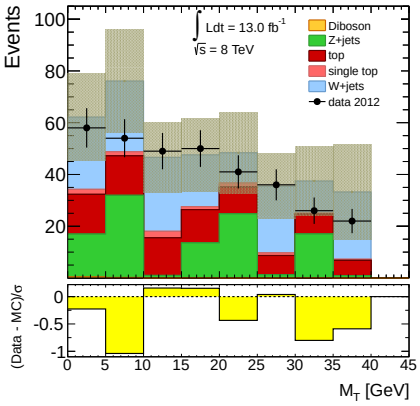

(b) Muon Channel, Tight

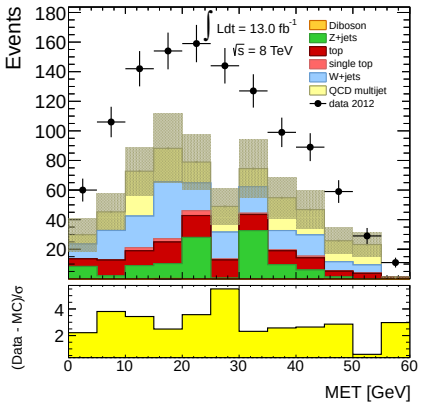

(c) Muon Channel, Loose

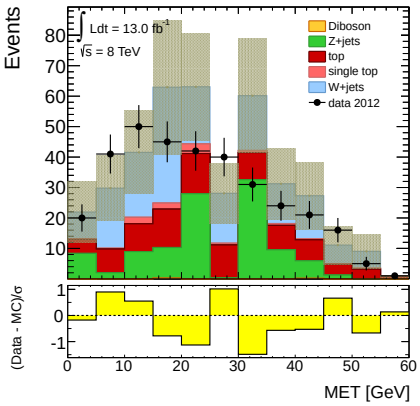

(d) Muon Channel, Tight

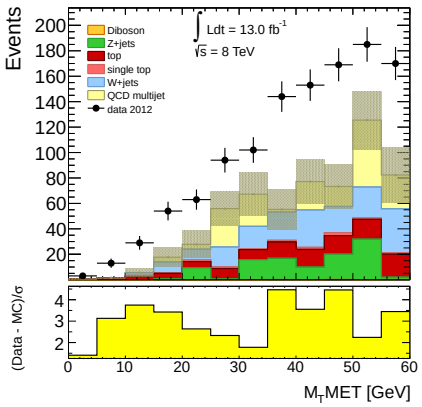

(e) Muon Channel, Loose

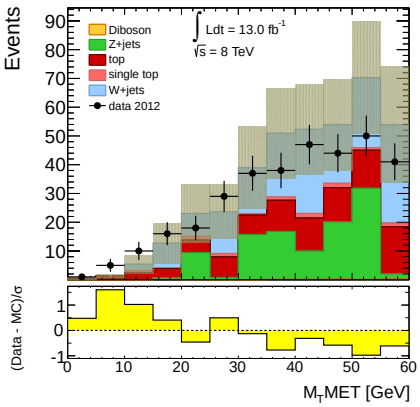

(f) Muon Channel, Tight

Figure 5.19. Loose and tight M_{T}, $E_{\mathrm{T}}^{\mathrm{miss}}$ and $M_{\mathrm{T}} + E_{\mathrm{T}}^{\mathrm{miss}}$ distributions in the muon channel used to define a QCD multijet control region. The Monte Carlo simulation is normalized to an integrated luminosity of 13.0 fb^{-1}. The error bars include the statistical error only. The bottom pane of each subfigure displays the difference between data and simulation over their statistical uncertainty.

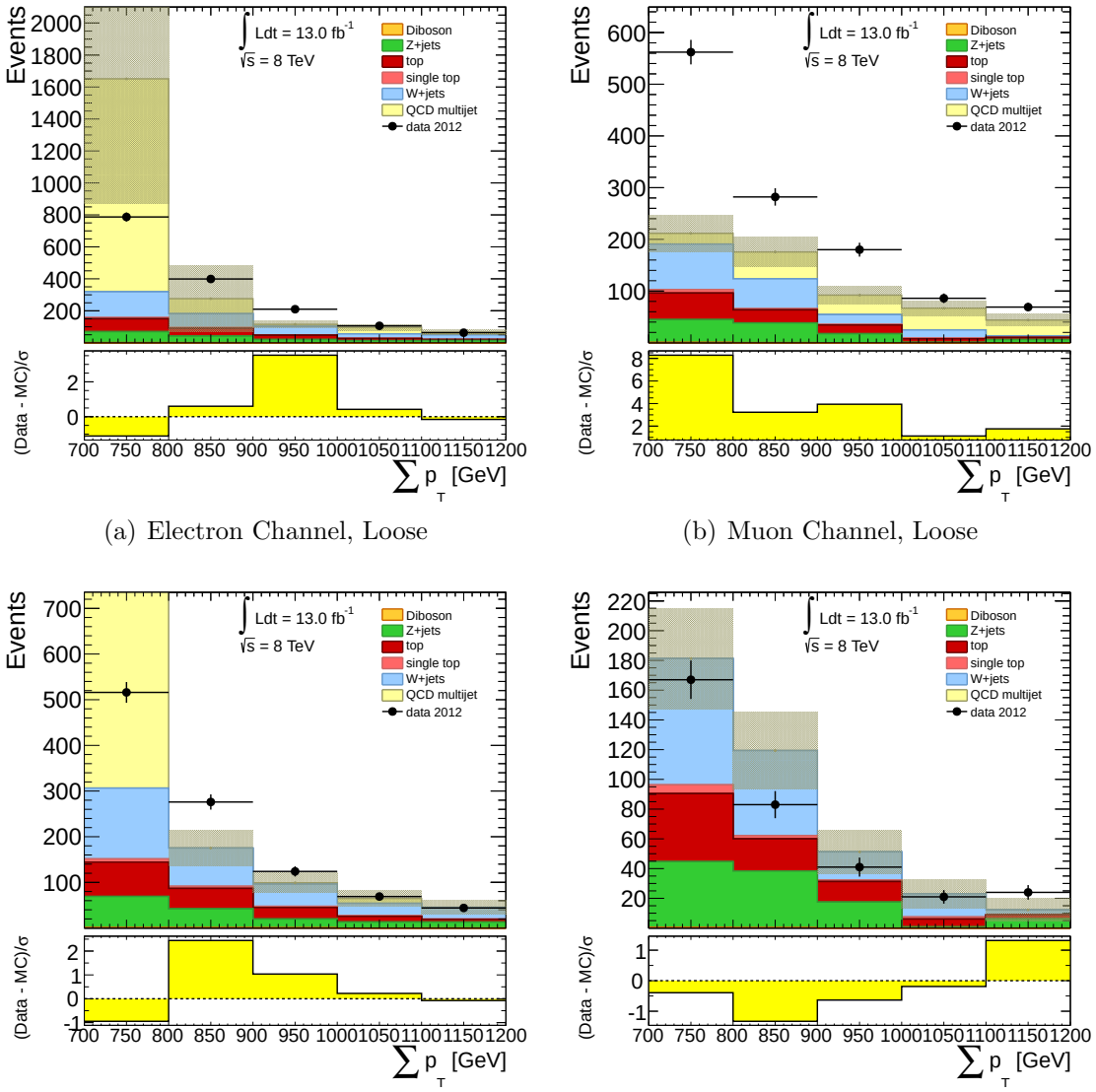

(a) Electron Channel, Loose

(b) Muon Channel, Loose

(c) Electron Channel, Tight

(d) Muon Channel, Tight

Figure 5.20. Loose and tight $\sum p_{\mathrm{T}}$ distributions in the QCD multijet CR, after scaling all prompt backgrounds. The Monte Carlo simulation is normalized to an integrated luminosity of 13.0 fb^{-1}. The error bars include the statistical error only. The bottom pane of each subfigure displays the difference between data and simulation over their statistical uncertainty. Appendix E shows the corresponding distributions when using the alternate `Alpgen` generator for W/Z+jets.

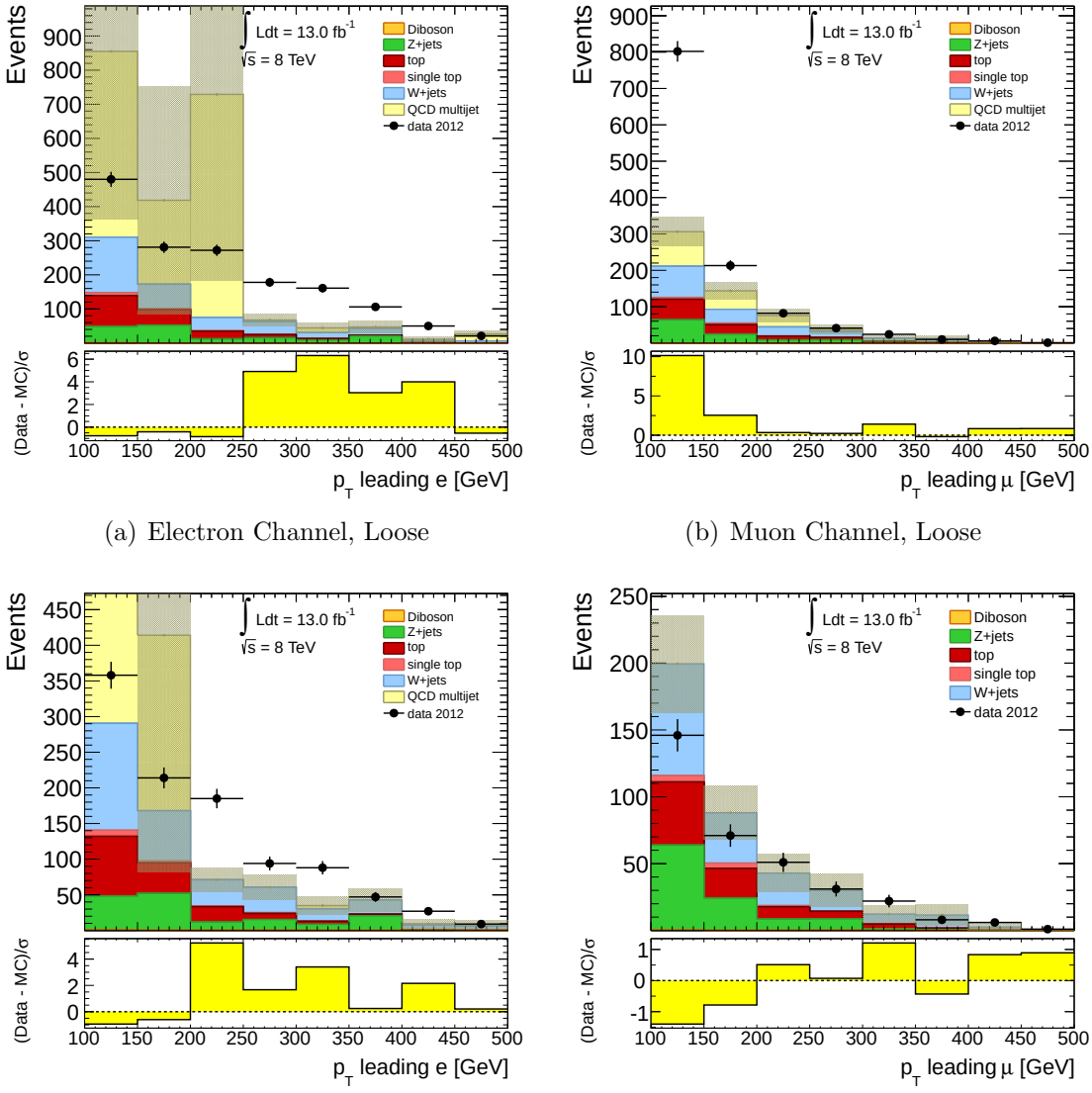

(a) Electron Channel, Loose

(b) Muon Channel, Loose

(c) Electron Channel, Tight

(d) Muon Channel, Tight

Figure 5.21. Loose and tight leading lepton p_{T} distributions in the QCD multijet CR, after scaling all prompt backgrounds. The Monte Carlo simulation is normalized to an integrated luminosity of 13.0 fb^{-1}. The error bars include the statistical error only. The bottom pane of each subfigure displays the difference between data and simulation over their statistical uncertainty.

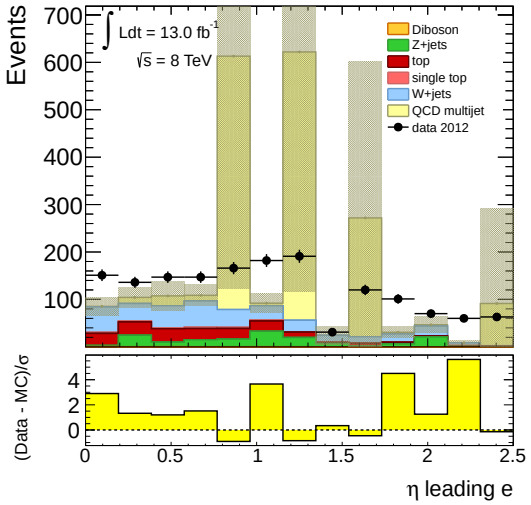

(a) Electron Channel, Loose

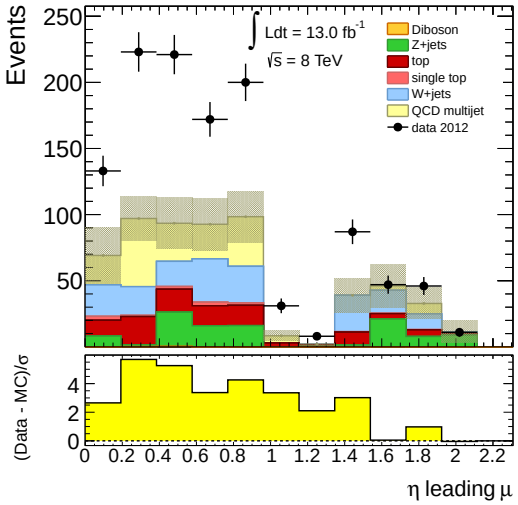

(b) Muon Channel, Loose

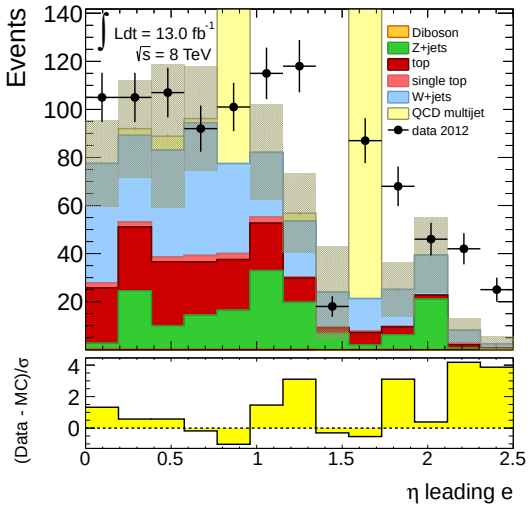

(c) Electron Channel, Tight

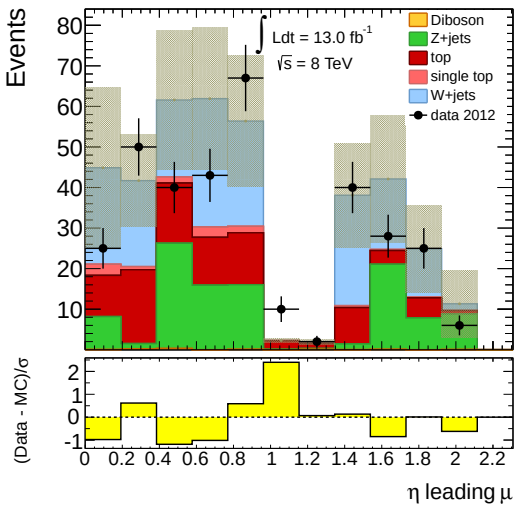

(d) Muon Channel, Tight

Figure 5.22. Loose and tight leading lepton η distributions in the QCD multijet CR, after scaling all prompt backgrounds. The Monte Carlo simulation is normalized to an integrated luminosity of 13.0 fb^{-1}. The error bars include the statistical error only. The bottom pane of each subfigure displays the difference between data and simulation over their statistical uncertainty.

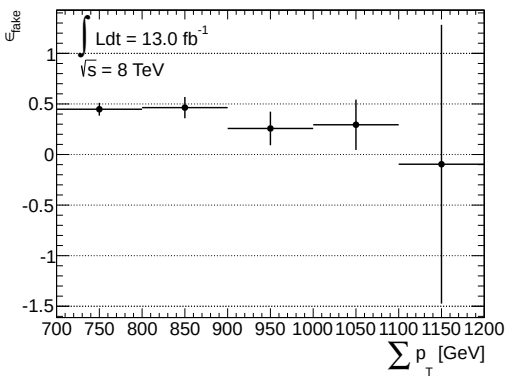

(a) Electron Channel

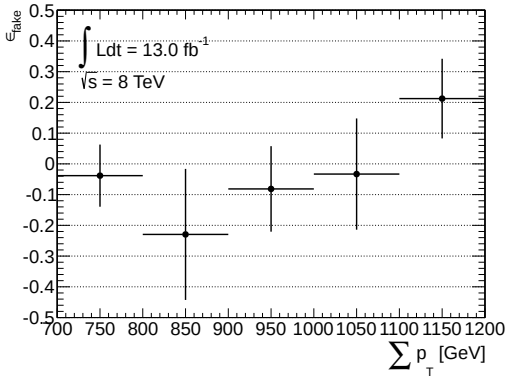

(b) Muon Channel

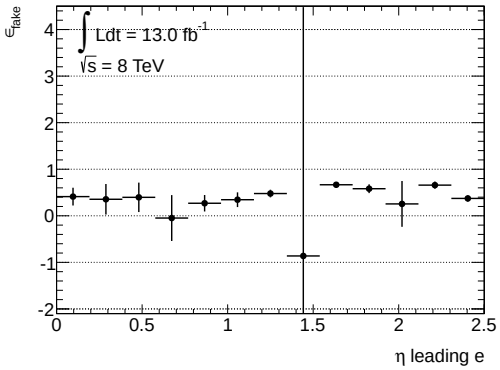

(c) Electron Channel

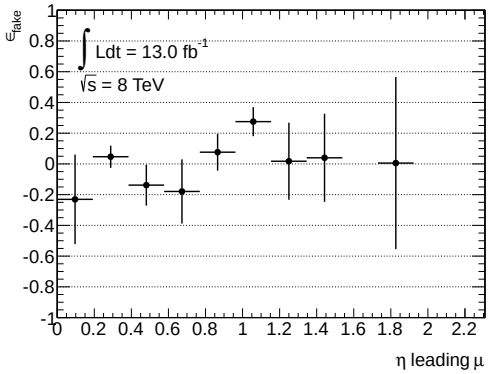

(d) Muon Channel

Figure 5.23. The ϵ_{fake} versus $\sum p_{\text{T}}$ and lepton η. These plots correspond to the ratio of tight QCD events over loose QCD events in Fig. 5.20.

Table 5.7. Fake lepton efficiencies and uncertainties in the electron channel. Systematics variations are propagated through the whole analysis and a new efficiency is derived. The difference from the nominal is taken as the systematic uncertainty.

Systematics	ϵ_{fake}	Deviation from Nominal (%)
Nominal	0.432 ± 0.052	-
JES Up	0.447 ± 0.045	+18.400
JES Down	0.511 ± 0.037	+ 3.556
JER	0.506 ± 0.035	+17.098
b-tag Up	0.423 ± 0.057	− 2.171
b-tag Down	0.444 ± 0.047	+ 2.787
EES Up	0.428 ± 0.054	− 0.982
EES Down	0.422 ± 0.055	− 2.377
EER Up	0.427 ± 0.053	− 1.033
EER Down	0.420 ± 0.055	− 2.878
Final	$0.432 \pm 0.052^{+0.110}_{-0.020}$	

Table 5.8. Fake lepton efficiencies and uncertainties in the muon channel. Systematics variations are propagated through the whole analysis and a new efficiency is derived. The difference from the nominal is taken as the systematic uncertainty. The upper limit at 95% CL is quoted.

Systematics	ϵ_{fake}	Deviation from Nominal (%)
Nominal	< 0.062 (95% CL)	-
JES Up	< 0.062 (95% CL)	-
JES Down	< 0.062 (95% CL)	-
JER	0.068 ± 0.045	-
b-tag Up	< 0.062 (95% CL)	-
b-tag Down	< 0.062 (95% CL)	-
MS Up	< 0.062 (95% CL)	-
MS Down	< 0.062 (95% CL)	-
ID Up	< 0.062 (95% CL)	-
ID Down	< 0.062 (95% CL)	-
Final	< 0.062 (95% CL)	

5.1.5 Real (Prompt) Lepton Efficiency (ϵ_{real})

The real lepton efficiency ϵ_{real}, as defined in Sec. 4.5.2, is given by the quotient of tight real lepton events over loose real lepton events. The number of loose (tight) real lepton events in data is taken as the total number of loose (tight) data events in a Z+jets control region, minus the MC simulation prediction for non-Z backgrounds. It is assumed that these non-Z backgrounds are small and no scaling or correction to the MC simulation prediction is necessary. The purity of this CR, defined as the number of loose real lepton events over the total number of events passing the loose selection criteria, is $\sim 97\%$ for both the electron and muon channels.

Figures 5.24-5.27 show a plurality of distributions, such as dilepton invariant mass, $\sum p_{\text{T}}$, and lepton kinematics in this real lepton (Z+jets) CR. The error bars for each subfigure displays only the statistical uncertainty. The Z+jets Monte Carlo prediction is presented to illustrate the agreement of data and simulation.

The obtained values for ϵ_{real}, whether in the nominal condition or systematic variations thereof, are summarized in tables 5.9 and 5.10. As described in Sec. 4.5.2, the real lepton efficiency and statistical uncertainty is given by

$$\epsilon_{\text{real}} = \frac{N^{\text{real}}_{\text{tight}}}{N^{\text{real}}_{\text{loose}}} = \frac{N^{\text{data}}_{\text{tight}} - N^{\text{MC,non}-Z}_{\text{tight}}}{N^{\text{data}}_{\text{loose}} - N^{\text{MC,non}-Z}_{\text{loose}}}$$

$$\delta\epsilon_{\text{real}} \approx \frac{1}{N^{\text{real}}_{\text{loose}}} \sqrt{(1-\epsilon_{\text{real}})^2 \left[\left(\sqrt{N^{\text{data}}_{\text{tight}}} \right)^2 + \left(\delta N^{\text{MC,non}-Z}_{\text{tight}} \right)^2 \right] + \epsilon^2_{\text{real}} \left(\sqrt{N^{\text{data}}_{\text{not}-\text{tight}}} \right)^2}$$

where $N^{\text{data}}_{\text{not}-\text{tight}} = N^{\text{data}}_{\text{loose}} - N^{\text{data}}_{\text{tight}}$, and $\delta N^{\text{MC}}_{\text{not}-\text{tight}}$ is considered negligible. The resulting real lepton efficiencies for the different channels are

$$\epsilon_{\text{real}}(\text{electron}) = 0.939 \pm 0.008^{+6.4\times10^{-5}}_{-1.1\times10^{-5}}$$

$$\epsilon_{\text{real}}(\text{muon}) = 0.983 \pm 0.007^{+1.4\times10^{-5}}_{-0.004}$$

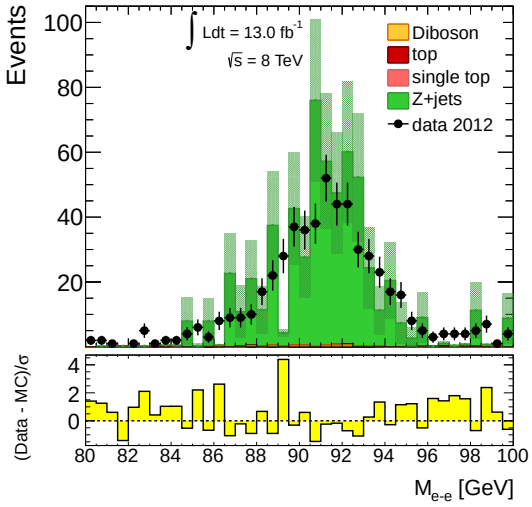

(a) Electron Channel, Loose

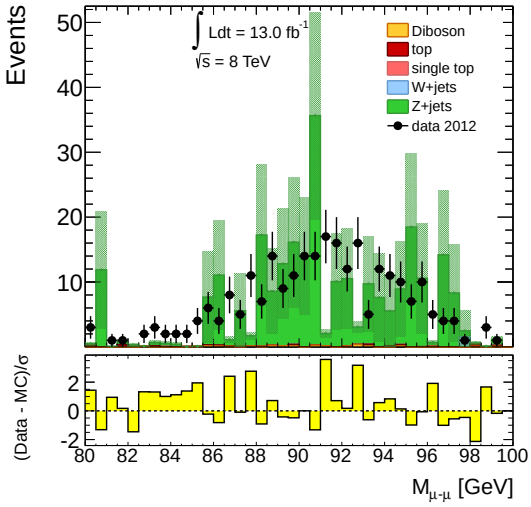

(b) Muon Channel, Loose

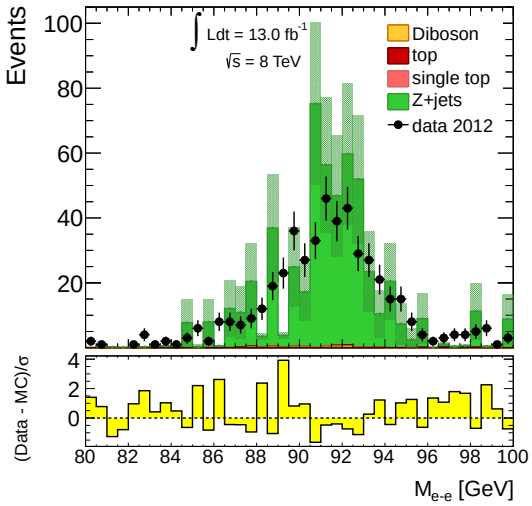

(c) Electron Channel, Tight

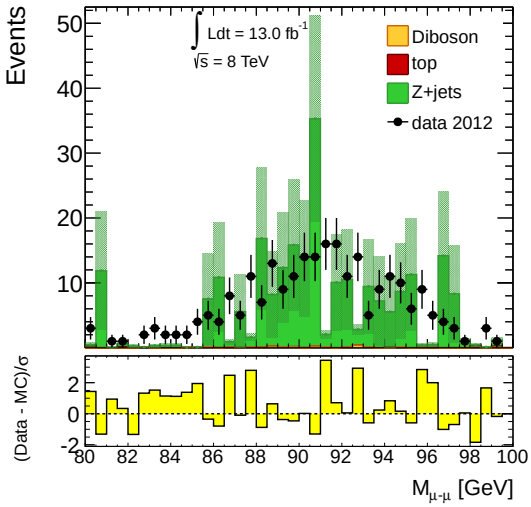

(d) Muon Channel, Tight

Figure 5.24. Loose and tight dilepton invariant mass distributions in the real lepton (Z+jets) control region. The Monte Carlo simulation is normalized to an integrated luminosity of 13.0 fb^{-1}. The error bars include the statistical error only. The bottom pane of each subfigure displays the difference between data and simulation over their statistical uncertainty.

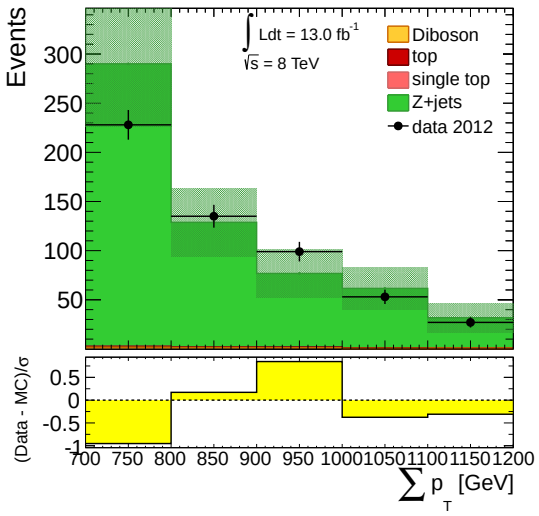

(a) Electron Channel, Loose

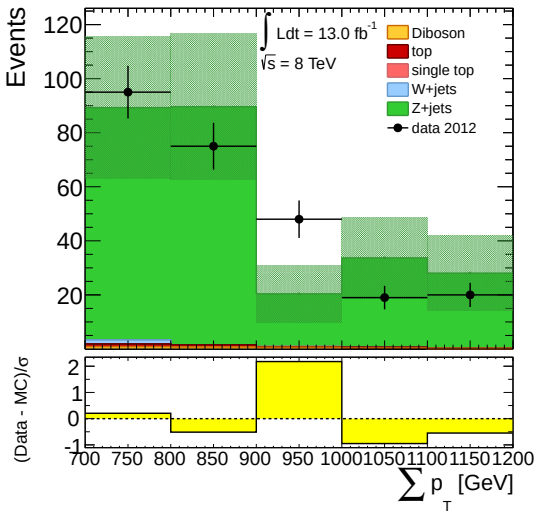

(b) Muon Channel, Loose

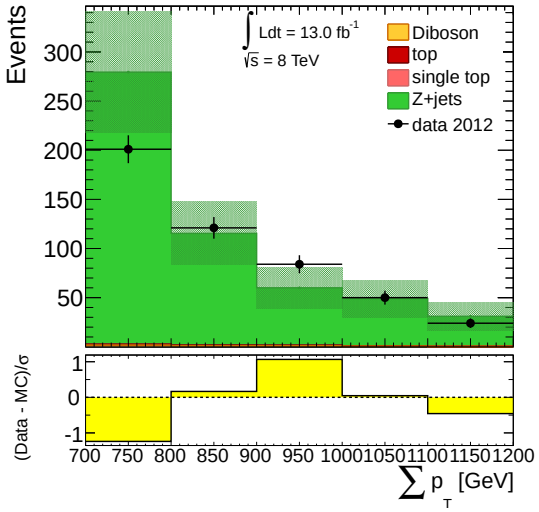

(c) Electron Channel, Tight

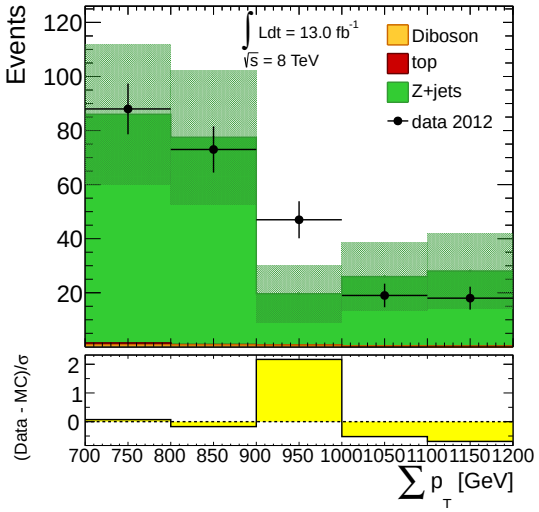

(d) Muon Channel, Tight

Figure 5.25. Loose and tight $\sum p_{\mathrm{T}}$ distributions in the real lepton (Z+jets) control region. The Monte Carlo simulation is normalized to an integrated luminosity of 13.0 fb^{-1}. The error bars include the statistical error only. The bottom pane of each subfigure displays the difference between data and simulation over their statistical uncertainty.

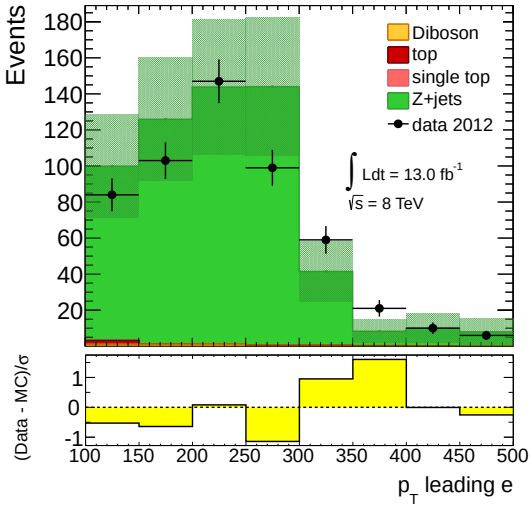

(a) Electron Channel, Loose

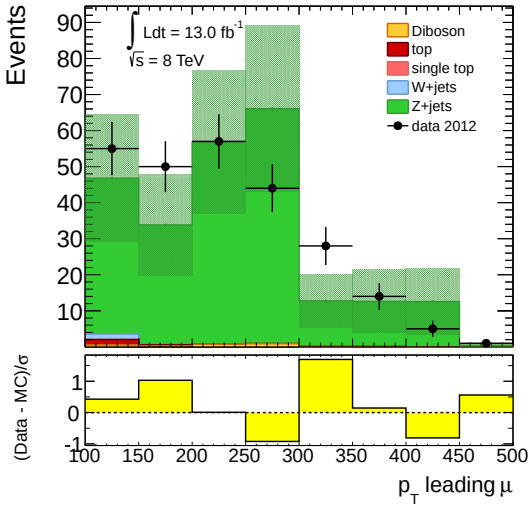

(b) Muon Channel, Loose

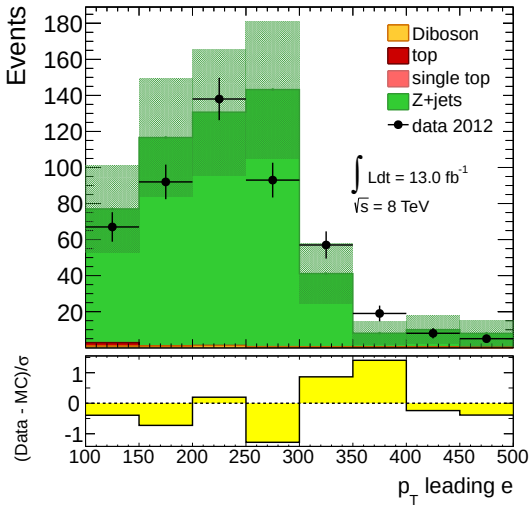

(c) Electron Channel, Tight

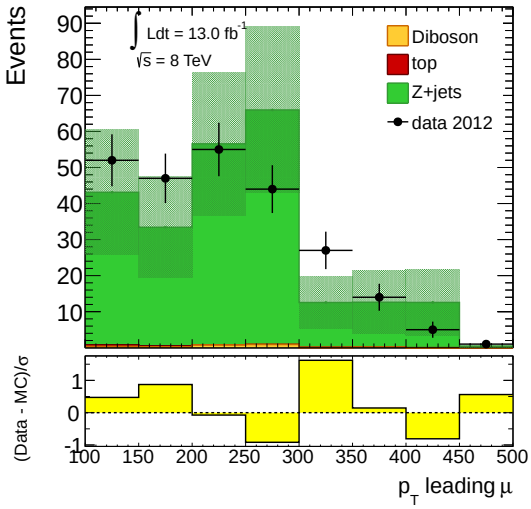

(d) Muon Channel, Tight

Figure 5.26. Loose and tight leading lepton p_{T} distributions in the real lepton (Z+jets) control region. The Monte Carlo simulation is normalized to an integrated luminosity of 13.0 fb^{-1}. The error bars include the statistical error only. The bottom pane of each subfigure displays the difference between data and simulation over their statistical uncertainty.

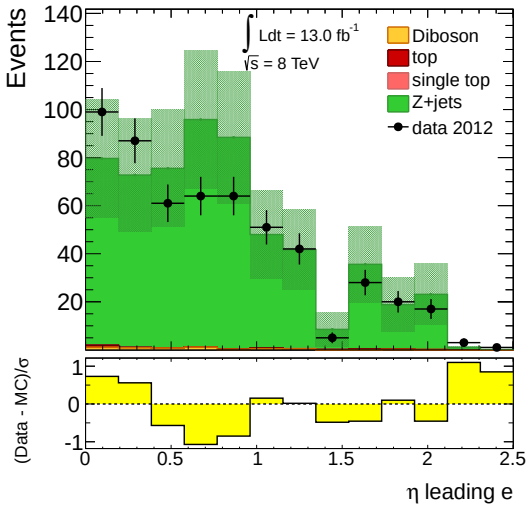

(a) Electron Channel, Loose

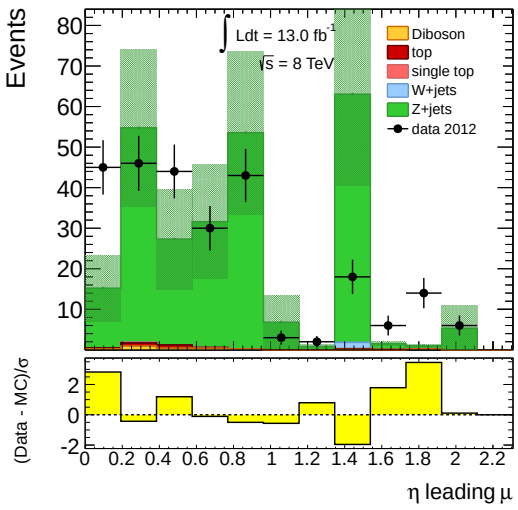

(b) Muon Channel, Loose

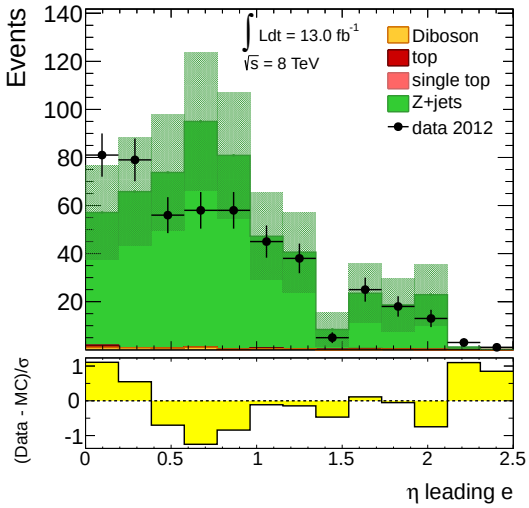

(c) Electron Channel, Tight

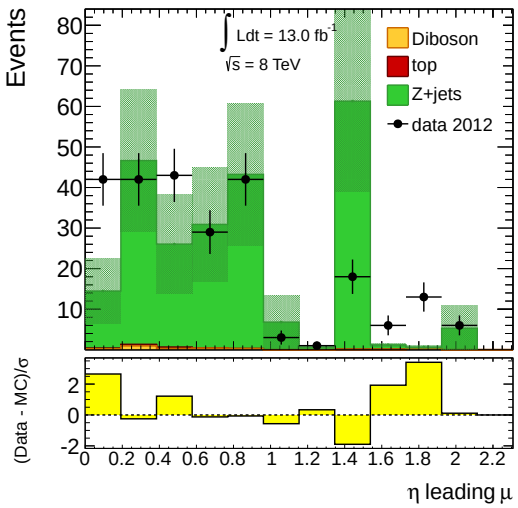

(d) Muon Channel, Tight

Figure 5.27. Loose and tight leading lepton η distributions in the real lepton (Z+jets) control region. The Monte Carlo simulation is normalized to an integrated luminosity of 13.0 fb^{-1}. The error bars include the statistical error only. The bottom pane of each subfigure displays the difference between data and simulation over their statistical uncertainty.

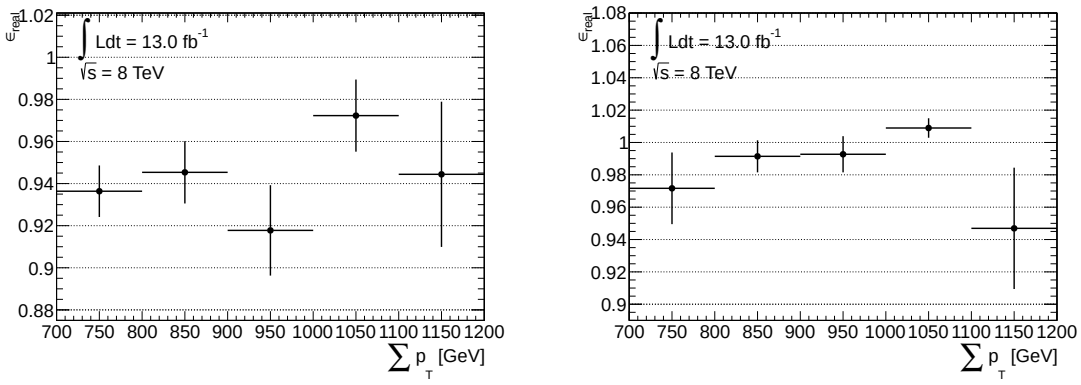

(a) Electron Channel (b) Muon Channel

Figure 5.28. The ϵ_{real} versus $\sum p_{\text{T}}$. These plots correspond to the ratio of tight over loose real lepton events in Fig. 5.25.

The ϵ_{real} as a function of $\sum p_{\text{T}}$ is displayed in Fig. 5.28. For both channels, when the uncertainties are taken into account, the value of ϵ_{real} stays constant over the $\sum p_{\text{T}}$ range. Appendix F shows the ϵ_{real} values and distributions obtained when the W/Z+jets backgrounds are generated with `Alpgen`.

Table 5.9. Real lepton efficiencies and uncertainties in the electron channel. Systematics variations are propagated through the whole analysis and a new efficiency is derived. The difference from the nominal is taken as the systematic uncertainty.

Systematics	ϵ_{real}	Deviation from Nominal (%)
Nominal	0.939 ± 0.008	-
JES Up	0.939 ± 0.008	$+1.20 \times 10^{-3}$
JES Down	0.939 ± 0.008	$+4.20 \times 10^{-3}$
JER	0.939 ± 0.008	$+1.20 \times 10^{-3}$
b-tag Up	0.939 ± 0.008	0
b-tag Down	0.939 ± 0.008	0
EES Up	0.939 ± 0.008	$+0.20 \times 10^{-3}$
EES Down	0.939 ± 0.008	-1.20×10^{-3}
EER Up	0.939 ± 0.008	$+3.60 \times 10^{-3}$
EER Down	0.939 ± 0.008	$+3.60 \times 10^{-3}$
Final	$0.939 \pm 0.008^{+6.4\times10^{-5}}_{-1.1\times10^{-5}}$	

Table 5.10. Real lepton efficiencies and uncertainties in the muon channel. Systematics variations are propagated through the whole analysis and a new efficiency is derived. The difference from the nominal is taken as the systematic uncertainty.

Systematics	ϵ_{real}	Deviation from Nominal (%)
Nominal	0.983 ± 0.007	-
JES Up	0.983 ± 0.007	$+0.001$
JES Down	0.979 ± 0.007	-0.415
JER	0.982 ± 0.007	-0.034
b-tag Up	0.983 ± 0.007	0
b-tag Down	0.983 ± 0.007	0
MS Up	0.983 ± 0.007	0
MS Down	0.983 ± 0.007	0
ID Up	0.983 ± 0.007	0
ID Down	0.983 ± 0.007	0
Final	$0.983 \pm 0.007^{+1.4\times10^{-5}}_{-0.004}$	

5.1.6 Summary of Results in the Control Regions

The scale factors and lepton efficiencies calculated in the different control regions are summarized in table 5.11.

Table 5.11. Scale factors and lepton efficiencies in the electron and muon channels. The results include the statistical and systematic errors.

Scale Factor or Efficiency	Electron Channel	Muon Channel
Z+jets SF	$0.902 \pm 0.099^{+0.061}_{-0.067}$	$0.980 \pm 0.164^{+0.021}_{-0.055}$
$t\bar{t}$ SF	$1.020 \pm 0.086^{+0.292}_{-0.264}$	$1.118 \pm 0.120^{+0.345}_{-0.304}$
W+jets SF	$0.801 \pm 0.099^{+0.106}_{-0.221}$	$0.818 \pm 0.112^{+0.219}_{-0.204}$
ϵ_{fake}	$0.432 \pm 0.052^{+0.110}_{-0.020}$	$< 0.062\,(95\%\,\text{CL})$
ϵ_{real}	$0.939 \pm 0.008^{+6.4\times10^{-5}}_{-1.1\times10^{-5}}$	$0.983 \pm 0.007^{+1.4\times10^{-5}}_{-0.004}$

5.2 Final Distributions in the Sideband Region

The control regions allow the definition of scale factors and lepton efficiencies to improve the agreement between the data and the Monte Carlo simulated (dominant) backgrounds, in a region with negligible signal contamination. Given that the scale factors, as well as the real and fake lepton efficiencies, are substantially constant in the sideband, it is assumed that the calculated scalings or corrections are also applicable in the signal region.

Figure 5.29 shows the $\sum p_{\text{T}}$ distributions in the sideband region before and after the application of the scale factors, for both the electron and muon channels. Leading lepton and jet kinematics are illustrated in Figs. 5.30 and 5.31. After scaling the W/Z+jets and $t\bar{t}$ background, and using the matrix method to estimate the QCD contribution, the data-simulation agreement in the majority of the distributions is within $\pm1\sigma$. Appendix G shows the corresponding distribution when the W/Z+jets backgrounds are generated with `Alpgen`.

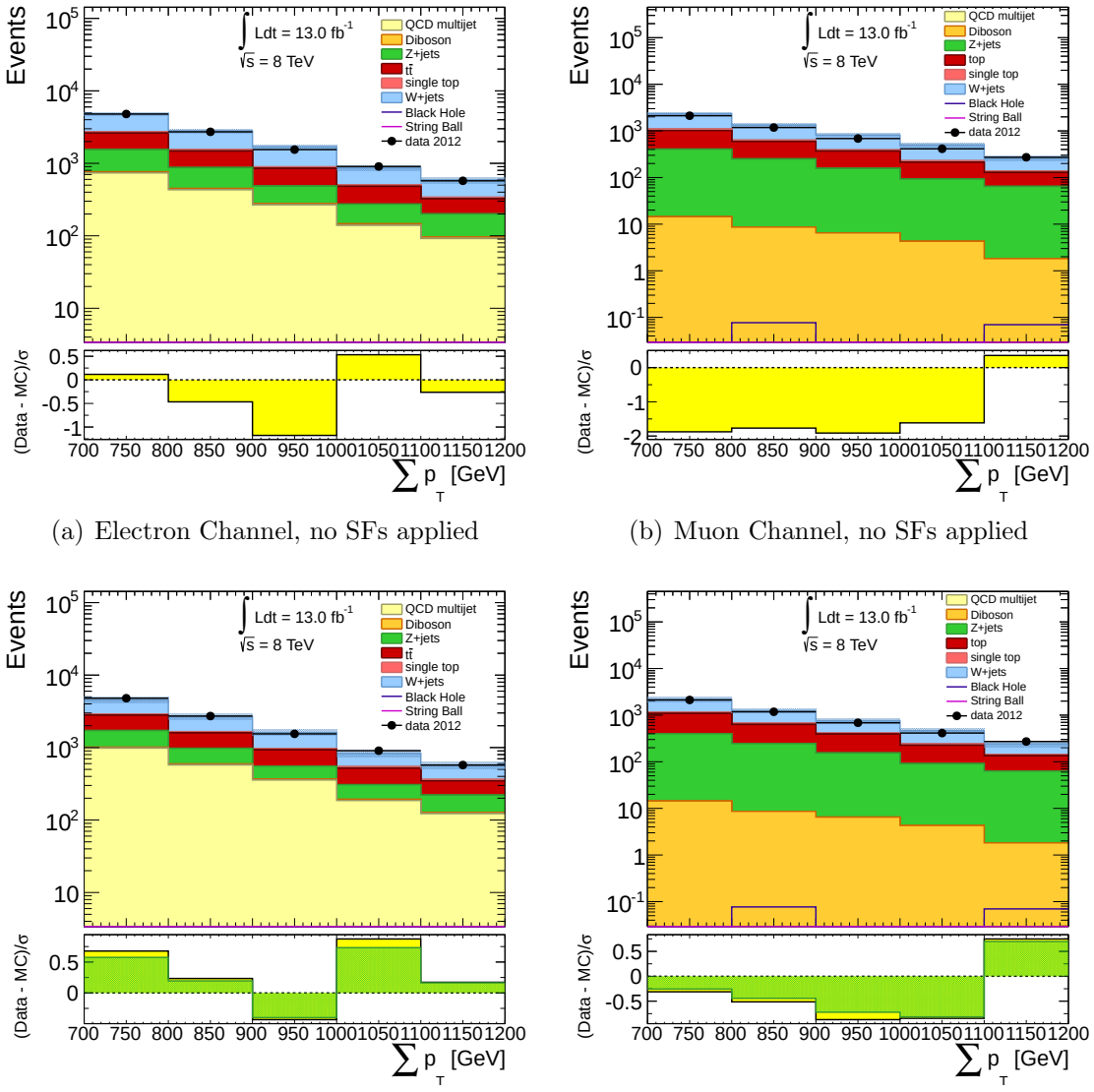

(a) Electron Channel, no SFs applied

(b) Muon Channel, no SFs applied

(c) Electron Channel, SFs applied

(d) Muon Channel, SFs applied

Figure 5.29. $\sum p_{\mathrm{T}}$ distributions in the sideband region, before (upper plots) and after (lower plots) the application of the scale factors. The Monte Carlo simulation is normalized to an integrated luminosity of 13.0 fb^{-1}. The error bars include both statistical and systematic uncertainties. The bottom pane of each subfigure displays the difference between data and simulation over their statistical uncertainty (yellow band) or statistical+systematic uncertainties (green band). The corresponding distributions when using the alternate `Alpgen` generator are shown in App. G.

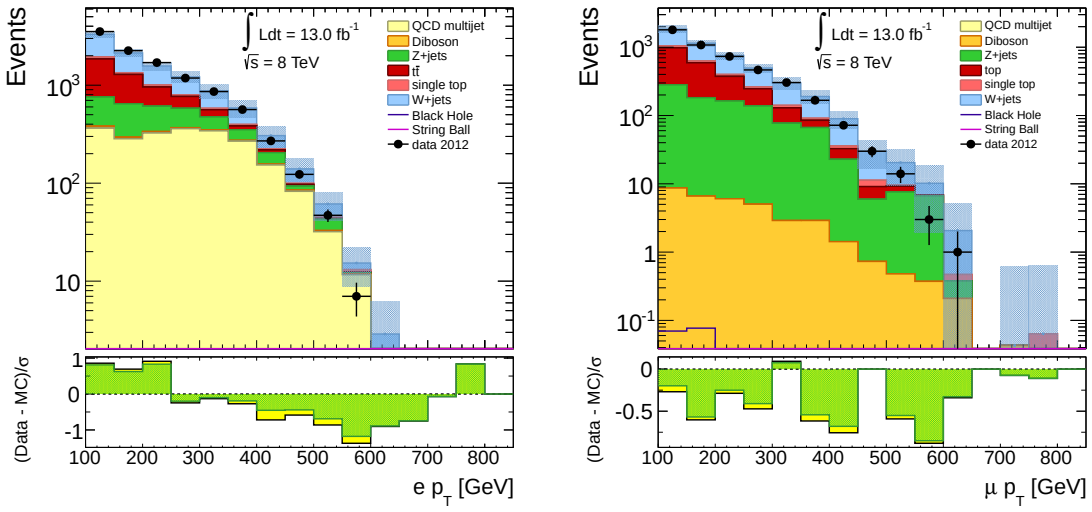

(a) Electron Channel

(b) Muon Channel

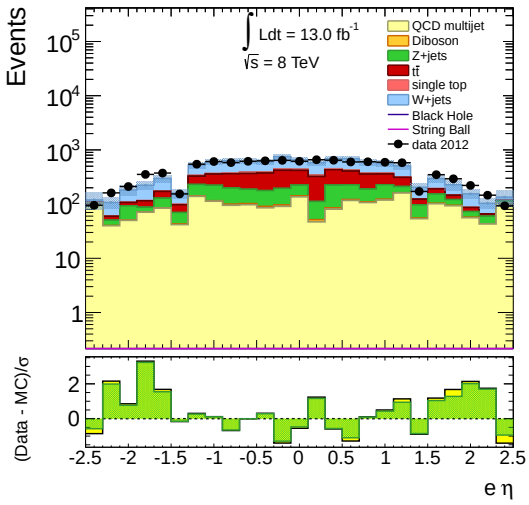

(c) Electron Channel

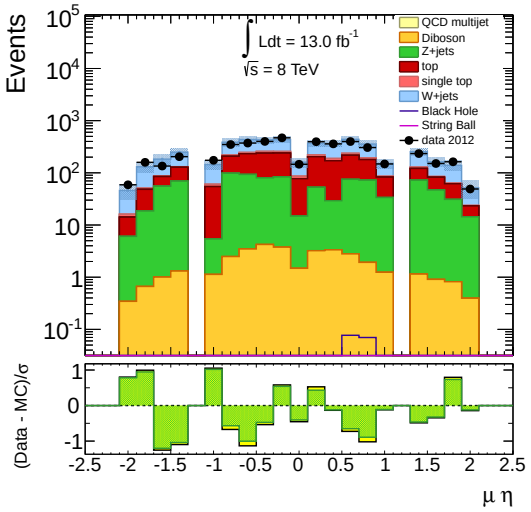

(d) Muon Channel

Figure 5.30. Leading lepton p_{T} and η distributions in the sideband region after the application of the scale factors. The Monte Carlo simulation is normalized to an integrated luminosity of 13.0 fb^{-1}. The error bars include both statistical and systematic uncertainties. The bottom pane of each subfigure displays the difference between data and simulation over their statistical uncertainty (yellow band) or statistical+systematic uncertainties (green band).

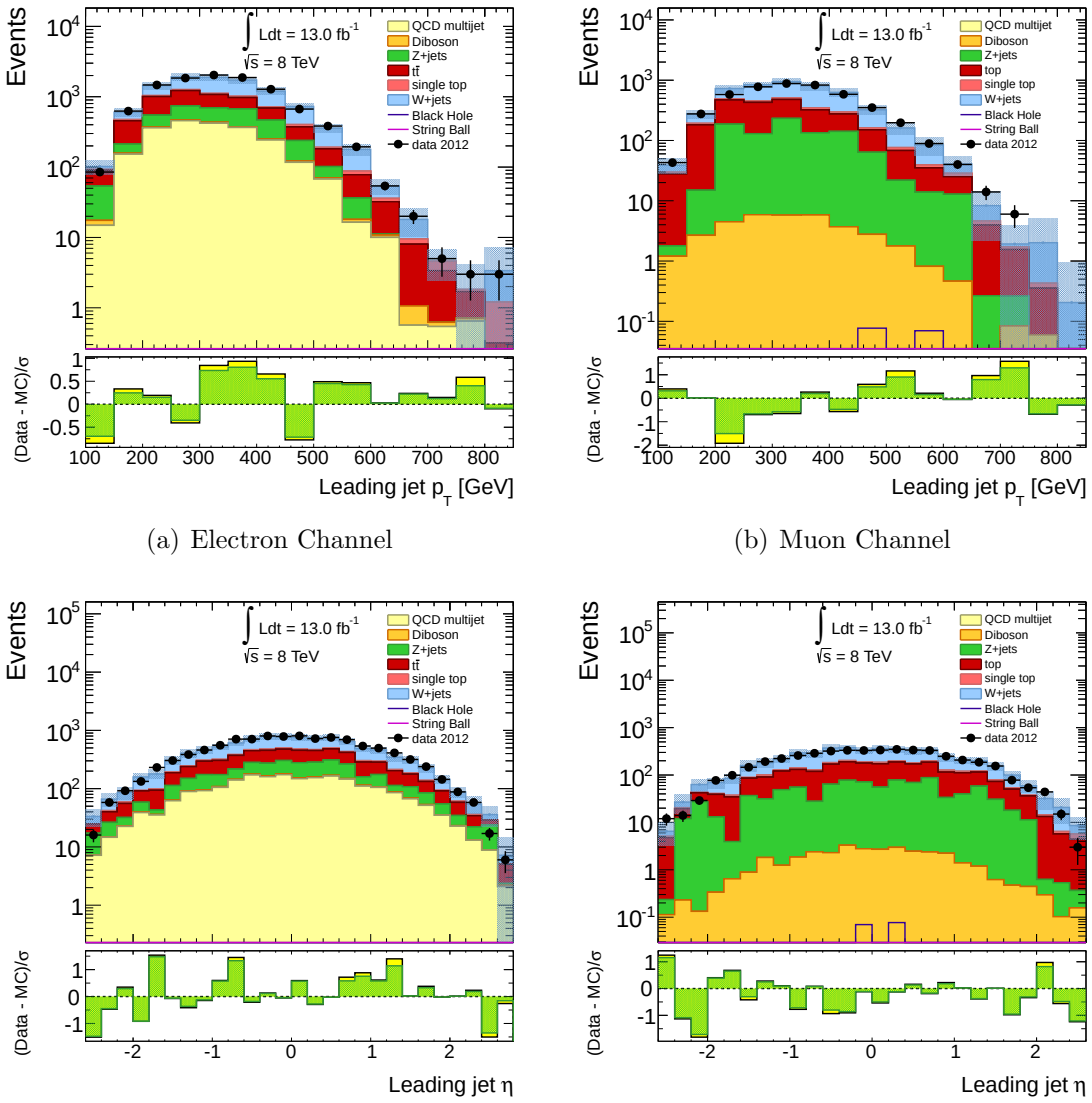

(a) Electron Channel

(b) Muon Channel

(c) Electron Channel

(d) Muon Channel

Figure 5.31. Leading jet p_{T} and η distributions in the sideband region after the application of the scale factors. The Monte Carlo simulation is normalized to an integrated luminosity of 13.0 fb^{-1}. The error bars include both statistical and systematic uncertainties. The bottom pane of each subfigure displays the difference between data and simulation over their statistical uncertainty (yellow band) or statistical+systematic uncertainties (green band).

5.3 Background Prediction in the Signal Region

The observed and predicted event yields, following the estimation procedure described in Sec. 4.5 and the scale factors and lepton efficiencies calculated in Sec. 5.1, are plotted in Fig. 5.32. The $\sum p_{\mathrm{T}}$ and event invariant mass distributions include the validation region (1200 GeV$\leq \sum p_{\mathrm{T}} \leq$ 1500 GeV) and the signal region ($\sum p_{\mathrm{T}} >$ 1500 GeV). Two representative samples depict the expected behavior for black holes and string balls. The Standard Model background estimates are in good agreement with the observed data. No excess of events is observed beyond the SM expectations. Taking into account the statistical and systematic uncertainties, the data-simulation agreement is within $\pm 1\sigma$ for both the electron and muon channels.

Figures 5.33-5.35 show the leading lepton and leading jet kinematics in the signal region, as well as the reconstructed $E_{\mathrm{T}}^{\mathrm{miss}}$ and the event sphericity. For all these distributions, the Standard Model backgrounds effectively describe the behavior of the data.

Tables 5.12 and 5.13 illustrate the contribution of each major background to the total MC simulation prediction, in the nominal condition or systematic variations thereof, for the electron channel and the muon channel, respectively. The application of scale factors, calculated in kinematically similar control regions, to backgrounds in the signal region, effectively cancels most of the systematic effects. The limited statistics dominate the uncertainties.

The background predictions, including statistical and systematic uncertainties for several $\sum p_{\mathrm{T}}$ thresholds, are shown in tables 5.14 and 5.15.

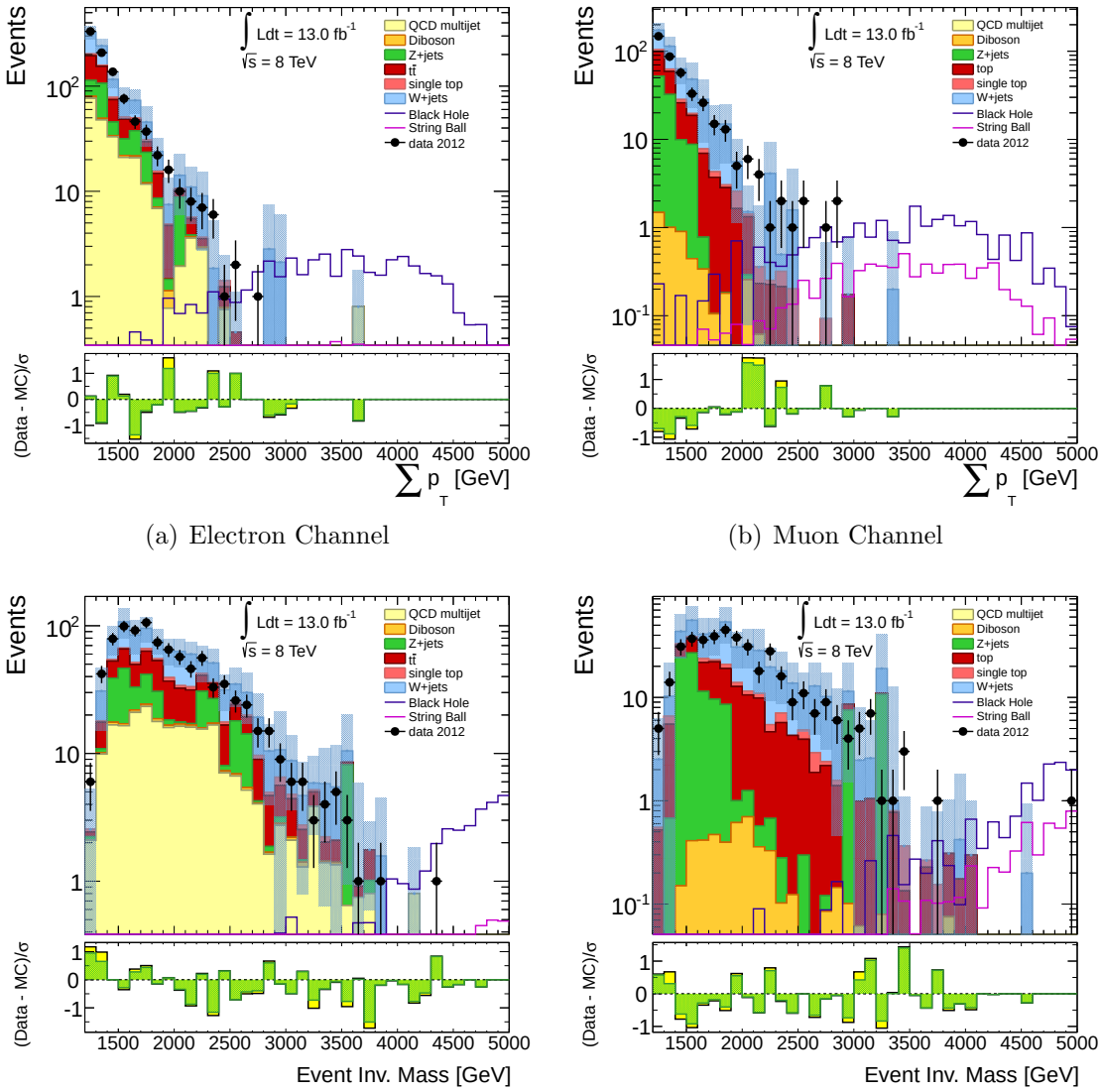

(a) Electron Channel

(b) Muon Channel

(c) Electron Channel

(d) Muon Channel

Figure 5.32. $\sum p_{\mathrm{T}}$ and event invariant mass distributions in the validation and signal regions, after the application of the scale factors. The Monte Carlo simulation is normalized to an integrated luminosity of 13.0 fb^{-1}. The error bars include both statistical and systematic uncertainties. The bottom pane of each subfigure displays the difference between data and predicted background over their statistical uncertainty (yellow band) or statistical+systematic uncertainties (green band). The corresponding distributions when using the alternate `Alpgen` generator for W/Z+jets are shown in App. H.

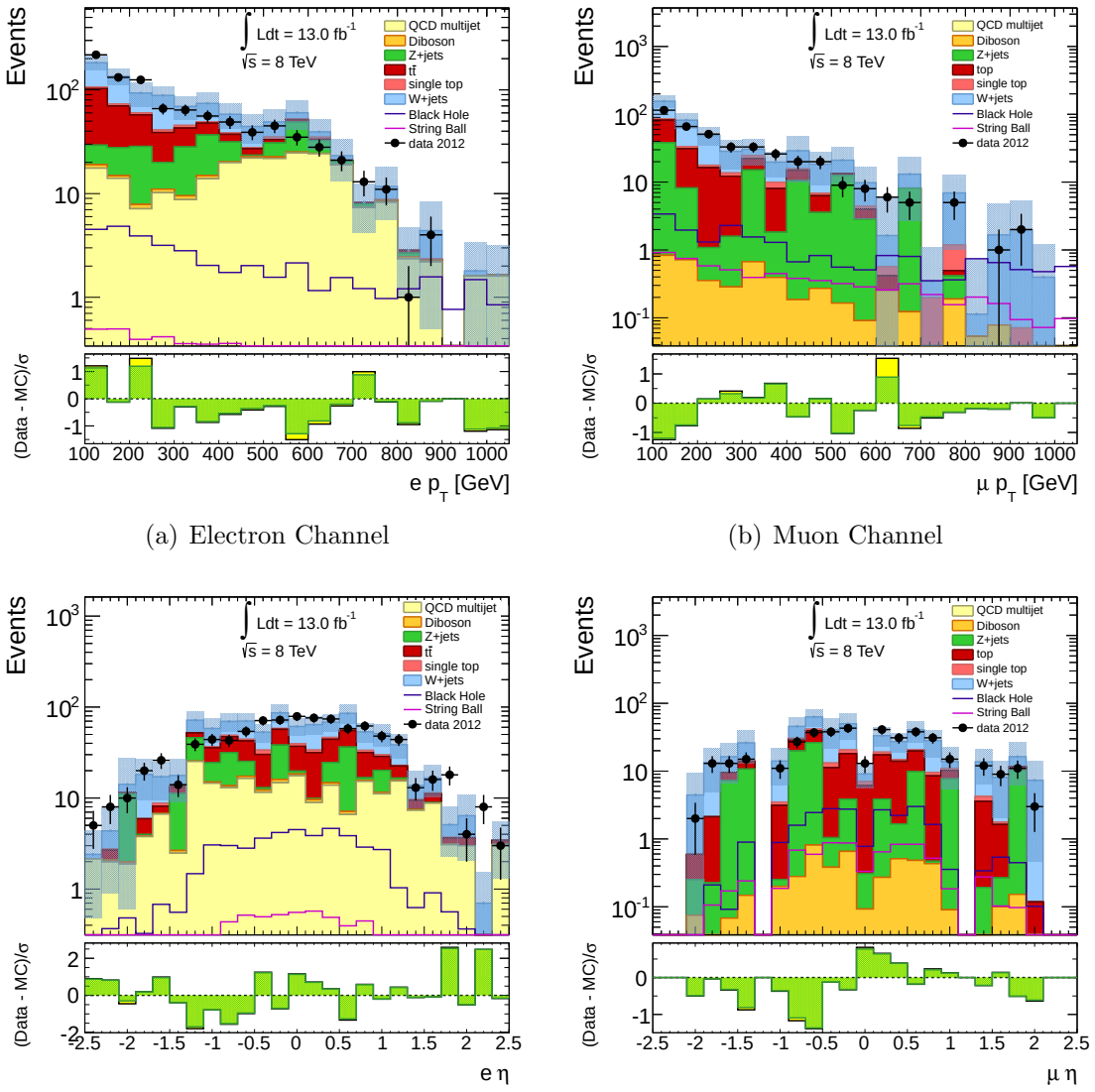

(a) Electron Channel

(b) Muon Channel

(c) Electron Channel

(d) Muon Channel

Figure 5.33. Leading lepton p_{T} and η distributions in the validation and signal regions, after the application of the scale factors. The Monte Carlo simulation is normalized to an integrated luminosity of 13.0 fb^{-1}. The error bars include both statistical and systematic uncertainties. The bottom pane of each subfigure displays the difference between data and predicted background over their statistical uncertainty (yellow band) or statistical+systematic uncertainties (green band).

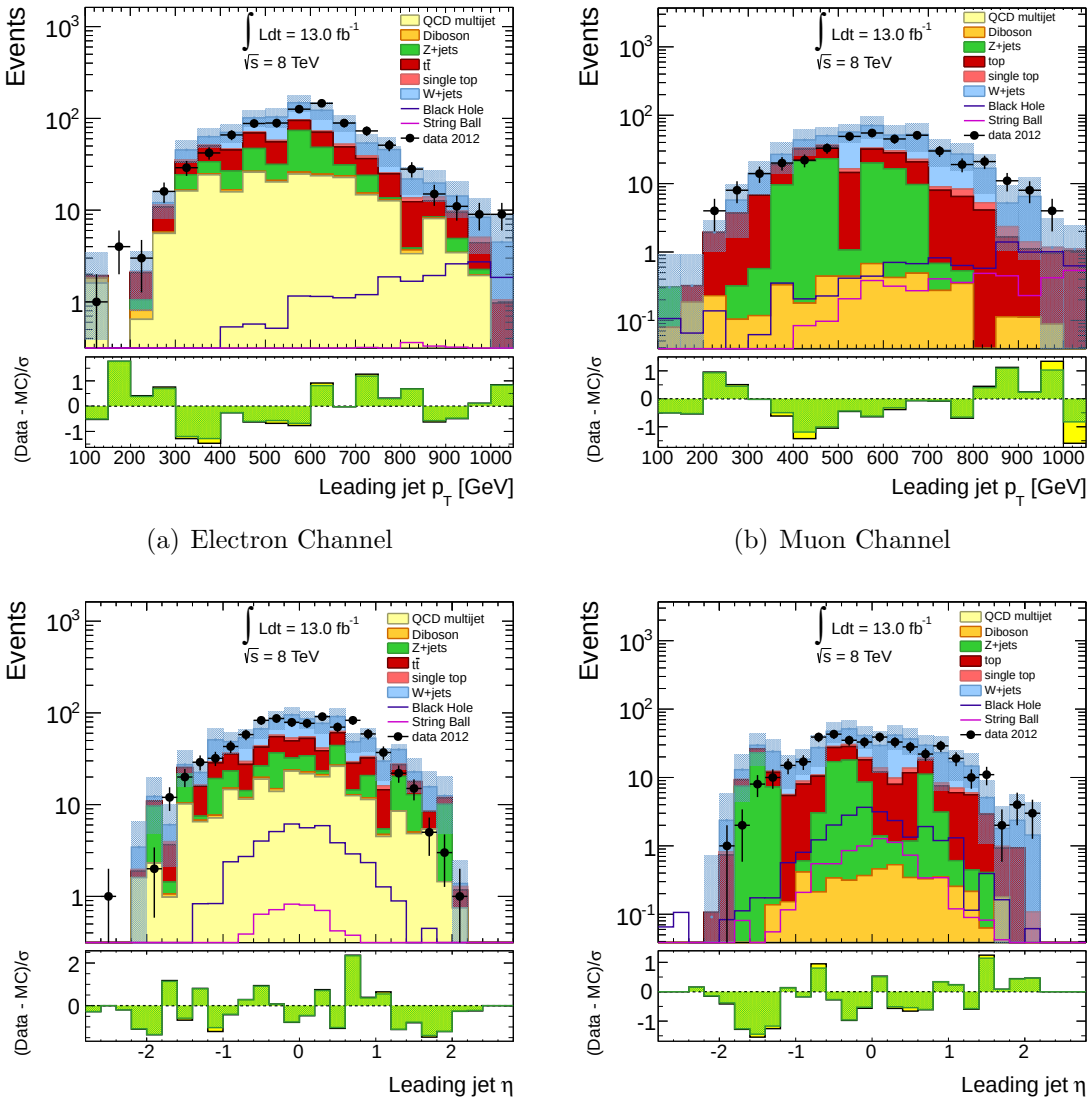

(a) Electron Channel

(b) Muon Channel

(c) Electron Channel

(d) Muon Channel

Figure 5.34. Leading jet p_{T} and η distributions in the validation and signal regions, after the application of the scale factors. The Monte Carlo simulation is normalized to an integrated luminosity of 13.0 fb^{-1}. The error bars include both statistical and systematic uncertainties. The bottom pane of each subfigure displays the difference between data and predicted background over their statistical uncertainty (yellow band) or statistical+systematic uncertainties (green band).

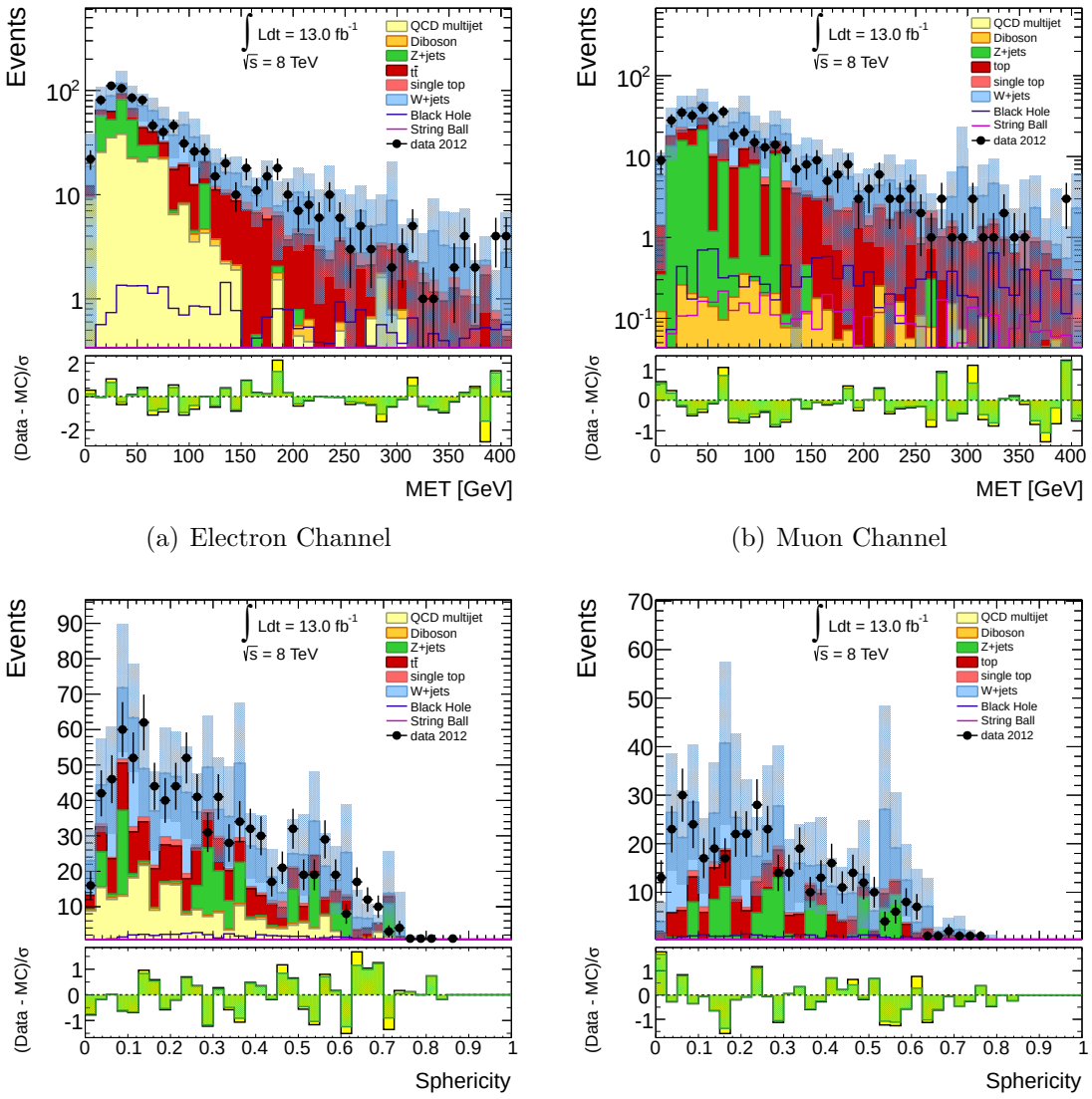

(a) Electron Channel

(b) Muon Channel

(c) Electron Channel

(d) Muon Channel

Figure 5.35. $E_{\mathrm{T}}^{\mathrm{miss}}$ and event sphericity distributions in the validation and signal regions, after the application of the scale factors. The Monte Carlo simulation is normalized to an integrated luminosity of 13.0 fb^{-1}. The error bars include both statistical and systematic uncertainties. The bottom pane of each subfigure displays the difference between data and predicted background over their statistical uncertainty (yellow band) or statistical+systematic uncertainties (green band).

Table 5.12. Background predictions and uncertainties in the signal region for the electron channel. Systematics variations are propagated through the whole analysis and a new prediction is derived. The difference from the nominal is taken as the systematic uncertainty. The observed and expected values correspond to an integrated luminosity of 13.0 fb^{-1}.

Systematics	qcd	diboson	z+jet	ttbar	singletop	W+jets	Total MC
Nominal	70.5 ± 18.4	3.0 ± 0.4	46.0 ± 16.8	47.2 ± 4.6	7.5 ± 1.0	92.2 ± 26.2	266.5 ± 36.5
JES Up	75.3 ± 17.8	3.3 ± 0.4	43.7 ± 15.6	46.6 ± 4.5	8.8 ± 1.1	86.0 ± 23.1	263.9 ± 33.4
JES Down	99.0 ± 21.2	2.5 ± 0.3	48.4 ± 17.9	45.7 ± 4.8	6.1 ± 0.8	89.1 ± 27.2	290.9 ± 39.5
JER	96.7 ± 20.0	3.0 ± 0.4	47.1 ± 17.1	49.5 ± 5.0	7.5 ± 1.0	79.0 ± 24.0	282.7 ± 36.0
b-tag Up	67.7 ± 18.8	3.0 ± 0.4	46.0 ± 16.8	38.3 ± 3.9	7.5 ± 1.0	104.0 ± 29.1	266.6 ± 38.7
b-tag Down	74.3 ± 18.1	3.0 ± 0.4	46.0 ± 16.8	59.0 ± 5.6	7.5 ± 1.0	76.5 ± 22.6	266.3 ± 34.0
EES Up	69.3 ± 18.5	3.1 ± 0.4	46.6 ± 17.0	47.2 ± 4.6	7.6 ± 1.0	96.0 ± 27.0	269.7 ± 37.2
EES Down	67.5 ± 18.3	2.9 ± 0.4	46.9 ± 17.1	46.8 ± 4.5	7.5 ± 0.9	90.0 ± 25.8	261.5 ± 36.3
EER Up	69.2 ± 18.3	2.9 ± 0.3	46.5 ± 17.0	47.6 ± 4.6	7.5 ± 1.0	90.9 ± 26.0	264.6 ± 36.4
EER Down	66.9 ± 12.3	3.0 ± 0.4	46.6 ± 17.0	47.0 ± 4.6	7.6 ± 1.0	92.3 ± 26.3	263.3 ± 36.6
Total	$70.5 \pm 18.4^{+39.1}_{-5.8}$	$3.0 \pm 0.4^{+0.3}_{-0.5}$	$46.0 \pm 16.8^{+2.9}_{-2.3}$	$47.2 \pm 4.6^{+12.1}_{-9.0}$	$7.5 \pm 1.0^{+1.3}_{-1.4}$	$92.2 \pm 26.2^{+12.4}_{-21.8}$	$266.5 \pm 36.5^{+29.6}_{-6.7}$

Table 5.13. Background predictions and uncertainties in the signal region for the muon channel. Systematics variations are propagated through the whole analysis and a new prediction is derived. The difference from the nominal is taken as the systematic uncertainty. The observed and expected values correspond to an integrated luminosity of 13.0 fb^{-1}.

Systematics	qcd	diboson	z+jet	ttbar	singletop	W+jets	Total MC
Nominal	< 0.6 (95% CL)	1.4 ± 0.2	8.8 ± 7.4	25.6 ± 3.3	4.2 ± 0.8	80.2 ± 30.4	120.3 ± 31.4
JES Up	< 0.6 (95% CL)	1.7 ± 0.3	8.4 ± 7.0	25.4 ± 3.3	4.9 ± 0.8	71.4 ± 26.0	111.8 ± 27.1
JES Down	< 0.6 (95% CL)	1.3 ± 0.2	9.0 ± 7.5	24.5 ± 3.2	3.9 ± 0.8	88.4 ± 35.6	127.1 ± 36.6
JER	< 0.6 (95% CL)	1.5 ± 0.2	8.9 ± 7.4	25.4 ± 3.3	4.4 ± 0.8	74.5 ± 28.4	122.2 ± 30.1
b-tag Up	< 0.6 (95% CL)	1.4 ± 0.2	8.8 ± 7.4	20.8 ± 2.8	4.2 ± 0.8	90.9 ± 34.0	126.1 ± 34.9
b-tag Down	< 0.6 (95% CL)	1.4 ± 0.2	8.8 ± 7.4	32.2 ± 4.0	4.2 ± 0.8	65.8 ± 25.6	112.4 ± 27.0
MS Up	< 0.6 (95% CL)	1.4 ± 0.2	8.8 ± 7.4	25.5 ± 3.3	4.2 ± 0.8	80.2 ± 30.3	120.1 ± 31.4
MS Down	< 0.6 (95% CL)	1.4 ± 0.2	8.8 ± 7.4	25.7 ± 3.3	4.2 ± 0.8	80.5 ± 30.4	120.6 ± 31.5
ID Up	< 0.6 (95% CL)	1.4 ± 0.2	8.8 ± 7.4	25.5 ± 3.3	4.2 ± 0.8	79.8 ± 30.2	119.8 ± 31.2
ID Down	< 0.6 (95% CL)	1.4 ± 0.2	8.6 ± 7.2	25.5 ± 3.3	4.2 ± 0.8	80.6 ± 30.4	120.3 ± 31.5
Total	< 0.6 (95% CL)	$1.4 \pm 0.2^{+0.3}_{-0.1}$	$8.8 \pm 7.4^{+0.2}_{-0.5}$	$25.6 \pm 3.3^{+6.5}_{-5.0}$	$4.2 \pm 0.8^{+0.7}_{-0.3}$	$80.2 \pm 30.4^{+13.4}_{-17.9}$	$120.3 \pm 31.4^{+9.1}_{-11.6}$

Table 5.14. Final background predictions and uncertainties in the signal region for the electron channel, for different $\sum p_{\mathrm{T}}$ thresholds. The observed and expected values correspond to an integrated luminosity of 13.0 fb^{-1}.

$\sum p_{\mathrm{T}}$ [GeV]	qcd	diboson	z+jet	ttbar	singletop	W+jets
> 1200	$227.7 \pm 56.3^{+126.3}_{-18.8}$	$8.9 \pm 0.6^{+1.2}_{-1.1}$	$147.8 \pm 33.1^{+2.0}_{-19.5}$	$204.6 \pm 18.0^{+51.6}_{-41.6}$	$23.6 \pm 1.7^{+3.6}_{-3.5}$	$338.2 \pm 59.6^{+44.2}_{-84.9}$
> 1500	$70.5 \pm 18.4^{+39.1}_{-5.8}$	$3.0 \pm 0.4^{+0.3}_{-0.5}$	$46.0 \pm 16.8^{+2.9}_{-2.3}$	$47.2 \pm 4.6^{+12.1}_{-9.0}$	$7.5 \pm 1.0^{+1.3}_{-1.4}$	$92.2 \pm 26.2^{+12.4}_{-21.8}$
> 2000	$9.4 \pm 3.7^{+5.2}_{-0.8}$	$0.4 \pm 0.1 \pm 0.1$	$7.0 \pm 6.3^{+0.2}_{-6.3}$	$4.9 \pm 0.9^{+1.3}_{-1.0}$	$0.7 \pm 0.2 \pm 0.3$	$21.1 \pm 10.9^{+2.7}_{-7.0}$

$\sum p_{\mathrm{T}}$ [GeV]	Total MC	Data
> 1200	$950.7 \pm 90.3^{+49.5}_{-36.9}$	909
> 1500	$266.5 \pm 36.5^{+29.6}_{-6.7}$	232
> 2000	$43.5 \pm 13.2^{+1.4}_{-7.2}$	35

Table 5.15. Final background predictions and uncertainties in the signal region for the muon channel, for different $\sum p_{\mathrm{T}}$ thresholds. The observed and expected values correspond to an integrated luminosity of 13.0 fb^{-1}.

$\sum p_{\mathrm{T}}$ [GeV]	qcd	diboson	z+jet	ttbar	singletop	W+jets
> 1200	< 0.6 (95% CL)	$4.8 \pm 0.4^{+0.3}_{-0.5}$	$99.6 \pm 30.0^{+17.0}_{-26.0}$	$115.7 \pm 13.0^{+29.5}_{-23.4}$	$15.7 \pm 1.6^{+3.1}_{-1.5}$	$235.9 \pm 51.7^{+38.1}_{-48.4}$
> 1500	< 0.6 (95% CL)	$1.4 \pm 0.2^{+0.3}_{-0.1}$	$8.8 \pm 7.4^{+0.2}_{-0.5}$	$25.6 \pm 3.3^{+6.5}_{-5.0}$	$4.2 \pm 0.8^{+0.7}_{-0.3}$	$80.2 \pm 30.4^{+13.4}_{-17.9}$
> 2000	< 0.6 (95% CL)	$0.3 \pm 0.1 \pm 0.1$	$0.4 \pm 0.7^{+0.01}_{-0.02}$	$1.8 \pm 0.5^{+0.6}_{-0.8}$	$0.7 \pm 0.2 \pm 0.1$	$5.7 \pm 5.6^{+1.4}_{-1.1}$

$\sum p_{\mathrm{T}}$ [GeV]	Total MC	Data
> 1200	$471.6 \pm 61.2^{+26.5}_{-20.1}$	403
> 1500	$120.3 \pm 31.4^{+9.1}_{-11.6}$	111
> 2000	$8.6 \pm 5.7^{+1.2}_{-0.6}$	19

5.4 Limit Setting

The Standard Model background estimates, shown in tables 5.14 and 5.15, are in good agreement with the observed data for all choices of $\sum p_{\mathrm{T}}$ threshold. No excess is observed beyond the SM expectation. Given the absence of any evidence for new physics processes, the data, expected background contributions, and their uncertainties are used to set model-independent exclusion limits on the fiducial cross section for non-SM production of states with high p_{T} leptons and jets, $\sigma_{\mathrm{fid}}(pp \to \ell^{\pm} X)$, as a function of minimum $\sum p_{\mathrm{T}}$.

To translate from an upper limit on the number of events $(\mathrm{N}_{S\,max})$[3] to a fiducial cross section, requires knowledge of the selection efficiency ϵ_{fid} from the true signal production in the fiducial region to the reconstructed one. The true fiducial region for the electron and muon channels is defined from simulated events with final states that pass the following requirements at generator level:

- a leading lepton with $p_{\mathrm{T}} > 100$ GeV;
- at least two more objects (leptons or jets) with $p_{\mathrm{T}} > 100$ GeV;
- $|\eta| < 2.47$ for electrons, 2.4 for muons and 2.8 for jets; and
- $\sum p_{\mathrm{T}}$ (of all leptons and jets with $p_{\mathrm{T}} > 60$ GeV) above the respective signal threshold.

Any additional selection not explicitly stated is considered part of the reconstruction efficiency.

---

[3]The setting of confidence limits for the signal rate in the presence of background is performed following the technique disclosed by Ref. [79]. The limits are computed by the method of profile likelihood which provides a general treatment of nuisance parameters with statistical and/or systematic errors, within a frequentist framework.

The technique of Ref. [79] comprises the combination of the particle likelihood approach with the large-sample approximation to the likelihood ratio (or $\ln \mathcal{L} + \frac{1}{2}$). It computes confidence intervals for a signal with a Poisson distribution, in the presence of a background with either a Poisson or Gaussian distribution and an efficiency with either a binomial or a Gaussian distribution. The method is very similar to the one used in MINUIT (MINOS) [80, 81]. It is implemented as a class, TRolke, in ROOT [82].

For the models considered, ϵ_{fid} ranges from 48-53% in the electron channel, and from 26-29% in the muon channel. For the derivation of upper limits on the fiducial cross section, the lowest observed efficiency for each channel is used for all signal region thresholds. The upper limits on the number of signal events and the fiducial cross section, at 95% confidence level, are shown in tables 5.16 and 5.17. For $\sum p_{\text{T}} >$ 2000 GeV, the observed 95% CL upper limit on the non-SM fiducial cross section is 3.3 fb in the electron channel and 7.0 fb in the muon channel. Due to limited statistics (and lower c.o.m. energy), the previous search described in Ref. [15] was unable to set limits at this $\sum p_{\text{T}}$ threshold. Thus, this analysis provides the first model-independent limits on $\sigma_{\text{fid}}(pp \to \ell^{\pm}X)$ at $\sum p_{\text{T}} > 2000$ GeV. Considering the highest $\sum p_{\text{T}}$ threshold accessible to Ref. [15], i.e. 1500 GeV, the current analysis provides stringent limits for the electron channel, but looser limits for the muon channel[4].

The observed counts of data events and background expectations in the signal region (for $\sum p_{\text{T}} > 2000$ GeV) are used to obtain model-dependent limits on the black hole production. For the models considered, the signal acceptance is highly model-dependent, driven primarily by the fraction of events containing a lepton in the final states. For the representative signal samples, it is about 7% for the electron channel and about 4% for the muon channel. The limit on the production cross section at a 95% CL, for a black hole with $M_{\text{D}} = 2.0$ TeV and $M_{\text{TH}} = 5.0$ TeV is $\sigma_{prod}(pp \to \text{BH}) = 33$ fb.

Table A.2 in the Appendix illustrates the signal samples available as a function of M_{D} with $M_{\text{TH}} = 5.0$ TeV, and their respective cross sections. In view of the aforementioned limit, about 50% of the samples are excluded at 95% CL. For the same M_{TH}, black holes with M_{D} values smaller or equal to 1.5 TeV are excluded.

[4]The observed $\sigma_{\text{fid}}(pp \to \ell^{\pm}X)$ at $\sum p_{\text{T}} > 1500$ GeV, as described in Ref. [15], is 12.8 fb in the electron channel and 11.0 fb in the muon channel.

Fixing M_{TH} at 5.0 TeV, this analysis excludes, at a 95% CL, M_{D} values up to the range between 1.5 TeV and 2.0 TeV, while for Ref. [15], said exclusion range is between 0.5 TeV and 1.0 TeV.

Table 5.16. Observed 95% CL upper limits on the fiducial cross sections $\sigma(pp \to \ell^{\pm}X)$ for the production of final states with at least 3 objects above a 100 GeV p_{T} requirement including at least one lepton, and $\sum p_{\mathrm{T}}$ above threshold, in the electron channel.

$\sum p_{\mathrm{T}}$ [GeV]	Total MC	Data	$N_{S_{max}}$ (95% CL)	$\sigma(pp \to \ell^{\pm}X)$ [fb]
> 1200	$950.7 \pm 90.3 \pm 43.2$	909	153	22
> 1500	$266.5 \pm 36.5 \pm 18.2$	232	50	7.2
> 2000	$43.5 \pm 13.2 \pm 4.3$	35	22	3.3
> 2500	$6.3 \pm 5.4 \pm 1.1$	3	10	1.6

Table 5.17. Observed 95% CL upper limits on the fiducial cross sections $\sigma(pp \to \ell^{\pm}X)$ for the production of final states with at least 3 objects above a 100 GeV p_{T} requirement including at least one lepton, and $\sum p_{\mathrm{T}}$ above threshold, in the muon channel.

$\sum p_{\mathrm{T}}$ [GeV]	Total MC	Data	$N_{S_{max}}$ (95% CL)	$\sigma(pp \to \ell^{\pm}X)$ [fb]
> 1200	$471.6 \pm 61.2 \pm 23.3$	403	66	19
> 1500	$120.3 \pm 31.4 \pm 10.4$	111	59	17
> 2000	$8.6 \pm 5.7 \pm 0.9$	19	25	7.0
> 2500	$0.5 \pm 0.4 \pm 0.4$	5	10	2.6

CHAPTER 6

CONCLUSIONS

Extensions to the Standard Model offer the possibility of observing gravitational effects at TeV-scale center-of-mass energies. This thesis presents a search for microscopic black hole and string ball states in ATLAS using a total integrated luminosity of 13.0 fb^{-1}. This search considers final states with three or more high transverse momentum objects, at least one of which is required to be an electron or a muon. No deviation from the Standard Model prediction was observed in either the electron or the muon channels. Consequently, limits are set on TeV-scale gravity models. For black holes with $M_{\mathrm{D}} = 2$ TeV and $M_{\mathrm{TH}} = 5$ TeV, the upper limit in the production cross section at 95% CL is 33 fb. Black hole models with $M_{\mathrm{D}} \leq 1.5$ TeV and $M_{\mathrm{TH}} = 5$ TeV are excluded. Model-independent upper limits, at 95% CL, are set on the effective cross section for new physics production of high-$\sum p_{\mathrm{T}}$ multi-object final states containing a high-p_{T} (> 100 GeV) isolated lepton inside experimental acceptance. For final states with $\sum p_{\mathrm{T}} > 2.0$ TeV, a limit of 3.3 fb in the electron channel and 7.0 fb in the muon channel is placed.

APPENDIX A

MONTE CARLO SIMULATED SAMPLES

A.1 Background Datasets

Table A.1: Monte Carlo simulated background samples, their cross sections and k-factors.

sample	Process	σ [pb]	kFactor
W+jets	Sherpa_CT10_WenuMassiveBPt0_BFilter	11030	1.105*0.0167
`Sherpa`	Sherpa_CT10_WmunuMassiveBPt0_BFilter	11030	1.105*0.0167
	Sherpa_CT10_WtaunuMassiveBPt0_BFilter	11028	1.105*0.0167
	Sherpa_CT10_WenuMassiveBPt0_VetoB	11028	1.105*0.98
	Sherpa_CT10_WmunuMassiveBPt0_VetoB	11030	1.105*0.98
	Sherpa_CT10_WtaunuMassiveBPt0_VetoB	11033	1.105*0.98
W+jets	AlpgenPythia_P2011C_WenuNp0	8136.80	1.143
`Alpgen`	AlpgenPythia_P2011C_WenuNp1	1791.50	1.143
	AlpgenPythia_P2011C_WenuNp2	541.600	1.143
	AlpgenPythia_P2011C_WenuNp3	146.650	1.143
	AlpgenPythia_P2011C_WenuNp4	37.2950	1.143
	AlpgenPythia_P2011C_WenuNp5	11.3690	1.143
	AlpgenPythia_P2011C_WmunuNp0	8133.40	1.143
	AlpgenPythia_P2011C_WmunuNp1	1792.70	1.143
	AlpgenPythia_P2011C_WmunuNp2	541.270	1.143
	AlpgenPythia_P2011C_WmunuNp3	146.490	1.143
	AlpgenPythia_P2011C_WmunuNp4	37.3340	1.143
	AlpgenPythia_P2011C_WmunuNp5	11.4140	1.143
	AlpgenPythia_P2011C_WtaunuNp0	8135.70	1.143
	AlpgenPythia_P2011C_WtaunuNp1	1793.70	1.143
	AlpgenPythia_P2011C_WtaunuNp2	541.240	1.143
	AlpgenPythia_P2011C_WtaunuNp3	146.480	1.143
	AlpgenPythia_P2011C_WtaunuNp4	37.2640	1.143
	AlpgenPythia_P2011C_WtaunuNp5	11.5370	1.143
	AlpgenPythia_P2011C_WbbNp0	52.2550	1.143
	AlpgenPythia_P2011C_WbbNp1	45.5400	1.143
	AlpgenPythia_P2011C_WbbNp2	23.6710	1.143
	AlpgenPythia_P2011C_WbbNp3	12.5250	1.143
	AlpgenPythia_P2011C_WcNp0	758.930	1.143
	AlpgenPythia_P2011C_WcNp1	274.240	1.143

Continued on next page

Table A.1 – continued from previous page

sample	Process	σ [pb]	kFactor
	AlpgenPythia_P2011C_WcNp2	71.6340	1.143
	AlpgenPythia_P2011C_WcNp3	16.4250	1.143
	AlpgenPythia_P2011C_WcNp4	4.74680	1.143
	AlpgenPythia_P2011C_WccNp0	143.070	1.143
	AlpgenPythia_P2011C_WccNp1	143.680	1.143
	AlpgenPythia_P2011C_WccNp2	80.7620	1.143
	AlpgenPythia_P2011C_WccNp3	35.9320	1.143
Z+jets	Sherpa_CT10_WenuMassiveBPt0_BFilter	11030	1.105*0.0167
`Sherpa`	Sherpa_CT10_ZeeLightJets	1051.2	1.0
	Sherpa_CT10_ZmumuLightJets	1052.3	1.0
	Sherpa_CT10_ZtautauLightJets	1051.3	1.0
	Sherpa_CT10_ZnunuLightJets	5679.8	1.0
	Sherpa_CT10_ZeeHeavyJets	58.78	1.0
	Sherpa_CT10_ZmumuHeavyJets	58.786	1.0
	Sherpa_CT10_ZtautauHeavyJets	58.794	1.0
	Sherpa_CT10_ZnunuHeavyJets	315.37	1.0
Z+jets	AlpgenPythia_P2011C_ZeeNp0	718.890	1.180
`Alpgen`	AlpgenPythia_P2011C_ZeeNp1	175.600	1.180
	AlpgenPythia_P2011C_ZeeNp2	58.8460	1.180
	AlpgenPythia_P2011C_ZeeNp3	15.5600	1.180
	AlpgenPythia_P2011C_ZeeNp4	3.93220	1.180
	AlpgenPythia_P2011C_ZeeNp5	1.19940	1.180
	AlpgenPythia_P2011C_ZmumuNp0	718.910	1.180
	AlpgenPythia_P2011C_ZmumuNp1	175.810	1.180
	AlpgenPythia_P2011C_ZmumuNp2	58.8050	1.180
	AlpgenPythia_P2011C_ZmumuNp3	15.5890	1.180
	AlpgenPythia_P2011C_ZmumuNp4	3.90720	1.180
	AlpgenPythia_P2011C_ZmumuNp5	1.19330	1.180
	AlpgenPythia_P2011C_ZtautauNp0	718.850	1.180
	AlpgenPythia_P2011C_ZtautauNp1	175.830	1.180
	AlpgenPythia_P2011C_ZtautauNp2	58.6300	1.180
	AlpgenPythia_P2011C_ZtautauNp3	15.5080	1.180
	AlpgenPythia_P2011C_ZtautauNp4	3.95260	1.180
	AlpgenPythia_P2011C_ZtautauNp5	1.18050	1.180
	AlpgenPythia_P2011C_ZeeccNp0	15.1070	1.180
	AlpgenPythia_P2011C_ZeeccNp1	7.21310	1.180
	AlpgenPythia_P2011C_ZeeccNp2	3.03200	1.180
	AlpgenPythia_P2011C_ZeeccNp3	1.17670	1.180
	AlpgenPythia_P2011C_ZmumuccNp0	15.1150	1.180
	AlpgenPythia_P2011C_ZmumuccNp1	7.19800	1.180
	AlpgenPythia_P2011C_ZmumuccNp2	3.03030	1.180
	AlpgenPythia_P2011C_ZmumuccNp3	1.17380	1.180
	AlpgenPythia_P2011C_ZtautauccNp0	15.1190	1.180
	AlpgenPythia_P2011C_ZtautauccNp1	7.20160	1.180

Continued on next page

Table A.1 – continued from previous page

sample	Process	σ [pb]	kFactor
	AlpgenPythia_P2011C_ZtautauccNp2	3.03850	1.180
	AlpgenPythia_P2011C_ZtautauccNp3	1.16770	1.180
	AlpgenPythia_P2011C_ZeebbNp0	8.03970	1.180
	AlpgenPythia_P2011C_ZeebbNp1	3.23530	1.180
	AlpgenPythia_P2011C_ZeebbNp2	1.13880	1.180
	AlpgenPythia_P2011C_ZeebbNp3	0.49066	1.180
	AlpgenPythia_P2011C_ZmumubbNp0	8.04220	1.180
	AlpgenPythia_P2011C_ZmumubbNp1	3.21550	1.180
	AlpgenPythia_P2011C_ZmumubbNp2	1.14000	1.180
	AlpgenPythia_P2011C_ZmumubbNp3	0.50943	1.180
	AlpgenPythia_P2011C_ZtautaubbNp0	8.03580	1.180
	AlpgenPythia_P2011C_ZtautaubbNp1	3.22990	1.180
	AlpgenPythia_P2011C_ZtautaubbNp2	1.14450	1.180
	AlpgenPythia_P2011C_ZtautaubbNp3	0.49266	1.180
$t\bar{t}$	PowhegPythia_CT10_ttbar_LeptonFilter	238.1*0.543	1
single t	McAtNloJimmy_CT10_SingleTopSChanWenu	0.56444	1.074
	McAtNloJimmy_CT10_SingleTopSChanWmunu	0.56426	1.074
	McAtNloJimmy_CT10_SingleTopSChanWtaunu	0.56404	1.074
	McAtNloJimmy_CT10_SingleTopWtChanIncl	20.6580	1.083
	AcerMCPythia_CTEQ6L1_singletop_tchan_e	8.604	1.10
	AcerMCPythia_CTEQ6L1_singletop_tchan_mu	8.604	1.10
	AcerMCPythia_CTEQ6L1_singletop_tchan_tau	8.604	1.10
diboson	Sherpa_CT10_llnunu_WW	5.4982	1.07
	Sherpa_CT10_lllnu_WZ	9.7534	1.06
	Sherpa_CT10_llll_ZZ	8.7356	1.11
	Sherpa_CT10_llnunu_ZZ	0.4962	1.14

A.2 Signal Datasets

Table A.2: Monte Carlo simulated signal black hole samples, their cross sections and k-factors.

M_{D} [TeV]	Process	σ [pb]	kFactor
1.5	Charybdis2Pythia8_MSTW2008LO_BH1_n6_Mth5_0	0.08939	1.0
	Charybdis2Pythia8_MSTW2008LO_BH2_n6_Mth5_0	0.08939	1.0
	BlackMaxPythia8_MSTW2008LO_BH2_n4_Mth5_0	0.052	1.0
	Charybdis2Pythia8_MSTW2008LO_BH6_n4_Mth5_0	0.05202	1.0
	Charybdis2Pythia8_MSTW2008LO_BH6_n6_Mth5_0	0.08939	1.0
	BlackMaxPythia8_MSTW2008LO_BH11_n4_Mth5_0	0.052	1.0
	BlackMaxPythia8_MSTW2008LO_BH11_n6_Mth5_0	0.08935	1.0

Continued on next page

Table A.2 – continued from previous page

M_{D} [TeV]	Process	σ [pb]	kFactor
2.0	Charybdis2Pythia8_MSTW2008LO_BH1_n6_Mth5_0	0.04631	1.0
	Charybdis2Pythia8_MSTW2008LO_BH2_n6_Mth5_0	0.04631	1.0
	BlackMaxPythia8_MSTW2008LO_BH2_n4_Mth5_0	0.026075	1.0
	Charybdis2Pythia8_MSTW2008LO_BH6_n4_Mth5_0	0.02608	1.0
	Charybdis2Pythia8_MSTW2008LO_BH6_n6_Mth5_0	0.04631	1.0
	BlackMaxPythia8_MSTW2008LO_BH11_n4_Mth5_0	0.026075	1.0
	BlackMaxPythia8_MSTW2008LO_BH11_n6_Mth5_0	0.046295	1.0
2.5	Charybdis2Pythia8_MSTW2008LO_BH1_n6_Mth5_0	0.02781	1.0
	Charybdis2Pythia8_MSTW2008LO_BH2_n6_Mth5_0	0.02781	1.0
	BlackMaxPythia8_MSTW2008LO_BH2_n4_Mth5_0	0.01526	1.0
	Charybdis2Pythia8_MSTW2008LO_BH6_n4_Mth5_0	0.01527	1.0
	Charybdis2Pythia8_MSTW2008LO_BH6_n6_Mth5_0	0.02781	1.0
	BlackMaxPythia8_MSTW2008LO_BH11_n4_Mth5_0	0.01526	1.0
	BlackMaxPythia8_MSTW2008LO_BH11_n6_Mth5_0	0.0278	1.0
3.0	Charybdis2Pythia8_MSTW2008LO_BH1_n4_Mth5_0	0.009856	1.0
	Charybdis2Pythia8_MSTW2008LO_BH1_n6_Mth5_0	0.01833	1.0
	Charybdis2Pythia8_MSTW2008LO_BH2_n4_Mth5_0	0.009856	1.0
	Charybdis2Pythia8_MSTW2008LO_BH2_n6_Mth5_0	0.01833	1.0
	BlackMaxPythia8_MSTW2008LO_BH2_n4_Mth5_0	0.0098525	1.0
	BlackMaxPythia8_MSTW2008LO_BH2_n6_Mth5_0	0.018325	1.0
	BlackMaxPythia8_MSTW2008LO_BH2_c1_n4_Mth5_0	0.0098525	1.0
	Charybdis2Pythia8_MSTW2008LO_BH2_n2_Mth5_0	0.003136	1.0
	Charybdis2Pythia8_MSTW2008LO_BH6_n4_Mth5_0	0.009856	1.0
	Charybdis2Pythia8_MSTW2008LO_BH6_n6_Mth5_0	0.01833	1.0
	BlackMaxPythia8_MSTW2008LO_BH11_n4_Mth5_0	0.0098525	1.0
	BlackMaxPythia8_MSTW2008LO_BH11_n6_Mth5_0	0.018325	1.0
3.5	Charybdis2Pythia8_MSTW2008LO_BH1_n6_Mth5_0	0.01289	1.0
	Charybdis2Pythia8_MSTW2008LO_BH2_n6_Mth5_0	0.01289	1.0
	BlackMaxPythia8_MSTW2008LO_BH2_n4_Mth5_0	0.006806	1.0
	Charybdis2Pythia8_MSTW2008LO_BH6_n4_Mth5_0	0.006808	1.0
	Charybdis2Pythia8_MSTW2008LO_BH6_n6_Mth5_0	0.01289	1.0
	BlackMaxPythia8_MSTW2008LO_BH11_n4_Mth5_0	0.006806	1.0
	BlackMaxPythia8_MSTW2008LO_BH11_n6_Mth5_0	0.01288	1.0
4.0	Charybdis2Pythia8_MSTW2008LO_BH1_n6_Mth5_0	0.009498	1.0
	Charybdis2Pythia8_MSTW2008LO_BH2_n6_Mth5_0	0.009498	1.0
	BlackMaxPythia8_MSTW2008LO_BH2_n4_Mth5_0	0.00494	1.0
	Charybdis2Pythia8_MSTW2008LO_BH6_n4_Mth5_0	0.004941	1.0
	Charybdis2Pythia8_MSTW2008LO_BH6_n6_Mth5_0	0.009498	1.0
	BlackMaxPythia8_MSTW2008LO_BH11_n4_Mth5_0	0.00494	1.0
	BlackMaxPythia8_MSTW2008LO_BH11_n6_Mth5_0	0.009494	1.0

Table A.3. Monte Carlo simulated signal string ball samples, their cross sections and k-factors. The string constant is set to 0.4.

M_s [TeV]	Process	σ [pb]	kFactor
0.8	Charybdis2Pythia8_MSTW2008LO_SB1_n6_Mth5_0	0.2228	1.0
	Charybdis2Pythia8_MSTW2008LO_SB2_n6_Mth5_0	0.2228	1.0
1.0	Charybdis2Pythia8_MSTW2008LO_SB1_n6_Mth5_0	0.007789	1.0
	Charybdis2Pythia8_MSTW2008LO_SB2_n6_Mth5_0	0.007789	1.0
1.2	Charybdis2Pythia8_MSTW2008LO_SB1_n6_Mth5_0	0.005216	1.0
	Charybdis2Pythia8_MSTW2008LO_SB2_n6_Mth5_0	0.005216	1.0
1.4	Charybdis2Pythia8_MSTW2008LO_SB1_n6_Mth5_0	0.003832	1.0
	Charybdis2Pythia8_MSTW2008LO_SB2_n6_Mth5_0	0.003832	1.0
1.6	Charybdis2Pythia8_MSTW2008LO_SB1_n6_Mth5_0	0.002934	1.0
	Charybdis2Pythia8_MSTW2008LO_SB2_n6_Mth5_0	0.002934	1.0
1.8	Charybdis2Pythia8_MSTW2008LO_SB1_n6_Mth5_0	0.002318	1.0
	Charybdis2Pythia8_MSTW2008LO_SB2_n6_Mth5_0	0.002318	1.0

APPENDIX B

BACKGROUND DISTRIBUTIONS: Z+JETS

B.1 Distributions After the Application of SFs (Sherpa)

The following distributions correspond to Figs. 5.1-5.4, after the application of the scale factors calculated in Sec. 5.1.1, for the Z+jets samples generated with Sherpa.

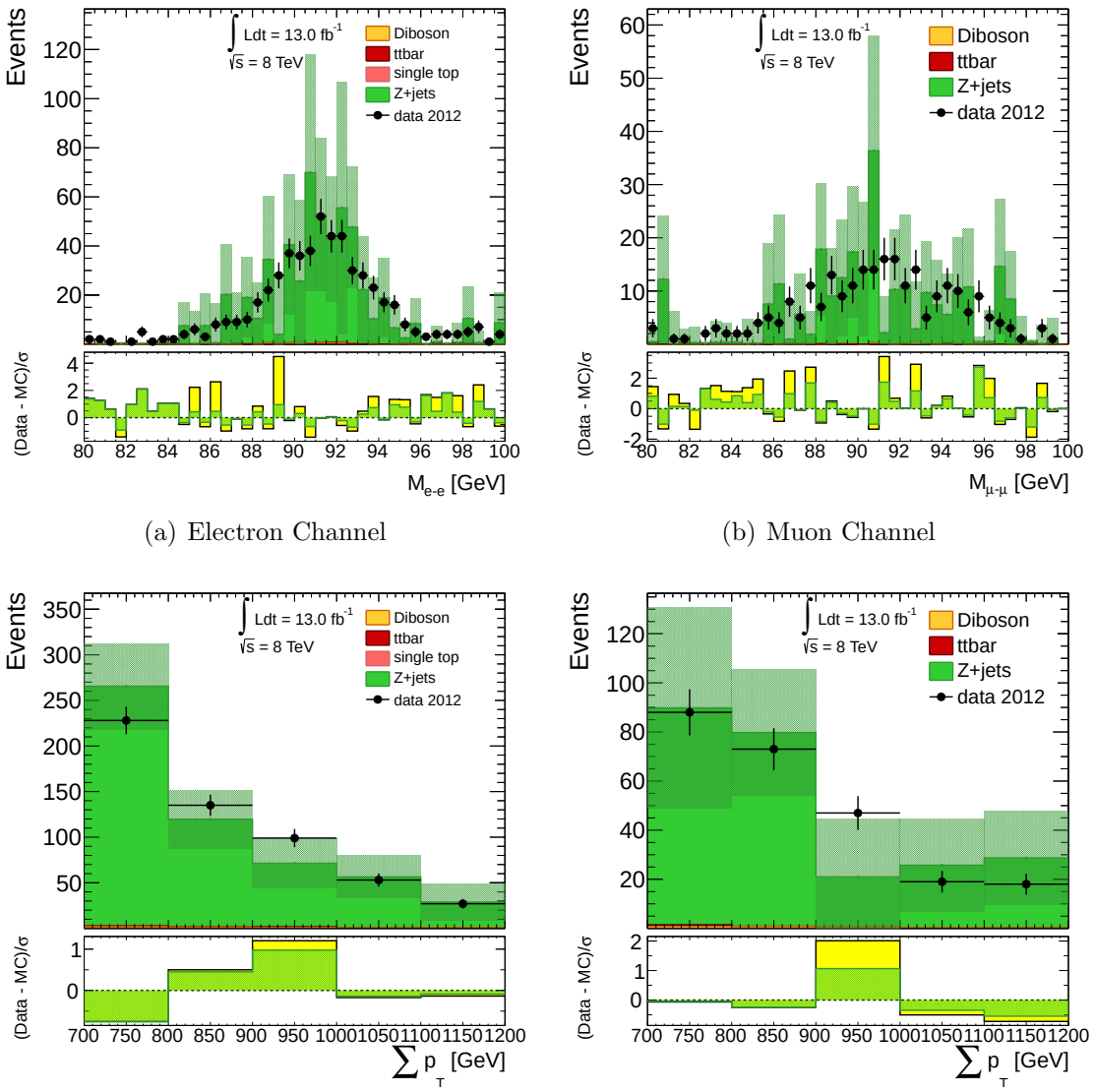

(a) Electron Channel

(b) Muon Channel

(c) Electron Channel

(d) Muon Channel

Figure B.1. Dilepton invariant mass and $\sum p_{\mathrm{T}}$ distributions in the Z+jets CR, after the application of the scale factor. The Monte Carlo simulation is normalized to an integrated luminosity of 13.0 fb[1]. The error bars include both statistical and systematic uncertainties. The bottom pane of each subfigure displays the difference between data and simulation over their statistical uncertainty (yellow band) or statistical+systematic uncertainties (green band).

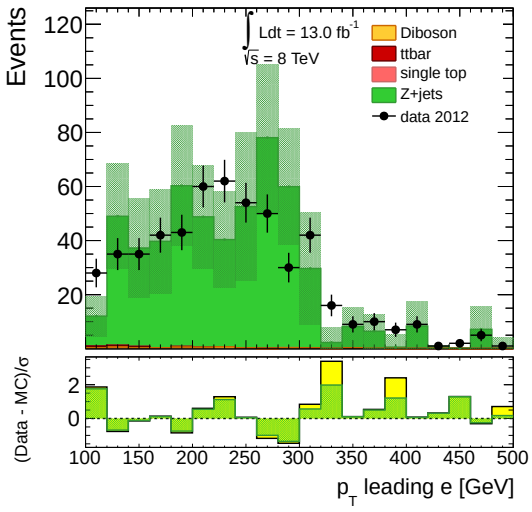

(a) Electron Channel

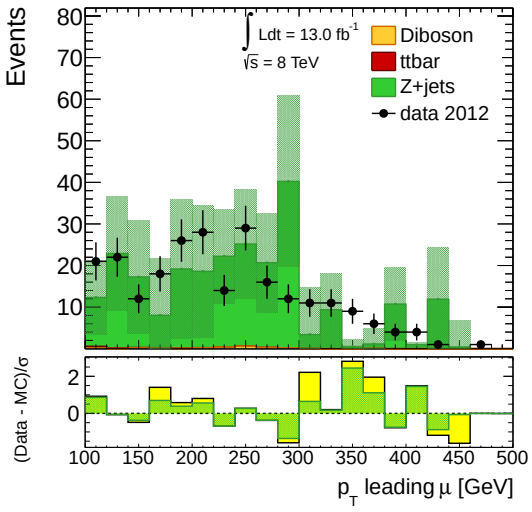

(b) Muon Channel

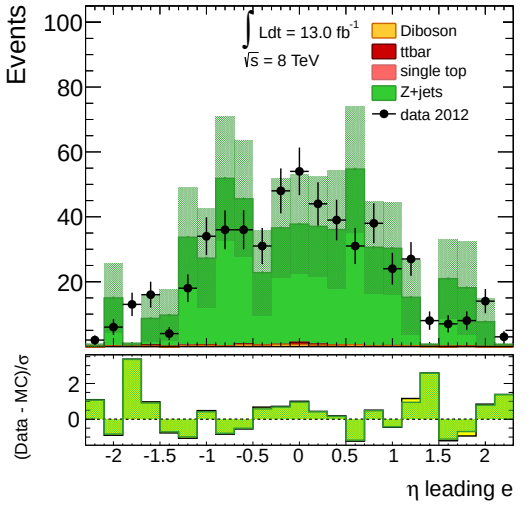

(c) Electron Channel

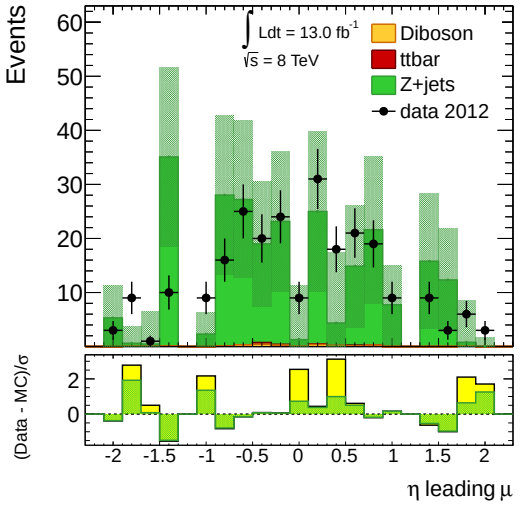

(d) Muon Channel

Figure B.2. Leading lepton p_{T} and η distributions in the Z+jets CR, after the application of the scale factor. The Monte Carlo simulation is normalized to an integrated luminosity of 13.0 fb^1. The error bars include both statistical and systematic uncertainties. The bottom pane of each subfigure displays the difference between data and simulation over their statistical uncertainty (yellow band) or statistical+systematic uncertainties (green band).

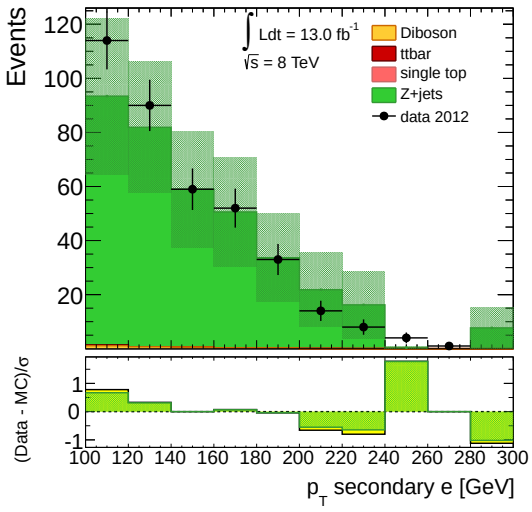

(a) Electron Channel

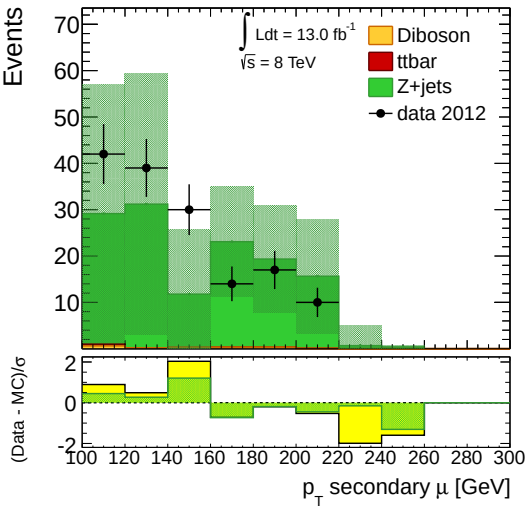

(b) Muon Channel

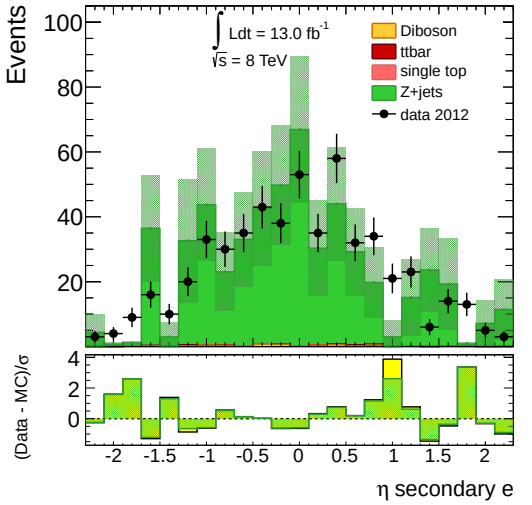

(c) Electron Channel

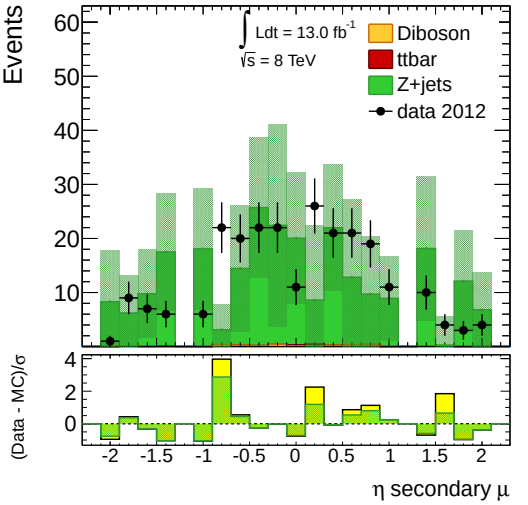

(d) Muon Channel

Figure B.3. Secondary lepton p_{T} and η distributions in the Z+jets CR, after the application of the scale factor. The Monte Carlo simulation is normalized to an integrated luminosity of 13.0 fb[1]. The error bars include both statistical and systematic uncertainties. The bottom pane of each subfigure displays the difference between data and simulation over their statistical uncertainty (yellow band) or statistical+systematic uncertainties (green band).

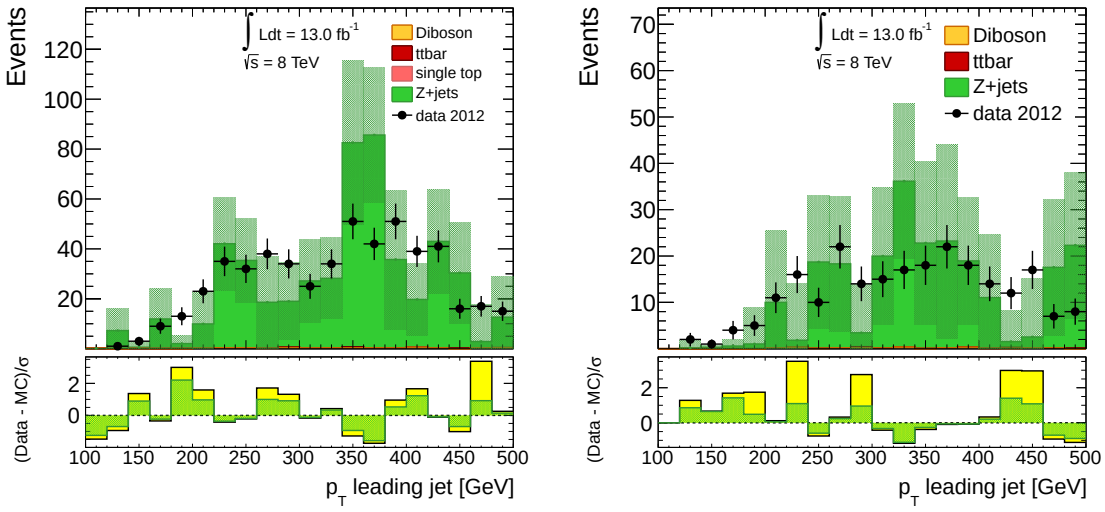

(a) Electron Channel

(b) Muon Channel

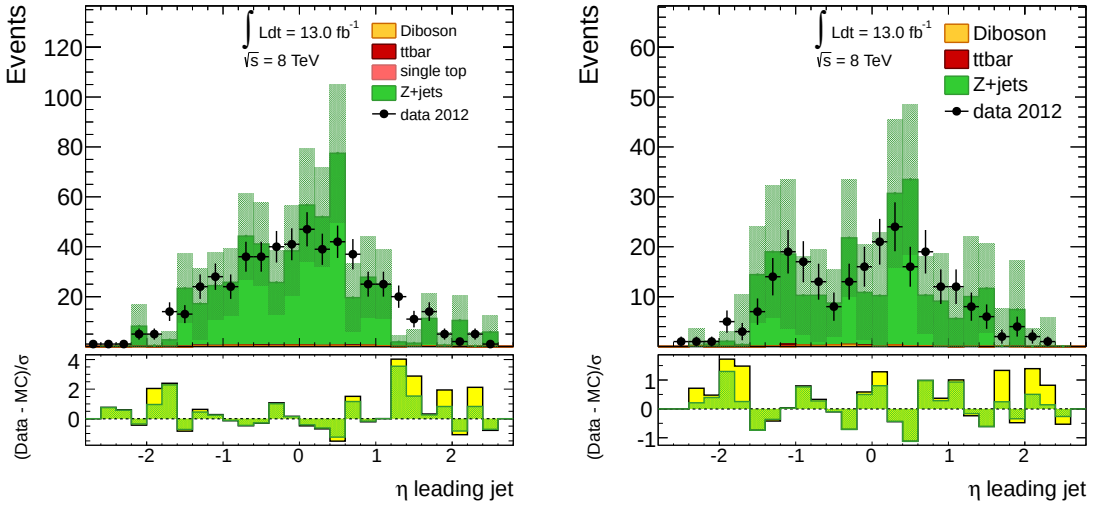

(c) Electron Channel

(d) Muon Channel

Figure B.4. Leading jet p_{T} and η distributions in the Z+jets CR, after the application of the scale factor. The Monte Carlo simulation is normalized to an integrated luminosity of 13.0 fb[1]. The error bars include both statistical and systematic uncertainties. The bottom pane of each subfigure displays the difference between data and simulation over their statistical uncertainty (yellow band) or statistical+systematic uncertainties (green band).

B.2 Distributions for the `Alpgen` Generator

The following distributions correspond to Figs. 5.1-5.4 and App. B.1 for Z+jets samples generated with `Alpgen`. The histograms are shown before and after the application of the derived scale factor.

The obtained values for the Z+jets scale factors for the different channels are

$$\mathrm{SF(electron)} = 0.590 \pm 0.037^{+0.038}_{-0.013}$$

$$\mathrm{SF(muon)} = 0.674 \pm 0.066^{+0.053}_{-0.039}.$$

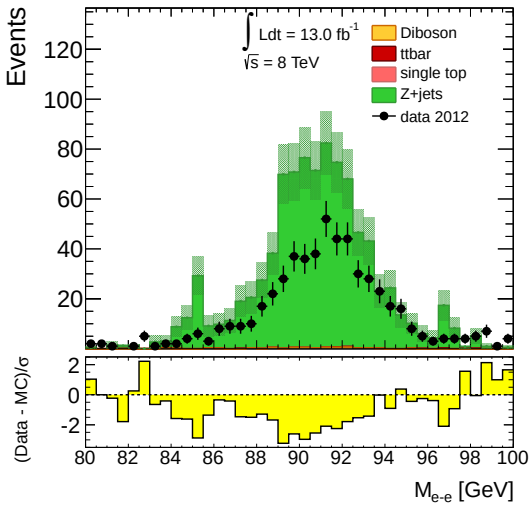

(a) Electron Channel, no SFs applied

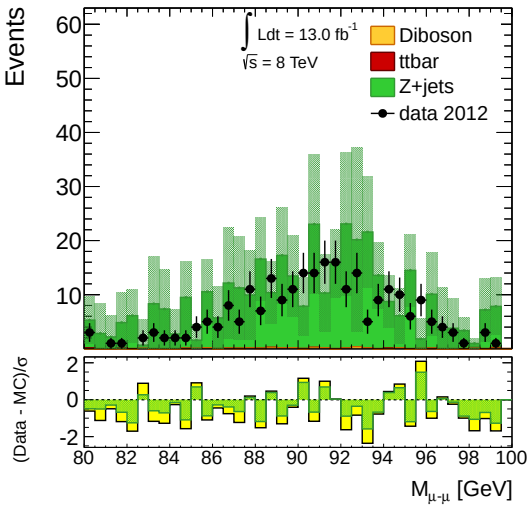

(b) Muon Channel, no SFs applied

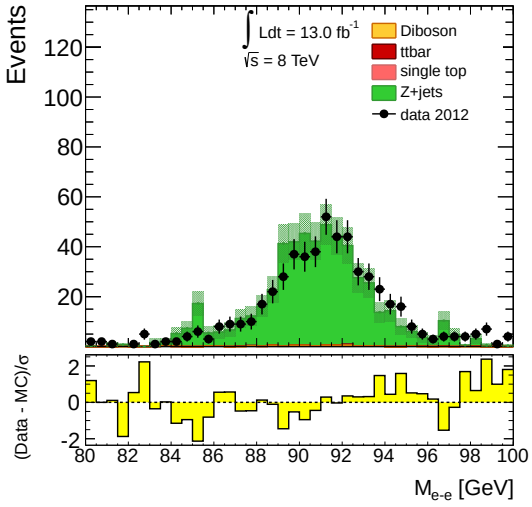

(c) Electron Channel, SFs applied

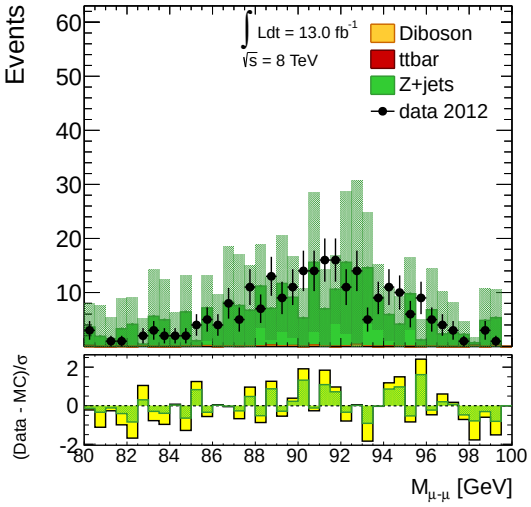

(d) Muon Channel, SFs applied

Figure B.5. Dilepton invariant mass distributions in the Z+jets CR, before and after the application of the scale factor. The Monte Carlo simulation is normalized to an integrated luminosity of 13.0 fb[1]. The error bars include both statistical and systematic uncertainties. The bottom pane of each subfigure displays the difference between data and simulation over their statistical uncertainty (yellow band) or statistical+systematic uncertainties (green band).

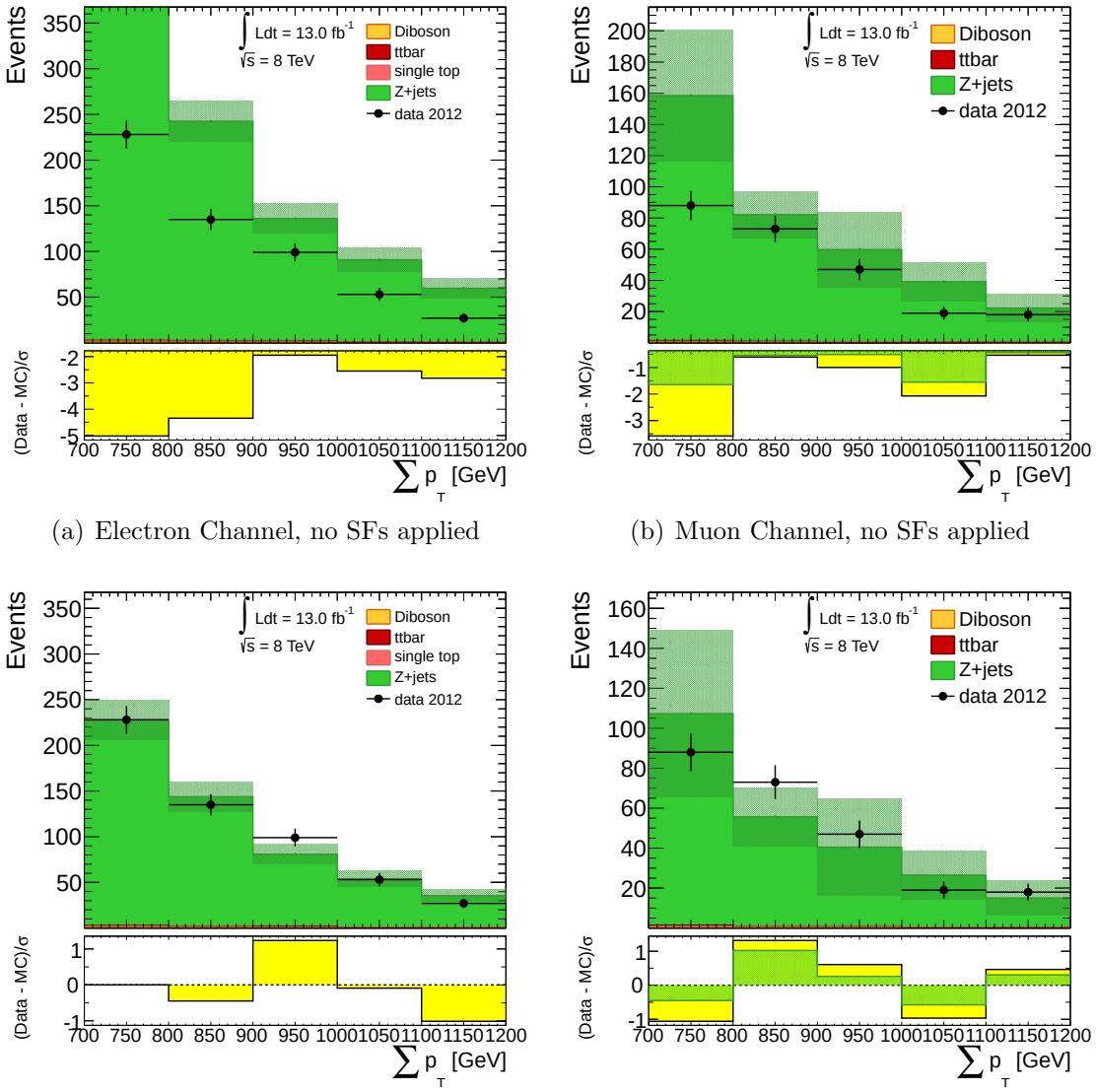

(a) Electron Channel, no SFs applied

(b) Muon Channel, no SFs applied

(c) Electron Channel, SFs applied

(d) Muon Channel, SFs applied

Figure B.6. $\sum p_{\mathrm{T}}$ distributions in the Z+jets CR, before and after the application of the scale factor. The Monte Carlo simulation is normalized to an integrated luminosity of 13.0 fb^{1}. The error bars include both statistical and systematic uncertainties. The bottom pane of each subfigure displays the difference between data and simulation over their statistical uncertainty (yellow band) or statistical+systematic uncertainties (green band).

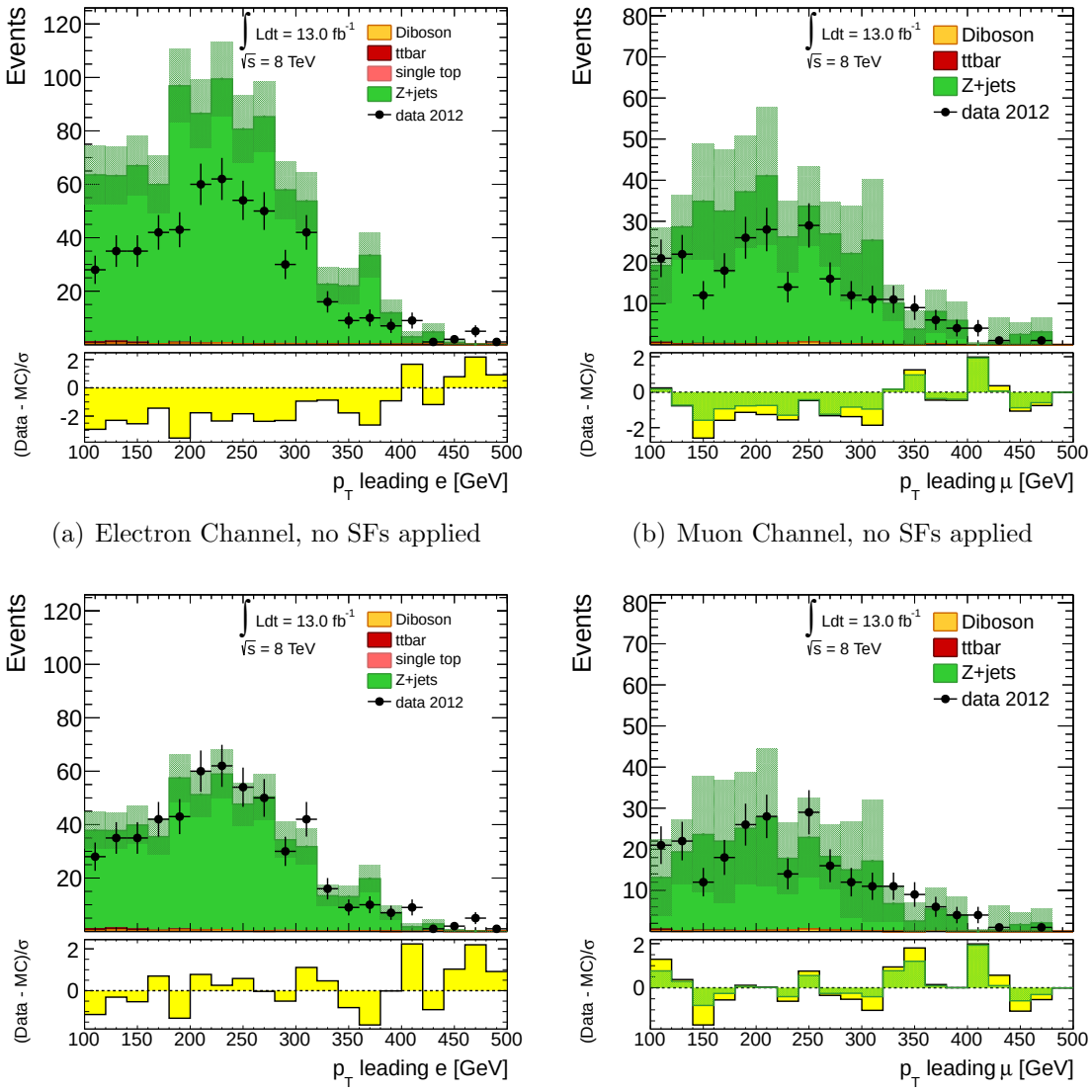

(a) Electron Channel, no SFs applied

(b) Muon Channel, no SFs applied

(c) Electron Channel, SFs applied

(d) Muon Channel, SFs applied

Figure B.7. Leading lepton p_{T} distributions in the Z+jets CR, before and after the application of the scale factor. The Monte Carlo simulation is normalized to an integrated luminosity of 13.0 fb[1]. The error bars include both statistical and systematic uncertainties. The bottom pane of each subfigure displays the difference between data and simulation over their statistical uncertainty (yellow band) or statistical+systematic uncertainties (green band).

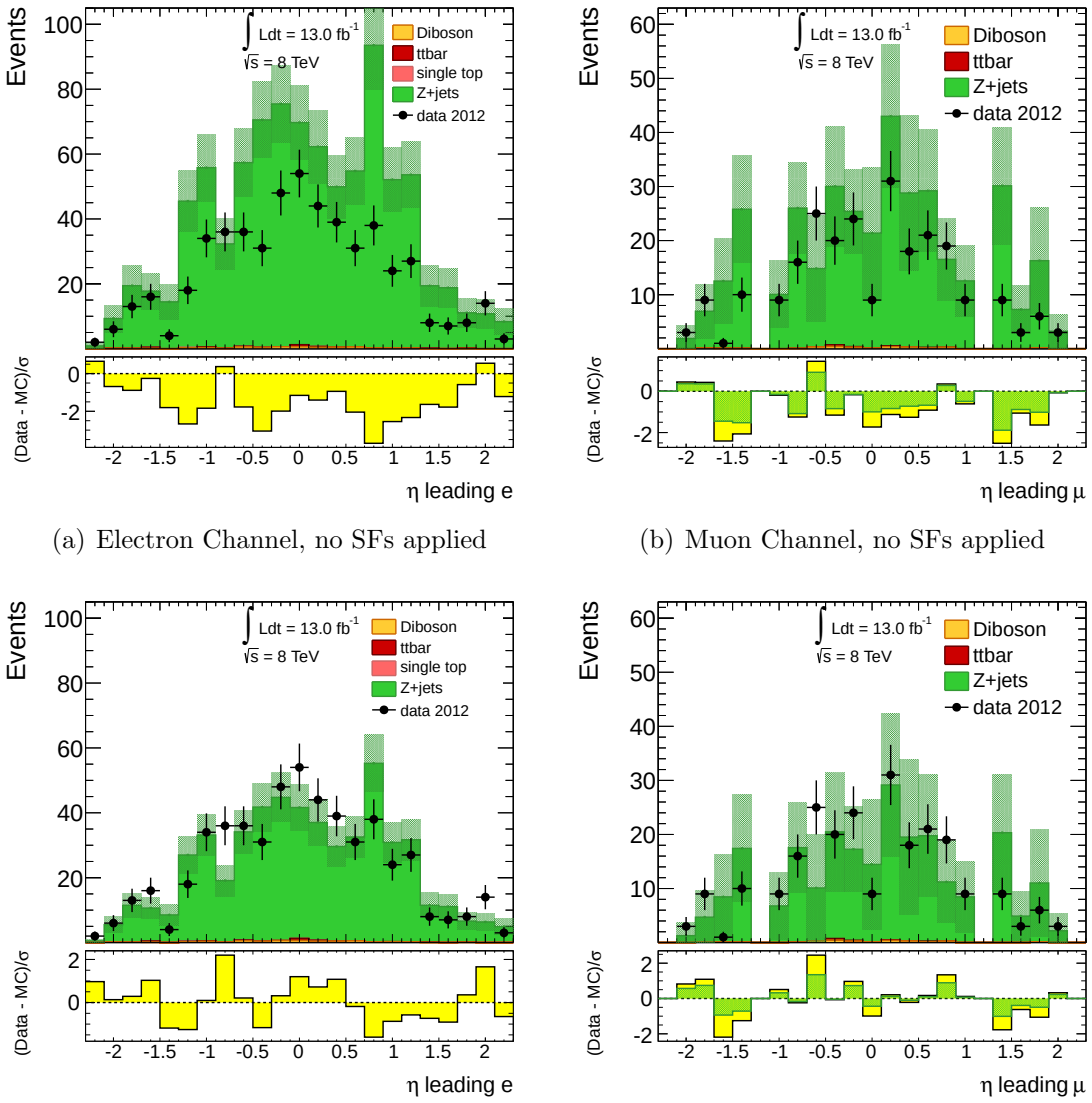

(a) Electron Channel, no SFs applied

(b) Muon Channel, no SFs applied

(c) Electron Channel, SFs applied

(d) Muon Channel, SFs applied

Figure B.8. Leading lepton η distributions in the Z+jets CR, before and after the application of the scale factor. The Monte Carlo simulation is normalized to an integrated luminosity of 13.0 fb[1]. The error bars include both statistical and systematic uncertainties. The bottom pane of each subfigure displays the difference between data and simulation over their statistical uncertainty (yellow band) or statistical+systematic uncertainties (green band).

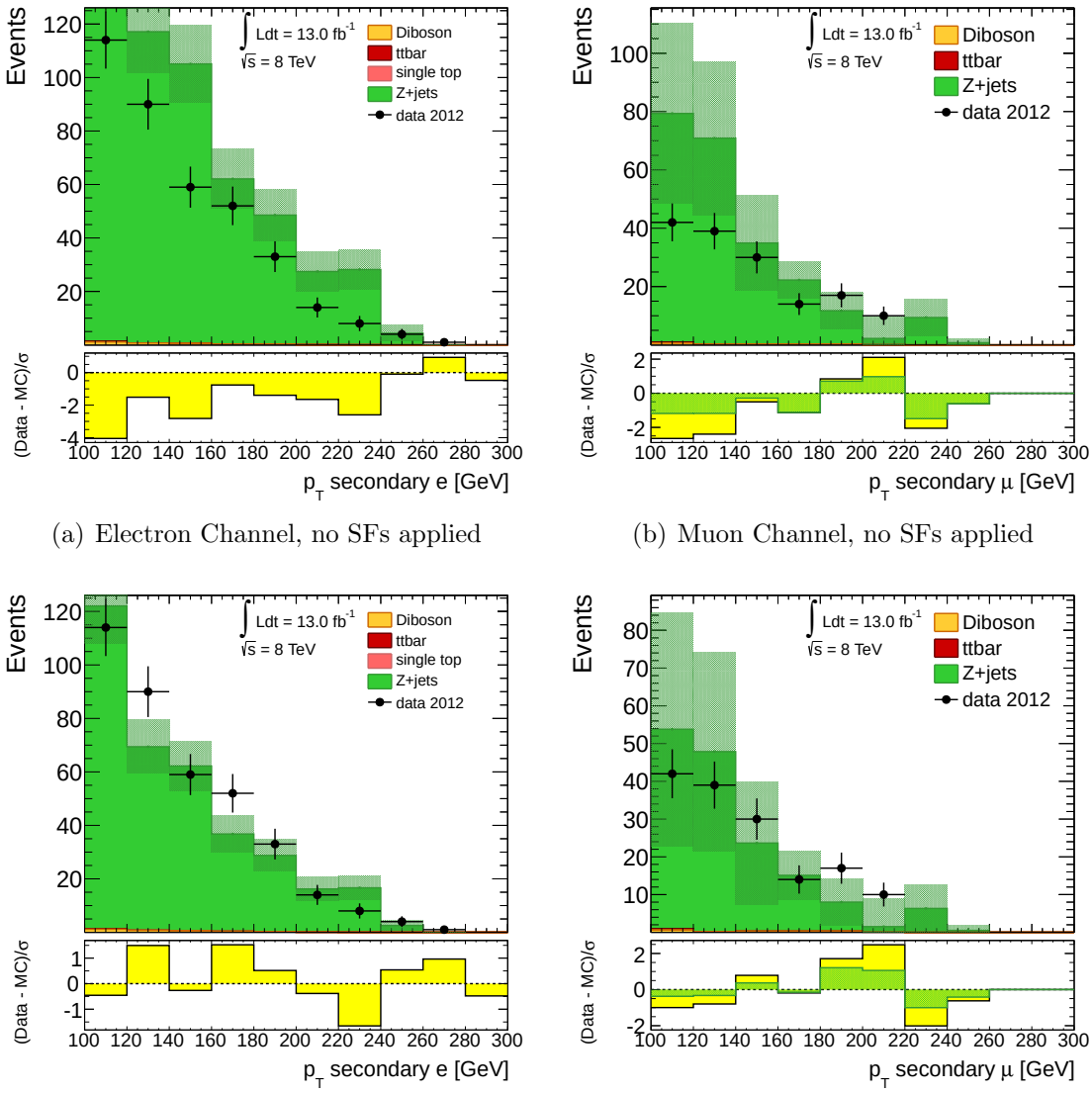

(a) Electron Channel, no SFs applied

(b) Muon Channel, no SFs applied

(c) Electron Channel, SFs applied

(d) Muon Channel, SFs applied

Figure B.9. Secondary lepton p_{T} distributions in the Z+jets CR, before and after the application of the scale factor. The Monte Carlo simulation is normalized to an integrated luminosity of 13.0 fb[1]. The error bars include both statistical and systematic uncertainties. The bottom pane of each subfigure displays the difference between data and simulation over their statistical uncertainty (yellow band) or statistical+systematic uncertainties (green band).

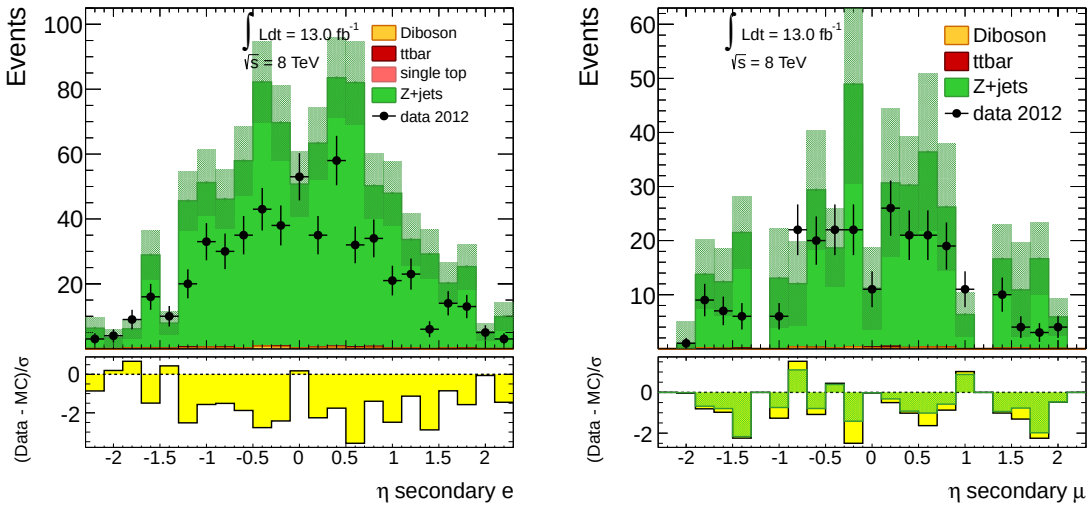

(a) Electron Channel, no SFs applied

(b) Muon Channel, no SFs applied

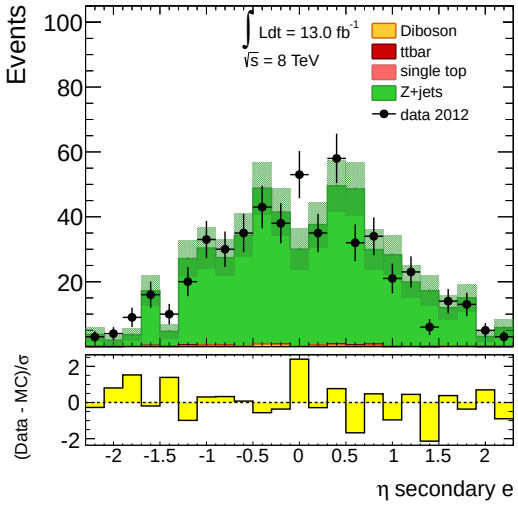

(c) Electron Channel, SFs applied

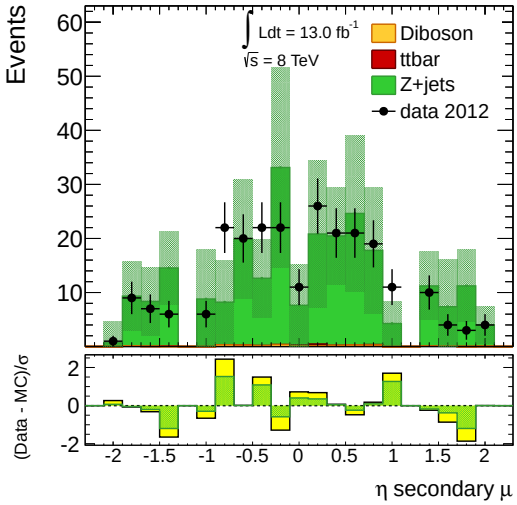

(d) Muon Channel, SFs applied

Figure B.10. Secondary lepton η distributions in the Z+jets CR, before and after the application of the scale factor. The Monte Carlo simulation is normalized to an integrated luminosity of 13.0 fb[1]. The error bars include both statistical and systematic uncertainties. The bottom pane of each subfigure displays the difference between data and simulation over their statistical uncertainty (yellow band) or statistical+systematic uncertainties (green band).

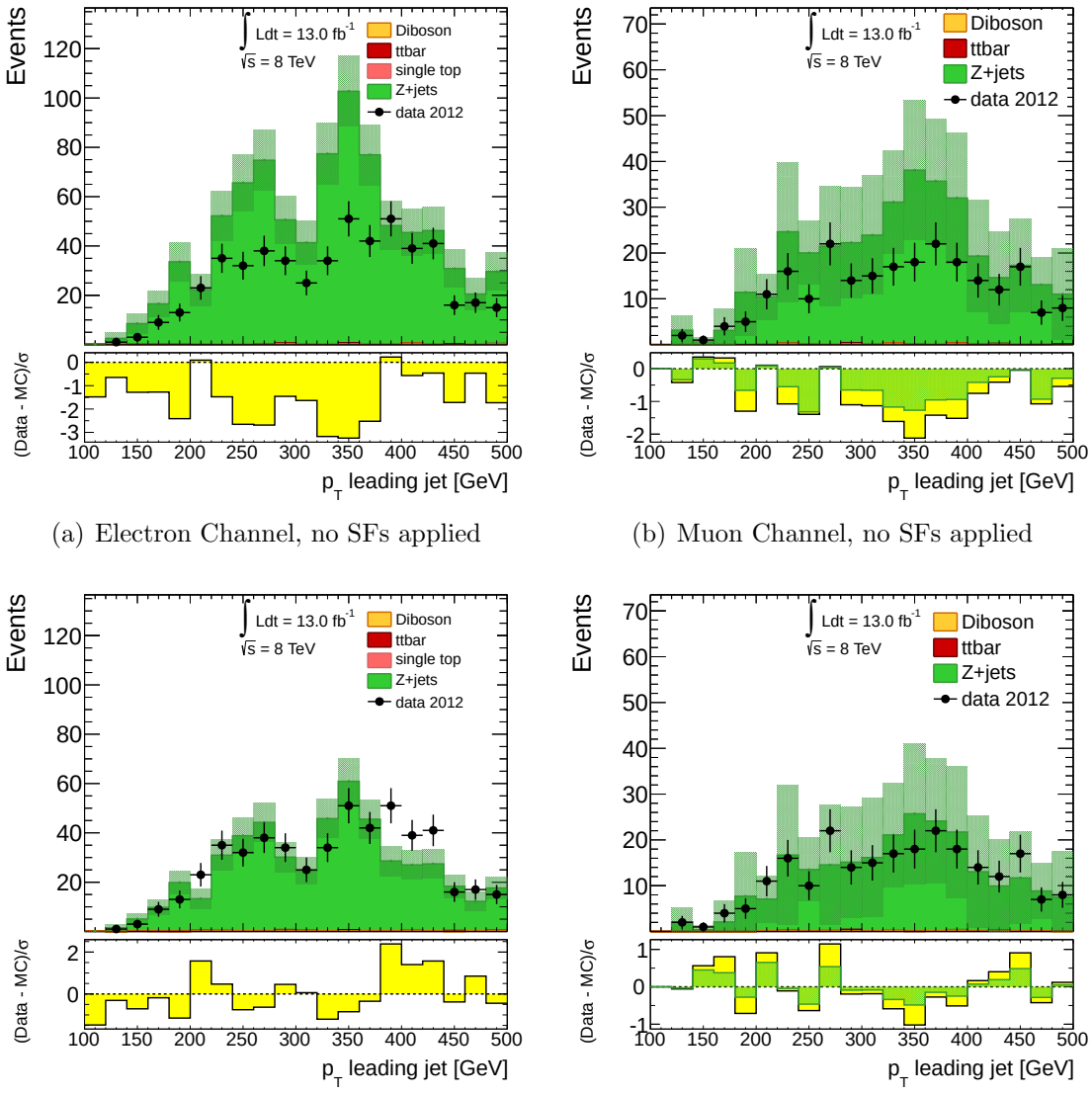

(a) Electron Channel, no SFs applied

(b) Muon Channel, no SFs applied

(c) Electron Channel, SFs applied

(d) Muon Channel, SFs applied

Figure B.11. Leading jet p_{T} distributions in the Z+jets CR, before and after the application of the scale factor. The Monte Carlo simulation is normalized to an integrated luminosity of 13.0 fb[1]. The error bars include both statistical and systematic uncertainties. The bottom pane of each subfigure displays the difference between data and simulation over their statistical uncertainty (yellow band) or statistical+systematic uncertainties (green band).

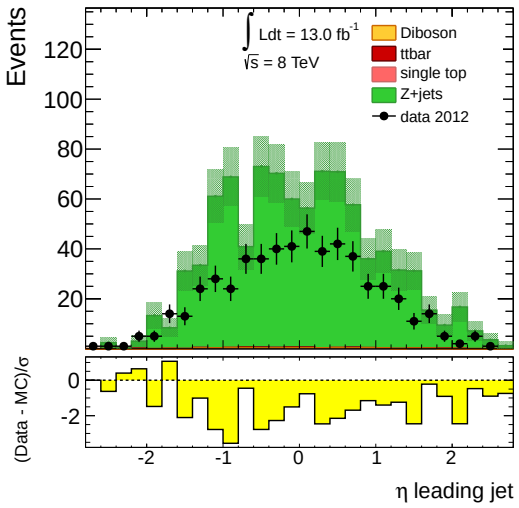

(a) Electron Channel, no SFs applied

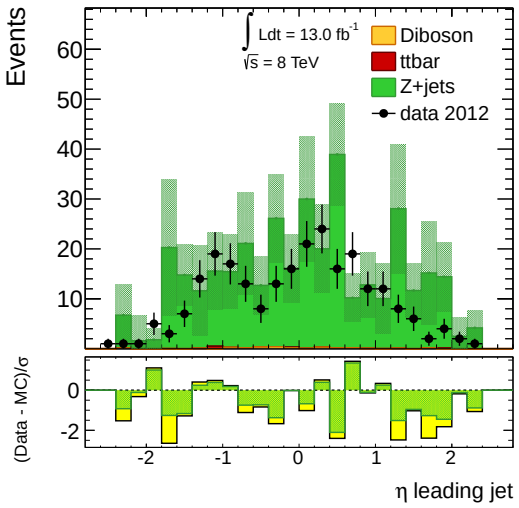

(b) Muon Channel, no SFs applied

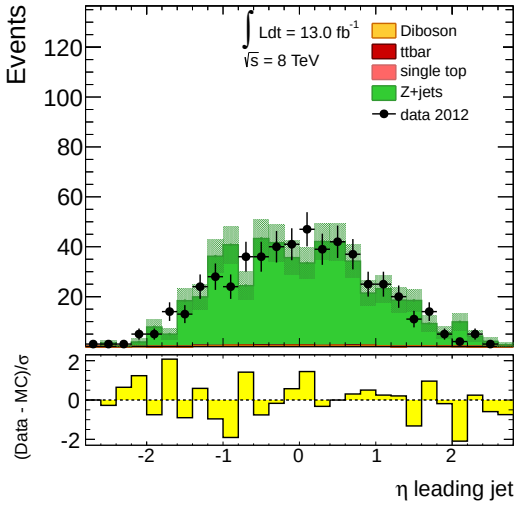

(c) Electron Channel, SFs applied

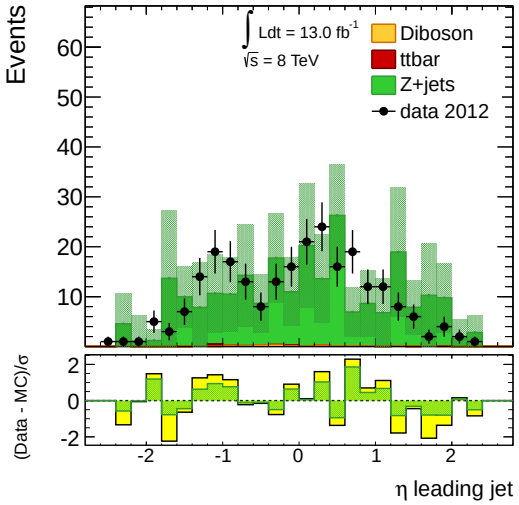

(d) Muon Channel, SFs applied

Figure B.12. Leading jet η distributions in the Z+jets CR, before and after the application of the scale factor. The Monte Carlo simulation is normalized to an integrated luminosity of 13.0 fb^1. The error bars include both statistical and systematic uncertainties. The bottom pane of each subfigure displays the difference between data and simulation over their statistical uncertainty (yellow band) or statistical+systematic uncertainties (green band).

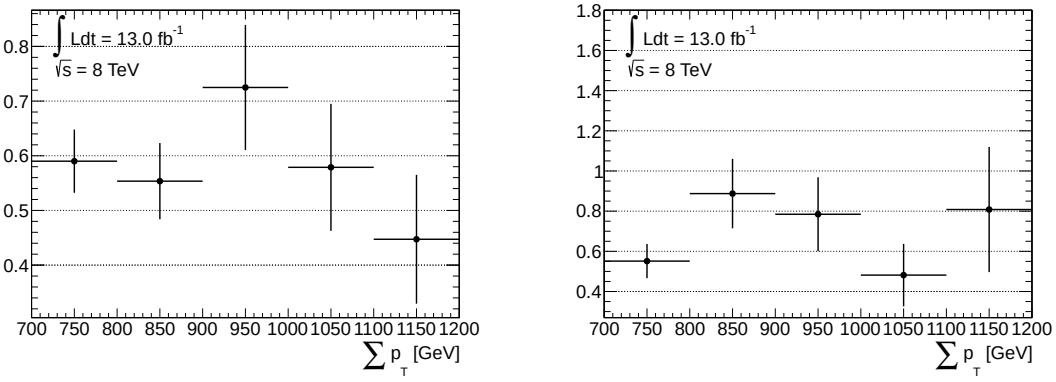

(a) Electron Channel (b) Muon Channel

Figure B.13. Z+jets scale factor as a function of $\sum p_{\mathrm{T}}$ for samples generated with `Alpgen`.

APPENDIX C

BACKGROUND DISTRIBUTIONS: TTBAR

C.1 Distributions After the Application of SFs (Sherpa)

The following distributions correspond to Figs. 5.7-5.10, after the application of the scale factors calculated in Sec. 5.1.2, for the $t\bar{t}$ samples generated with Sherpa.

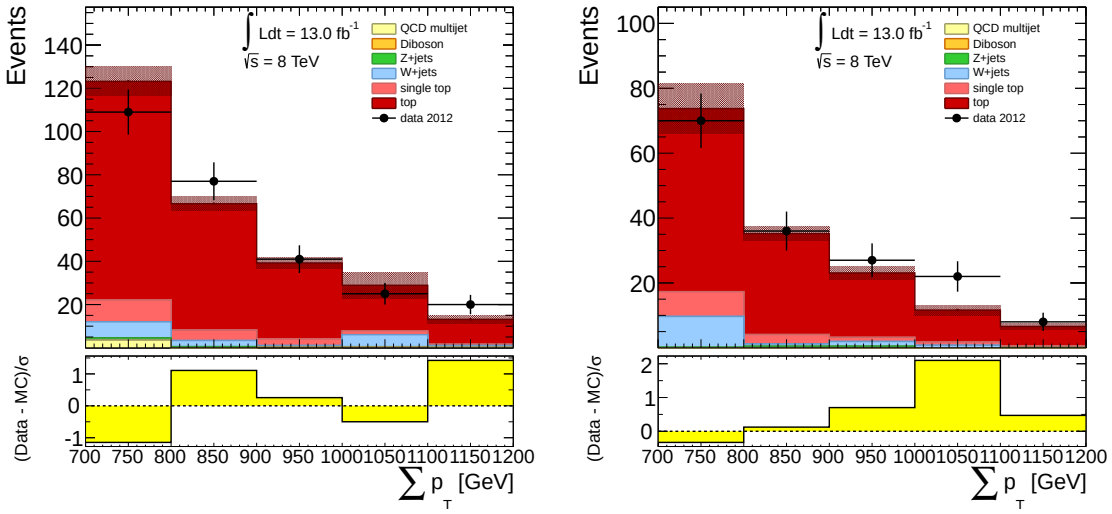

(a) Electron Channel

(b) Muon Channel

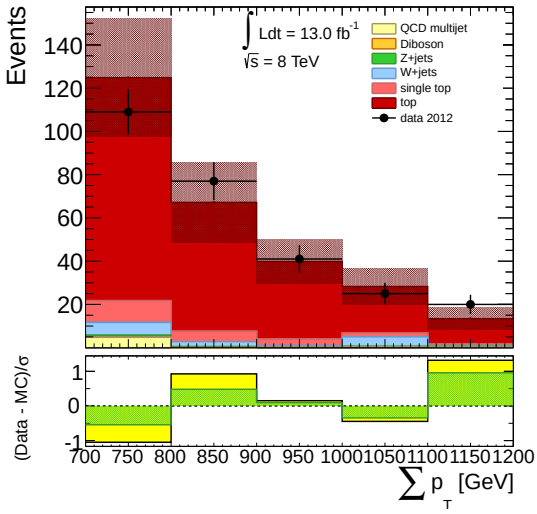

(c) Electron Channel

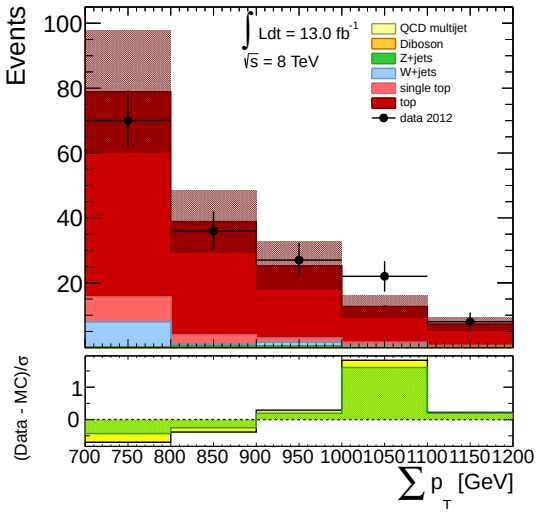

(d) Muon Channel

Figure C.1. $\sum p_{\mathrm{T}}$ distributions in the $t\bar{t}$ CR, before and after the application of the scale factor. The Monte Carlo simulation is normalized to an integrated luminosity of 13.0 fb^1. The error bars include both statistical and systematic uncertainties. The bottom pane of each subfigure displays the difference between data and simulation over their statistical uncertainty (yellow band) or statistical+systematic uncertainties (green band).

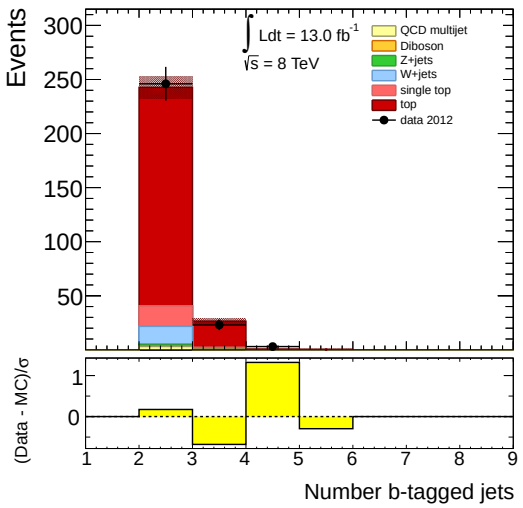

(a) Electron Channel

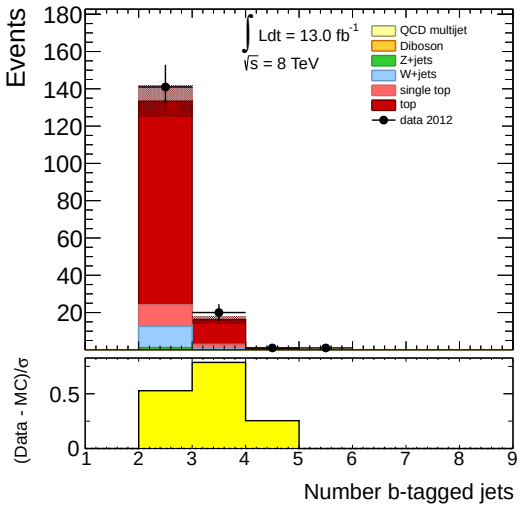

(b) Muon Channel

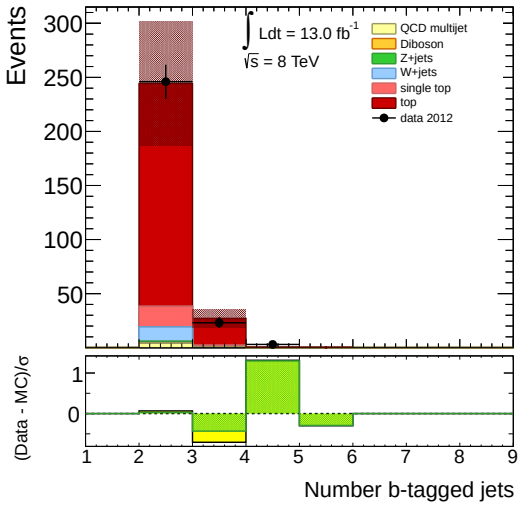

(c) Electron Channel

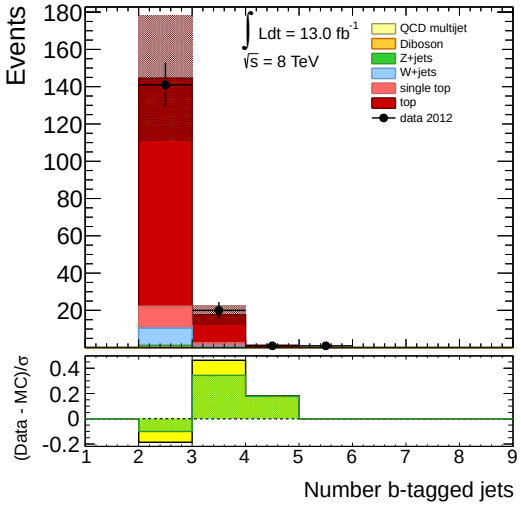

(d) Muon Channel

Figure C.2. Number of b-tagged jets in the $t\bar{t}$ CR, before and after the application of the scale factor. The Monte Carlo simulation is normalized to an integrated luminosity of 13.0 fb[1]. The error bars include both statistical and systematic uncertainties. The bottom pane of each subfigure displays the difference between data and simulation over their statistical uncertainty (yellow band) or statistical+systematic uncertainties (green band).

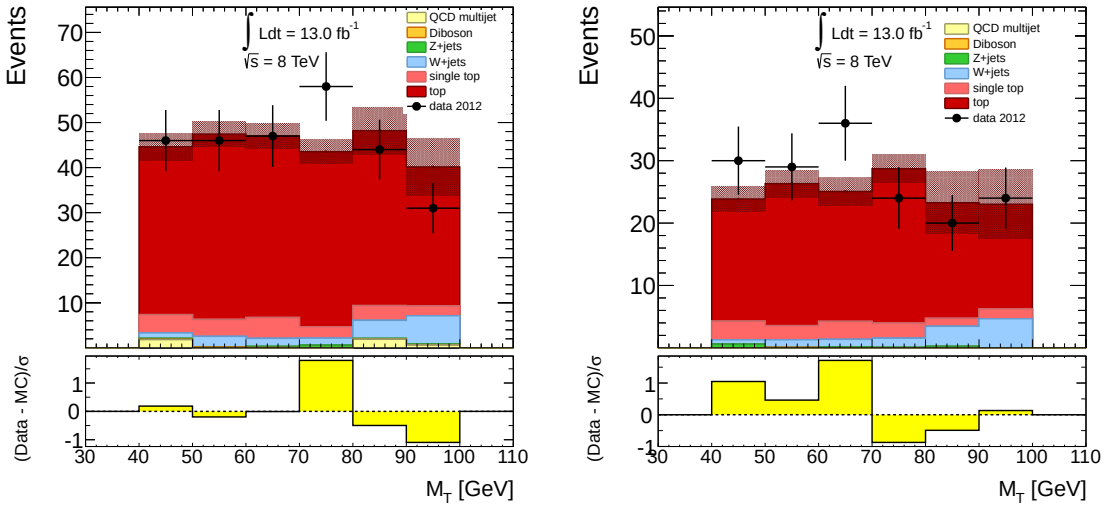

(a) Electron Channel

(b) Muon Channel

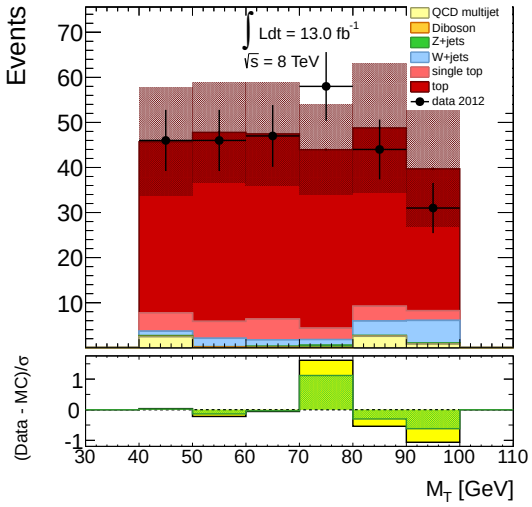

(c) Electron Channel

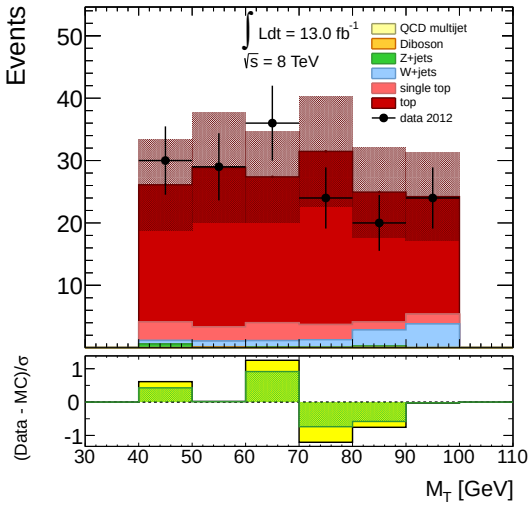

(d) Muon Channel

Figure C.3. M_{T} distributions in the $t\bar{t}$ CR, before and after the application of the scale factor. The Monte Carlo simulation is normalized to an integrated luminosity of 13.0 fb^1. The error bars include both statistical and systematic uncertainties. The bottom pane of each subfigure displays the difference between data and simulation over their statistical uncertainty (yellow band) or statistical+systematic uncertainties (green band).

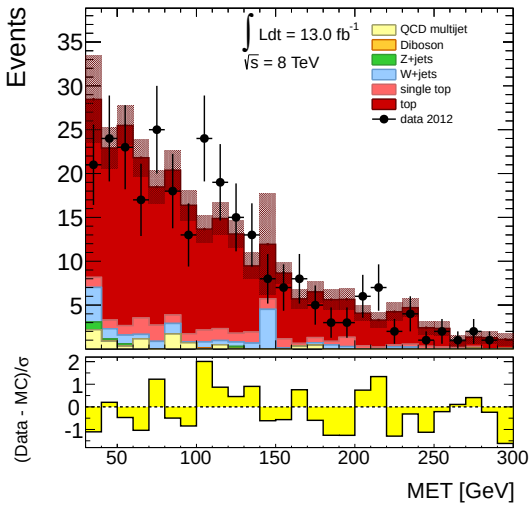

(a) Electron Channel

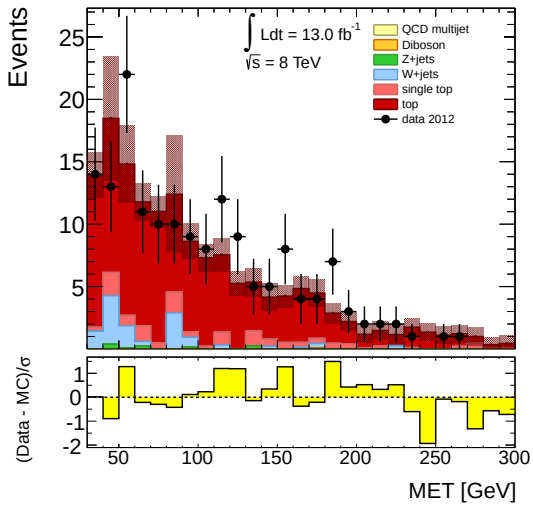

(b) Muon Channel

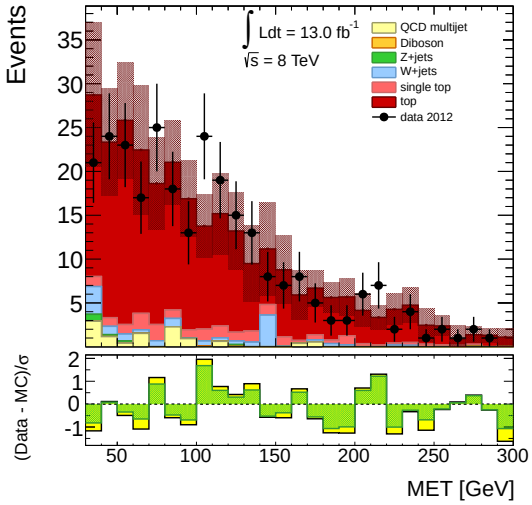

(c) Electron Channel

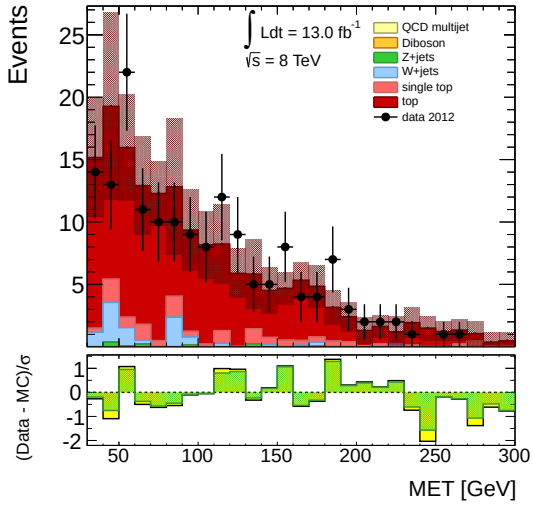

(d) Muon Channel

Figure C.4. $E_{\mathrm{T}}^{\mathrm{miss}}$ distributions in the $t\bar{t}$ CR, before and after the application of the scale factor. The Monte Carlo simulation is normalized to an integrated luminosity of 13.0 fb[1]. The error bars include both statistical and systematic uncertainties. The bottom pane of each subfigure displays the difference between data and simulation over their statistical uncertainty (yellow band) or statistical+systematic uncertainties (green band).

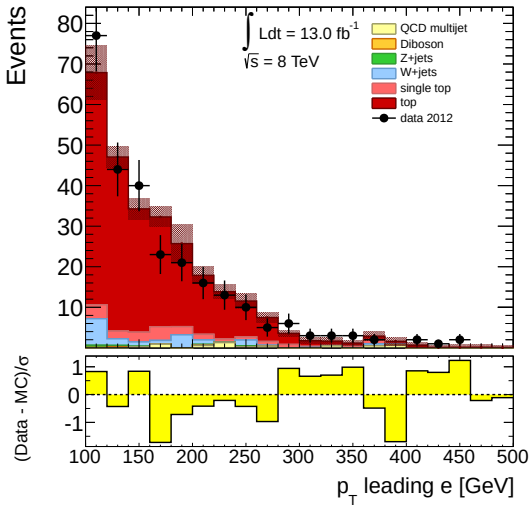

(a) Electron Channel

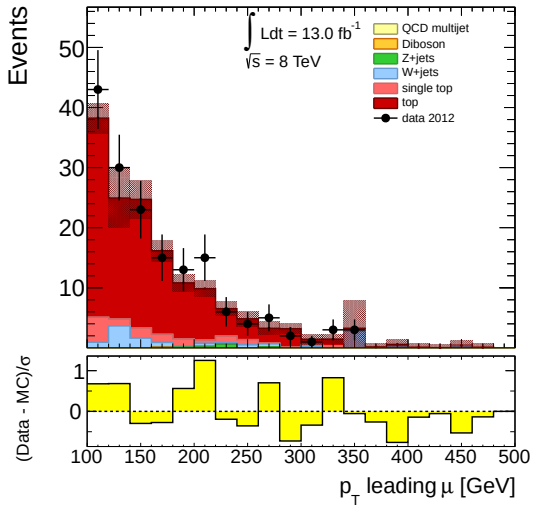

(b) Muon Channel

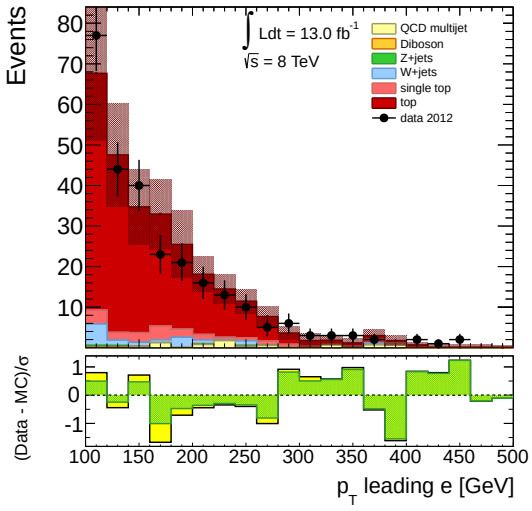

(c) Electron Channel

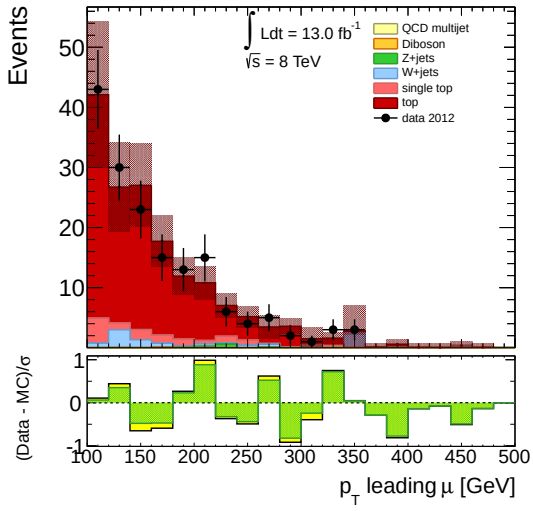

(d) Muon Channel

Figure C.5. Leading lepton p_{T} distributions in the $t\bar{t}$ CR, before and after the application of the scale factor. The Monte Carlo simulation is normalized to an integrated luminosity of 13.0 fb[1]. The error bars include both statistical and systematic uncertainties. The bottom pane of each subfigure displays the difference between data and simulation over their statistical uncertainty (yellow band) or statistical+systematic uncertainties (green band).

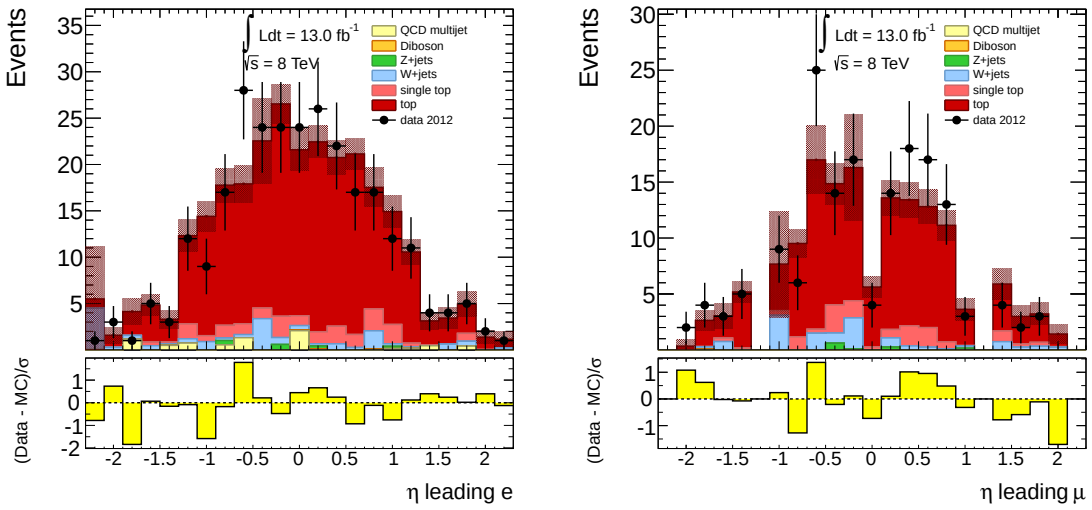

(a) Electron Channel

(b) Muon Channel

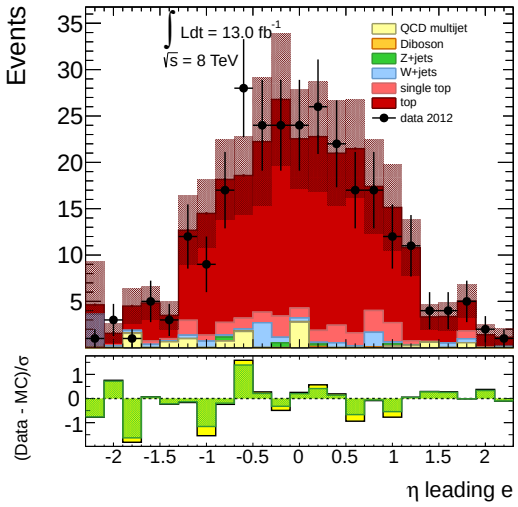

(c) Electron Channel

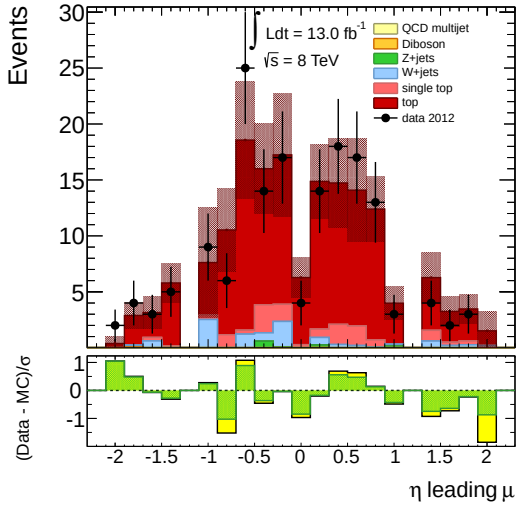

(d) Muon Channel

Figure C.6. Leading lepton η distributions in the $t\bar{t}$ CR, before and after the application of the scale factor. The Monte Carlo simulation is normalized to an integrated luminosity of 13.0 fb^1. The error bars include both statistical and systematic uncertainties. The bottom pane of each subfigure displays the difference between data and simulation over their statistical uncertainty (yellow band) or statistical+systematic uncertainties (green band).

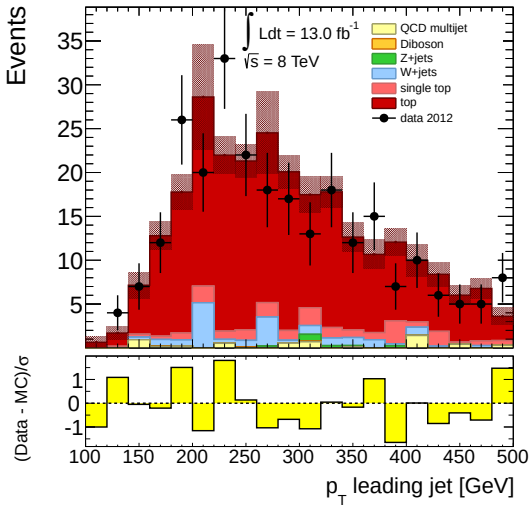

(a) Electron Channel

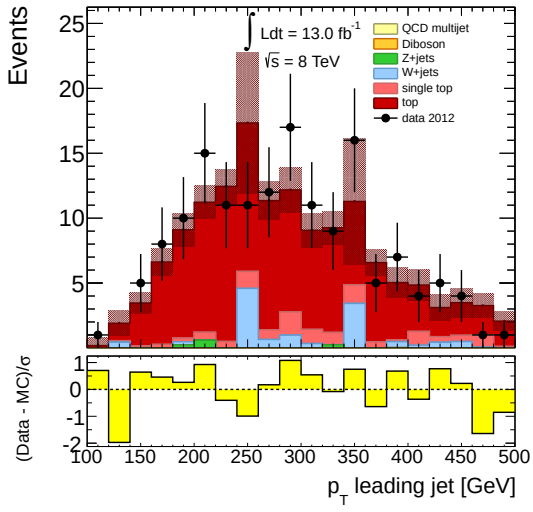

(b) Muon Channel

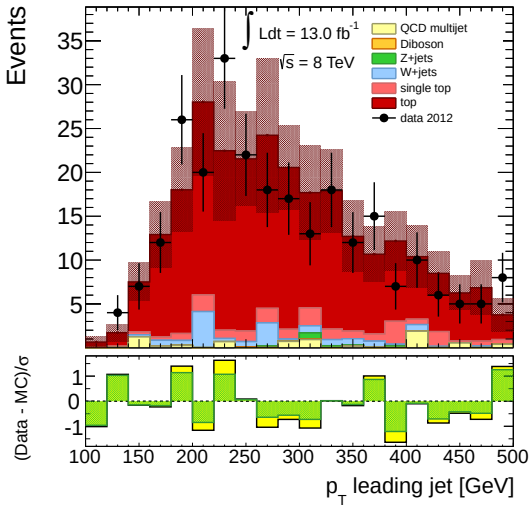

(c) Electron Channel

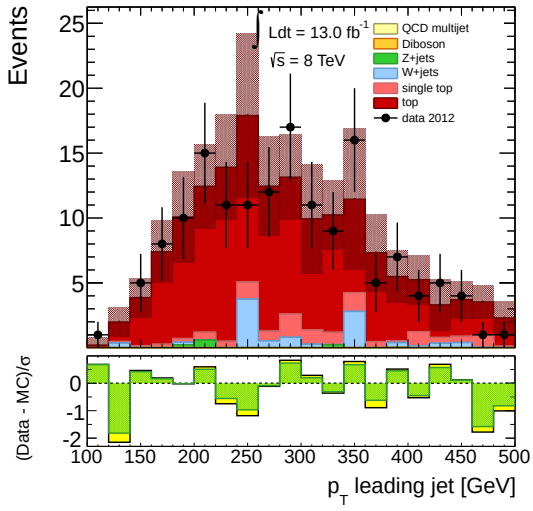

(d) Muon Channel

Figure C.7. Leading jet p_{T} distributions in the $t\bar{t}$ CR, before and after the application of the scale factor. The Monte Carlo simulation is normalized to an integrated luminosity of 13.0 fb[1]. The error bars include both statistical and systematic uncertainties. The bottom pane of each subfigure displays the difference between data and simulation over their statistical uncertainty (yellow band) or statistical+systematic uncertainties (green band).

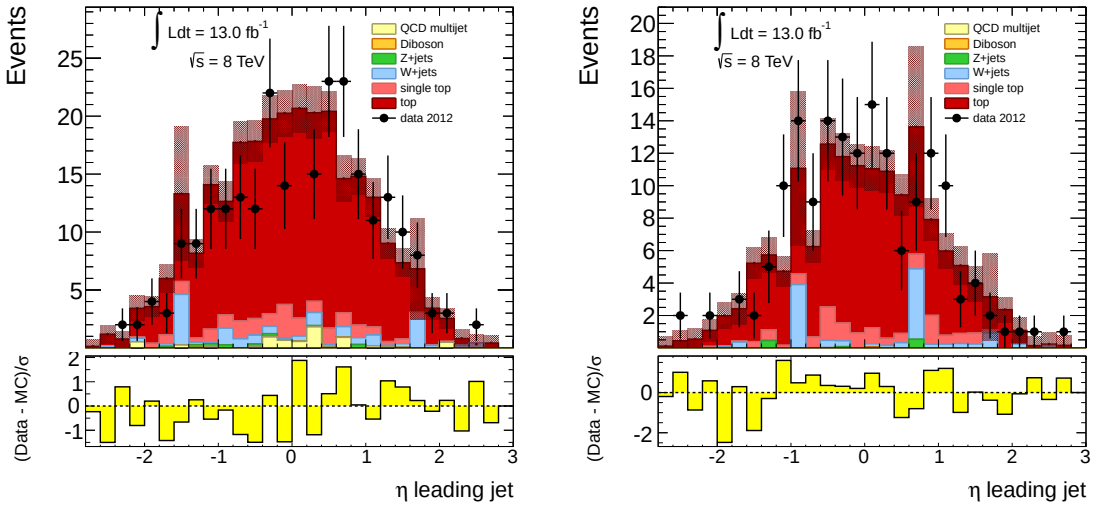

(a) Electron Channel

(b) Muon Channel

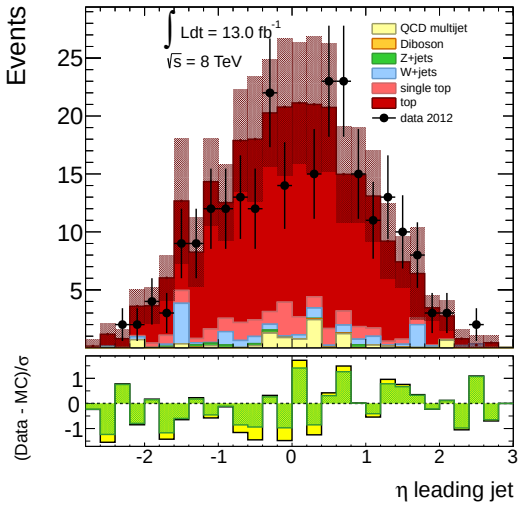

(c) Electron Channel

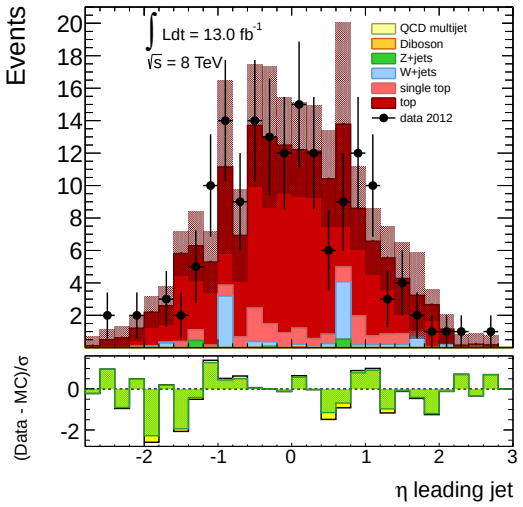

(d) Muon Channel

Figure C.8. Leading jet η distributions in the $t\bar{t}$ CR, before and after the application of the scale factor. The Monte Carlo simulation is normalized to an integrated luminosity of 13.0 fb^1. The error bars include both statistical and systematic uncertainties. The bottom pane of each subfigure displays the difference between data and simulation over their statistical uncertainty (yellow band) or statistical+systematic uncertainties (green band).

C.2 Distributions for the Alpgen Generator

The following distributions correspond to Figs. 5.7-5.10 and App. C.1 for $t\bar{t}$ samples generated with Alpgen. The histograms are shown before and after the application of the derived scale factor.

The obtained values for the $t\bar{t}$ scale factors for the different channels are

$$\mathrm{SF(electron)} = 1.053 \pm 0.086^{+0.269}_{-0.281}$$

$$\mathrm{SF(muon)} = 1.176 \pm 0.114^{+0.296}_{-0.301}.$$

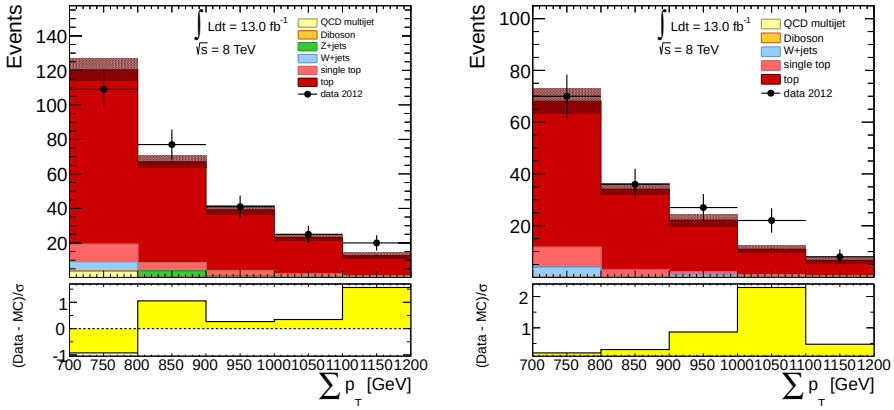

(a) Electron Channel

(b) Muon Channel

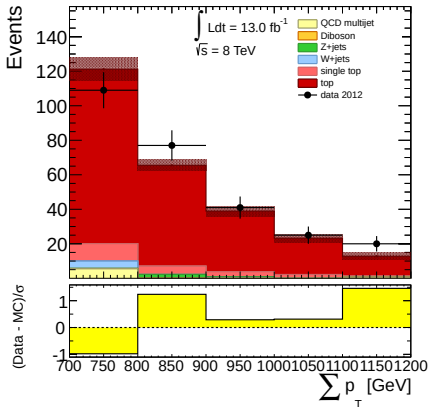

(c) Electron Channel

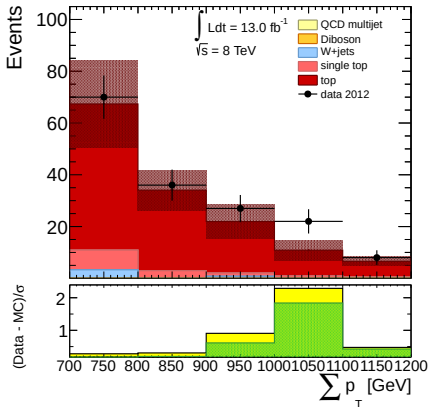

(d) Muon Channel

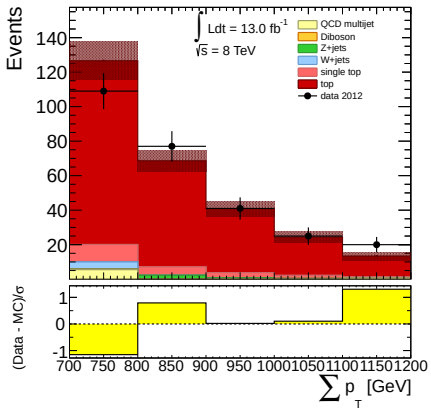

(e) Electron Channel

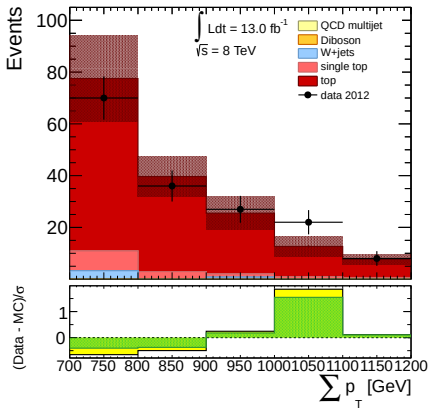

(f) Muon Channel

Figure C.9. $\sum p_{\mathrm{T}}$ distributions in the $t\bar{t}$ CR with no SFs applied (top), scaling non-$t\bar{t}$ backgrounds only (middle) and after the application of all SFs (bottom). The Monte Carlo simulation (`Alpgen` generator) is normalized to an integrated luminosity of 13.0 fb^{1}.

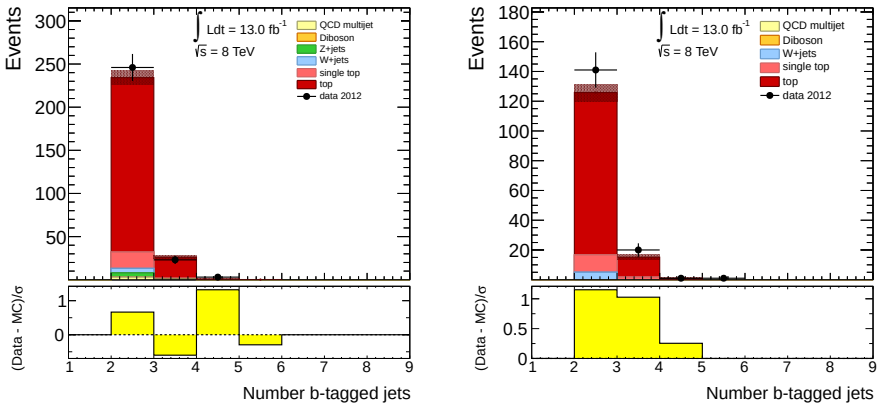

(a) Electron Channel

(b) Muon Channel

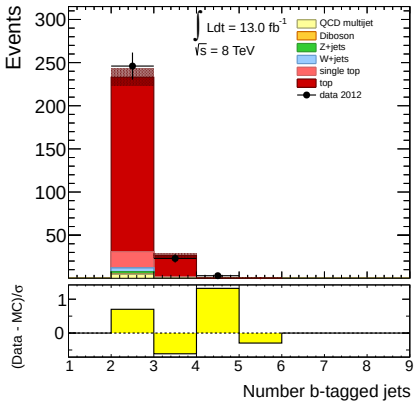

(c) Electron Channel

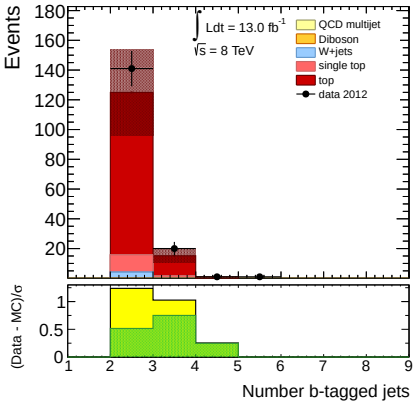

(d) Muon Channel

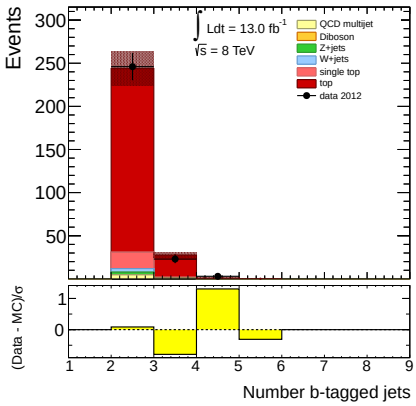

(e) Electron Channel

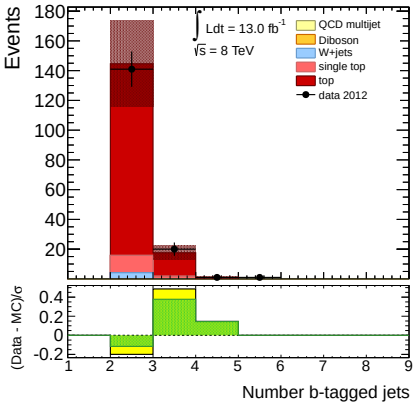

(f) Muon Channel

Figure C.10. Number of b-tagged jets in the $t\bar{t}$ CR with no SFs applied (top), scaling non-$t\bar{t}$ backgrounds only (middle) and after the application of all SFs (bottom). The Monte Carlo simulation (`Alpgen` generator) is normalized to an integrated luminosity of 13.0 fb^1.

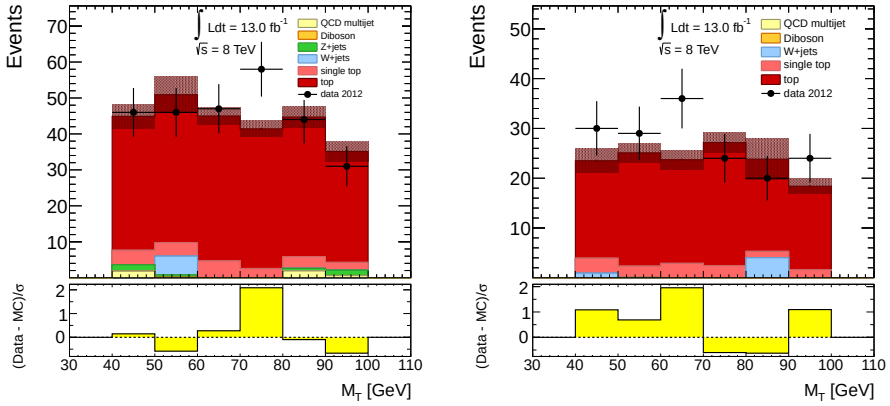

(a) Electron Channel

(b) Muon Channel

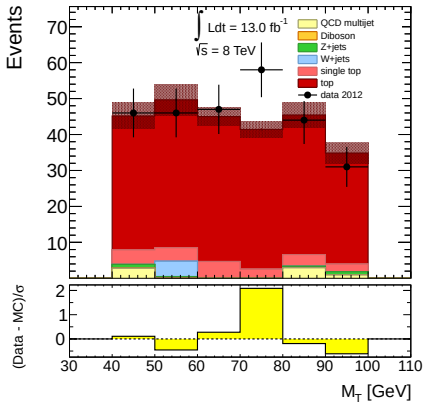

(c) Electron Channel

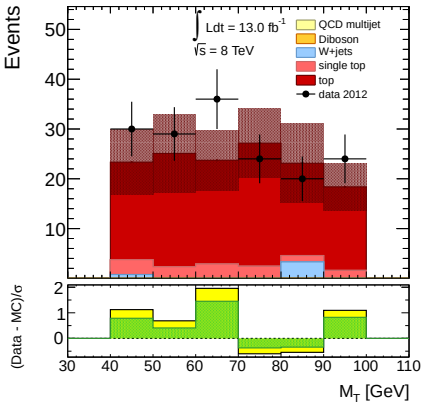

(d) Muon Channel

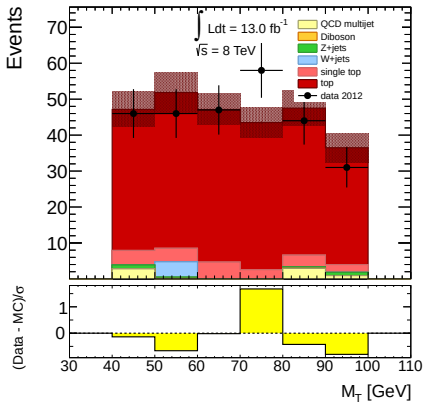

(e) Electron Channel

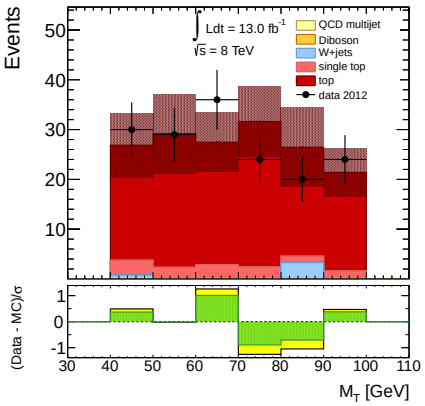

(f) Muon Channel

Figure C.11. M_{T} distributions in the $t\bar{t}$ CR with no SFs applied (top), scaling non-$t\bar{t}$ backgrounds only (middle) and after the application of all SFs (bottom). The Monte Carlo simulation (`Alpgen` generator) is normalized to an integrated luminosity of 13.0 fb^1.

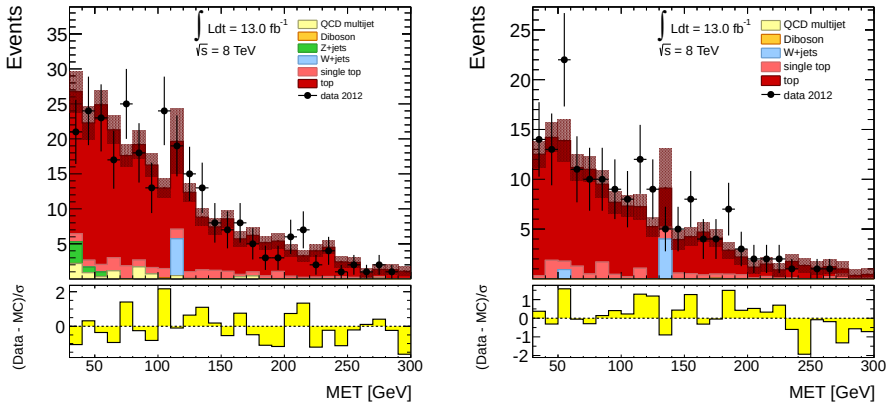

(a) Electron Channel (b) Muon Channel

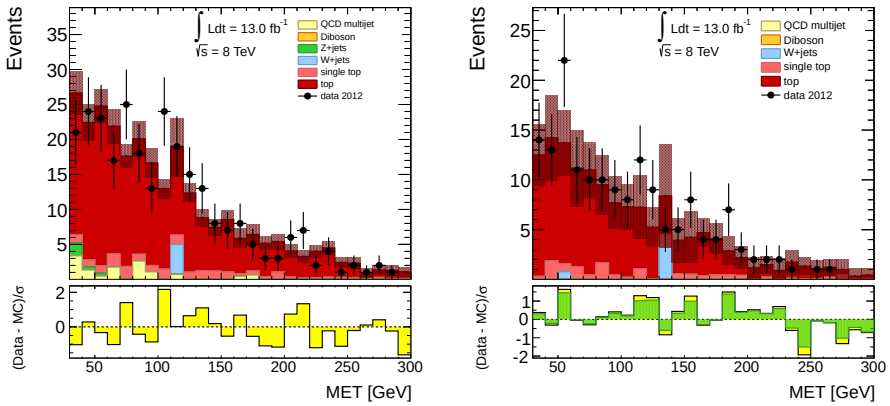

(c) Electron Channel (d) Muon Channel

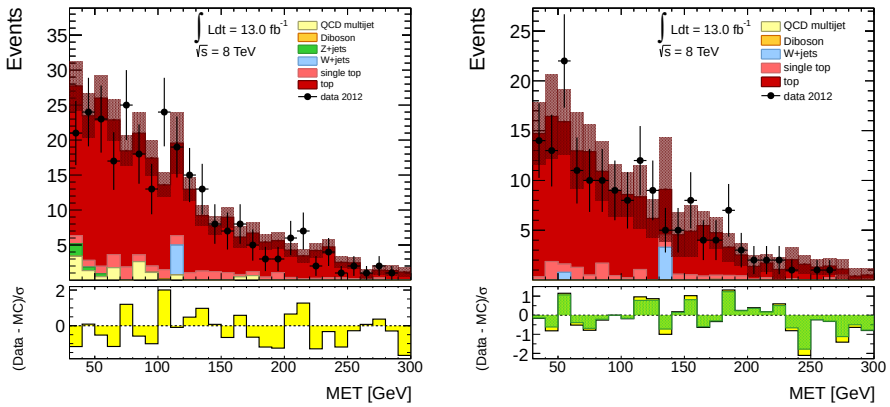

(e) Electron Channel (f) Muon Channel

Figure C.12. $E_{\mathrm{T}}^{\mathrm{miss}}$ distributions in the $t\bar{t}$ CR with no SFs applied (top), scaling non-$t\bar{t}$ backgrounds only (middle) and after the application of all SFs (bottom). The Monte Carlo simulation (`Alpgen` generator) is normalized to an integrated luminosity of 13.0 fb[1].

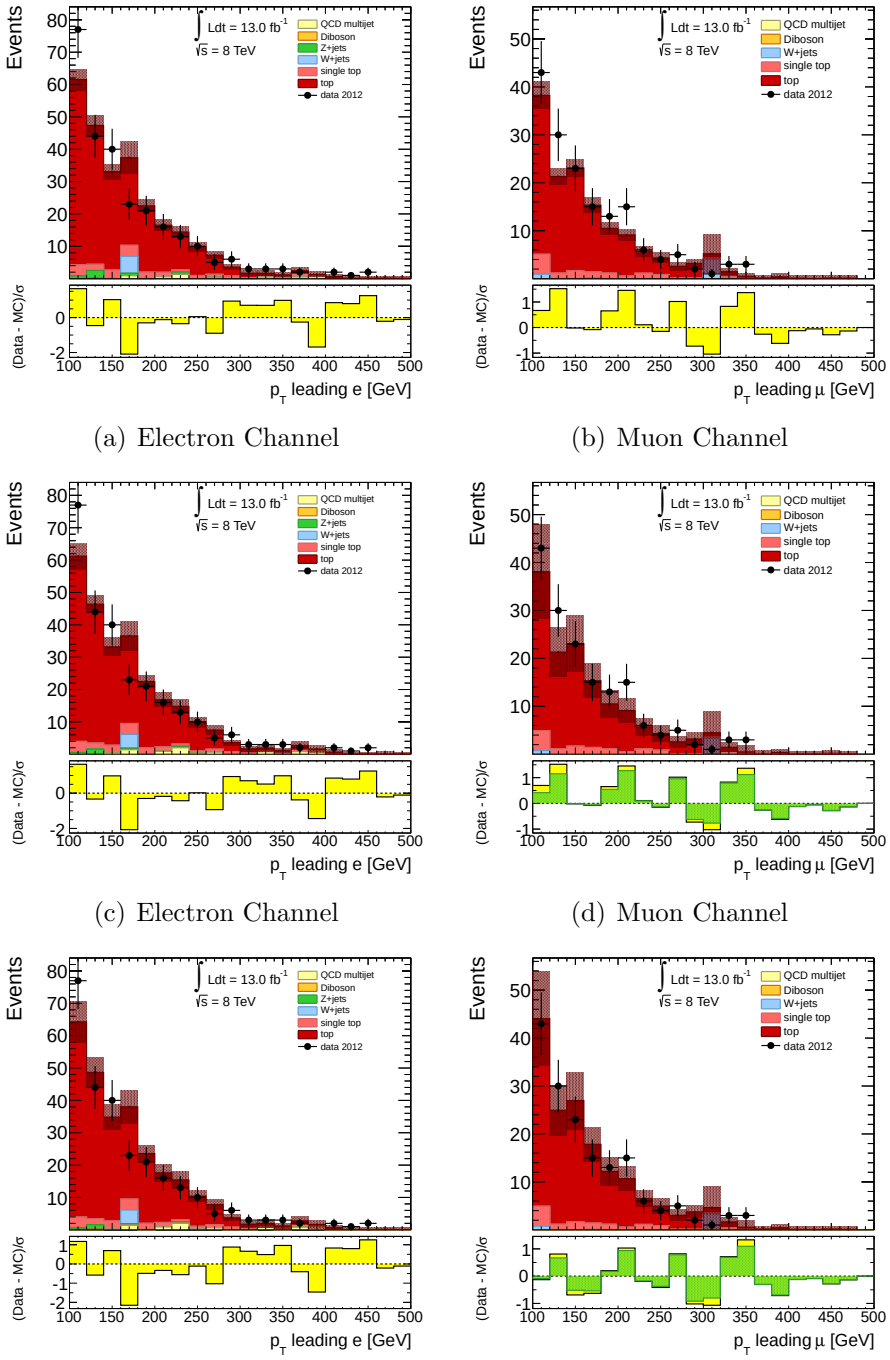

(a) Electron Channel (b) Muon Channel

(c) Electron Channel (d) Muon Channel

(e) Electron Channel (f) Muon Channel

Figure C.13. Leading lepton p_{T} ptdistributions in the $t\bar{t}$ CR with no SFs applied (top), scaling non-$t\bar{t}$ backgrounds only (middle) and after the application of all SFs (bottom). The Monte Carlo simulation (`Alpgen` generator) is normalized to an integrated luminosity of 13.0 fb^1.

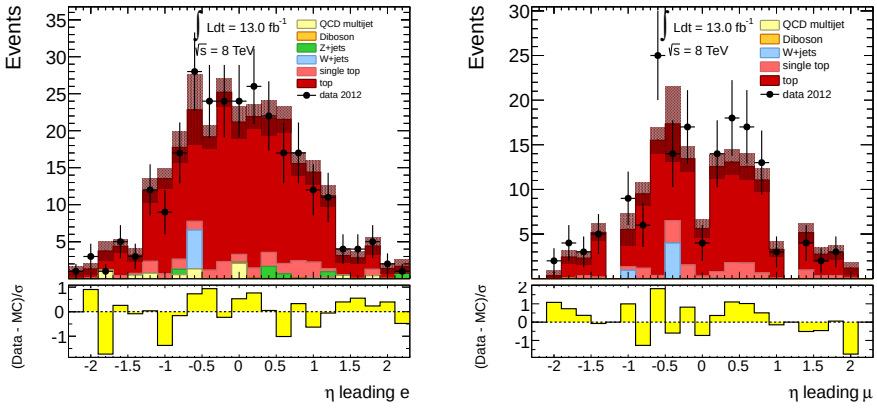

(a) Electron Channel

(b) Muon Channel

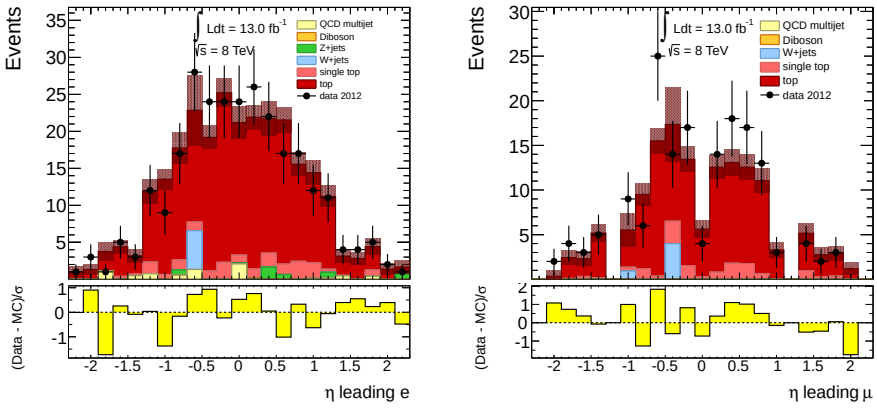

(c) Electron Channel

(d) Muon Channel

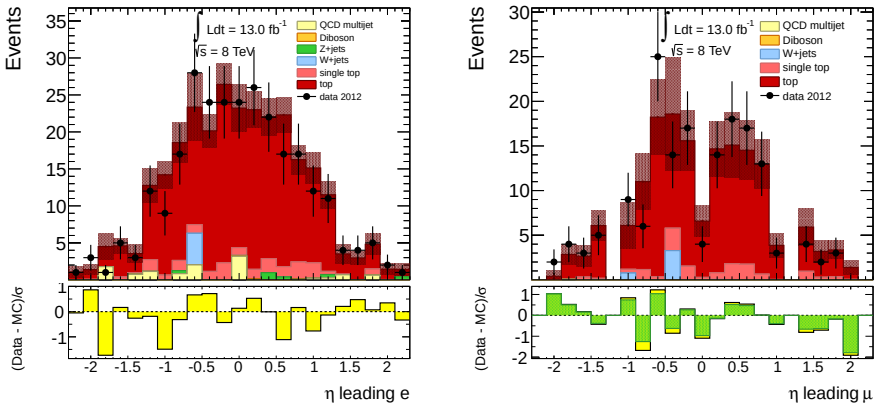

(e) Electron Channel

(f) Muon Channel

Figure C.14. Leading lepton η distributions in the $t\bar{t}$ CR with no SFs applied (top), scaling non-$t\bar{t}$ backgrounds only (middle) and after the application of all SFs (bottom). The Monte Carlo simulation (`Alpgen` generator) is normalized to an integrated luminosity of 13.0 fb^{1}.

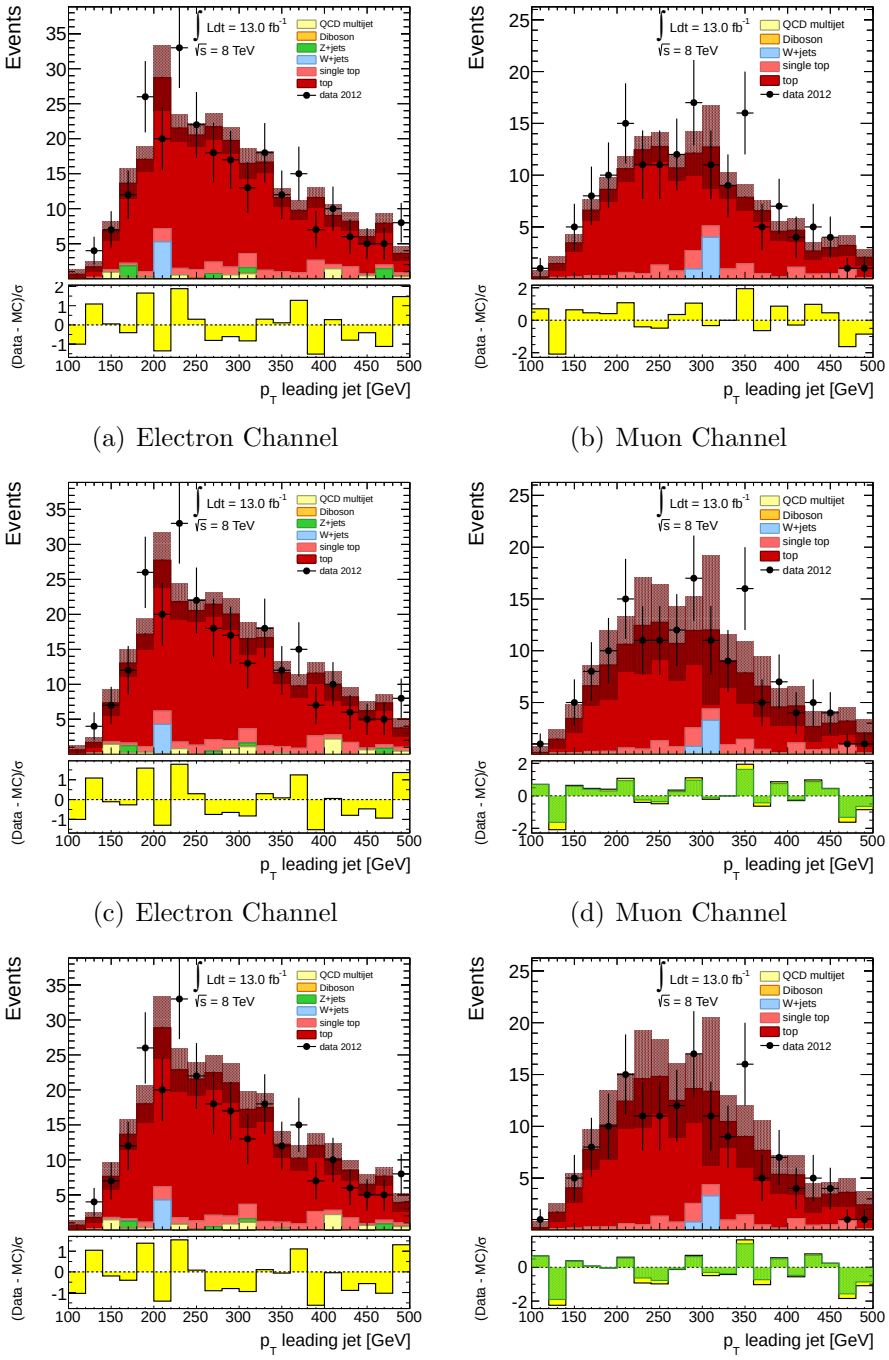

(a) Electron Channel (b) Muon Channel

(c) Electron Channel (d) Muon Channel

(e) Electron Channel (f) Muon Channel

Figure C.15. Leading jet p_{T} distributions in the $t\bar{t}$ CR with no SFs applied (top), scaling non-$t\bar{t}$ backgrounds only (middle) and after the application of all SFs (bottom). The Monte Carlo simulation (`Alpgen` generator) is normalized to an integrated luminosity of 13.0 fb^{1}.

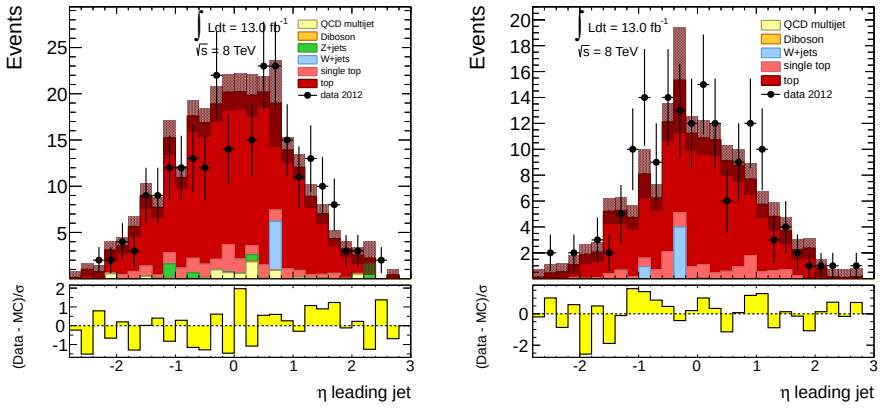

(a) Electron Channel

(b) Muon Channel

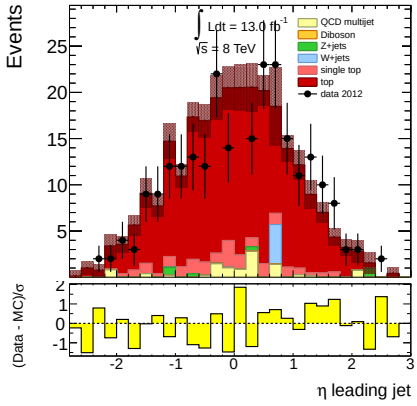

(c) Electron Channel

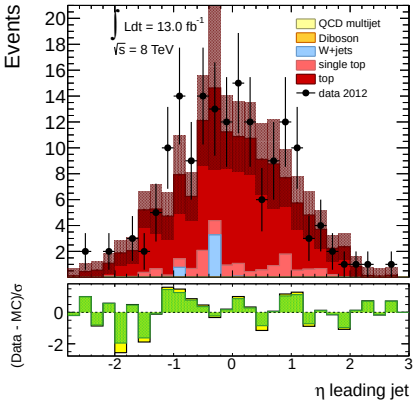

(d) Muon Channel

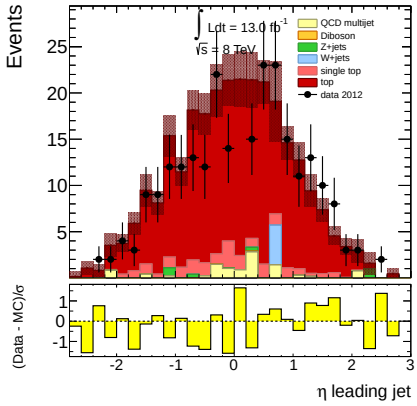

(e) Electron Channel

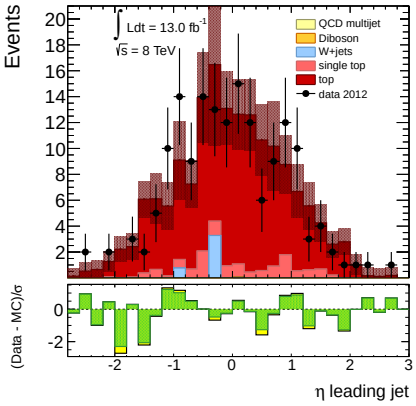

(f) Muon Channel

Figure C.16. Leading jet η distributions in the $t\bar{t}$ CR with no SFs applied (top), scaling non-$t\bar{t}$ backgrounds only (middle) and after the application of all SFs (bottom). The Monte Carlo simulation (`Alpgen` generator) is normalized to an integrated luminosity of 13.0 fb^1.

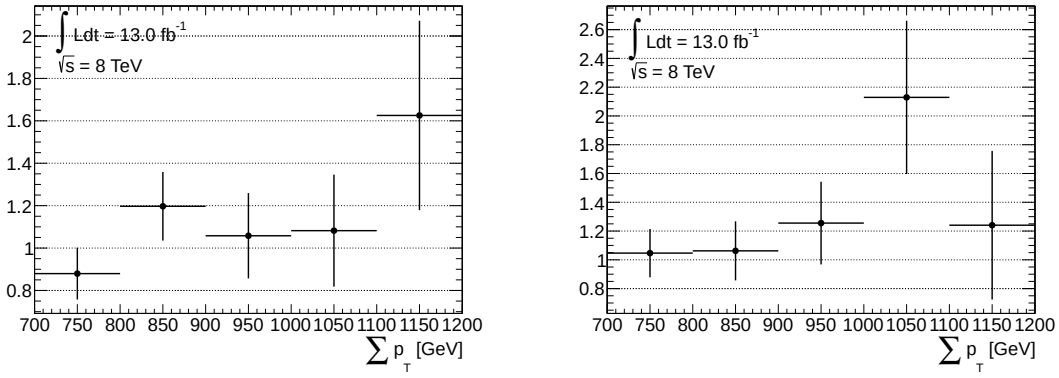

(a) Electron Channel (b) Muon Channel

Figure C.17. $t\bar{t}$ scale factor as a function of $\sum p_{\mathrm{T}}$ for samples generated with `Alpgen`.

APPENDIX D

BACKGROUND DISTRIBUTIONS: W+JETS

D.1 Distributions After the Application of SFs (Sherpa)

The following distributions correspond to Figs. 5.13-5.16, after the application of the scale factors calculated in Sec. 5.1.3, for the W+jets samples generated with Sherpa.

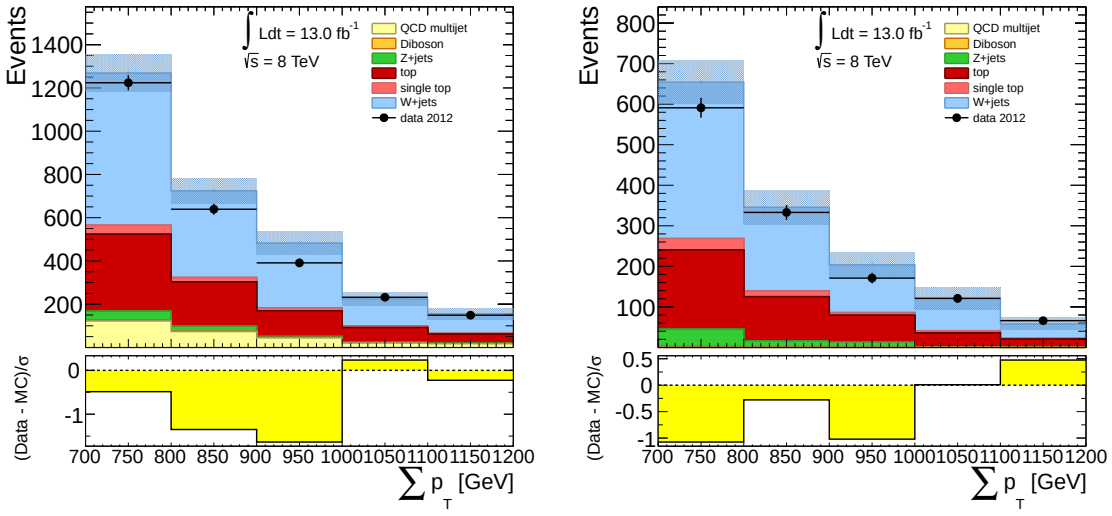

(a) Electron Channel

(b) Muon Channel

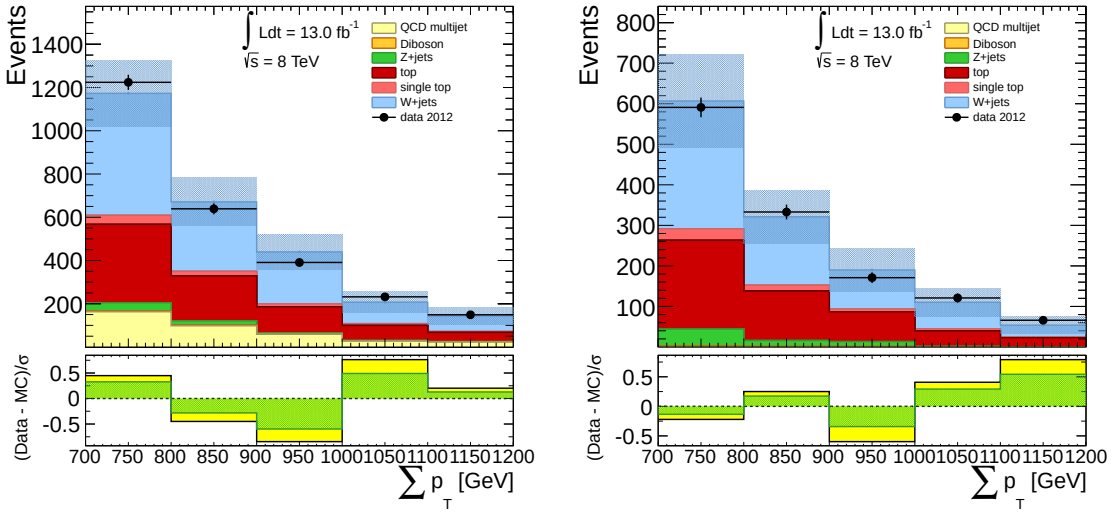

(c) Electron Channel

(d) Muon Channel

Figure D.1. $\sum p_{\mathrm{T}}$ distributions in the W+jets CR, before and after the application of the scale factor. The Monte Carlo simulation is normalized to an integrated luminosity of 13.0 fb^{1}. The error bars include both statistical and systematic uncertainties. The bottom pane of each subfigure displays the difference between data and simulation over their statistical uncertainty (yellow band) or statistical+systematic uncertainties (green band).

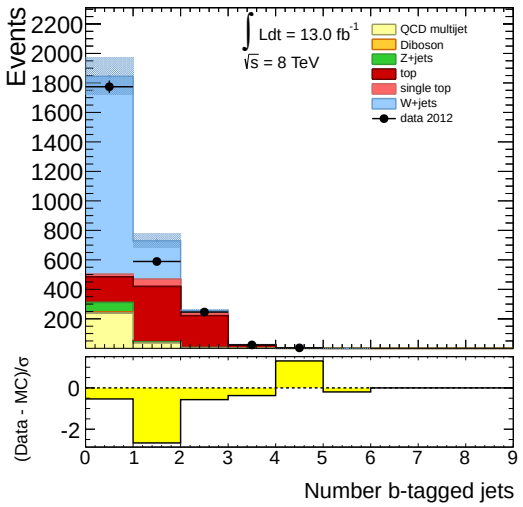

(a) Electron Channel

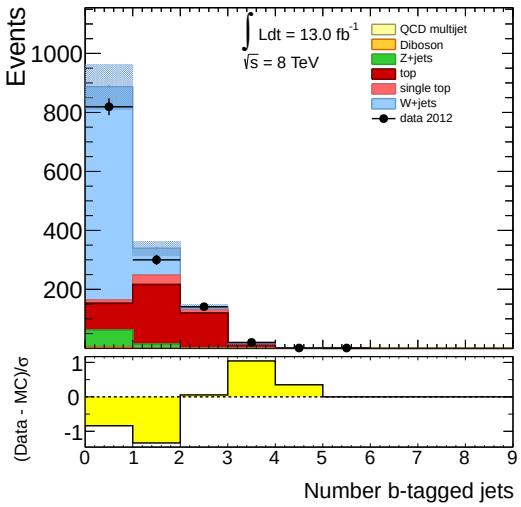

(b) Muon Channel

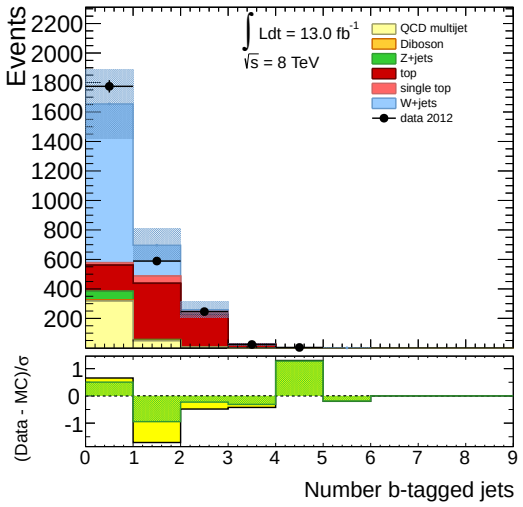

(c) Electron Channel

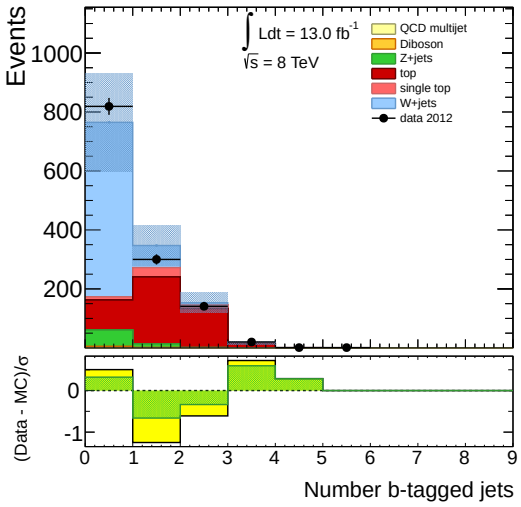

(d) Muon Channel

Figure D.2. Number of b-tagged jets in the W+jets CR, before and after the application of the scale factor. The Monte Carlo simulation is normalized to an integrated luminosity of 13.0 fb^1. The error bars include both statistical and systematic uncertainties. The bottom pane of each subfigure displays the difference between data and simulation over their statistical uncertainty (yellow band) or statistical+systematic uncertainties (green band).

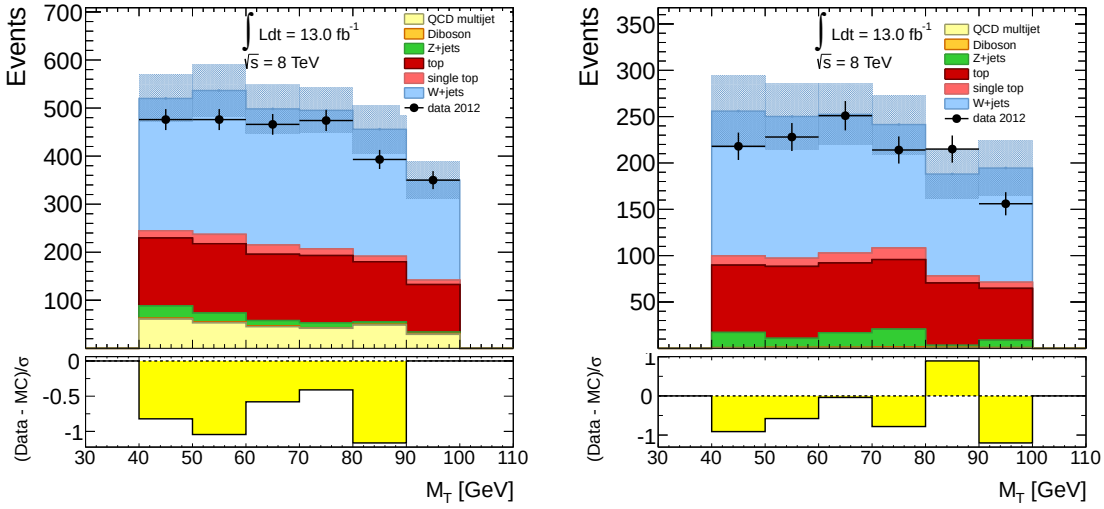

(a) Electron Channel

(b) Muon Channel

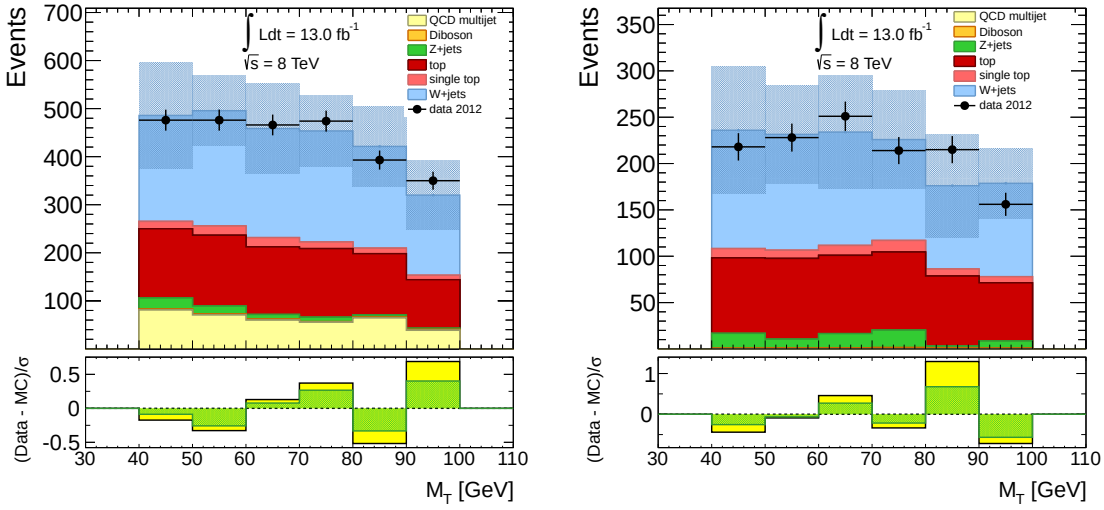

(c) Electron Channel

(d) Muon Channel

Figure D.3. M_{T} distributions in the W+jets CR, before and after the application of the scale factor. The Monte Carlo simulation is normalized to an integrated luminosity of 13.0 fb[1]. The error bars include both statistical and systematic uncertainties. The bottom pane of each subfigure displays the difference between data and simulation over their statistical uncertainty (yellow band) or statistical+systematic uncertainties (green band).

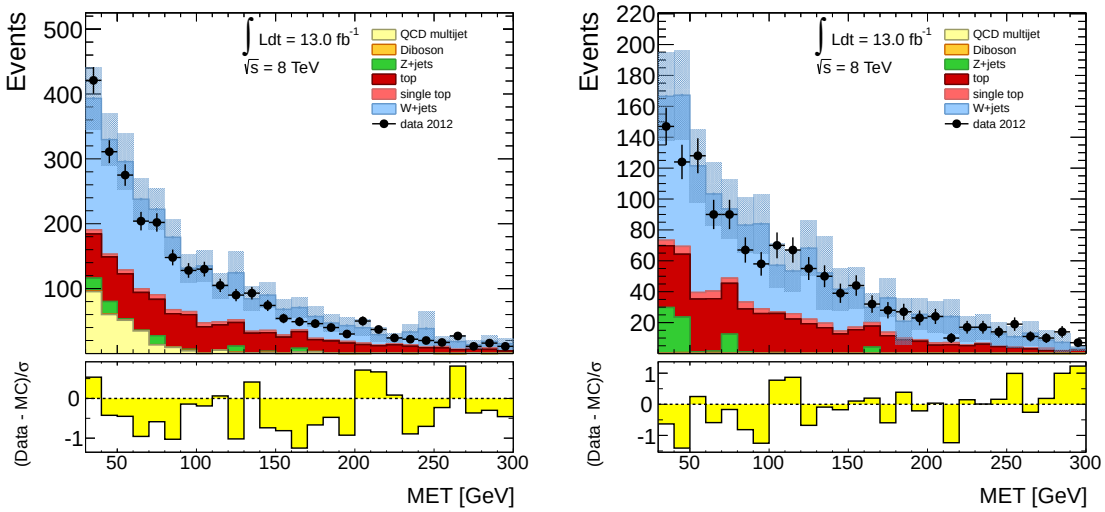

(a) Electron Channel

(b) Muon Channel

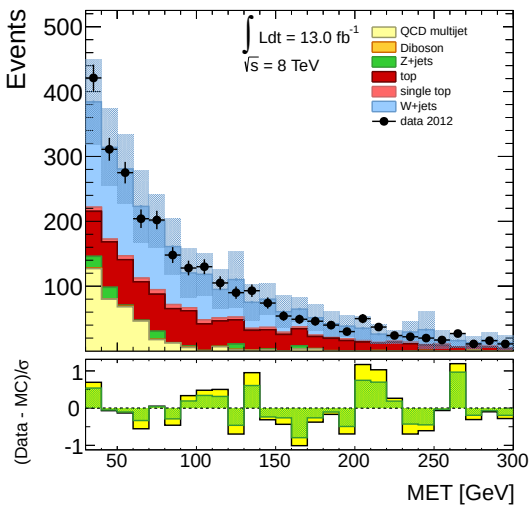

(c) Electron Channel

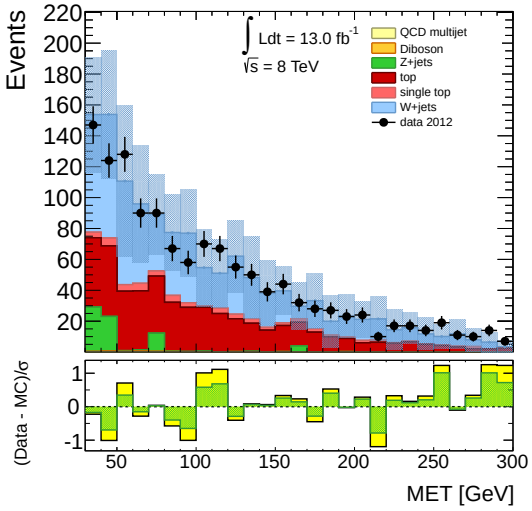

(d) Muon Channel

Figure D.4. $E_{\mathrm{T}}^{\mathrm{miss}}$ distributions in the W+jets CR, before and after the application of the scale factor. The Monte Carlo simulation is normalized to an integrated luminosity of 13.0 fb[1]. The error bars include both statistical and systematic uncertainties. The bottom pane of each subfigure displays the difference between data and simulation over their statistical uncertainty (yellow band) or statistical+systematic uncertainties (green band).

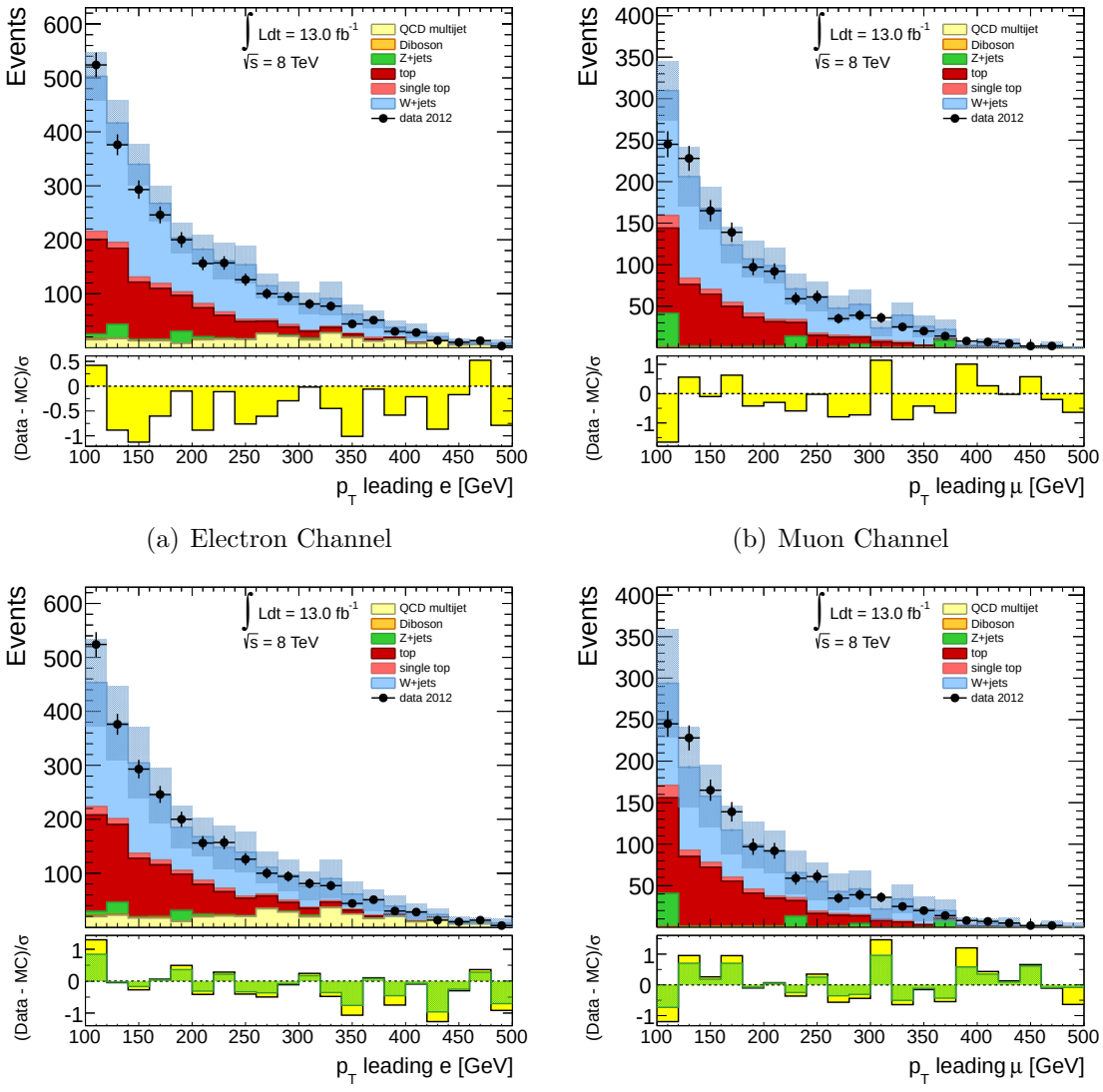

(a) Electron Channel

(b) Muon Channel

(c) Electron Channel

(d) Muon Channel

Figure D.5. Leading lepton p_{T} distributions in the W+jets CR, before and after the application of the scale factor. The Monte Carlo simulation is normalized to an integrated luminosity of 13.0 fb^1. The error bars include both statistical and systematic uncertainties. The bottom pane of each subfigure displays the difference between data and simulation over their statistical uncertainty (yellow band) or statistical+systematic uncertainties (green band).

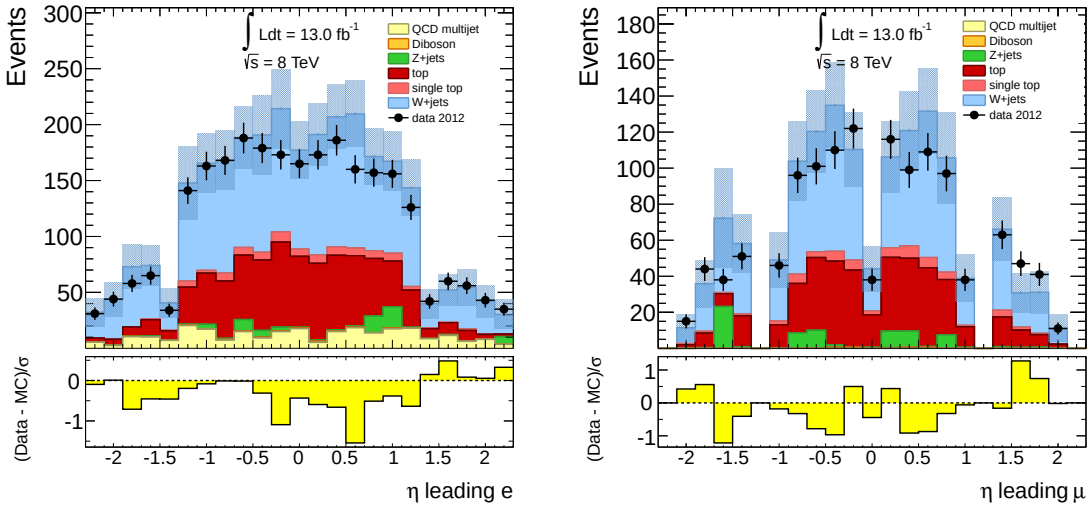

(a) Electron Channel

(b) Muon Channel

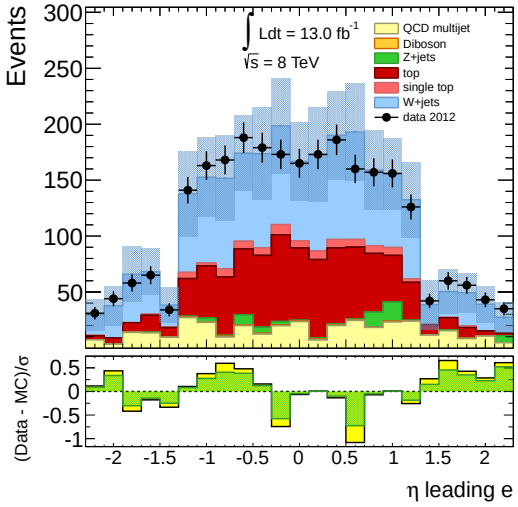

(c) Electron Channel

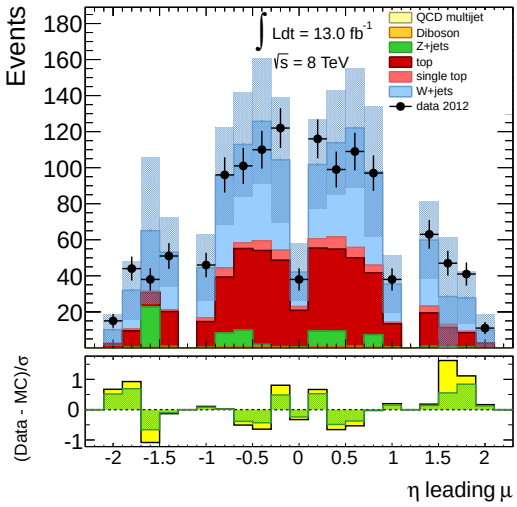

(d) Muon Channel

Figure D.6. Leading lepton η distributions in the W+jets CR, before and after the application of the scale factor. The Monte Carlo simulation is normalized to an integrated luminosity of 13.0 fb^1. The error bars include both statistical and systematic uncertainties. The bottom pane of each subfigure displays the difference between data and simulation over their statistical uncertainty (yellow band) or statistical+systematic uncertainties (green band).

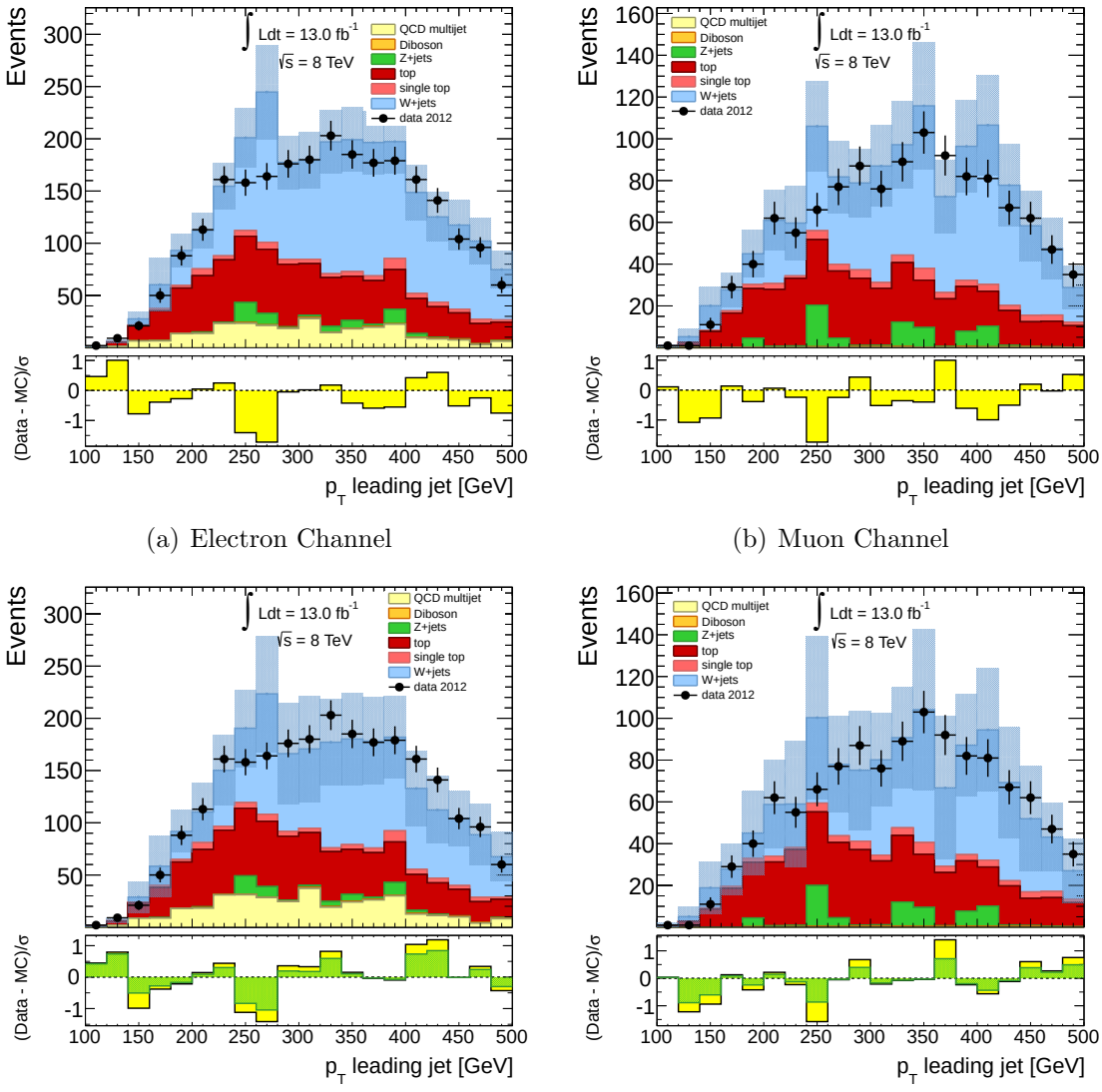

(a) Electron Channel

(b) Muon Channel

(c) Electron Channel

(d) Muon Channel

Figure D.7. Leading jet p_{T} distributions in the W+jets CR, before and after the application of the scale factor. The Monte Carlo simulation is normalized to an integrated luminosity of 13.0 fb[1]. The error bars include both statistical and systematic uncertainties. The bottom pane of each subfigure displays the difference between data and simulation over their statistical uncertainty (yellow band) or statistical+systematic uncertainties (green band).

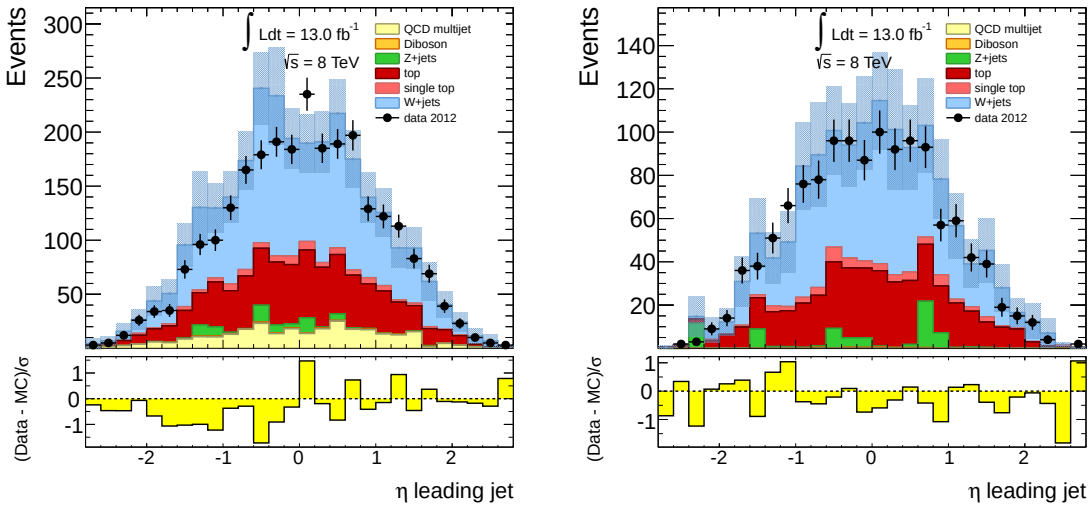

(a) Electron Channel

(b) Muon Channel

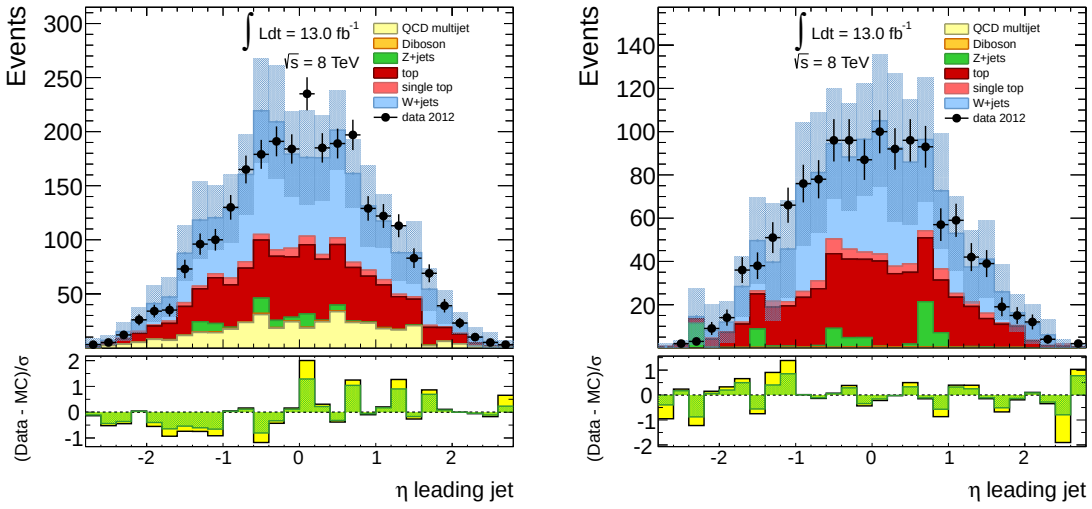

(c) Electron Channel

(d) Muon Channel

Figure D.8. Leading jet η distributions in the W+jets CR, before and after the application of the scale factor. The Monte Carlo simulation is normalized to an integrated luminosity of 13.0 fb^1. The error bars include both statistical and systematic uncertainties. The bottom pane of each subfigure displays the difference between data and simulation over their statistical uncertainty (yellow band) or statistical+systematic uncertainties (green band).

D.2 Distributions for the `Alpgen` Generator

The following distributions correspond to Figs. 5.13-5.16 and App. C.1 for W+jets samples generated with `Alpgen`. The histograms are shown before and after the application of the derived scale factor.

The obtained values for the W+jets scale factors for the different channels are

$$\mathrm{SF(electron)} = 0.811 \pm 0.096^{+0.130}_{-0.217}$$

$$\mathrm{SF(muon)} = 0.820 \pm 0.090^{+0.121}_{-0.193}.$$

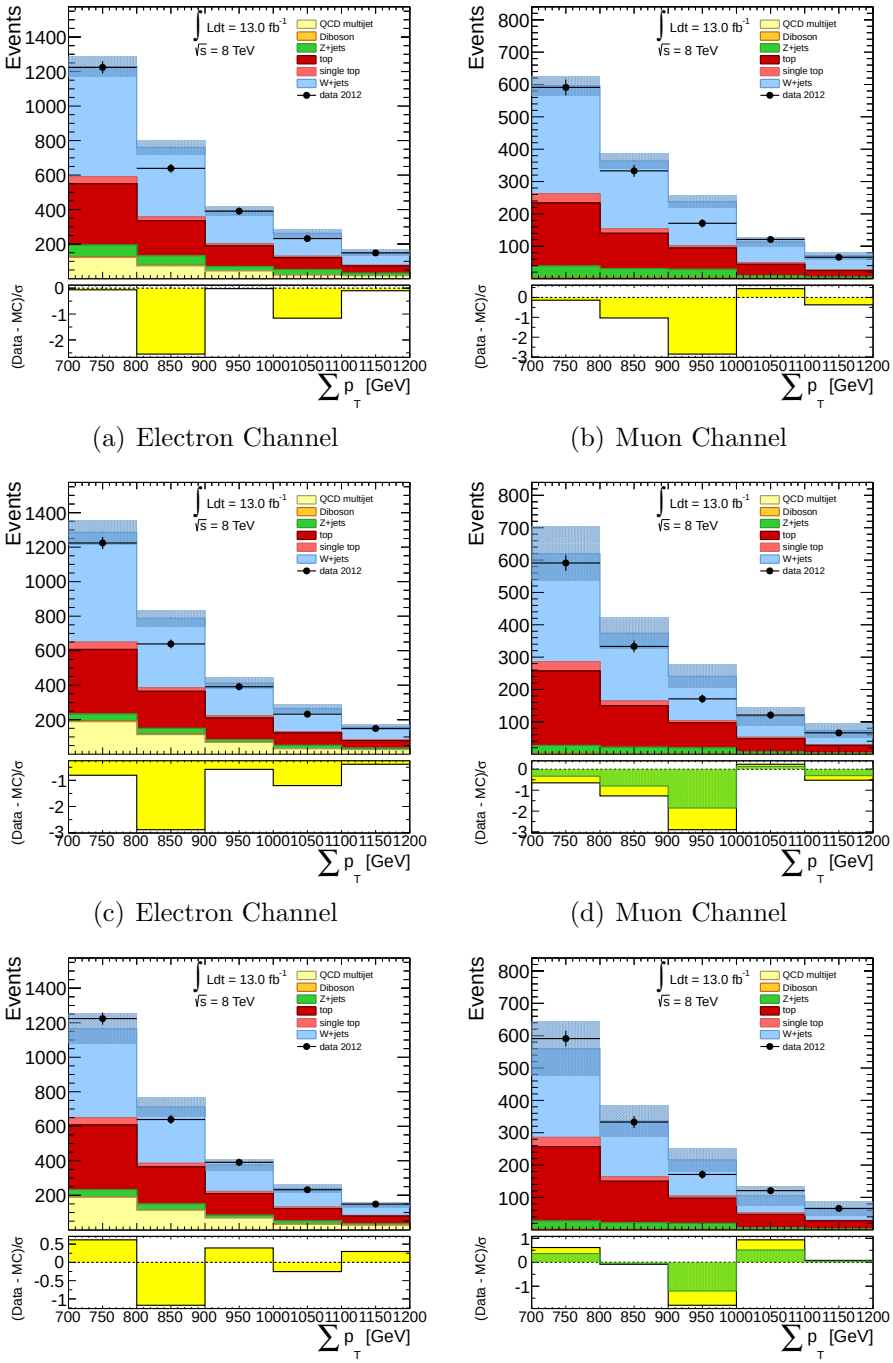

(a) Electron Channel (b) Muon Channel

(c) Electron Channel (d) Muon Channel

(e) Electron Channel (f) Muon Channel

Figure D.9. $\sum p_{\mathrm{T}}$ distributions in the W+jets CR with no SFs applied (top), scaling non-W+jets backgrounds only (middle) and after the application of all SFs (bottom). The Monte Carlo simulation (`Alpgen` generator) is normalized to an integrated luminosity of 13.0 fb^{1}.

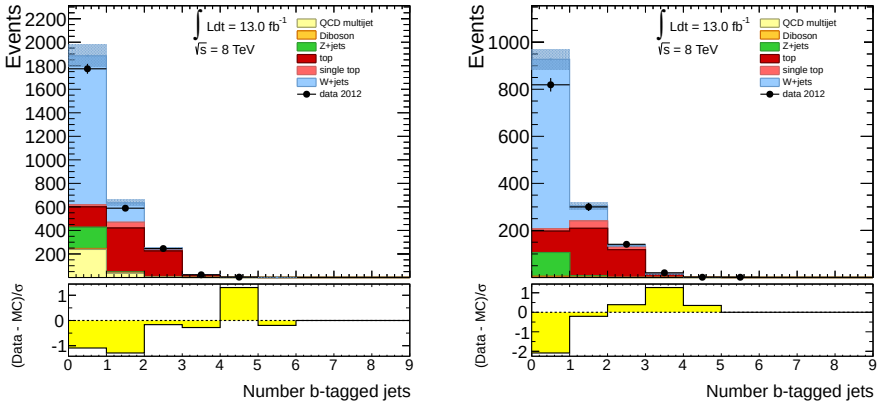

(a) Electron Channel

(b) Muon Channel

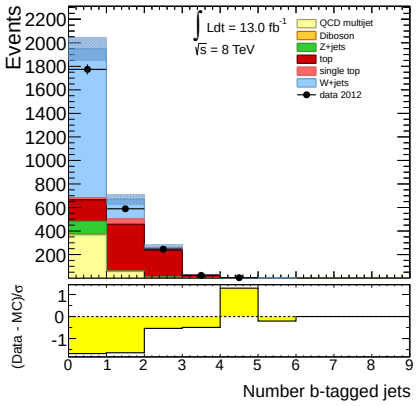

(c) Electron Channel

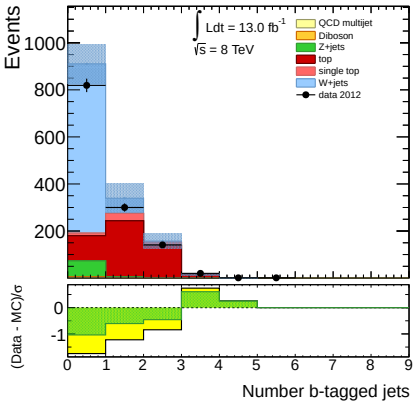

(d) Muon Channel

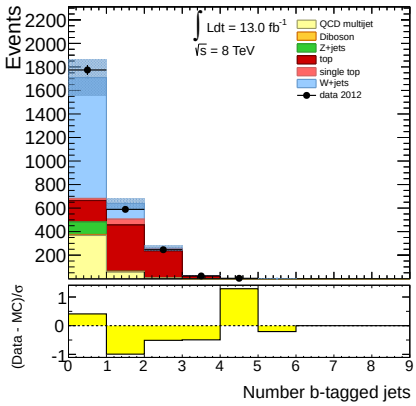

(e) Electron Channel

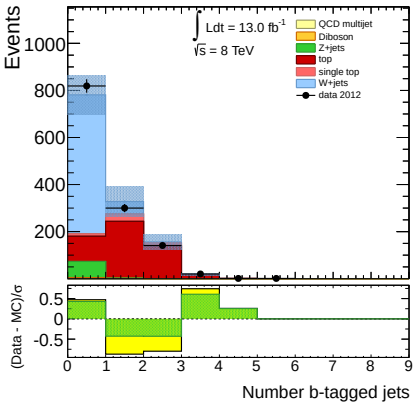

(f) Muon Channel

Figure D.10. Number of b-tagged jets in the W+jets CR with no SFs applied (top), scaling non-W+jets backgrounds only (middle) and after the application of all SFs (bottom). The Monte Carlo simulation (`Alpgen` generator) is normalized to an integrated luminosity of 13.0 fb^{1}.

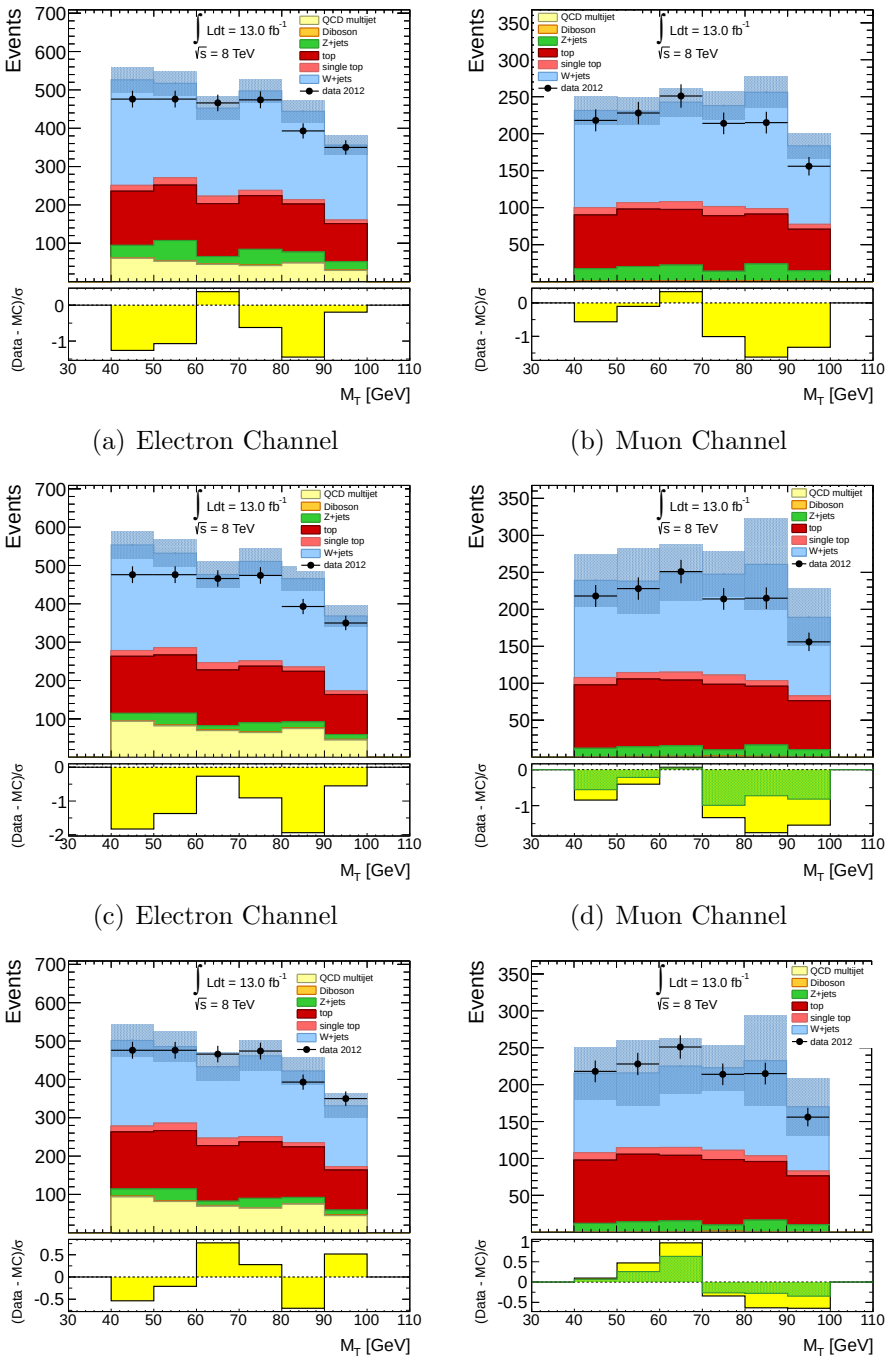

(a) Electron Channel

(b) Muon Channel

(c) Electron Channel

(d) Muon Channel

(e) Electron Channel

(f) Muon Channel

Figure D.11. M_{T} distributions in the W+jets CR with no SFs applied (top), scaling non-W+jets backgrounds only (middle) and after the application of all SFs (bottom). The Monte Carlo simulation (`Alpgen` generator) is normalized to an integrated luminosity of 13.0 fb^1.

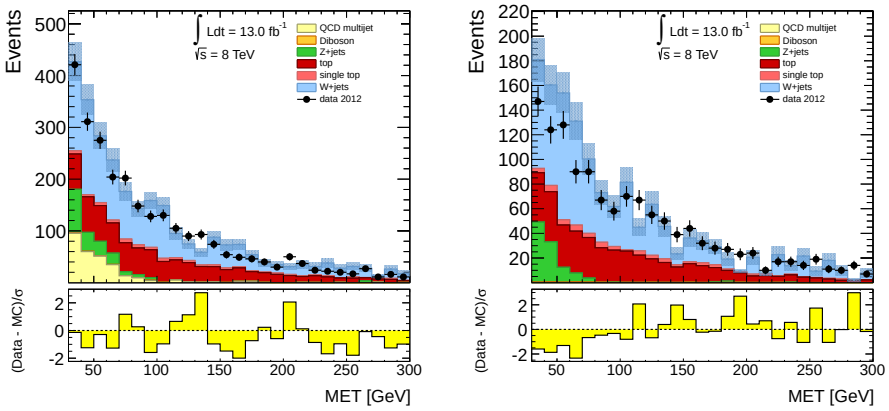

(a) Electron Channel

(b) Muon Channel

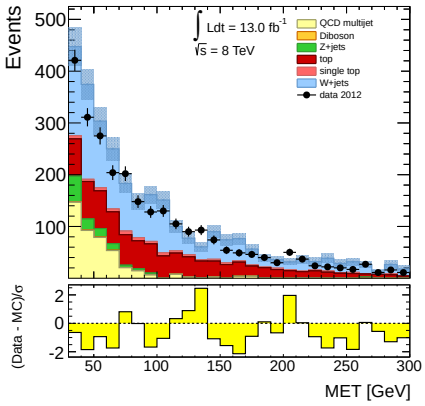

(c) Electron Channel

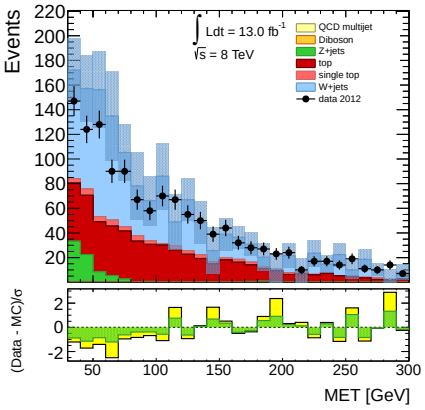

(d) Muon Channel

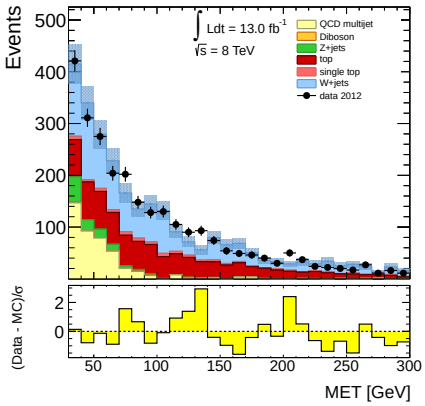

(e) Electron Channel

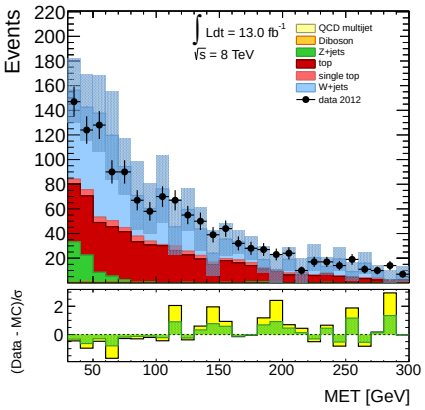

(f) Muon Channel

Figure D.12. $E_{\mathrm{T}}^{\mathrm{miss}}$ distributions in the W+jets CR with no SFs applied (top), scaling non-W+jets backgrounds only (middle) and after the application of all SFs (bottom). The Monte Carlo simulation (`Alpgen` generator) is normalized to an integrated luminosity of 13.0 fb^{1}.

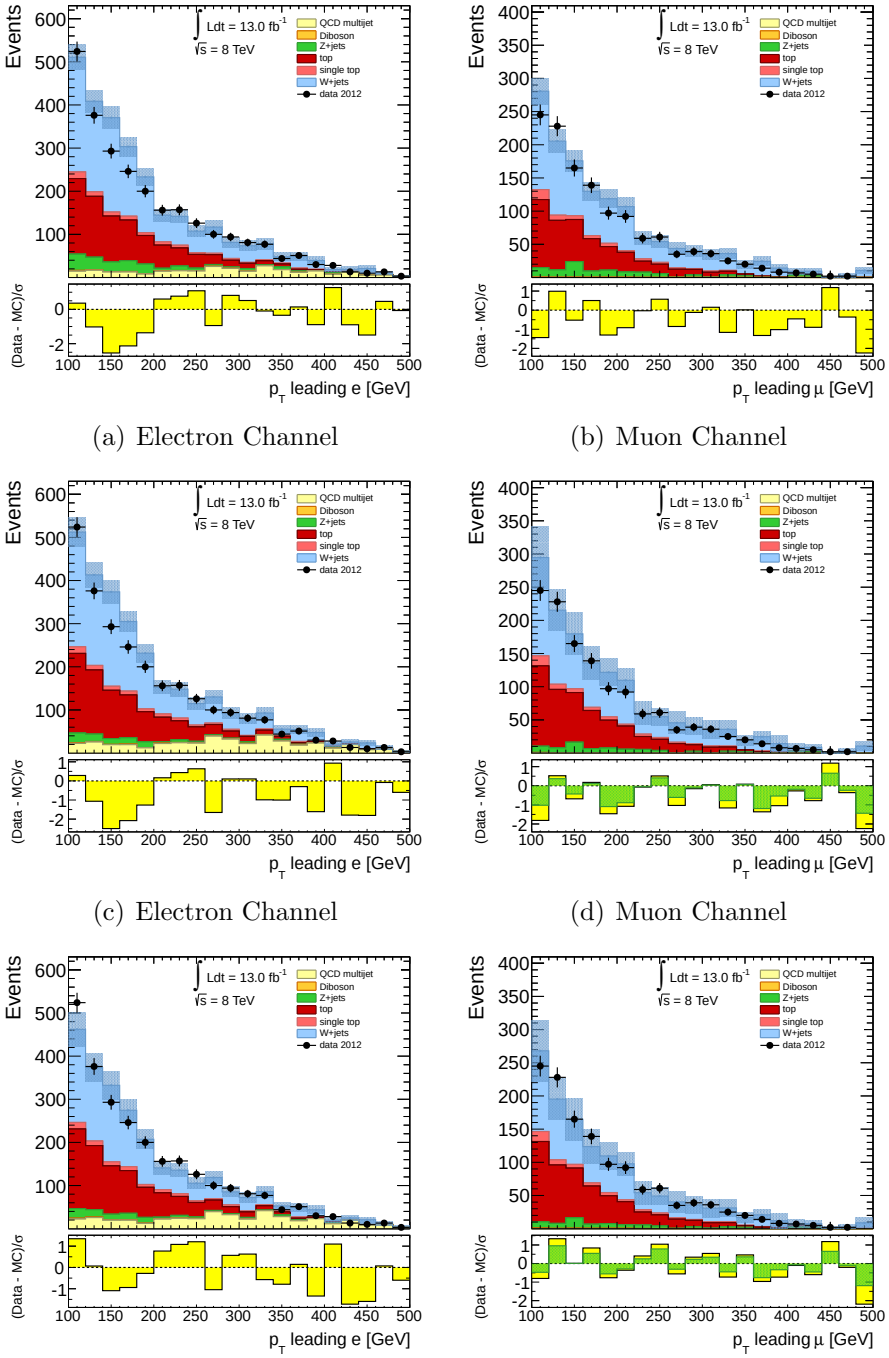

(a) Electron Channel

(b) Muon Channel

(c) Electron Channel

(d) Muon Channel

(e) Electron Channel

(f) Muon Channel

Figure D.13. Leading lepton p_{T} distributions in the W+jets CR with no SFs applied (top), scaling non-W+jets backgrounds only (middle) and after the application of all SFs (bottom). The Monte Carlo simulation (`Alpgen` generator) is normalized to an integrated luminosity of 13.0 fb^{1}.

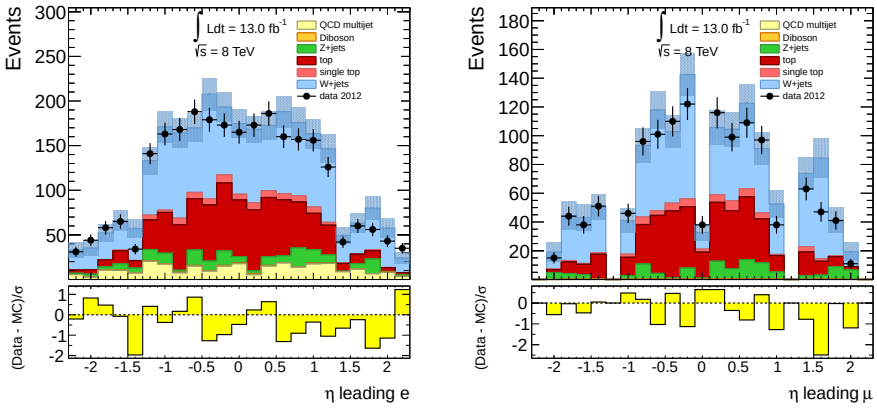

(a) Electron Channel

(b) Muon Channel

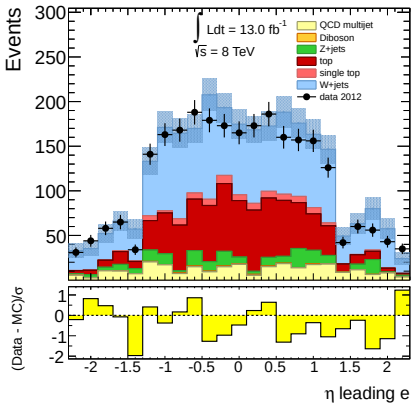

(c) Electron Channel

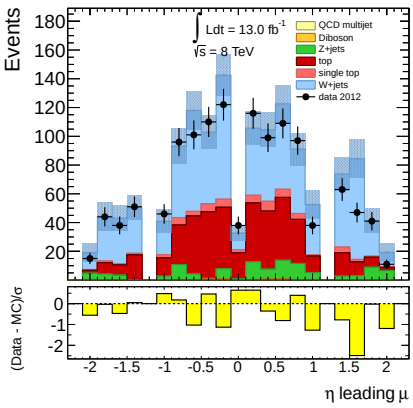

(d) Muon Channel

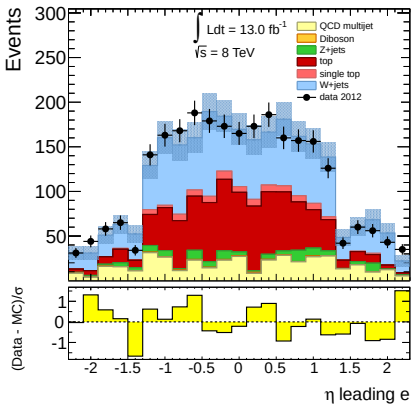

(e) Electron Channel

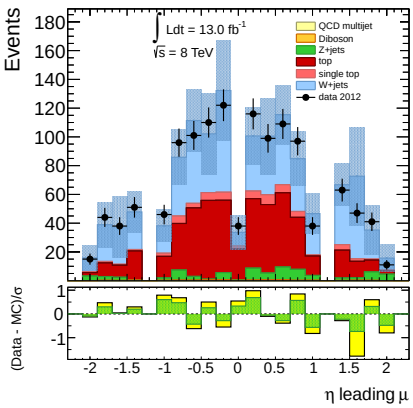

(f) Muon Channel

Figure D.14. Leading lepton η distributions in the W+jets CR with no SFs applied (top), scaling non-W+jets backgrounds only (middle) and after the application of all SFs (bottom). The Monte Carlo simulation (`Alpgen` generator) is normalized to an integrated luminosity of 13.0 fb^1.

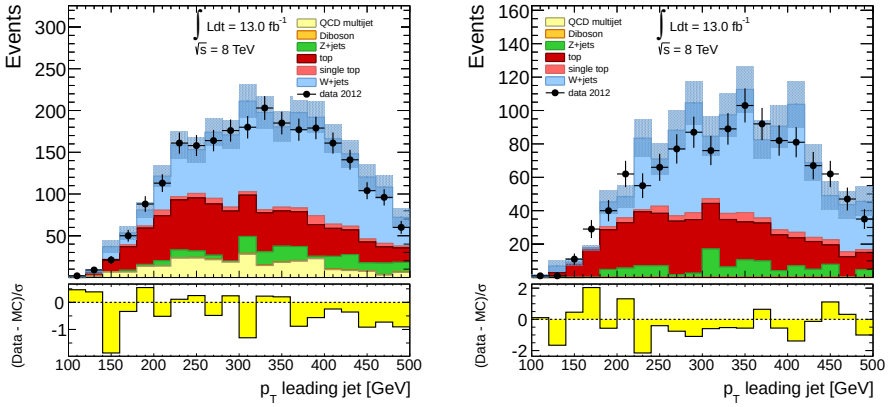

(a) Electron Channel

(b) Muon Channel

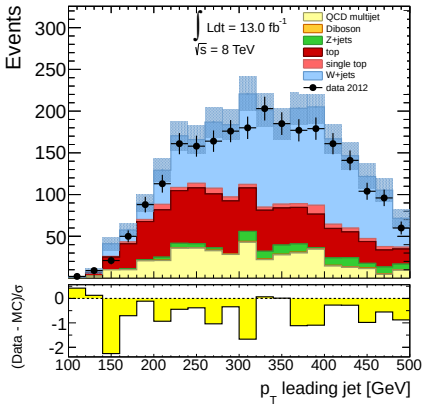

(c) Electron Channel

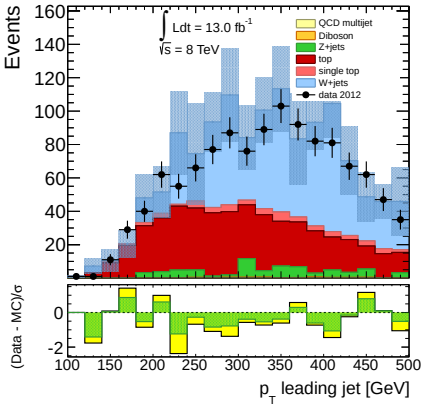

(d) Muon Channel

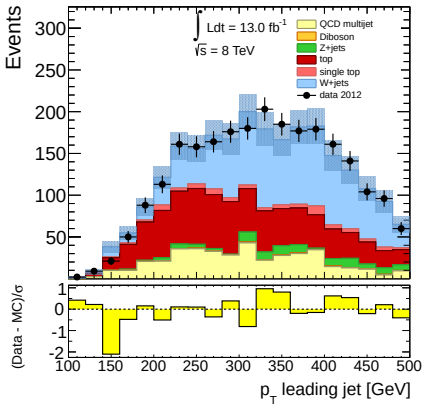

(e) Electron Channel

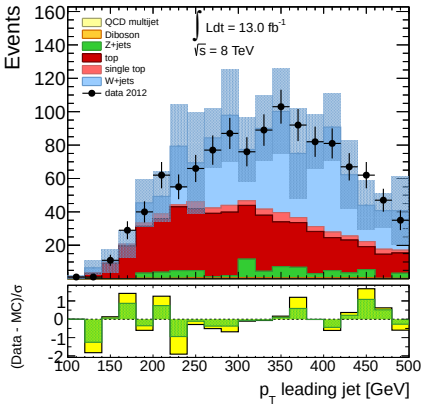

(f) Muon Channel

Figure D.15. Leading jet p_{T} distributions in the W+jets CR with no SFs applied (top), scaling non-W+jets backgrounds only (middle) and after the application of all SFs (bottom). The Monte Carlo simulation (`Alpgen` generator) is normalized to an integrated luminosity of 13.0 fb^1.

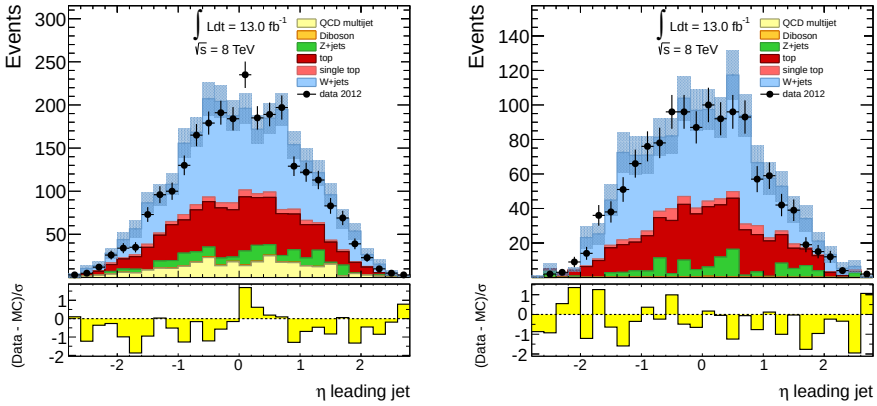

(a) Electron Channel

(b) Muon Channel

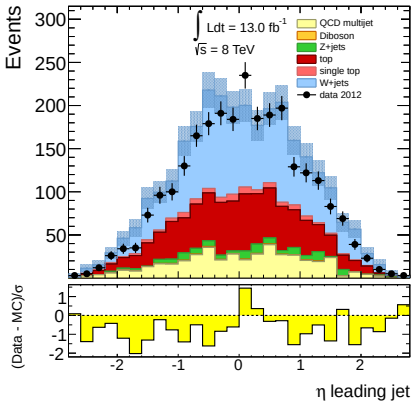

(c) Electron Channel

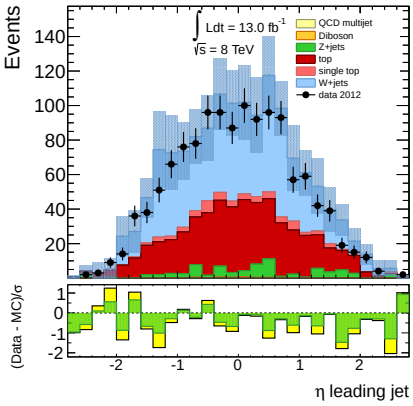

(d) Muon Channel

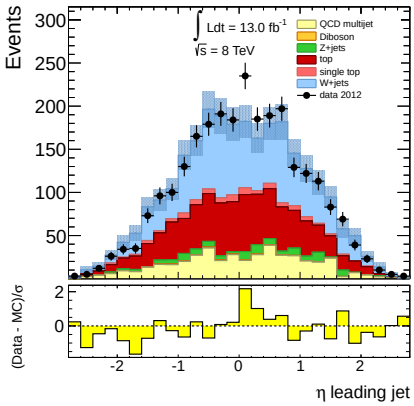

(e) Electron Channel

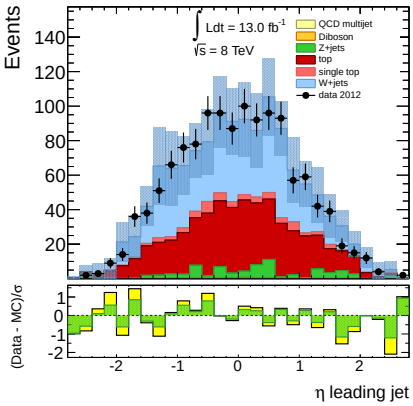

(f) Muon Channel

Figure D.16. jLeading jet η distributions in the W+jets CR with no SFs applied (top), scaling non-W+jets backgrounds only (middle) and after the application of all SFs (bottom). The Monte Carlo simulation (`Alpgen` generator) is normalized to an integrated luminosity of 13.0 fb^{1}.

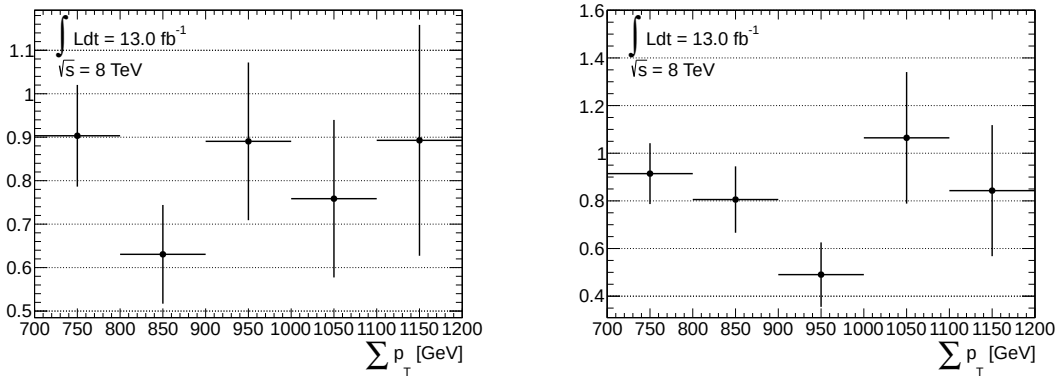

(a) Electron Channel (b) Muon Channel

Figure D.17. W+jets scale factor as a function of $\sum p_{\mathrm{T}}$ for samples generated with `Alpgen`.

APPENDIX E

BACKGROUND DISTRIBUTIONS: ϵ_{FAKE} - ALPGEN GENERATOR

The following distributions correspond to Fig. 5.20, when the W/Z+jets samples are generated with `Alpgen`.

The obtained values for the fake lepton efficiency, ϵ_{fake}, for the different channels are

$$\text{SF(electron)} = 0.465 \pm 0.035^{+0.045}_{-0.015}$$

$$\text{SF(muon)} < 0.062\,(95\%\,\text{CL}).$$

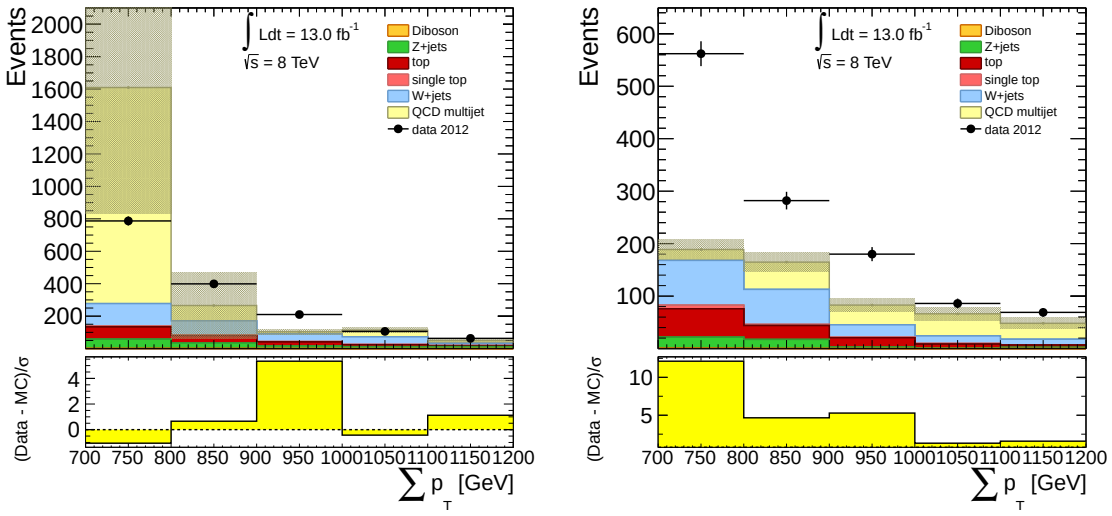

(a) Electron Channel, Loose

(b) Muon Channel, Loose

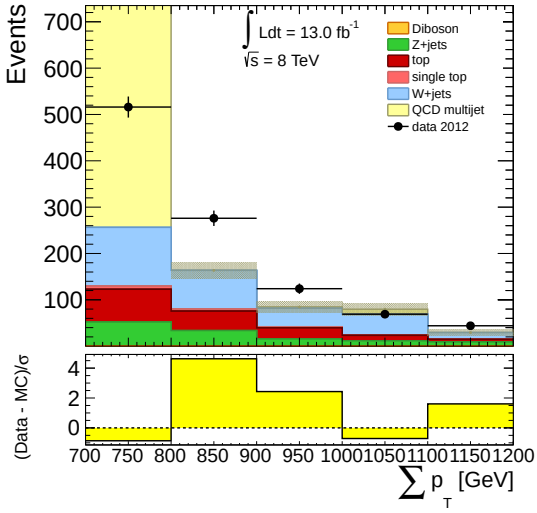

(c) Electron Channel, Tight

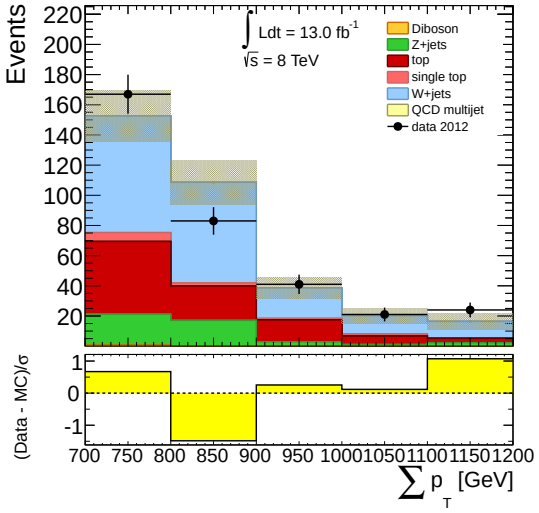

(d) Muon Channel, Tight

Figure E.1. Loose and tight $\sum p_{\mathrm{T}}$ distributions in the QCD multijet CR, after scaling all prompt backgrounds. The Monte Carlo simulation is normalized to an integrated luminosity of 13.0 fb^{-1}. The error bars include the statistical error only. The bottom pane of each subfigure displays the difference between data and simulation over their statistical uncertainty.

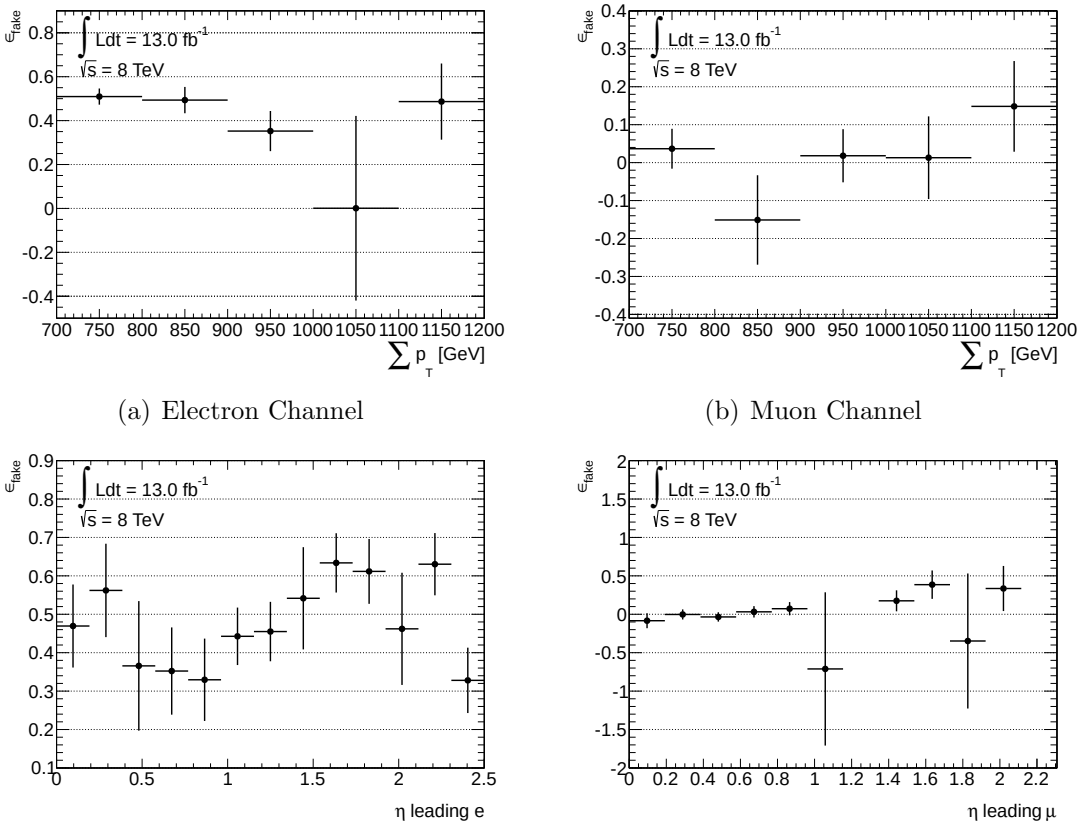

(a) Electron Channel

(b) Muon Channel

(c) Electron Channel

(d) Muon Channel

Figure E.2. The ϵ_{fake} versus $\sum p_{\text{T}}$ and lepton η. These plots correspond to the ratio of tight QCD events over loose QCD events in Fig. E.1.

APPENDIX F

BACKGROUND DISTRIBUTIONS: ϵ_{REAL} - ALPGEN GENERATOR

The following distributions correspond to Fig. 5.25, when the W/Z+jets samples are generated with `Alpgen`.

The obtained values for the real lepton efficiency, ϵ_{real}, for the different channels are

$$\mathrm{SF(electron)} = 0.939 \pm 0.008^{+5.4\times10^{-5}}_{-1.3\times10^{-5}}$$

$$\mathrm{SF(muon)} = 0.979 \pm 0.007^{+4.8\times10^{-4}}_{-1.0\times10^{-5}}.$$

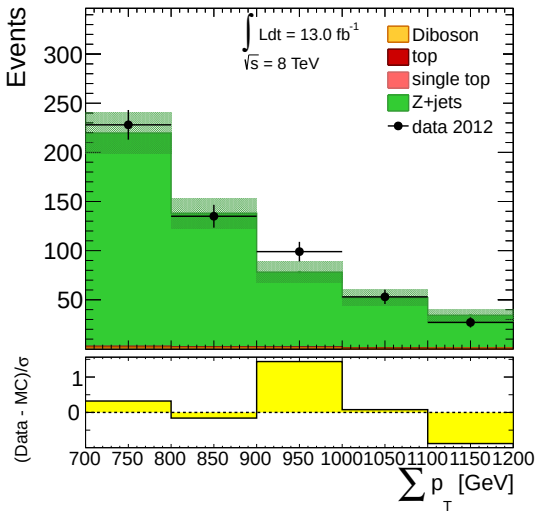

(a) Electron Channel, Loose

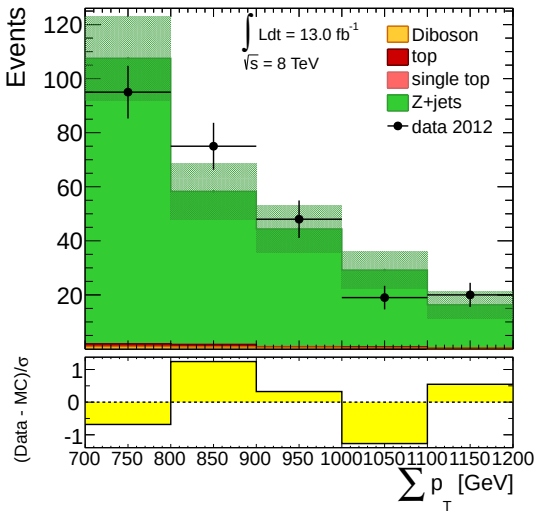

(b) Muon Channel, Loose

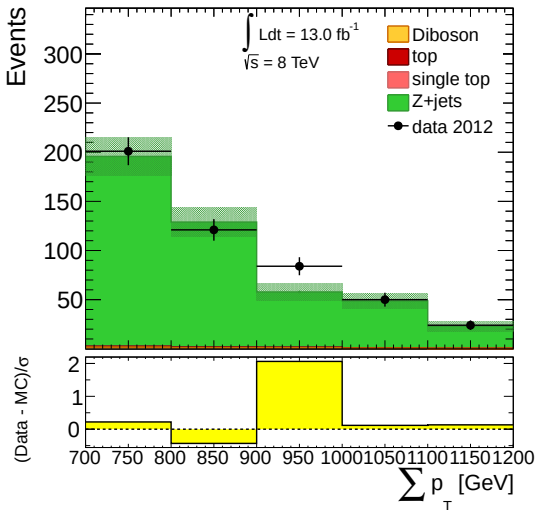

(c) Electron Channel, Tight

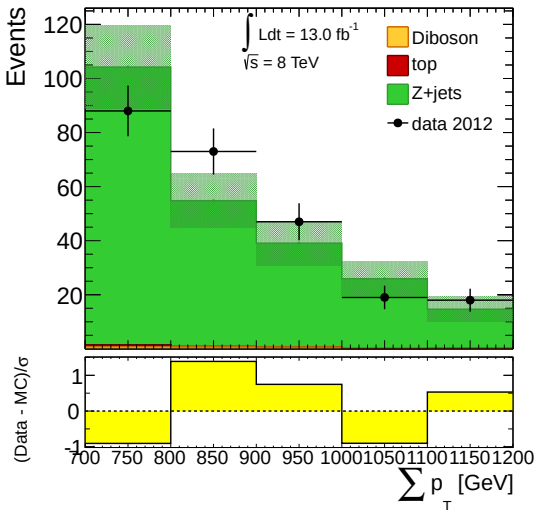

(d) Muon Channel, Tight

Figure F.1. Loose and tight $\sum p_{\mathrm{T}}$ distributions in the real lepton (Z+jets) control region. The Monte Carlo simulation is normalized to an integrated luminosity of 13.0 fb^{-1}. The error bars include the statistical error only. The bottom pane of each subfigure displays the difference between data and simulation over their statistical uncertainty.

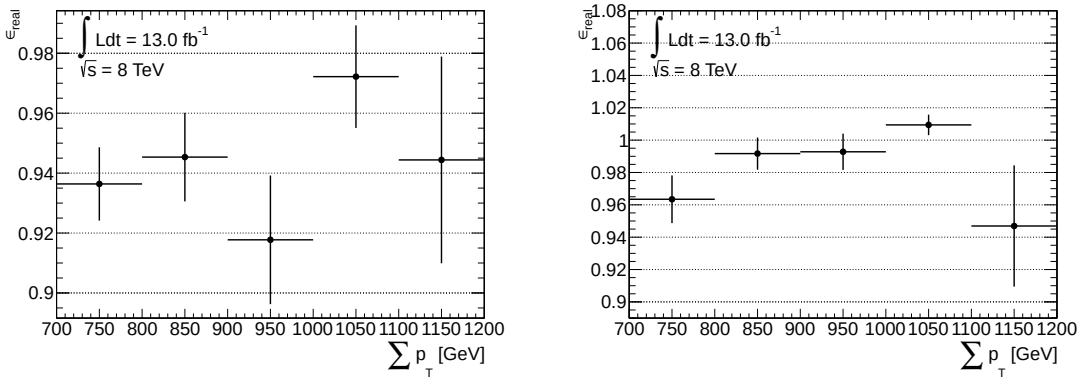

(a) Electron Channel (b) Muon Channel

Figure F.2. The ϵ_{real} versus $\sum p_{\text{T}}$. These plots correspond to the ratio of tight over loose real lepton events in Fig. F.1.

APPENDIX G

FINAL DISTRIBUTIONS IN THE SIDEBAND REGION - ALPGEN GENERATOR

Figure G.1 shows the $\sum p_{\mathrm{T}}$ distributions in the sideband region before and after the application of the scale factors, for both the electron and muon channels. Leading lepton and jet kinematics are illustrated in Figs. G.2 and G.3. After scaling the W/Z+jets and $t\bar{t}$ background, and using the matrix method to estimate the QCD contribution, the data-simulation agreement in the majority of the distributions is within $\pm 2\sigma$.

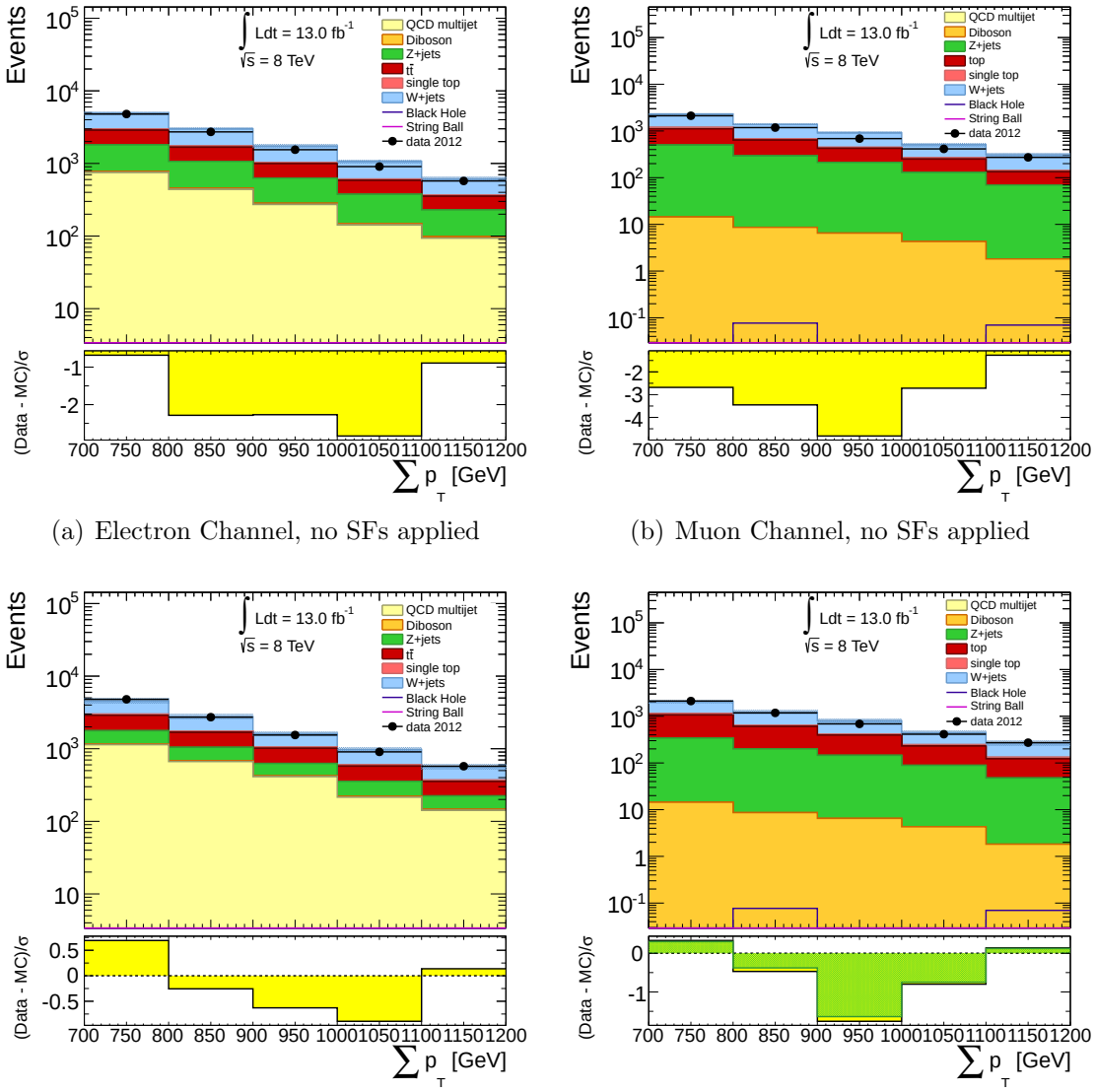

(a) Electron Channel, no SFs applied

(b) Muon Channel, no SFs applied

(c) Electron Channel, SFs applied

(d) Muon Channel, SFs applied

Figure G.1. $\sum p_{\mathrm{T}}$ distributions in the sideband region, before (upper plots) and after (lower plots) the application of the scale factors. The Monte Carlo simulation (`Alpgen` generator) is normalized to an integrated luminosity of 13.0 fb^{-1}. The error bars include both statistical and systematic uncertainties. The bottom pane of each subfigure displays the difference between data and simulation over their statistical uncertainty (yellow band) or statistical+systematic uncertainties (green band).

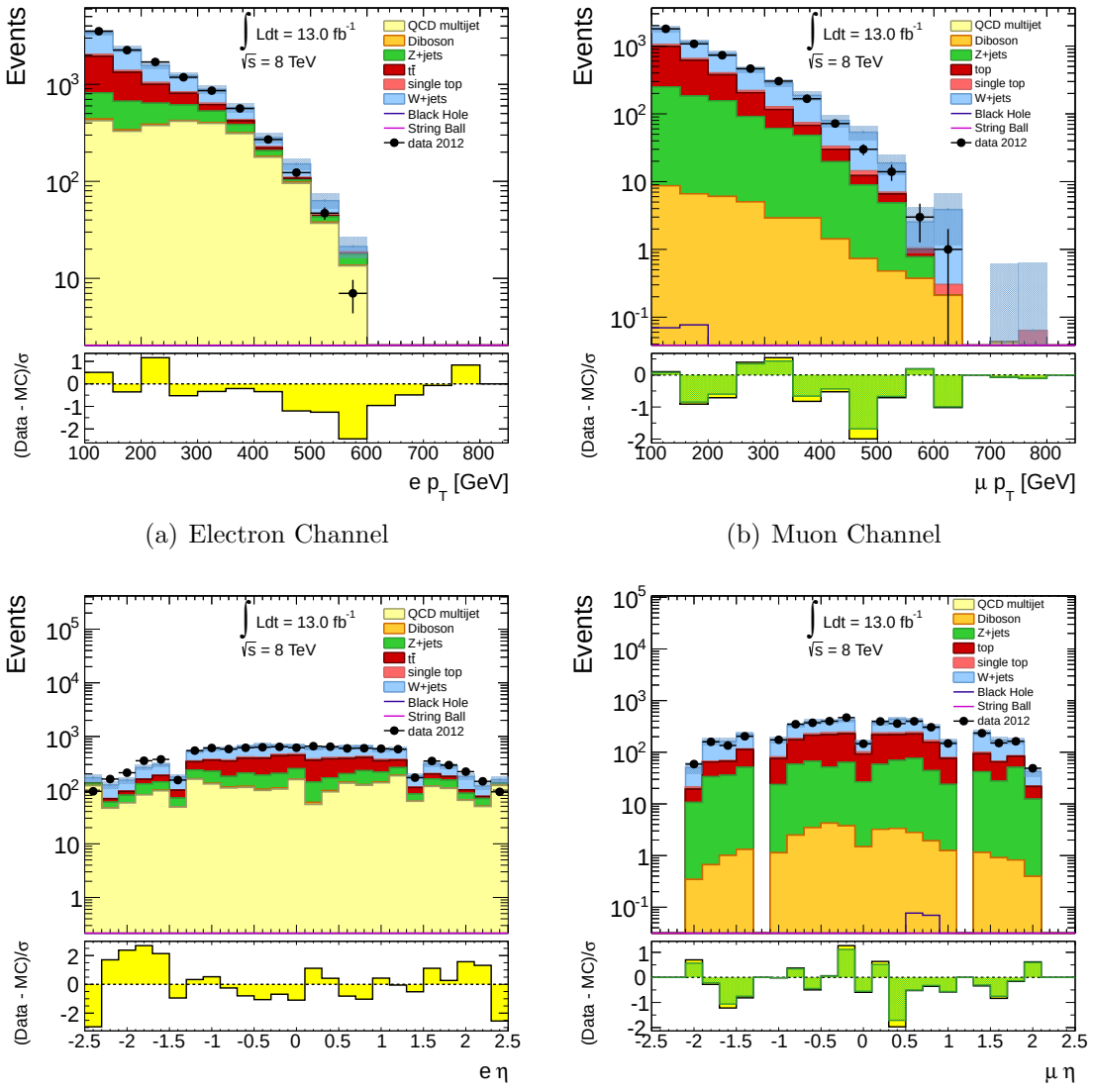

(a) Electron Channel

(b) Muon Channel

(c) Electron Channel

(d) Muon Channel

Figure G.2. Leading lepton p_{T} and η distributions in the sideband region after the application of the scale factors. The Monte Carlo simulation (`Alpgen` generator) is normalized to an integrated luminosity of 13.0 fb^{-1}. The error bars include both statistical and systematic uncertainties. The bottom pane of each subfigure displays the difference between data and simulation over their statistical uncertainty (yellow band) or statistical+systematic uncertainties (green band).

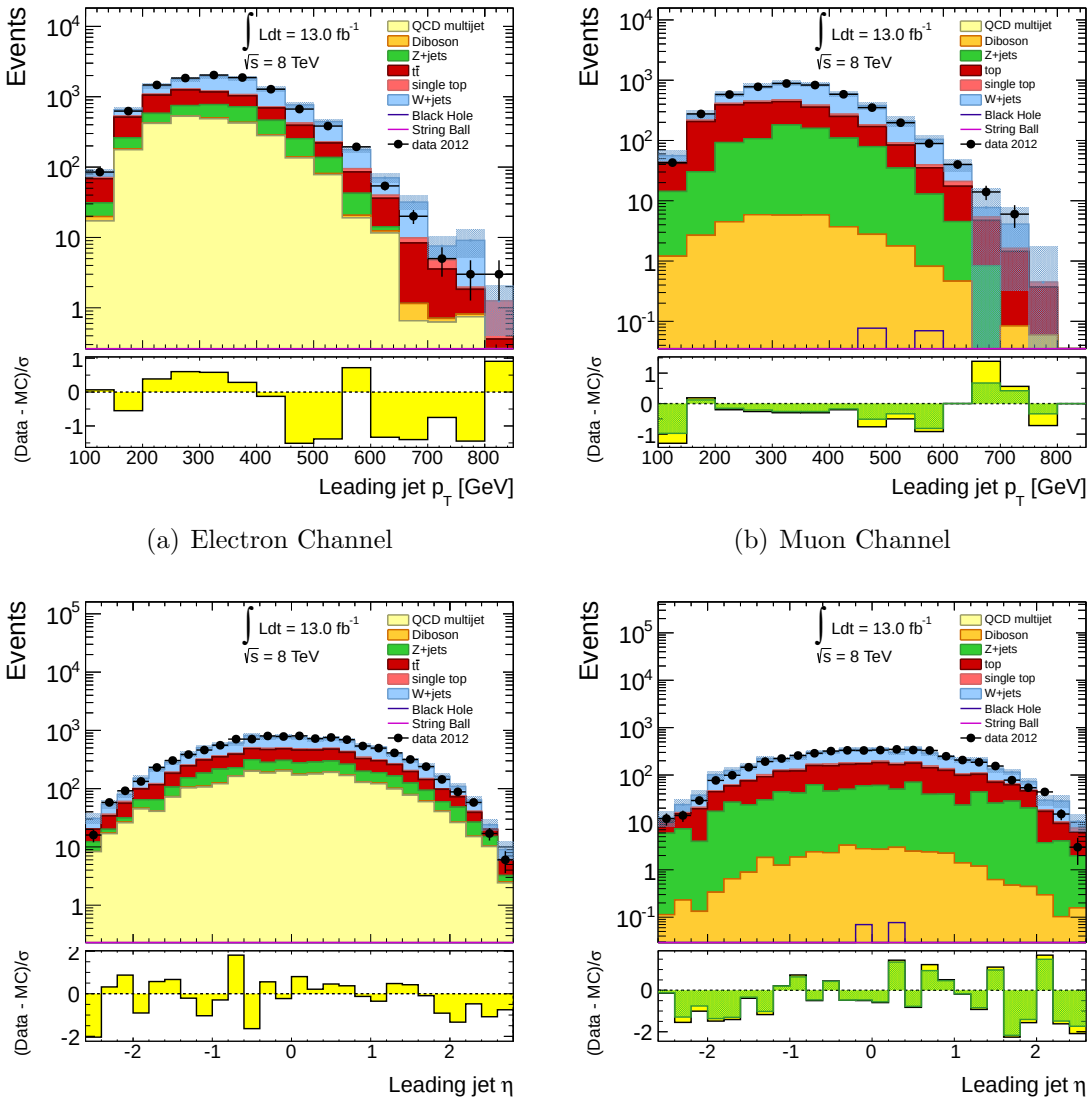

(a) Electron Channel

(b) Muon Channel

(c) Electron Channel

(d) Muon Channel

Figure G.3. Leading jet p_{T} and η distributions in the sideband region after the application of the scale factors. The Monte Carlo simulation (`Alpgen` generator) is normalized to an integrated luminosity of 13.0 fb^{-1}. The error bars include both statistical and systematic uncertainties. The bottom pane of each subfigure displays the difference between data and simulation over their statistical uncertainty (yellow band) or statistical+systematic uncertainties (green band).

APPENDIX H

BACKGROUND PREDICTION IN THE SIGNAL REGION - ALPGEN GENERATOR

The observed and predicted event yields, following the estimation procedure described in Sec. 4.5 and the scale factors and lepton efficiencies calculated in Sec. 5.1, are plotted in Fig. H.1. The $\sum p_{\mathrm{T}}$ and event invariant mass distributions include the validation region (1200 GeV$\leq \sum p_{\mathrm{T}} \leq$ 1500 GeV) and the signal region ($\sum p_{\mathrm{T}} >$ 1500 GeV). Two representative samples depict the expected behavior for black holes and string balls. The Standard Model background estimates are in good agreement with the observed data. No excess of events is observed beyond the SM expectations. Taking into account the statistical and systematic uncertainties, the data-simulation agreement is within $\pm 2\sigma$ for both the electron and muon channels.

Table H.1. Final background predictions (`Alpgen`) and uncertainties in the signal region for the electron channel, for different $\sum p_{\mathrm{T}}$ thresholds. The observed and expected values correspond to an integrated luminosity of 13.0 fb^{-1}.

$\sum p_{\mathrm{T}}$ [GeV]	Total MC	Data
> 1200	$1016.0 \pm 73.2 \pm 25.2$	909
> 1500	$250.0 \pm 22.9 \pm 15.1$	232
> 2000	$29.5 \pm 5.9 \pm 3.4$	35

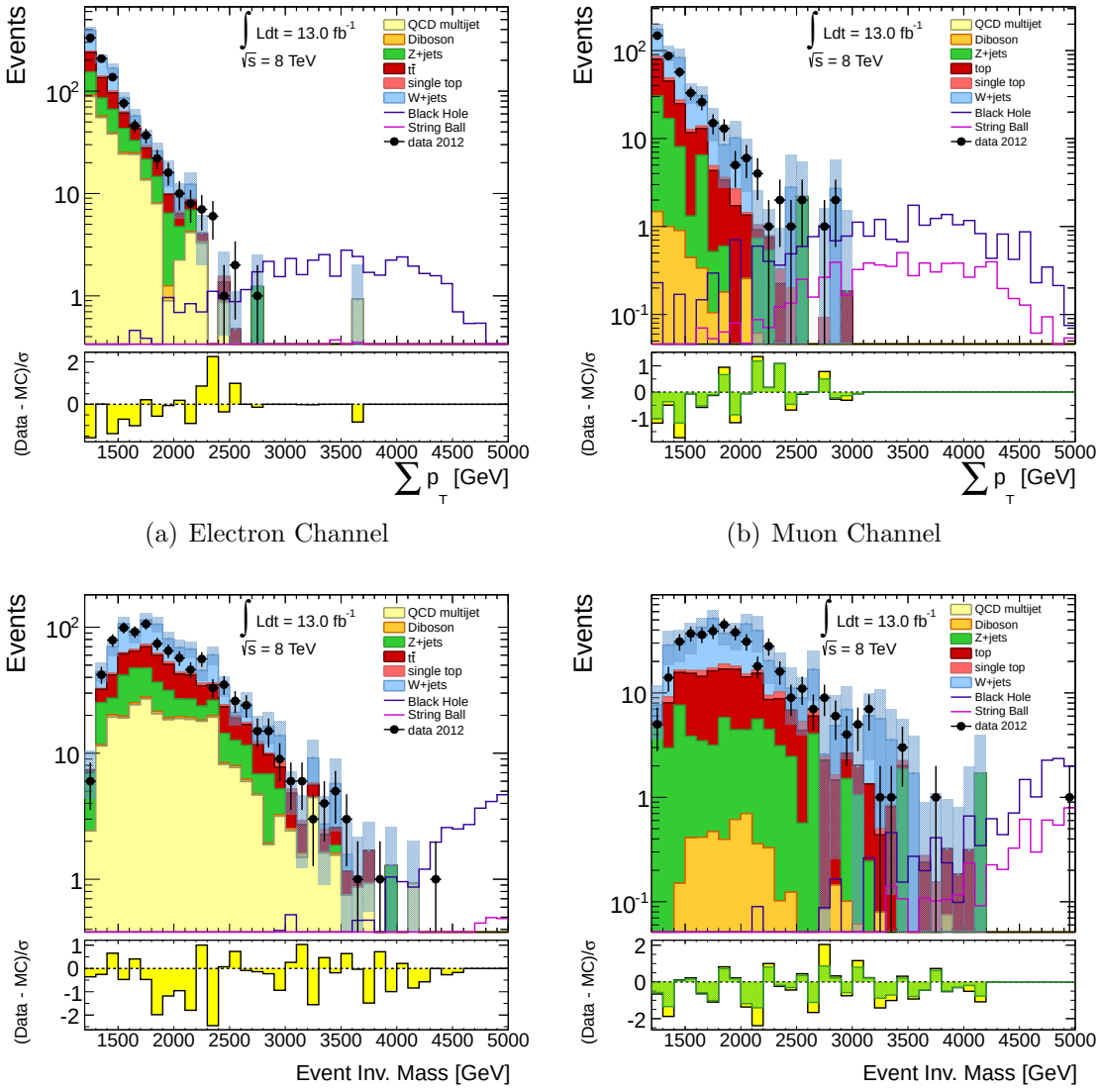

(a) Electron Channel

(b) Muon Channel

(c) Electron Channel

(d) Muon Channel

Figure H.1. $\sum p_{\mathrm{T}}$ and event invariant mass distributions in the validation and signal regions, after the application of the scale factors. The Monte Carlo simulation (`Alpgen` generator) is normalized to an integrated luminosity of 13.0 fb^{-1}. The error bars include both statistical and systematic uncertainties. The bottom pane of each subfigure displays the difference between data and predicted background over their statistical uncertainty (yellow band) or statistical+systematic uncertainties (green band).

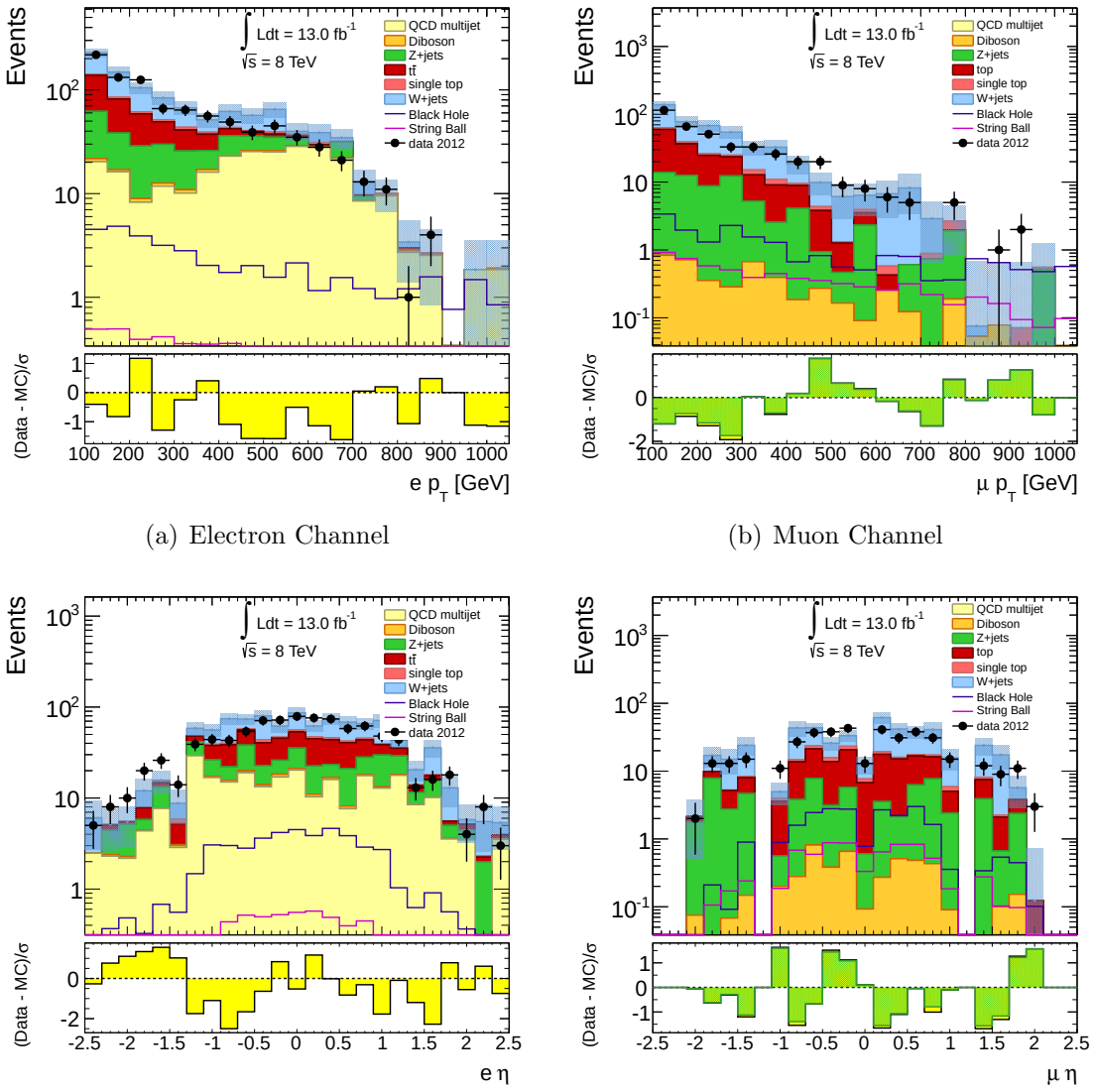

(a) Electron Channel

(b) Muon Channel

(c) Electron Channel

(d) Muon Channel

Figure H.2. Leading lepton p_{T} and η distributions in the validation and signal regions, after the application of the scale factors. The Monte Carlo simulation (`Alpgen` generator) is normalized to an integrated luminosity of 13.0 fb^{-1}. The error bars include both statistical and systematic uncertainties. The bottom pane of each subfigure displays the difference between data and predicted background over their statistical uncertainty (yellow band) or statistical+systematic uncertainties (green band).

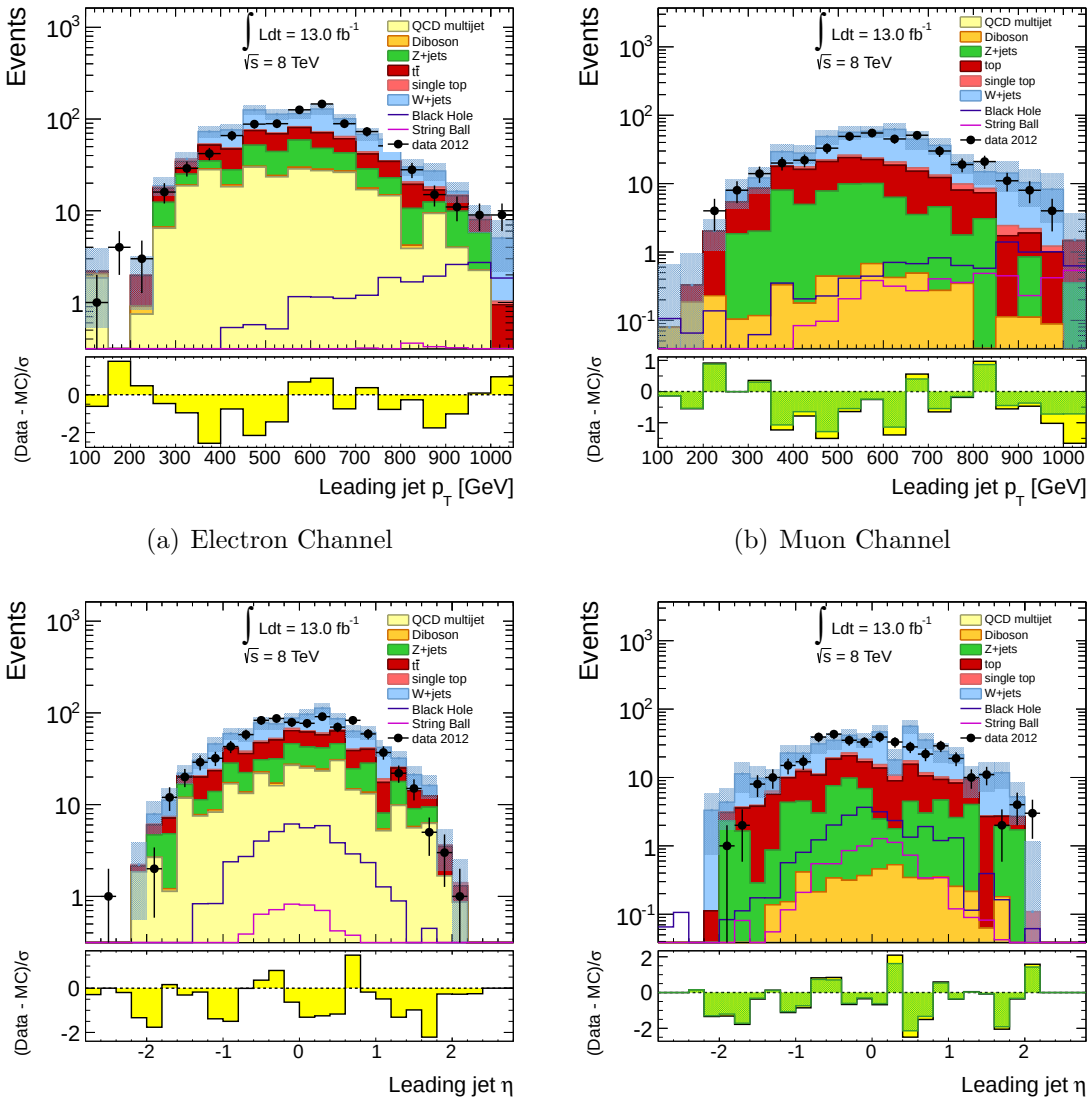

(a) Electron Channel

(b) Muon Channel

(c) Electron Channel

(d) Muon Channel

Figure H.3. Leading jet p_{T} and η distributions in the validation and signal regions, after the application of the scale factors. The Monte Carlo simulation (`Alpgen` generator) is normalized to an integrated luminosity of 13.0 fb^{-1}. The error bars include both statistical and systematic uncertainties. The bottom pane of each subfigure displays the difference between data and predicted background over their statistical uncertainty (yellow band) or statistical+systematic uncertainties (green band).

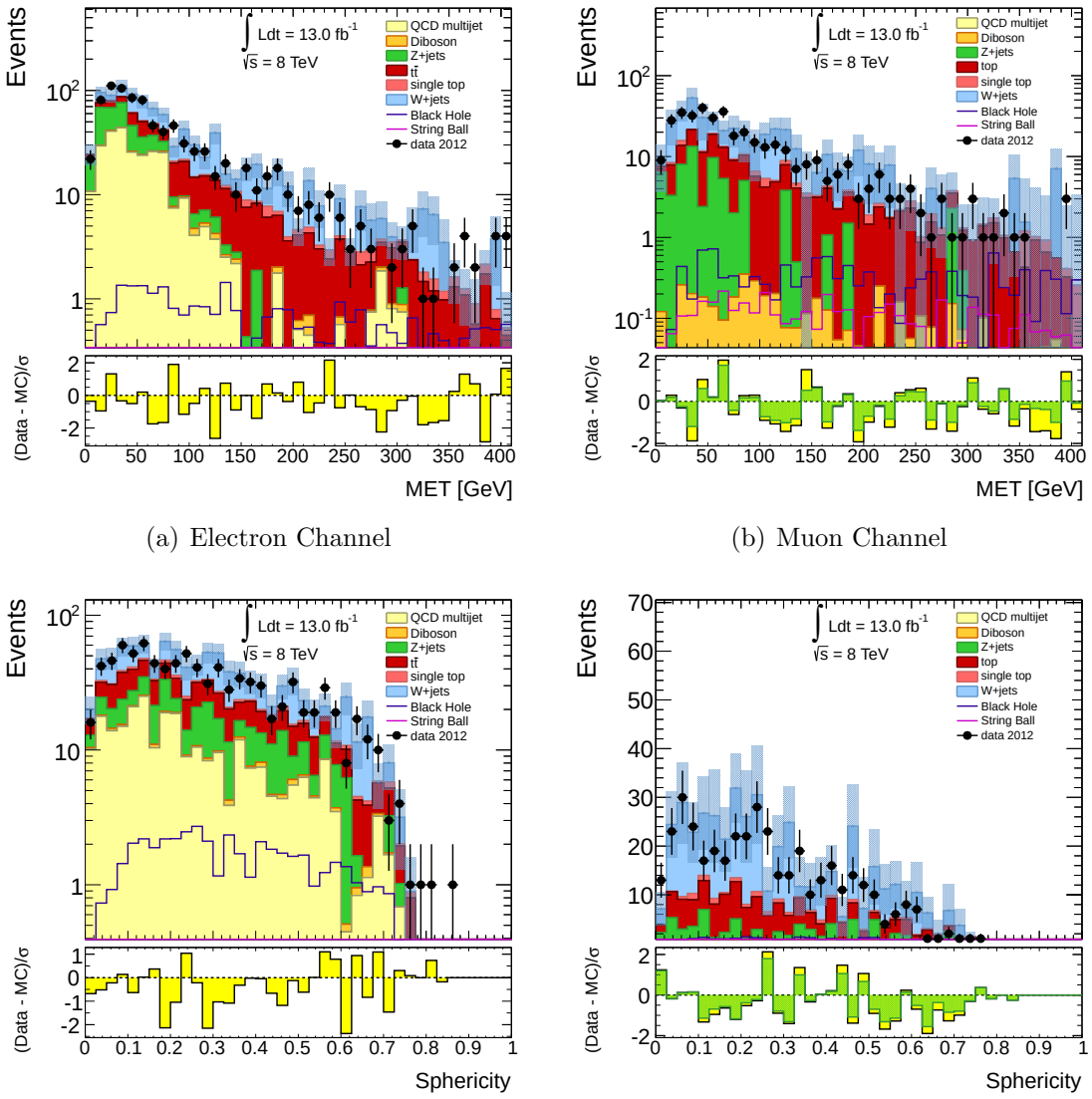

(a) Electron Channel

(b) Muon Channel

(c) Electron Channel

(d) Muon Channel

Figure H.4. $E_{\mathrm{T}}^{\mathrm{miss}}$ and event sphericity distributions in the validation and signal regions, after the application of the scale factors. The Monte Carlo simulation (`Alpgen` generator) is normalized to an integrated luminosity of 13.0 fb^{-1}. The error bars include both statistical and systematic uncertainties. The bottom pane of each subfigure displays the difference between data and predicted background over their statistical uncertainty (yellow band) or statistical+systematic uncertainties (green band).

Table H.2. Final background predictions (`Alpgen`) and uncertainties in the signal region for the muon channel, for different $\sum p_{\mathrm{T}}$ thresholds. The observed and expected values correspond to an integrated luminosity of 13.0 fb^{-1}.

$\sum p_{\mathrm{T}}$ [GeV]	Total MC	Data
> 1200	$467.6 \pm 40.4 \pm 24.2$	403
> 1500	$115.2 \pm 15.0 \pm 8.9$	111
> 2000	$16.4 \pm 5.1 \pm 1.5$	19

BIBLIOGRAPHY

[1] Kanti, P. Black holes in theories with large extra dimensions: A Review. *Int. J. Mod. Phys. A19* (2004), 4899–4951.

[2] The ATLAS Collaboration. The ATLAS Experiment at the CERN Large Hadron Collider. *JINST 3* (2008), S08003.

[3] C. Boellaard, et al. Signatures of extra dimensions. `http://staff.science.uva.nl/~jdeboer/education/projects/projects/extradim.pdf/`, 2005.

[4] A. J. Smith. Supersymmetry and parallel dimensions: Harvard physicst randall among worlds leading string theorists. `http://www.thecrimson.com/article/2006/1/6/supersymmetry-and-parallel-dimensions-professor-of/`, 2006.

[5] D. C. Dai, et al. BlackMax: A black hole event generator with rotation, recoil, split branes and brane tensions. *Phys. Rev. D 77* (2008), 076007.

[6] S. C. Park. Black holes and the LHC: A review. *Progress in Particle and Nuclear Physics 67*, 3 (July 2012), 617–650.

[7] S. Hossenfelder. What black holes can teach us. arXiv:0412265 (2004) [hep-ph].

[8] Pumplin, J., et al. New generation of parton distributions with uncertainties from global QCD analysis. *JHEP 07* (2002), 012.

[9] K. Nozari, and P. Shahini. TeV scale black holes thermodynamics with extra dimensions and quantum gravity effects. arXiv:1206.5624 (2012) [hep-th].

[10] P. Meade, and L. Randall. Black Holes and Quantum Gravity at the LHC. *JHEP 05* (2008), 003.

[11] D.M. Gingrich, and K. Martell. Study of highly-excited string states at the Large Hadron Collider. *Phys. Rev. D78* (2008), 115009.

[12] S. B. Giddings, and S. D. Thomas. High-energy colliders as black hole factories: The End of short distance physics. *Phys. Rev. D65* (2002), 056010.

[13] LEP Exotica Working Group, the ALEPH, DELPHI, L3 and OPAL Collaborations. Combination of lep results on direct searches for large extra dimensions. *CERN Note LEP Exotica WG 2004-03* (2004).

[14] CDF Collaboration. Search for large extra dimensions in final states containing one photon or jet and large missing transverse energy produced in $p\bar{p}$ collisions at $\sqrt{s} = 1.96$ TeV. *Phys. Rev. Lett. 101* (2008), 181602.

[15] The ATLAS Collaboration. Search for TeV-scale gravity signatures in final states with leptons and jets with the ATLAS detector at $\sqrt{s} = 7$ TeV. *Physics Letters B 716*, 1 (2012), 122 – 141.

[16] The CMS Collaboration. Search for Black Holes in pp Collisions at $\sqrt{s} = 8$ TeV with the CMS detector. *CMS-PAS-EXO-12-009* (2012).

[17] The ATLAS Collaboration. Search for new phenomena with the monojet and missing transverse momentum signature using the ATLAS detector in $\sqrt{s} = 7$ TeV proton-proton collisions. *Phys. Lett. B705* (2011), 294–312.

[18] L. Evans, and P. Bryant. LHC Machine. *Journal of Instrumentation 3*, 08 (2008), S08001.

[19] S. Weinberg. A Model of Leptons. *Phys. Rev. Lett. 19* (1967), 1264–1266.

[20] P. W. Higgs. Spontaneous Symmetry Breakdown without Massless Bosons. *Phys. Rev. 145* (1966), 1156–1163.

[21] F. Englert, and R. Brout. Broken symmetry and the mass of gauge vector mesons. *Phys. Rev. Lett. 13* (1964), 321.

[22] G. S. Guralnik, C.R. Hagen, and T.W.B. Kibble. Global conservation laws and massless particles. *Phys. Rev. Lett. 13* (1964), 585.

[23] T. L. Barklow, et al. *Electroweak Symmetry Breaking and New Physics at the TeV Scale*. Advanced Series on Directions in High Energy Physics. World Scientific Publ., Singapore, 1996.

[24] S. Dawson. Introduction to electroweak symmetry breaking. *hep-ph/9901280* (1998), 1–83.

[25] F. Halzen, and A. D. Martin. *Quarks & Leptons: An introductory course in modern particle physics*. John Wiley & Sons, New York, USA, 1984.

[26] I. J. R. Aitchison, and A. J. G. Hey. *Gauge theories in particle physics: a practical introduction; 3rd ed.* Graduate student series in physics. IOP, Bristol, 2004.

[27] J. F. Donoghue, E. Golowich, and B. R. Holstein. *Dynamics of the Standard Model*. Cambridge monographs on particle physics, nuclear physics, and cosmology. Cambridge Univ. Press, Cambridge, 1992. Includes exercises.

[28] The ATLAS Collaboration. Observation of a new particle in the search for the Standard Model Higgs boson with the ATLAS detector at the LHC. *Phys. Lett. B716* (2012), 1–29.

[29] The CMS Collaboration. Observation of a new boson at a mass of 125 GeV with the CMS experiment at the LHC. *Phys.Lett. B716* (2012), 30–61.

[30] J. C. Long, H. W. Chan, and J. C. Price. Experimental status of gravitational strength forces in the subcentimeter regime. *Nucl. Phys. B539* (1999), 23–34.

[31] T. Kaluza. Zum Unitätsproblem in der Physik. *Sitzungsber. Preuss. Akad. Wiss. Phys. Math.* (1921), 966–972.

[32] O. Klein. Quantentheorie und fünfdimensionale Relativitätstheorie. *Zeitschrift fur Physik 37* (Dec. 1926), 895–906.

[33] Gravity in large extra dimensions. `http://www.lbl.gov/Science-Articles/Research-Review/Magazine/2001/Fall/departments/frontline/physics.html/`, 2001.

[34] N. Arkani-Hamed, S. Dimopoulos, and G.R. Dvali. The hierarchy problem and new dimensions at a millimeter. *Phys. Lett. B 429* (1998), 263–272.

[35] L. Randall, and R. Sundrum. A large mass hierarchy from a small extra dimension. *Phys. Rev. Lett. 83* (1999), 3370–3373.

[36] N. Arkani-Hamed, S. Dimopoulos, and G. R. Dvali. Phenomenology, astrophysics and cosmology of theories with submillimeter dimensions and TeV scale quantum gravity. *Phys. Rev. D59* (1999), 086004.

[37] Hawking, S. Particle creation by black holes. *Commun. Math. Phys. 43* (1975), 199.

[38] L. A. Anchordoqui, et al. Black holes from cosmic rays: Probes of extra dimensions and new limits on tev-scale gravity. *Phys. Rev.* (2002), 124027.

[39] Cheung, K. Black hole production and large extra dimensions. *Phys. Rev. Lett. 88* (2002), 221602.

[40] S. Dimopoulos, and R. Emparan. String balls at the LHC and beyond. *Phys. Lett. B 526* (2002), 393–398.

[41] C. W. Misner, K. S. Thorne, and J. A. Wheeler. *Gravitation*, 2 ed. W H Freeman and Company, 1973.

[42] R. Emparan, G. T. Horowitz, and R. C. Myers. Black holes radiate mainly on the brane. *Phys. Rev. Lett. 85* (2000), 499–502.

[43] S. Dimopoulos, and G. Landsberg. Black holes at the large hadron collider. *Phys. Rev. Lett. 87* (Sep 2001), 161602.

[44] C. M. Harris, et al. Exploring higher dimensional black holes at the large hadron collider. *JHEP 0505* (2005), 053.

[45] D0 Collaboration. Search for large extra dimensions via single photon plus missing energy final states at $\sqrt{s} = 1.96$ TeV. *Phys. Rev. Lett. 101* (2008), 011601.

[46] The ATLAS Collaboration. Expected Performance of the ATLAS Experiment - Detector, Trigger and Physics. *CERN-OPEN-2008-020* (2009).

[47] T. Cornelissen, et al. Concepts, Design and Implementation of the ATLAS New Tracking (NEWT). *ATL-SOFT-PUB-2007-007* (2007).

[48] The ATLAS Collaboration. Performance of primary vertex reconstruction in proton-proton collisions at $\sqrt{s}$ =7 TeV in the ATLAS experiment. *ATLAS-CONF-2010-069* (2010).

[49] The ATLAS Collaboration. Performance of the ATLAS Inner Detector Track and Vertex Reconstruction in the High Pile-Up LHC Environment. *ATLAS-CONF-2012-042* (2012).

[50] The ATLAS Collaboration. Expected electron performance in the ATLAS experiment. *ATL-PHYS-PUB-2011-006* (2011).

[51] The ATLAS Collaboration. Improved electron reconstruction in ATLAS using the Gaussian Sum Filter-based model for bremsstrahlung. *ATLAS-CONF-2012-047* (2012).

[52] M. Cacciari, G. P. Salam, and G. Soyez. The anti-k_{T} jet clustering algorithm. *JHEP 04* (2008), 063.

[53] The ATLAS Collaboration. Jet energy measurement with the ATLAS detector in proton-proton collisions at $\sqrt{s} = 7$ TeV. *CERN-PH-EP-2011-191* (2011).

[54] The ATLAS Collaboration. Pile-up corrections for jets from proton-proton collisions at $\sqrt{s} = 7$ TeV in ATLAS in 2011. *ATLAS-CONF-2012-064* (2012).

[55] The ATLAS Collaboration. Jet energy scale and its systematic uncertainty in proton-proton collisions at $\sqrt{s} = 7$ TeV in ATLAS 2010 data. *ATLAS-CONF-2011-032* (2011).

[56] The ATLAS Collaboration. Light-quark and Gluon Jets: Calorimeter Response, Jet Energy Scale Systematics and Properties. *ATLAS-CONF-2012-138* (2012).

[57] The ATLAS Collaboration. Identification of muon candidates in pp collisions at $\sqrt{s} = 900$ GeV with the ATLAS detector. *ATLAS-CONF-2010-015* (2010).

[58] The ATLAS Collaboration. Muon Reconstruction Performance. *ATLAS-CONF-2010-064* (2010).

[59] S. Agostinelli, et al. Geant4–a simulation toolkit. *Nucl. Instr. and Meth. A 506* (2003), 250–303.

[60] J. Allison, et al. Geant4 developments and applications. *IEEE Trans. Nucl. Sci. 53* (2006), 270.

[61] The ATLAS Collaboration. The atlas simulation infrastructure. *Eur. Phys. J. C 70* (2010), 823–874.

[62] The ATLAS Collaboration. The simulation principle and performance of the ATLAS fast calorimeter simulation FastCaloSim. Tech. Rep. ATL-PHYS-PUB-2010-013, CERN, Geneva, Oct 2010.

[63] T. Gleisberg, et al. Event generation with SHERPA 1.1. *JHEP 0902* (2009), 007.

[64] H. Lai, et al. New parton distributions for collider physics. *Phys. Rev. D 82* (2010), 074024.

[65] S. Catani, et al. Vector boson production at hadron colliders: A Fully exclusive QCD calculation at NNLO. *Phys. Rev. Lett. 103* (2009), 082001.

[66] M. L. Mangano, et al. `ALPGEN`, a generator for hard multiparton processes in hadronic collisions. *JHEP 07* (2003), 001.

[67] T. Sjostrand, S. Mrenna, and P. Z. Skands. PYTHIA 6.4 Physics and Manual. *JHEP 05* (2006), 026.

[68] P. Nason. A New method for combining NLO QCD with shower Monte Carlo algorithms. *JHEP 0411* (2004), 040.

[69] M. Aliev, et al. HATHOR: hadronic Top and heavy quark cross section calculator. *Comput. Phys. Commun. 182* (2011), 1034.

[70] S. Frixione, and B.R Webber. Matching NLO QCD computations and parton shower simulations. *JHEP 06* (2002), 029.

[71] B. P. Kersevan, and E. Richter-Was. The Monte Carlo event generator AcerMC version 2.0 with interfaces to PYTHIA 6.2 and HERWIG 6.5. *arXiv:hep-ph/0405247* (2004).

[72] J. A. Frost, et al. Phenomenology of production and decay of spinning extra-dimensional black holes at hadron colliders. *JHEP 10* (2009), 014.

[73] A. D. Martin, et al. Parton distributions for the LHC. *Eur. Phys. J. C63* (2009), 189–285.

[74] D-C. Dai, G. Starkman, D. Stojkovic, C. Issever, E. Rizvi, and J. Tseng. `BlackMax`: A black-hole event generator with rotation, recoil, split branes, and brane tension. *Phys. Rev. D 77* (2008), 076007.

[75] D-C. Dai, C. Issever, E. Rizvi, G. Starkman, D. Stojkovic, and J. Tseng. Manual of `blackmax`, a black-hole event generator with rotation, recoil, split branes, and brane tension. arXiv:0902.3577 [hep-ph].

[76] The ATLAS Collaboration. Luminosity Determination in pp Collisions at $\sqrt{s} = 7$ TeV Using the ATLAS Detector at the LHC. *Eur. Phys. J. C71* (2011), 1630.

[77] The ATLAS Collaboration. Measurement of the top quark-pair production cross section with ATLAS in pp collisions at $\sqrt{s} = 7$ TeV. *Eur. Phys. J. C 71* (2011), 1–36.

[78] The ATLAS Collaboration. Search for s-Channel Single Top-Quark Production in pp Collisions at $\sqrt{s} = 7$ TeV. *ATLAS-CONF-2011-118* (2011).

[79] W. A. Rolke, A. M. López, and J. Conrad. Limits and confidence intervals in the presence of nuisance parameters. *Nuclear Instruments and Methods in Physics Research A 551* (October 2005), 493–503.

[80] F. James, and M. Roos. Minuit: A System for Function Minimization and Analysis of the Parameter Errors and Correlations. *Comput. Phys. Commun. 10* (1975), 343–367.

[81] F. James. INTERPRETATION OF THE SHAPE OF THE LIKELIHOOD FUNCTION AROUND ITS MINIMUM. (TALK). *Comput. Phys. Commun. 20* (1980), 29–35.

[82] R. Brun, and F. Rademakers. ROOT: An object oriented data analysis framework. *Nucl. Instrum. Meth. A389* (1997), 81–86.